JAERI-Research
96-018

REVIEW OF JT-60U EXPERIMENTAL RESULTS FROM FEBRUARY TO OCTOBER, 1995

March 1996

JT-60 Team

日本原子力研究所
Japan Atomic Energy Research Institute

本レポートは，日本原子力研究所が不定期に公刊している研究報告書です。
入手の問合わせは，日本原子力研究所技術情報部情報資料課（〒319-11 茨城県那珂郡東海村）あて，お申し越しください。なお，このほかに財団法人原子力弘済会資料センター（〒319-11 茨城県那珂郡東海村日本原子力研究所内）で複写による実費領布をおこなっております。

This report is issued irregularly.
Inquiries about availability of the reports should be addressed to Information Division, Department of Technical Information, Japan Atomic Energy Research Institute, Tokai-mura, Naka-gun, Ibaraki-ken 319-11, Japan.

編集兼発行　日本原子力研究所
印　　刷　㈱原子力資料サービス

JAERI−Research 96−018

Review of JT-60U Experimental Results from February to October, 1995

JT-60 Team※

Depertment of Fusion Plasma Research
and
Depertment of Fusion Facility
Naka Fusion Research Establishment
Japan Atomic Energy Research Institute
Naka-machi, Naka-gun, Ibaraki-ken

(Received February 28, 1996)

The hot-ion H-mode regime was extended to I_p=4.5MA by using rotation velocity control to avoid mode locking in low q(q<3) regime, which is equivalent ITER operation regime. To improve the H-mode confinement, the effect of plasma shape has been investigated with the change of triangularity (δ) by the rearrangement of PF power supplies. Edge density and edge temperature at the onset of ELMs were improved by 30-40% and 80% respectively with increasing δ from 0.1 to 0.4. As a result, limit of the normalized edge pressure gradient at the onset of ELMs increased. The reversed shear regime has been established with the formation of internal transport barrier (ITB) and enhanced confinement both for ions and electrons. The radius of ITB was extended to r/a~0.65. The electron temperature was increased at the comparable of ion temperature. The β_N value is as large as one of high β_P H-mode. The reversed magnetic shear has been sustained by LHCD for 7.5 s. On the other hand, Helium density inside the ITB kept high, which suggests that it is difficult to purge from the ITB for Helium ash exhaust. The TAE mode can be controlled by changing the profile of toroidal rotation velocity responsible to the tangential beam injection such as co- and counter directions. Combined Neon and Hydrogen gas puffing was used for the formation of radiative divertor. We found that the H-factor on high density regime became higher than that in case of Hydrogen gas-puff only. ELMy H-mode has been sustained to keep the density of just before MARFE using

radiation feedback function. Characteristics of radiative divertor has been investigated with reversed shear configuration. The radiative divertor was formed to keep the ITB during 3 s with the low radiation level of main plasma. SOL characteristics has been systematically studied by reciprocating probe. We found the two region of SOL which characterized spatial gradients of electron temperature and density. Optimization of 100% neon-iced pellet injection has been attempted to demonstrate the fast plasma shut down (killer pellet). Heat load on the divertor during disruptions has been reduced drastically. Break down conditions were optimized with LHRF assistance to reduce the toroidal one-turn voltage. The world record of breakdown electric field of 0.1 V/m was achieved by using Helium as a pre-filling gas and by the reduction of stray fields.

Keywords: Tokamak, H-mode, Triangularity, Reversed Shear, ELM, MARFE, Transport Barrier, TAE, Radiative Divertor, Disruption, SOL, Breakdown

※ JT-60 Team

V.I. Afanassiev[10], H. Akasaka, K. Akiba[1], N. Akino, K. Annoh, T. Aoyagi, T. Arai, K. Arakawa, N. Asakura, M. Azumi, S. Chiba, R. E. Chien[5], N. Ebisawa, Y. Fang[7], T. Fujii, T. Fujita, H. Fukuda[1], T. Fukuda, A. Funahashi, S. Gunji[1], H. Haginoya[1], K. Hamamatsu, H. Harano[2], T. Hatae, S. Higashijima, H. Hiratsuka, T. Hirayama, A. Honda, M. Honda, N. Hosogane, C. Hwang[8], H. Ichige, S. Ide, S. Tsuji-Iio[13], Y. Ikeda, M. Isaka, A. Isayama, N. Isei, S. Ishida, Y. Ishii, M. Isobe[4], N. Isozaki[1], K. Itami, T. Ito, T. Iwahashi[1], N. Iwama[16], R. Jinbo[1], Y. Kamada, A. Kaminaga, M. Kawai, Y. Kawamata, Y. Kawano, M. Kawanobe, D. Kazama[1], M. Kazawa, M. Kikuchi, J.K. Kim[6], H. Kimura, T. Kimura, H. Kishimoto, Y. Kishimoto, A.I. Kislyakov[10], T. Kitai[1], S. Kitamura, K. Kiyono, A.V. Klasilnikov1[2], K. Kodama, Y. Koide, S. Kokusen[1], K. Komuro[1], T. Kondoh, S. Konoshima, S.S. Kozlovskij[11], H. Kubo, K. Kurihara, G. Kurita, M. Kuriyama, M. Kusaka[1], Y. Kusama, K. Masaki, T. Matoba, K. Mima[14], N. Miya, K. Miyachi, Y. Miyo, K. Mogaki, K. Mori[1], M. Mori, A. Morioka, S. Moriyama, M. Nagami, A. Nagashima, K. Nagashima, S. Nagaya, O. Naito, S. Nakagawa[1], Y. Nakamura, M. Nemoto, S.V. Neudatchin[9], Y. Neyatani, T. Nishitani, H. Nobusaka[1], N. Ogiwara, S. Oguri[1], T. Ohba[1], T. Ohga, K. Ohshima[1], T. Ohshima, T. Okabe, J. Okano, S. Omori, Y. Omori, Y. Onose[1], H. Oohara, T. Oyevaar[3], T. Ozeki, M.P. Petrov[10], S.Ya. Petrov[10], M. Saidoh, M. Saigusa, N. Saito, A. Sakasai, S. Sakata, S. Sakurai, T. Sasajima, N. Sasaki[1], Ma. Sato, Mi. Sato, T. Sato[1], M. Seimiya, M. Seki, M. Shibayama[1],Kat. Shimizu, Kaz. Shimizu[1], M. Shimizu, M. Shimono, S. Shinozaki, H. Shirai, M. Shitomi, K. Suganuma, T. Sugie, H. Sunaoshi, M. Takahashi, Sho. Takahashi[1], Shu. Takahashi, S. Takeji, H. Takenaga, T. Takenouchi[1], T. Takizuka, H. Tamai, M. Terakado, T. Terakado, M. Teranishi[16], K. Tobita, S. Tokoda, T. Totsuka, N. Toyoshima, K. Tsuchiya, T. Tsugita, Y. Tsukahara, A. Tsurumi[1], T. Tsuruoka[1], T. Tuda, K. Uchino[15], Y. Uramoto, H. Usami[1], K. Ushigusa, K. Usui, G.A. Wurden[5], J. Yagyu, M. Yamagiwa, M. Yamamoto, T. Yamamoto, O. Yamashita, K. Yokokura, H. Yoshida, M. Yoshida, R. Yoshino

1) Staff on loan
2) JAERI Research Fellow
(present address : FOM-Instituut voor Plasma Fysica Rijnhuizen, Holland)
3) Fellow of Advanced Science (present address : Tokyo University, Japan)
4) Fellow of Advanced Science
5) Los Alamos National Laboratory, U.S.A.
6) Texas University, U.S.A.
7) Institute of Plasma Physics Academia Sinica, China
8) Korea Atomic Energy Research Institute, Korea
9) I. V. Kurchatov Institute of Atomic Energy, Moscow, Russia
10) A. F. Ioffe Physico-Technical Institute, St. Petersburg 194921, Russia

11) State Technical University, St. Petersburg 195251, Russia
12) TRINITI, Russia
13) Research Laboratory for Nuclear Reactors, Tokyo Institute of Technology, Japan
14) Institute of Laser Engineering, Osaka University, Japan
15) Kyushu University, Japan
16) Toyama Prefectual University, Japan

ＪＴ－60Ｕ　1995年２月－10月期実験結果のレビュー

日本原子力研究所那珂研究所炉心プラズマ研究部・核融合装置試験部
ＪＴ－60チーム※

（1996年２月28日受理）

プラズマ電流を増大したＩＴＥＲと等価な低ｑ（ｑ＜３）領域でロックトモードを回避した立ち上げの最適化を行い，高I_p－Ｈモードの領域をI_p＝4.5ＭＡまで拡大した。ポロイダル電源の組み替えによって高三角度実験を実施し，Ｈモードの閉じ込め性能を三角度（δ）を～0.1から0.3－0.4に上昇させることでＥＬＭ発生直前の周辺の密度と温度を各々30－40％及び80％改善した。その結果，ＥＬＭ発生直前の周辺の圧力勾配の限界が増加した。プラズマ電流の立ち上げ中にＮＢ加熱を行い負磁気シアを生成し，さらにＮＢの追加熱を行うことで，イオンと電子双方について閉じ込め特性が改善される輸送障壁が得られた。ＩＴＢの位置は r/a＝0.65まで拡大し，電子温度はイオン温度と同程度であった。このときのベータ限界は，高βpHモードと同程度であった。この負磁気シア配位をＬＨＲＦを用いた電流分布制御により，約7.5秒間維持することに成功した。一方，このモードでは輸送障壁内部のヘリウムの排気が抑制され，炉心級プラズマへ適応する際の問題点が明らかになった。接線ＮＢによりトロイダル回転速度を制御することによって，ＴＡＥモードの発生を制御することに成功した。放射冷却ダイバータと高閉じ込め性能との両立を目指して，ネオン注入後に重水素ガスをパフすることにより，重水素単独注入に比べて高密度でのＨファクターの減少が緩和できることを確認した。ダイバータ部の放射損失パワーのフィードバック制御を行い，ＭＡＲＦＥ発生直前で，ＥＬＭｙ－Ｈモードを維持することに成功した。また，負磁気シア配位での放射冷却ダイバータの特性を調べ，主プラズマの放射損失低く抑えた放射冷却状態で，輸送障壁を約３秒間維持することができた。高密度ダイバータと高性能閉じ込めの両立のため，ＳＯＬの特性を系統的に調べ，セパラトリクス付近の内側ＳＯＬに温度及び密度の勾配により特徴付けられる２重構造があることが分かった。ネオンペレットを用いたキラーペレット実験に於いて，ダイバータへの熱負荷を低減し且つＶＤＥ及びハロー電流を抑制した急速電流消滅法のシナリオを確立した。ＬＨＲＦを用いてプラズマ着火時の一周電圧の低減化を試み，ヘリウムガスをプレフィルに使用した放電で着火時の誤差磁場の低減を行い，0.1V/mという着火電界の世界記録を達成した。

那珂研究所：〒311-01　茨城県那珂郡那珂町向山 801-1

※ JT-60チーム

青柳 哲雄 . 赤坂 博美 . 秋野 昇 . 秋葉 賢一[1] . 朝倉 伸幸 .
安積 正史 . 新井 貴 . 荒川喜代次 . 安納 勝人 . 飯尾 俊二[13] .
池田 幸治 . 井坂 正義 . 諫山 明彦 . 石井 康友 . 石田 真一 .
伊世井宣明 . 礒崎 信光[1] . 磯部 光孝[4] . 伊丹 潔 . 市毛 尚志 .
井手 俊介 . 伊藤 孝雄 . 岩橋 孝明[1] . 岩間 尚文[16] . 宇佐美広次[1] .
牛草 健吉 . 薄井 勝富 . 内野喜一郎[15] . 浦本 保幸 . 海老沢 昇 .
大賀 徳道 . 大島 克己[1] . 大島 貴幸 . 大場 俊夫[1] . 大原比呂志 .
大森 俊造 . 大森 栄和 . 岡野 潤 . 岡部 友和 . 荻原 徳男 .
小栗 滋[1] . 小関 隆久 . 小野瀬義秋[1] . 風間 大介[1] . 梶沢 稔 .
鎌田 裕 . 神永 敦嗣 . 河合視己人 . 河野 康則 . 川野辺 満 .
川俣 陽一 . 菊池 満 . 岸本 浩 . 岸本 泰明 . 北井 達也[1] .
北村 繁 . 木村 豊秋 . 木村 晴行 . 清野 公広 . 日下 誠[1] .
草間 義紀 . 久保 博孝 . 栗田 源一 . 栗原 研一 . 栗山 正明 .
軍司 操一[1] . 小出 芳彦 . 石仙 茂晴[1] . 児玉 幸三 . 木島 滋 .
小室 健一[1] . 近藤 貴 . 三枝 幹雄 . 斎藤 直之 . 西堂 雅博 .
逆井 章 . 坂田 信也 . 櫻井 真治 . 佐々木 昇[1] . 笹島 唯之 .
佐藤 稔 . 佐藤 正泰 . 佐藤 臣夫[1] . 蔀 守正 . 篠崎 信一 .
柴山 実[1] . 清水 和彦[1] . 清水 勝宏 . 清水 正亜 . 下野 貢 .
白井 浩 . 神保龍太郎[1] . 菅沼 和明 . 杉江 達夫 . 砂押 秀則 .
清宮 宗孝 . 関 正美 . 高橋 春次 . 高橋 昇竜[1] . 高橋 実 .
滝塚 知典 . 竹治 智 . 竹永 秀信 . 竹之内 忠[1] . 玉井 広史 .
千葉 真一 . 塚原 美光 . 次田 友宣 . 津田 孝 . 土屋 勝彦 .
鶴岡 卓哉[1] . 鶴見 聡[1] . 寺門 恒久 . 寺門 正之 . 寺西 大[16] .
徳田 伸二 . 戸塚 俊之 . 飛田 健次 . 豊島 昇 . 内藤 磨 .
長島 章 . 永島 圭介 . 永見 正幸 . 中川 勝二[1] . 中村 幸治 .
永谷 進 . 西谷 健夫 . 根本 正博 . 閨谷 譲 . 信坂 裕通[1] .
萩野谷裕文[1] . 波多江仰紀 . 濱松 清隆 . 原野 英樹[2] . 東島 智 .
平塚 一 . 平山 俊雄 . 福田 武司 . 福田 裕実[1] . 藤井 常幸 .
藤田 隆明 . 船橋 昭昌 . 細金 延幸 . 本田 敦 . 本田 正男 .
正木 圭 . 的場 徹 . 三間 圀興[14] . 宮 直之 . 宮地 謙吾 .
三代 康彦 . 藻垣 和彦 . 森 活春[1] . 森 雅博 . 森岡 篤彦 .
森山 伸一 . 柳生 純一 . 山極 満 . 山下 修 . 山本 巧 .
山本 正弘 . 横倉 賢治 . 吉田 通治 . 吉田 英俊 . 芳野 隆治 .

V.I. Afanassiev[10] . R. E. Chien[5] . Y. Fang[7] . C. Hwang[8] . J.K. Kim[6] .
A.I. Kislyakov[10] . A.V. Klasilnikov[12] . S.S. Kozlovskij[11] . S.V. Neudatchin[9] .
T. Oyevaar[3] . M.P. Petrov[10] . S.Ya. Petrov[10] . G.A. Wurden[5] .

1）業務協力員
2）特別研究生、現在、東京大学
3）原研フェローシップ、現在、オランダ、FOMプラズマ物理研究所
4）特別研究生
5）米国、ロスアラモス研究所
6）米国、テキサス大学
7）中国、科学院プラズマ物理研究所
8）韓国原子力研究所
9）ロシア、クルチャトフ原子力研究所
10）ロシア、ヨッフェ研究所
11）ロシア、サントペテルブルグ工科大学
12）ロシア、トリニティ研究所
13）東京工業大学
14）大阪大学レーザー核融合研究センター
15）九州大学
16）富山県立大学

Contents

目　　次

1. Overviews of the 1995 experiments

Renewed theme group organization started from October 1994 for the up-coming experiments in JT-60U. This regime has three theme groups each of which is composed of two sub-theme groups as; (1) Plasma Operation Theme (Leader Y. Neyatani) with Operation Sub-Theme and Disruption Sub-Theme, (2) High Performance (Leader S. Ishida) with Confinement and MHD Sub-Theme and High Energy Particle Sub-Theme and (3) Steady State Theme (Leader A. Sakasai) with Current Drive Sub-Theme and Divertor Sub-Theme. The main results from the JT-60U experiments in 1995 are summarized in the following overviews of the three theme group activities.

1.1 Plasma Operation Theme Group

Operation theme includes two tasks. One is the plasma control to obtain stable discharges for all kinds of experiment and to establish control methods toward the steady-state operation. The other is the disruption study for the reduction of the damage of the vacuum vessel and the plasma facing components.

(1) Plasma Control

In 1995, new operation regime has been achieved in the high Ip with low q regime. In order to obtain the stable low q ($q<2$) plasmas, the locked mode was successfully avoided to control the plasma rotation by tangential NB and the density by reduction of recycling at q equal integer. This technique was contributed to high Ip experiment (sec. 5.1).

The high triangularity operation was started in this year. To increase plasma triangularity (δ), vertical coils were divided two gropes (V_R and V_T coils) . By using power supply for DCW coil (H-PS) to V_T coils which can change δ, the δ up to 0.3 with Ip=1MA can be available (sec. 3.1). In this new regime, improved edge pressure gradient at the onset of ELM has been achieved with high δ (sec. 3.2-3.3). The plasma current with high δ is limited by the H-PS current (V_T coil current) of 22.5 kA in 1995. To extend the plasma current in high δ discharge (< 2 MA, triangularity < 0.3) , the present PF power supplies were rearranged in December.

New feedback (FB) functions were operated from 1995. The FB of neutron emission rate has been demonstrated and used for steady-state experiment (sec. 11.4). The radiation feedback system was begun to work for extending the steady-state radiative divertor (sec. 11.5, 6.4).

Break down conditions is optimized with LHRF assistance to reduce the toroidal oneturn voltage. The world record of breakdown electric field of 0.1 V/m was achieved by using He prefill and by the reduction of stray fields (sec. 11.6).

(2) Disruption Study

Optimization of 100% neon-iced pellet injection has been attempted to demonstrate fast plasma shut down (killer pellet). Heat load on the divertor during disruptions has been reduced drastically. At the same time, we demonstrate the fast shut down without VDE and the halo current (sec. 11.1).

The region of generation of runaway electrons has been obtained systematically as a relation to the electron density using high li disruptions. The electron density during the current quench was measured by CO2 interferometer (sec. 11.2).

1.2 High Performance Theme Group

The main objective of this group is to demonstrate the high performance of high current divertor discharges in JT-60U. The experiments conducted by this group proceeded essentially as approved. The main goals in the 1995 campaign are the confinement improvement of shear reversal discharges, the assessment of a new configuration operation with a high triangularity, the extension of high current hot-ion H-mode discharges above 3.5 MA and the contributions to the ITER physics R&D in EDA.

The shear reversal regime has been established in the range of 1.2-1.5 MA by using a fast current ramp up and early pre-beam injection to create a negative shear target plasma. The confinement was significantly improved with clear particle and thermal transport barriers up to H~2.6 against the ITER89-P L-mode scaling. Intense ICRF heating up to ~5 MW was applied for the shear reversal plasmas showing clear electron heating within the internal transport barrier at 2 MA.

High triangularity operation has been made possible up to d~0.4 by modifying electrical connections in the vertical coil system within the operation current limit up to around 1 MA. Density limit and stability limit related to the giant ELMs were substantially improved as the ELM activity became minute with triangularity. A full non-inductive current drive at 1 MA was demonstrated for about 2 s in combination with a high bootstrap current and beam current drive fraction with bN~3, bp~3 and H~2-2.5. The operational plasma current will be extended up to 2 MA with rearrangements of the electrical connections to the power supplies in 1996.

The hot-in H-mode regime was extended up to 4.5 MA in 1995 exceeding the previous results up to 3.5 MA in 1993, so that the confinement improvement in the high current low-q regime relevant to ITER was fully investigated. The stored energy reached ~8 MJ over Ip=3.5-4.5 MA where the degradation of attainable bN value with plasma current appeared to be an important issue for improvement in performance. The modification of the NBI system was tested and completed for 40 MW injection at 90-95 keV with higher beam fueling rate with narrowing the nominal electrode gap. This would ensure the eventual goal of an equivalent beak even condition towards which the

production of high-bp H-mode confinement at higher plasma current will be highlighted in 1996.

The power threshold scaling for the H-mode transition has been investigated in detail to contribute to the ITER physics R&D. Particular attention was paid to the low density limit of the power threshold, in which the role of the peripheral neutral particles in the threshold power is emphasized. Systematic non-dimensional scaling experiments for H-mode and high-bp mode discharges were also carried out. As for the high-bp mode physics, the threshold power was clarified and a new event named as BLE (barrier localized event) was found.

The field reversal experiment with an ITER-like up-down asymmetric ripple well configuration was conducted to ensure operational flexibility regarding the toroidal field direction in ITER, in which no significant effect of the toroidal field reversal on ripple losses was confirmed in support of ITER operation. Ripple enhanced diffusion of energetic tritons with 1 MeV was estimated with different ripple rates in which the triton loss is shown to be increased with the ripple rate as consistent with the present ripple transport theory.

In terms of TAE mode study with ICRF heating, it was shown that the TAE mode can be controlled by changing the toroidal plasma rotation velocity profile responsible to the tangential beam injection such as co- and counter directions. Current profile effect on TAE modes was investigated by drastic alternation of the current profile in shear reversal operation, so that no TAE mode signature was observed though the threshold ICRF power for TAE onset was sufficiently exceeded.

Long distance coupling between ICRF antenna and the plasma has been developed systematically for distances of 10-25 cm between the plasma surface and the antenna. Intense ICRF power up to 5 MW was successfully coupled with neutral beam heated plasmas in hot-ion H-mode up to 4 MA so that sawteeth were efficiently stabilized during the ELM-free phase. The frequency of ICRF is planned to be reduced down to 102 MHz for lower toroidal field experiments with 3.5 T in which H-mode transition would be possible by the ICRF heating alone.

Developments of motional Stark effect spectroscopy measurement with 5 channels and YAG laser Thomson scattering with 5 channels and a repetition rate of 10 Hz proceeded as planned. Upgraded measurements by these diagnostics with 14 channels and 12 channels with a repetition rate with 50 Hz, respectively, will appear in 1996. The second neutral particle analyzer covering a MeV range and tangentially looking at the plasma has been installed for fast ion study to be emphasized in the negative-ion based NBI experiments.

1.3 Steady State Theme Group

(1) Divertor Study

Main objectives are to sustain Radiative Divertor and Detached Plasma (including density limit), to measure SOL profiles for SOL database of ITER and to study Transport and Exhaust of Helium Ash.

Radiative divertor plasma was obtained in reversed shear mode by compound gas puffing of Neon and D2 gas. Heat removal and detachment was successfully established in the reversed shear discharge with the ITB for the first time. Heat load to the divertor plates was reduced to 20% of NB heating power (P_{NB}=15 MW) and the fraction of radiation power in the divertor was increased up to 60% of P_{NB}. Radiative divertor was also obtained in ELMy H-mode plasma with P_{NB}=23 MW.

High density limit, radiation power fraction in the divertor and the degradation of the H-factor were summarized. Density limit and density at the divertor MARFE onset were increased with P_{NB} up to 8 MW. However, it will not survive so far above Greenwald density limit $n^{Gr}[10^{20}\ m^{-3}] \equiv I_P / \pi a^2 [MA\ m^{-2}]$ at the high P_{NB} (8-22 MW) for the open divertor configuration, since the energy confinement was degraded less than L-mode level and the edge plasma was shrinking inside the LCFS (the last closed magnetic flux surface).

The fast reciprocating probe measurement were performed in L-mode discharges with P_{NB}=4 MW for SOL database of ITER. Inner and outer SOL regions with different *e*-folding lengths were observed both in the T_e and n_e profiles. The outer SOL was extending to the LCFS with n_e increasing, and *e*-folding lengths of the profiles were increased. p_e profiles at the midplane and at the divertor target were comparable. T_e,mid and T_e,div at the MARFE onset were similar for the different q_{eff} discharge.

Helium transport of reversed shear plasmas has been studied using He beam and He gas puff. The He density profiles in reversed shear mode were clearly different from those in ELMy H-mode and L-mode. The enhancement of the He particle confinement and low diffusivity were found in reversed shear mode. When mini-collapse occurred, He particles inside the ITB was expelled at the same time of the disappearance of the ITB.

In-out asymmetry with He influx in the divertor has been controlled by changing of neutral beam (NB) power and plasma current (Ip). The effect of the ion grad-B drift direction and Ip and BT (q_{eff}) dependence on He exhaust was investigated in ELMy H-mode and L-mode. The asymmetry with the He flux profiles do not depend on the ion grad-B drift direction. The asymmetry seems to be determined by β_P (including edge parameters: n_e, T_e, T_i et al.) and not be explicitly determined by NB power and I_P. Helium ash exhaust could be actively controlled in combination with the control of the asymmetry with He flux and He removal due to the Solid Target Boronization.

The effect of particle and heat fluxes and the surface temperature on the divertor plates on carbon generation during ELMy phase has been studied by fast sampling of Dα array and IRTV. Carbon burst from the divertor tiles was observed when the maximum surface

temperature of tiles exceeds 900°C at least. Emission of carbon impurity strongly depends on particle and/or heat fluxes at ELM event even if the tile temperature is kept lower than 900°C. The effect of ELM pulses on carbon generation are not negligible.

The in-out asymmetry of divertor heat flux was investigated for high β_P plasmas up to $\beta_P = 1.7$. The asymmetry strongly depends on the β_P value and the heat flux width is broader in the outer target in low density discharges with $n_e/n^{Gr} \leq 0.4$.

The effect of edge and central fueling on the particle confinement was investigated. The particle confinement time was increased with the ratio of NB fueling rate to wall recycling and gas-puffing fueling rate. The confinement times of edge fueled particle and central fueled particle were separated first. It was found that the confinement time of central fueled particle was five times longer than that of edge fueled particle.

It is estimated that the intensity ratios of He I spectral lines are available to measure the electron temperature and density profiles in divertor plasma, although more precise atomic data are necessary. Around the strike point, the temperature and density derived from the spectroscopic measurement agreed with those measured with Langmuir probes within a factor two. When a MARFE occurs and the temperature is low, the spectroscopic measurement is useful to derive the temperature and density profiles.

A new visible spectroscopic diagnostics viewing horizontally the X-point and the strike point in the divertor were installed to measure emission profiles of deuterium and low charge-states of carbon ion such as C^+ (657.8 nm), C^{2+} (569.1 nm) and C^{3+} (580.1 / 581.2 nm) in the divertor zone. It is composed of 32-channel optical fiber array and absolutely-calibrated photomultiplier tube (PMT) array and photo-diode arrays using optical interference filters. The spatial resolution is about 12 mm at the X-point, and profile data is sampled at typically 0.5 ms. This diagnostics is expected to understand mechanisms of X-point MARFE and detached plasmas in combination with the existing 60-ch optical fiber array viewing vertically the divertor.

(2) Current Drive Study

Main objectives are to study LH physics and to apply LHCD to control current profiles.

LHCD was applied to a target plasma that has a reversed shear. It was demonstrated that LHCD could successfully maintain reversed shear of about 7.5 s and q profile could be changed by varying the wave spectrum. The T_i profile could be also changed depending on the injected spectrum.

LH power was injected into the high-triangle shaped plasma in order to obtain coupling property of LH and to examine current drive performance. Because it is difficult to move plasma close to LH antenna for good coupling in the W-shaped divertor configuration. It seems that the triangularity does not affect the coupling property and current drive performance of LH. The peripheral plasma around LH antenna may govern LH waves even with high-triangle shaped plasma.

Good coupling property was obtained by applying ICRF power and gas puff at a large distance between plasma-antenna up to δ~15 cm. The low reflection of LH wave was maintained after stopping ICRF and/or gas puff. Current drive efficiency did not degrade up to δ~15 cm. This long distance coupling leads high flexibility in the operation of LHCD, moreover the reduction of heat load on the first wall and LH antenna.

Safety factor profile during LHCD was measured using MSE. The current profile gradually peaked for the case of faster wave injection ($N_{//}$=1.4) and broadened for the case of a lower wave injection ($N_{//}$=2.7).

LH wave deposition has been investigated by changing T_e and the direction of B_T in order to study the absorption mechanism of LHW. The change of hard X-ray profile depending on T_e has been confirmed. At higher T_e cases, the change of hard X-ray profile is consistent with a picture of one pass absorption. An evident difference in both the hard X-ray profile and the tail temperature from hard X-ray spectrum was found with B_T reversal.

An effect of LHCD on particle confinement was been observed. Flattening of n_e profile and a decrease of n_e in the central region have been observed especially, with lower $N_{//}$ waves injection, the operation at lower Ip and the operation at lower target n_e. The flattening should be attributed to a degradation of particle confinement.

2. Reversed Shear
2.1 Operation for Reversed Shear Discharge

T. Fujita, S. Ide and M. Kuriyama

1. Introduction

Advanced tokamak operation with a reversed shear configuration, which has the negative magnetic shear in the core and the positive magnetic shear in the periphery, has been proposed[1]. The magnetic shear is defined as $(\rho/q)dq/d\rho$, where q is the safety factor and ρ is the volume-averaged minor radius. The reversed shear configuration has a possibility of economical steady-state tokamak reactor with high β, good confinement and large bootstrap fraction. In TFTR[2] and DIII-D[3], the reversed shear was formed during the initial current ramp with NB heating. The high electron temperature with NB heating delays the current penetration and helps the formation of hollow current profile. Similar method was adopted in JT-60U.

2. Plasma Configuration

The q profile measurement is crucial for the reversed shear experiments. The q profile was measured with the motional Stark effect (MSE) diagnostics. During the experimental period in 1995, the MSE system of JT-60U[4] had 5 viewing points, which covered R = 3.04 - 3.42 m. (A new optics with 9 viewing points for R = 3.4 - 4.2 m has been installed in December 1995.) The position of plasma was decided so as to measure the q profile in as a wide region as possible with this limited observation area (see Fig. 1). The magnetic axis was located at R = 3.5 m and MSE data was obtained for $0.1<r/a<0.55$ for this configuration. Since MSE points were inside the plasma axis, the MSE signal became weak for the high density (line-averaged density $>3\times10^{19}m^{-3}$). The configuration of Fig. 1 was used for confinement study (2.3), helium exhaust study (2.5) and radiative divertor study (2.6) in this chapter. For LHCD (2.2) and ICRF heating (2.4) experiments, modified configurations were used to inject LH or IC waves into the plasma.

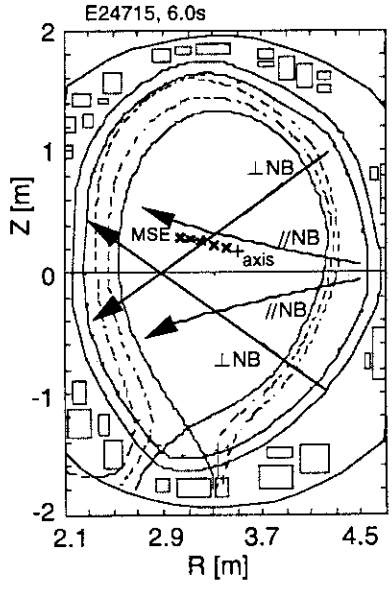

Fig. 1 Plasma configuration for reversed shear experiments. Crosses are MSE points, plus (+) is magnetic axis.

3. Discharge Scenario

To form the reversed shear configuration, it is desirable to inject NB as early as possible. In JT-60U, NB is usually injected later than t = 3 s (t = 0 s is the timing for usual plasma breakdown). To inject NB earlier, some problems had to be resolved. In the NBI system, residual beam ions after passing through the neutralizing cell

are deflected onto the beam dump by deflecting magnet coils. The stray magnetic field generated by the plasma current and poloidal field coil current is canceled with canceling coils so as to guide the ions exactly to the beam dump. The power supply of canceling coil is unipolar for most units of NBI except for two units. The direction of stray field depends on the polarity of OH coil current which is positive before the plasma breakdown, decreases and becomes negative during the course of discharge. The unipolar power supply can cancel the stray field only when the OH coil current is negative and hence we cannot inject NB as long as the OH coil current is positive. To inject NB just after the plasma breakdown, the OH coil current (I_{OH}) before the breakdown was set low so that I_{OH} became nearly zero just after the breakdown. However, it was not successful to inject NB just after the breakdown, for example at t = 0.3 s, by simply reducing $I_{OH}(0)$. The problem was associated with a control logic to check the hall probes for the measurement of the stray field for the control of the canceling coils power supply. In the NBI system of JT-60U, the check of hall probes is done by the stray field with OH coil just before the plasma breakdown. On the other hand, the deflecting magnet coil is excited about 3 s before the beam injection. If we intend to inject beams just after t = 0 s, the deflecting magnet coil has to be excited before the plasma breakdown and disturbs the stray field, which results in the judgment of "hall probes are out of order" and inhibits the beam injection.

This problem has been resolved by delaying the plasma breakdown by 3 s. The typical waveforms of OH coil current, plasma current and NBI power are shown in Fig. 2. The OH coil current started to rise at t = - 2 s and reached some value (typically 20 kA) at t = 0 s. The I_{OH} of 20 kA was necessary to produce sufficient stray field to check the hall probes. The OH coil current was ramped down slowly to 10 kA before the breakdown and initial gas puff was injected for t = 2-3 s. At t = 3.1 s, the I_{OH} was decreased rapidly to produce strong toroidal electric field for the plasma breakdown. The initial plasma current was 0.3 MA and I_{OH} became almost zero after the breakdown. The initial plasma current was set lower than the value of usual discharge (typically 0.6-0.8 MA) to inject NB at low current. A higher initial current may be worth trying. The divertor plasma configuration was established within 0.2 s. At t = 3.3 s, the injection of NB and the ramp of plasma current were started. Pulsed gas puff, typically 10 Pam^3/s x 0.1 s was applied at the same time as the start of NBI to raise the plasma density and increase the deposition power. The ramp-up rate of plasma current was typically 0.5 MA/s, but stable plasma was obtained with a

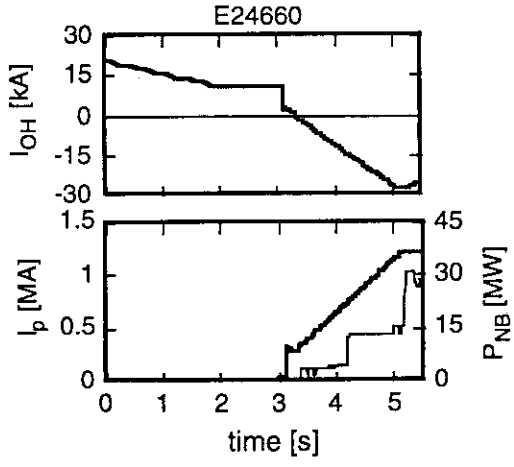

Fig. 2 Time evolution of OH coil current, plasma current and NBI power.

ramp-up rate of up to 0.67 MA/s. The NB power was increased stepwise on the way of ramp-up. Since the I_{OH} became negative just after the breakdown, it became larger into the negative direction during the discharge. Due to this large I_{OH}, the tilting force of torodial coils became severe and the current flat-top length was restricted.

4. Formation of Reversed Shear

Discharges with NB and without NB during ramp-up were compared in Fig. 3. The NB power was increased from 4 MW to 13 MW at 4.1 s. By NB heating, the electron temperature was almost doubled. Figure 4 shows the j and q profiles at the end of ramp-up of discharges shown in Fig. 3. The q profile without NB was almost flat within r/a = 0.5 while the reversed shear was formed in the discharge with NB. It is noted that the flat q profile with high q(0) (q(0)=3) was obtained without NB. This may result from the large volume divertor configuration in JT-60U.

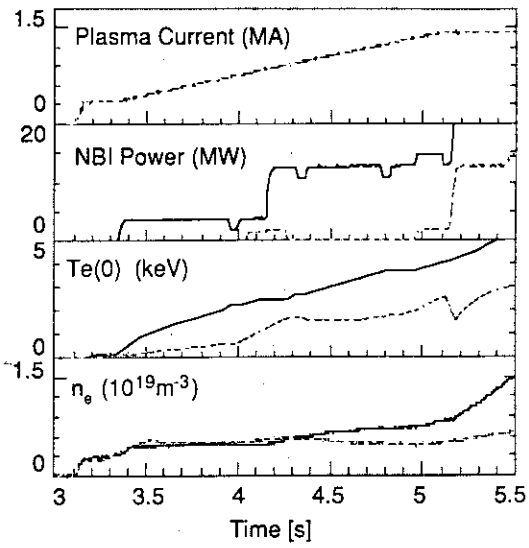

Fig. 3 Time evolution during Ip ramp-up of reversed shear discharge (solid) compared with no pre NB discharge (dashed).

In hydrogen discharges, scan of pre NB power and electron density was attempted. The dependence of electron temperature and q at the end of I_p ramp-up on pre NB power is shown in Fig. 5. The electron density was fixed to 1.1-1.2x$10^{19}m^{-3}$ at the end of ramp-up except for the discharge without NB where the density was 1.5x$10^{19}m^{-3}$. As the NB power was raised, higher T_e and q were obtained though the change of q is comparable to the error bar of the measurement. The difference of q with and without NB heating was not so large. The beam driven current may effect the q profile because the current within r/a = 0.3 is only 0.1 MA with the reversed shear configuration of q(0) = 5. Although the co- and counter- tangential NB power were nearly balanced (the former was larger than the latter by about 0.5 MW), the orbit loss of counter tangential NB may enhance the beam driven current.

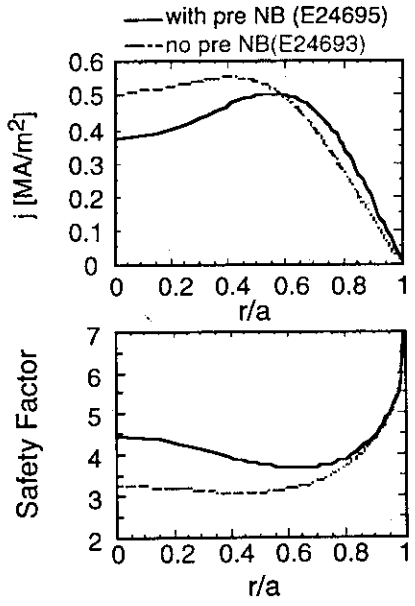

Fig. 4 Radial profiles of j and q at the end of Ip ramp-up of discharges shown in Fig. 3.

The results of density scan are shown in Fig. 6. In the early series of reversed shear experiments, no gas puff was injected except for the pulse gas puff at the beginning of NB heating to increase the electron temperature and q(0) as high as possible. Since high density plasmas with high H factor had been obtained by increasing the target density as described in section 2.3, a higher target density regime was tried. As shown in Fig. 6, the decrease of electron temperature was small when the density was raised from $0.8\times10^{19}m^{-3}$ to $1.9\times10^{19}m^{-3}$. The change of q was also small and we could obtain reversed shear profile even with $1.9\times10^{19}m^{-3}$ and could obtain the transport barrier at the high density regime as described in 2.3.

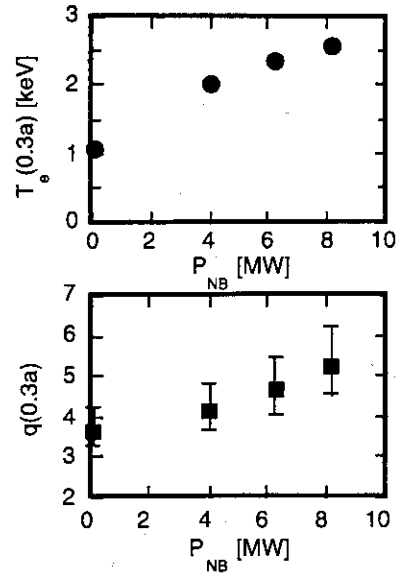

Fig. 5 Electron temperature and q at r=0.3a versus NB power. Line-averaged electron density is 1.1-1.5 $x10^{19}m^{-3}$.

Whether the current diffusion during I_p ramp-up is determined by neoclassical resistivity is not checked yet. Low m/n MHD modes were often observed during ramp-up and these modes were stabilized by higher beam power and/or by higher density. The check of neoclassical resistivity including the effect of NBCD is for future study.

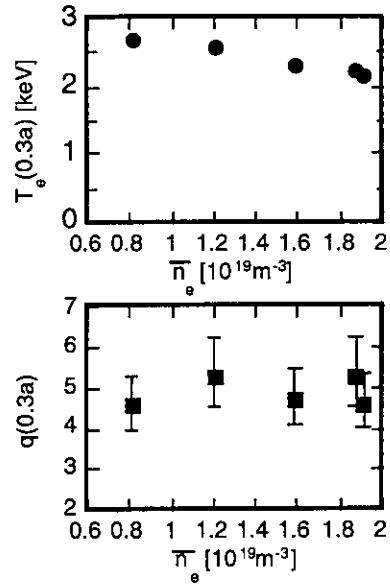

Fig.6 Electron temperature and q at r=0.3a versus line-averaged electron density. NB power is 8 MW.

5. Summary

The reversed shear was formed with NB injection during the initial current ramp. The beam was injected 0.2 s after the plasma breakdown by delaying the breakdown by 3 s with low value of initial OH coil current. The change of q profile by electron density was small and the reversed shear was obtained for wide range of density.

References

1) T. Ozeki, in Plasma Physics and Controlled Nuclear Fusion Research (Proc. 14th Conf, Würzburg, 1992) Vol. 2, p.187, 1993.

2) F. M. Levinton *et al.*, Phys. Rev. Lett. **75**, 4417 (1995).

3) E. J. Strait *et.al.*, Phys. Rev. Lett. **75**, 4421 (1995).

4) T. Fujita *et al.*, 1995 Toki Conference (submitted to Fusion Engineering and Design)

2.2 LHCD Experiments on Negative Shear Plasmas

S. Ide, T. Fujita, O. Naito

1. Introduction

Recently a plasma that has a negative magnetic shear in the central region has proved to have improved confinement characteristics in many tokamaks. From a viewpoint of enhancement and sustainment of the improved confinement characteristics, an application of non-inductive current drive on such a plasma is very interesting. In this section, experimental results of lower hybrid wave current drive (LHCD) on a negative shear plasma are presented.

2. Experimental Results

2.1.1. Long Pulse Sustainment of Negative Shear

In the experiments, the plasma current I_p = 1.0 MA, the toroidal field at the plasma center $B_T(0)$ = 2.8 T and the main working gas was hydrogen. The major radius R_p = 3.5 m and the minor radius a_p = 1.0 m.

In Fig.1 temporal evolution of the plasma parameters are show, I_p, the injected NB and LHW powers and q at ρ ~ 0.16, 0.36 and 0.51, here ρ is the normalized flux radius. The value of q is measured at five spatial points by the motional Stark effect (MSE) diagnostics. At the I_p ramp-up phase NB power was applied to raise the electron temperature T_e in order to retard the current penetration. As a result a strong negative magnetic shear is formed as shown in the figure at about 5 s. After the NB units except probe beam for MSE measurement was turned off LHW were applied in order to sustain the negative magnetic shear. From measured T_e, the current diffusion time is estimated as about 2 s. As clearly shown in the figure, the change of q is slower than this. Moreover the values of q in the central region (ρ

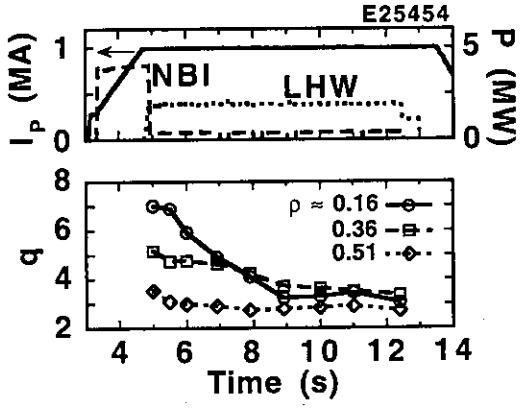

Fig.1 : Temporal evolution of I_p, P and q at three spatial points.

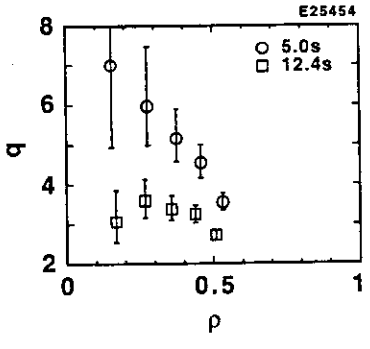

Fig.2 : Measured q profiles at 5 and 12.4 s, q_{eff} is about 7.5.

≤ 0.36) are always higher than that at the half radius. The measured q profiles at 5.0 and 12.4 s are plotted in Fig.2. The magnetic shear is kept negative until 12.4 s in the plasma inner region (ρ ≤ 0.5), except the central region (ρ ≤ 0.2). The evolution of q at the inner-most measured point can be explained taking account of a fact that the fraction of the LHW driven current in this case is 65 to 75 %. In Fig.3 (a) plotted are line averaged hard X-ray (HX) profiles integrated from 6 to 7 s and from 11 to 12 s. This suggests that LHW driven current profile is kept almost constant. On the contrary, the OH current of about 25 to 30 % of the total current continues to penetrate into the plasma center. In Fig.3 (b) the fitted current profile at 5 s of the shot shown in Fig.1 is plotted (solid line). In the same figure, a monotonic current profile of a similar parameter discharge is also shown (broken line). Taking the current profile shown with a solid line in Fig.3 (b) as an LH driven current profile and that shown with a broken line in the figure as a final OH current profile and mixing them at the rate of 70 % and 30 %, it can be shown that the q profile at 12.4 s is not inconsistent with this assumption. This suggests that a large negative shear such as one at 5 s of E25454 can be sustained non inductively if full LHCD is applied.

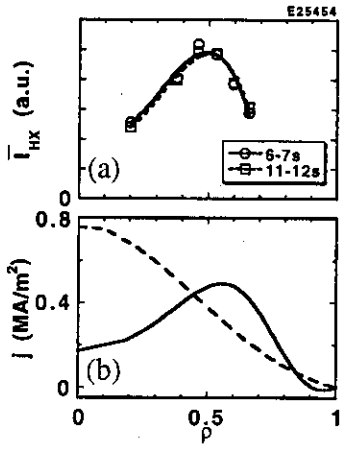

Fig.3 : (a) Line averaged HX profile of E25454, the shot shown in Fig.1. (b) Fitted current profile at 5 s of E25454 (solid line) and that of well current penetrated case (dashed line).

2.1.2. Active Control of Negative Shear

In order to investigate controllability of LHCD on a negative shear plasma, LHWs of different $N_{//}$ spectrum are injected. In the experiment two spectra are used, one is the same one used in the previous experiment (referred to as the broadening spectrum) and the other is one which is expected to drive more peaked driven current profile (referred to as the peaking spectrum). The line averaged I_{HX} intensity profiles are shown for these spectra respectively in Fig.4 (a),

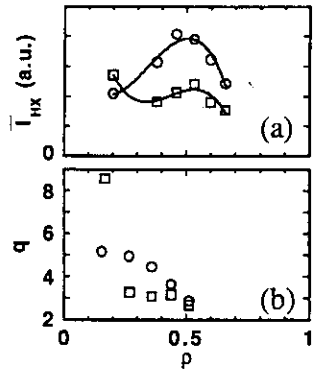

Fig.4 : The line averaged I_{HX} profiles (a) and q profiles (b) for the peaking spectrum injection (circles) and the broadening spectrum injection (squares).

circles indicate the broadening spectrum injection while squares indicate the peaking spectrum injection. In Fig.4 (b) plotted are measured q profile for these cases, the symbols are the same as in Fig.4 (a). As is seen in the figure, the q profile is different. Since the total current profile is expected to be peaked with the injection of peaking spectrum, a large value of q at the inner most point seems strange. The reason is not clear yet, this should be investigated in future. In these plasmas NB power of about 16 MW are injected. In both cases an MHD collapse occurs about 3 s after the onset of P_{NB}. In the broadening spectrum injection case, the collapse leads to a disruption. The ion temperature T_i profiles just the collapse measured by the charge exchange recombination spectroscopy diagnostics (CXRS) are shown in Fig.5. It is found in the figure that a position where T_i sharply increases is clearly different between these shots.

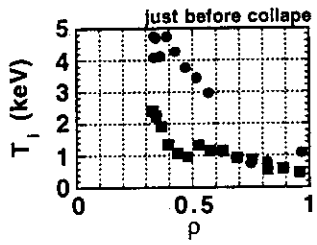

Fig.5 : T_i profiles of the broadening spectrum injection (circles) and the peaking spectrum injection (squares).

3. Summary

LHCD was applied to a target plasma that has a negative magnetic shear. It is demonstrated that LHCD can successfully maintain negative shear for about 7.5s.

It was also demonstrated that by varying the wave spectrum, q profile can be changed. The T_i profile can also be changed depending on the injected spectrum. The relation between the q profile and the profiles such as T_i, T_e and n_e or so on should be investigated in future.

2.3 Enhanced Core Confinement in Reversed Shear Discharges

T. Fujita, Y. Koide, S. Takeji,
H. Shirai, T. Ozeki, Y. Kamada and S. Ishida

1. Introduction

Improved ion thermal confinement in the central region was observed in TFTR and DIII-D reversed shear discharges[1,2]. In JT-60U, before these experiments, formation of internal transport barrier (ITB) and improved ion thermal confinement had been observed in the high β_p mode[3]. Here, we report the formation of internal transport barrier and enhanced confinement both for ions and for electrons in JT-60U reversed shear discharges. Especially, the clear barrier formation for electrons was observed for the first time. This enhanced confinement was obtained in the high density and equi-thermal ($T_i \sim T_e$) regime, which meets the reactor plasma condition.

2. Typical Waveforms and Profiles

In the experiments, the reversed shear configuration was formed during the initial current ramp with the neutral beam (NB) heating as described in section 2.1. The time evolution of typical discharge is shown in Fig. 1.

The current ramp-up rate was 0.5 MA/s. The q profile was measured with the five channel MSE polarimeter. The plasma major radius was relatively large (R = 3.4 m) for the MSE measurement. With this configuration, the beam deposition is rather broad and the ripple loss of fast ion is large. At the end of the ramp-up high power NB (about 27 MW) was injected. Though the ELMy H mode appeared about 0.2 s after the main heating, the central electron density continued to rise and the peaked density profile was formed. This suggests the more improved particle confinement than in the high β_p mode, where the density peaking stops or decelerates after the ELM

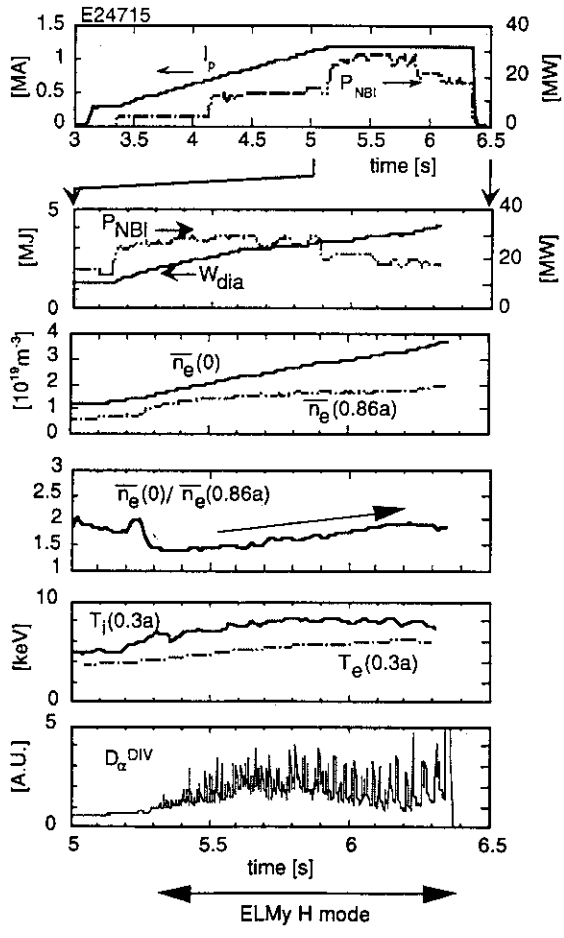

Fig. 1 Waveforms of a reversed shear discharge. Bt = 3.4 T. Deuterium.

appearance.

The central density and the pressure gradient continued to grow inside the transport barrier, reached the beta limit and terminated in collapse. The maximum normalized beta, β_N was 2.4 with B_t = 3.4 T, I_p = 1.2 MA, Plasma volume = 70 m^3 and q_{eff} = 7, which was similar to that of high β_p mode. However, the higher density has been achieved in the reversed shear discharges even with the same beta. Precursors were hardly detected at the disruptive collapses. At minor collapses, fast time scale (<100μs) low n modes were observed.

Figure 2 shows radial profiles of n_e, T_e, T_i and q at t = 6 s of the discharge of Fig. 1.

Steep gradients (internal transport barrier) of n_e and T_e are clearly seen in the negative shear region. The T_i profile had also steep gradient. The minimum value of q was 3.6 at r/a = 0.68, which corresponded to the outer edge of steep gradients of n_e, T_e and T_i. The steep gradient in T_e is not seen in the high β_p mode or in reversed shear discharges of TFTR or DIII-D and is a distinctive feature that indicates that the electron thermal confinement is improved as well as the ion thermal confinement. The preliminary results of transport analysis on profiles of Fig. 2 show that the thermal diffusivities of ions and of electrons were remarkably reduced and approximately equal inside the transport barrier. The fact that the position of the barrier was at r/a =0.65 and the improved region was large is also notable. This may be attributed to the fact that the large negative shear region can be obtained with current ramp on the large volume divertor plasma in JT-60U.

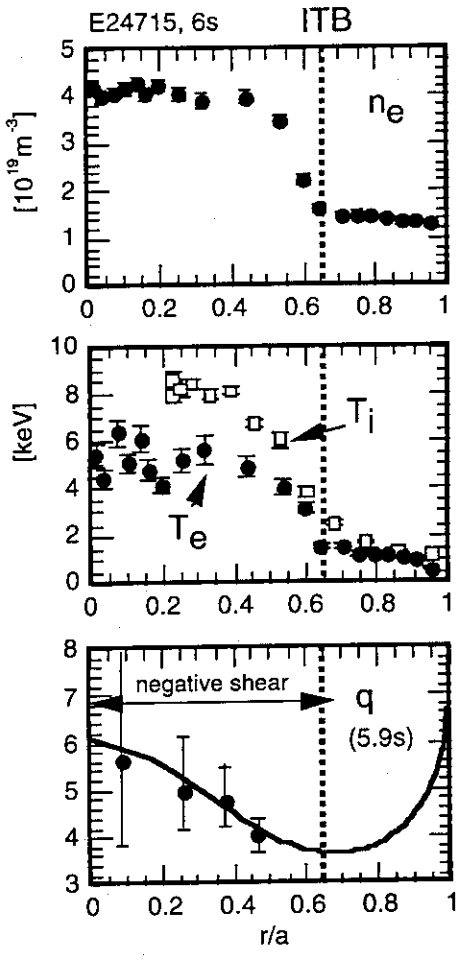

Fig. 2 Radial profiles of ne, Te, Ti and q at t = 6 s in the discharge shown in Fig. 1.

3. T_i/T_e and H Factor

In the discharge of Fig. 1, the line-averaged density just before the main heating (target density) was $1.2x10^{19}m^{-3}$ and the ratio of T_i/T_e was about

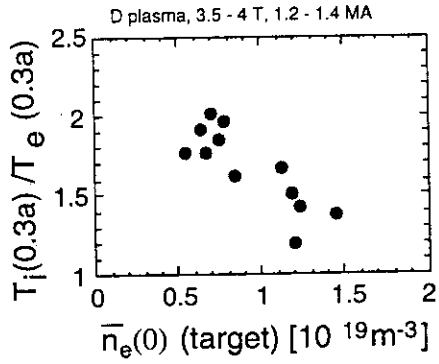

Fig. 3 Dependence of Ti/Te on the target density.

1.3 just before collapse. In Fig. 3, the dependence of T_i/T_e at the stored energy maximum on the target density is shown. T_i/T_e gets higher as the target density became lower and we obtained the higher ion temperature of 15 keV and the higher T_i/T_e of about 2 when the target density was $0.7\times10^{19}m^{-3}$. The H-factor defined as an enhancement over ITER89P scaling, however, barely depended on T_i/T_e as shown in Fig. 4, which seems to result from the fact that the both of ion and electron confinement are improved. Thus, we have obtained enhanced confinement both in a hot ion regime and in an equi-thermal regime.

This is in contrast to that the T_i/T_e is usually larger than 2 and the confinement improvement for ions is more remarkable than for electrons in the high β_p mode.

The relation between the H factor and the density normalized with the Greenwald limit is shown in Fig. 5. We obtained the maximum H factor of 2.6 with the ELM-free H mode edge. In the ELMy H mode edge, we obtained H factor of 2.3 in the high density regime of 68 % of the Greenwald limit. The H factor will be significantly improved by changing the configuration to an inner-shifted one with less ripple loss of fast ions.

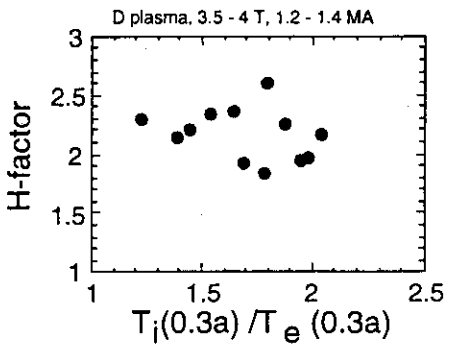

Fig. 4 Dependenc of H factor on Ti/Te.

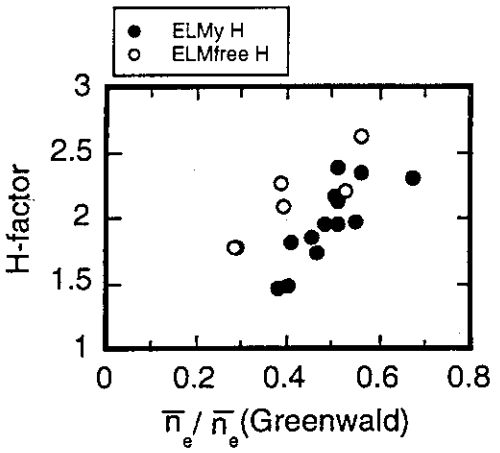

Fig. 5 Relation of H factor and the density normalized by the Greenwald limit. Open circles are ELM-free H mode and closed circles are ELMy H mode.

4. Threshold Power

In the hydrogen plasma with the hydrogen NB, reversed shear experiments with the low heating power were carried out and the barrier was formed with only 6.7 MW of absorbed power (without account of ripple loss of beam ions) at the density of $2\times10^{19}m^{-3}$. On the other hand, we could not obtain the barrier at the density of less than $1\times10^{19}m^{-3}$ with the maximum NB power

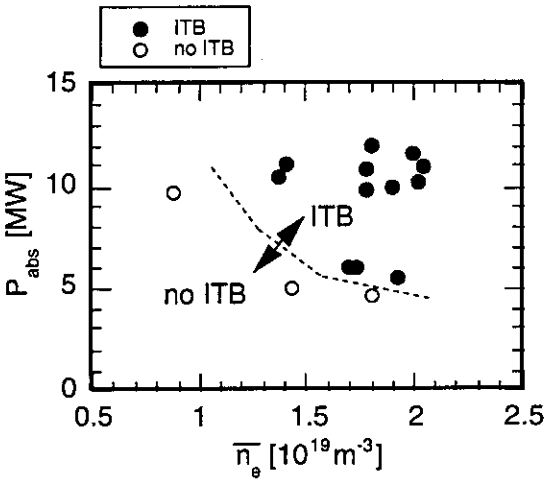

Fig. 6 Absroption power versus line-averaged electron density. Closed sysmbols are with ITB formation and open ones are without ITB. Hydrogen, 3.4 T, 1.2 MA.

(hydrogen operation) of 17.5 MW. Figure 6 shows the dependence of the threshold power on the line-averaged density. The threshold power decreases with the density for the density regime of 0.8-2.1x10^{19}m^{-3}. This tendency is opposite to the high β_p mode[4]. As the density was raised, the collapse became milder, the barrier was formed again quickly after the collapse and the quasi-steady state was obtained.

5. q Profile Scan

To investigate the effect of q profile on the barrier formation, q profile was scanned by delaying the timing of main NB heating. In this experiment, the pre NB power (hydrogen) was 7.7 MW and the main NB power was 15.5 MW. In the usual operation, the main NB was injected at the start of I_p flat-top when the q profile was strongly hollow (q(0.2a) / q(0.4a) = 1.6). When we delayed the main NB and kept the NB power constant (7.7 MW) during I_p flat-top, the q near the axis gradually dropped and it became flat within 3 s. Four discharges are compared in Fig. 7, where the timing of main NB was delayed by 1 s step. The density was about 1.9x10^{19}m^{-3} for all discharges. The profiles of q, T_i and T_e are shown at the stored energy maximum of each shot. As the q near the axis drops, the barrier moves inward. This seems to indicate that the barrier position and the q_{min} position has close relationship.

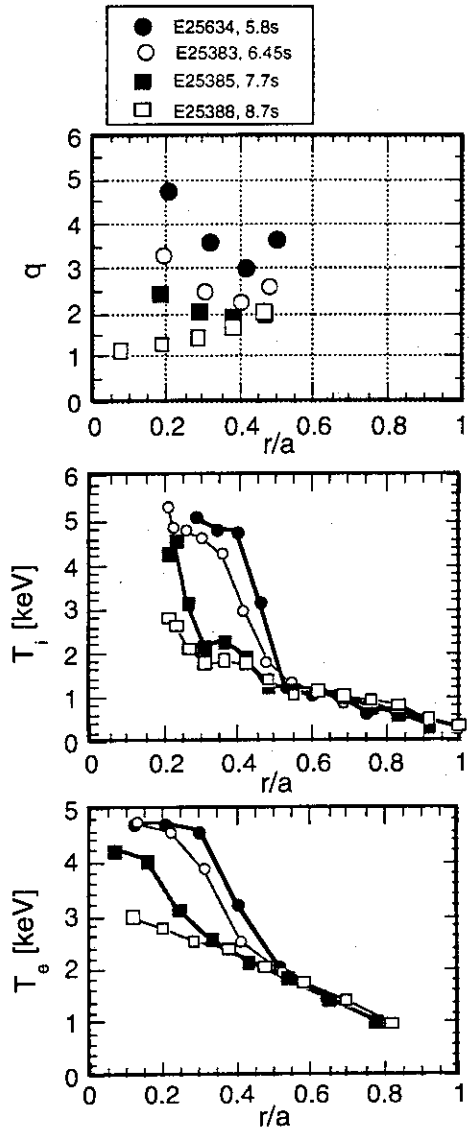

Fig. 7 Radial porfiles of q, Ti and Te for q scan discharges. The times of start of main NB are 5, 6, 7 and 8 s in E25364,E25383, E25385 and E25388, respectively.

References

1) F. M. Levinton *et al.*, Phys. Rev. Lett. **75**, 4417 (1995).
2) E. J. Strait *et al.*, Phys. Rev. Lett. **75**, 4421 (1995).
3) Y. Koide *et al.*, Phys. Rev. Lett. **72**, 3662 (1994).
4) Y. Koide *et al.*, section 4.1 in this review.

2.4 ICRF Central Heating of Reversed Shear Plasmas

H. Kimura, T. Fujita, T. Fujii, Y. Kusama, Y. Kamada, S. Moriyama, and M. Saigusa

1. Introduction

ICRF central heating has been attempted in series of reversed shear experiments on JT-60U. In JET, ICRF heating was applied to the pellet fuelled discharges and an enhanced performance associated with the shear reversal (PEP mode) was observed.[1] In PEP modes, the core electron density was significantly high ($\geq 10^{20}$ m^{-3}). Then energetic tail of minority ions did not grow so much. However, in the present reversed shear experiments without pellet nor central beam fuelling, the core electron density is at most several times 10^{19} m^{-3}. In this situation, energetic tail ions may be produced in the core. Our concern is whether ICRF heating is still efficient in the reversed shear configuration, where the poloidal magnetic field in the core is much weaker than in the normal shear case. In order to compensate weak poloidal field, high plasma current regime up to 2.45 MA of I_p was investigated in application of ICRF heating to the reversed shear configuration.

2. Operating Regime

ICRF heating was applied in combination with NBI heating after reaching the current flat-top in the operation scenario of the reversed shear experiment, where reversed shear was maintained by delaying current penetration with early beam injection during a current ramp-up phase. Here hydrogen and helium mixture plasmas and hydrogen beam were employed. A heating scheme of the ICRF heating was hydrogen second harmonic heating on axis, where the toroidal field was set at 3.8 T in the plasma center. Figure 1 shows an operating domain in a plane defined by the line-average electron density just at starting the current flat-top ($\bar{n}_e^{target}$) and the plasma current in the present experiments. Open circles indicate that the electron density peaking factor, $n_{e0}/\langle n_e \rangle$, is larger than 1.8, while crosses indicate that the electron density peaking factor is less than 1.8. The density peaking factor is a kind of an index indicating whether the transport barrier appeared or not. We found a clear correlation between the density peaking factor and the H-factor ($\equiv \tau_E^{ITER89P}/\tau_E$). Open circles imply that the transport barrier appeared clearly. One can find from Fig. 1 that the target density to produce the transport barrier tends to increase with increasing plasma current. Figure 2 shows an operating domain defined by the combined heating power and $\bar{n}_e^{target}$. Open symbols indicate that the electron density peaking factor is larger than 1.8, while closed symbols indicate that the electron density peaking factor is less than 1.8. The operating regimes were completely different between the higher I_p case ($\geq$2 MA) and the lower I_p ($\leq$1.7 MA) case. In the higher I_p case, experiments were done over a wide range of the target density with comparable amounts of ICRF and NBI heating power. It was found that the heating power needed to obtain the transport barrier was

relatively low. Typically, the transport barrier was formed at I_p of 2.45 MA (q_{eff} of 4) and the target $\bar{n}_e$ of 3.4×10^{19} m^{-3} with the additional power as low as about 8 MW (i.e., P_{IC}=3 MW and P_{NB}=5 MW). It seems that the heating power needed to obtain transport barrier tends to increase with increasing target density. A typical radial profile of the safety factor observed in the 2.4 MA shear reversal experiment is shown in Fig. 3.

On the other hand, in the lower I_p ($\leq$1.7 MA) case, experiments were done with higher heating power, which was mainly from NBI (~15 MW), at a narrow range of the target density. Reproducibility of the transport barrier formation was not so good, as is seen from mixing of data points with and without transport barrier in a narrow area in Fig. 2. We found that a value of the density peaking factor tends to increase with increasing target diamagnetic stored energy, as is shown in Fig. 4 for the case of I_p=1.4 MA. The result suggests that the target stored energy is one of key factors to obtain strong transport barrier.

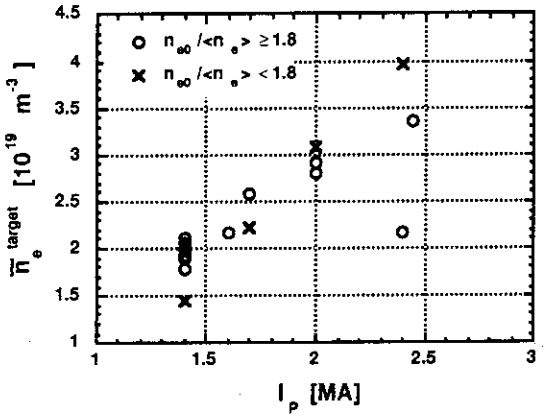

Fig. 1 Operating regime in a plane defined by the target electron density and the plasma current.

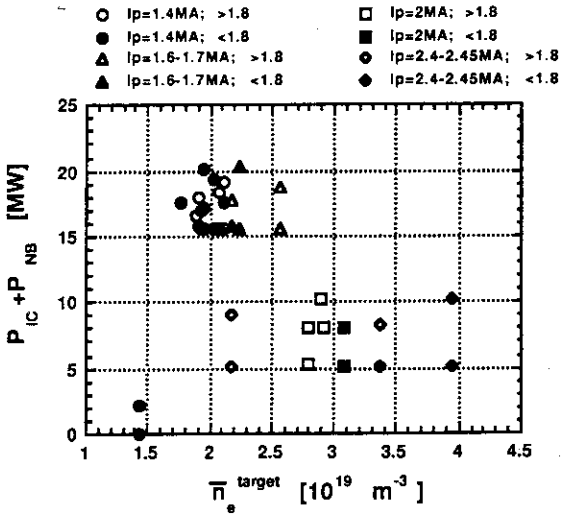

Fig. 2 Operating regime in a plane defined by the combined ICRF and NBI heating power and the target electron density.

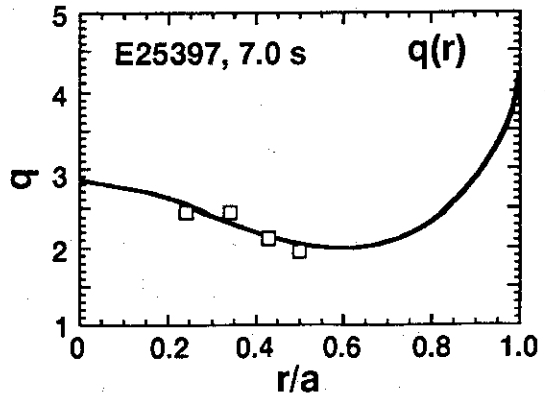

Fig. 3 Radial profile of the safety factor measured by the MSE method in 2.4 MA shear reversal experiment with combined ICRF and NBI heating.

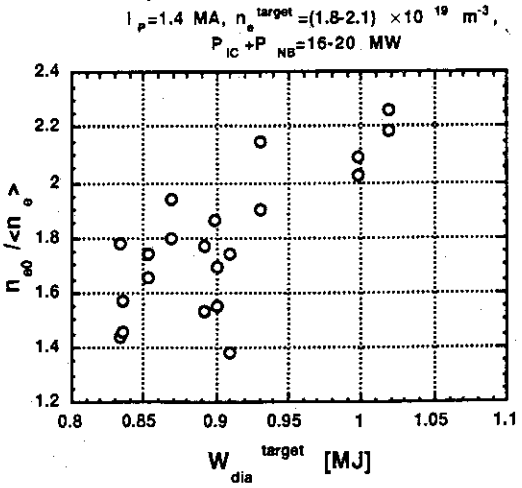

Fig. 4 The electron density peaking factor against the target diamagnetic stored energy.

3. Typical Example

A typical time evolution of the combined ICRF and NBI heating for the reversed shear configuration at I_p=2 MA with $\bar{n}_e^{target}$=2.9×10^{19} m^{-3} is shown in Fig. 5. The plasma current reached a flat-top at 5.8 s with a ramp-up rate of 0.6 MA/s. The NBI heating power was decreased from 9 MW in the current ramp-up phase to 5 MW in the main heating phase, where a fraction of the perpendicular NBI power to the total (tangential and perpendicular) NBI power was restricted to about 20% to minimize ripple-induced fast ion losses. After starting ICRF injection (5 MW), the plasma stored energy and the central electron temperature notably increased. The toroidal rotation velocity at r=0.4a, V_t(0.4a), changed significantly to negative direction, indicating formation of the transport barrier. The line-average electron density increased only slightly after formation of the transport barrier, because ICRF heating does not supply particles in the plasma core. A partial collapse occurred at t=7.1 sec. But the transport barrier was still kept up to 0.2 sec after the ICRF turn-off.

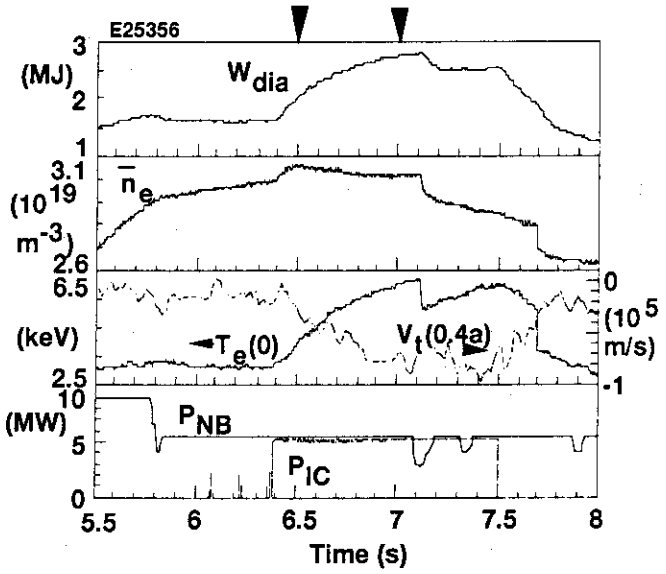

Fig. 5 Time evolution of the reversed shear experiment with combined ICRF and NBI heating at Ip=2 MA.

Figure 6 displays radial profiles of the electron density, the toroidal rotation velocity and the electron and ion temperatures at 6.5 s and 7 s of the same shot as in Fig. 5. Existence of the internal transport barrier is seen from the steep gradient layers in those profiles. Both electron and ion temperatures increased significantly inside the transport barrier during the ICRF injection. A profile shape of T_e is very flat within ρ~0.4 m, in contrast to a peaked T_e-profile in normal shear discharges with the same I_p and similar electron density. The result suggests that an orbit size of fast ions becomes comparable to the minor radius of the transport barrier in the reversed shear discharge. Nonetheless, the H-factor increased from 1.2 just before ICRF injection to 1.6 during ICRF injection. Thus, the ICRF central heating was quite successful for the reversed shear configuration, probably due to peaking of the electron density in the core, which suppresses excessive tail formation of resonating fast ions. The incremental energy confinement time ($\Delta W_{dia}/P_{IC}$) is ~0.24 s, which is comparable to the best one with sawtooth

stabilization.[2] It should be noted that TAE modes were not excited in reversed shear plasmas with ICRF heating power up to 5 MW, which is well above the threshold heating power (3-4 MW) in normal shear plasmas.[3]

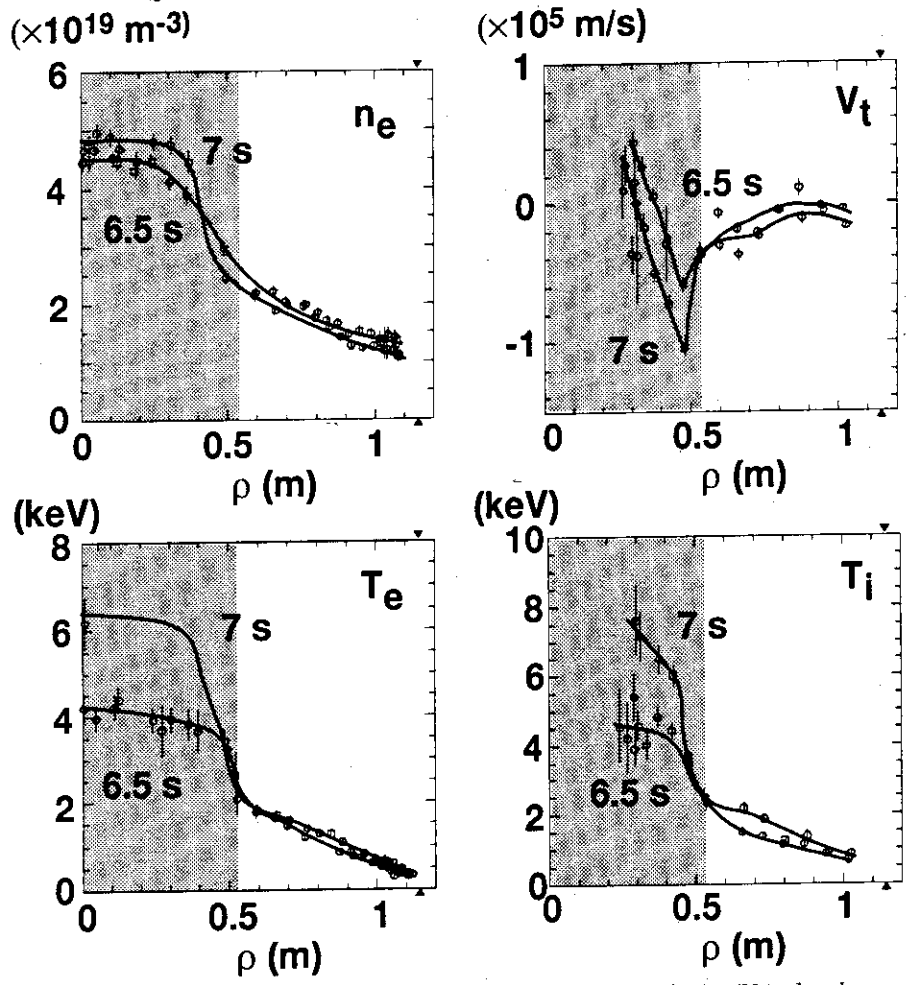

Fig. 6 Radial profiles of the electron density (n_e), the toroidal rotation velocity (V_t), the electron temperature (T_e) and the ion temperature (T_i) at 6.5 sec and 7 sec of the shot E25356 in Fig. 5. The T_e profile in the core region at 7 sec was determined from data of the ECE polychromator system, which were calibrated with the Thomson scattering data at 6.5 sec.

4. Conclusions

ICRF central heating was successful in reversed shear plasmas, although flattening of the electron temperature profile was seen inside the transport barrier probably due to a large orbit effect. The H-factor reached 1.6 at I_p=2 MA, which is the highest level among hydrogen dischages of JT-60U.

References

1) B.J.D. Tubbing, et al.: Nucl. Fusion, **31**, 839 (1991).

2) T. Fujii, et al.: Section 8.2 in this report.

3) H. Kimura, et al.: Journal of Plasma and Fusion Research, **71**, 1147 (1995).

2.5 Helium Transport of Reversed Shear plasmas

A. Sakasai, H. Kubo, K. Itami, N. Asakura

1. Introduction

Helium transport of reversed shear plasmas have been studied using He beam and He gas puff in the hydrogen operation. Reversed shear discharges have been established with a fast rump up of plasma current and pre-NB heating during the rump up phase. Reversed shear plasmas were obtained in the hydrogen operation (working gas was hydrogen and heating beam was hydrogen NB) as well as the deuterium operation.

In reversed shear modes, the electron density in the central region is peaked and the confinement is remarkably enhanced. In particular, a internal transport barrier(ITB) was formed at the position of pitch minimum q(safety factor) and ne(r), Te(r) and Ti(r) profiles inside the ITB are peaked in JT-60U. It is expected that particle confinement is enhanced in the position of q_{min} in reversed shear modes. Helium ash exhaust from the revered shear plasma is a matter of concern. It is very important to make clear He transport characteristics of the reversed shear plasma because of the enhancement of He particle confinement.

2. Experimental Arrangement and Method

Reversed shear plasmas were obtained in the hydrogen operation of I_P=1.2 MA, B_T=3.5 T, q_{eff}=6.4, P_{NB}=13, 11 and 8 MW. ^{4}He beam injection and He gas puff did not affect the ITB formation. Time evolution of He density profiles with charge exchange recombination spectroscopy (CXRS) is important to study the helium transport. The time dependence of the He^{2+} density profiles in the plasma core was measured by CXRS at 8 radial locations in JT-60U.

3. Helium Transport of Reversed Shear Plasma

Helium transport characteristics of the reversed shear plasma (I_P=1.2 MA and B_T=3.5 T) was investigated using He beam and a short pulsed He gas puff. Figure 1 shows the ion temperature profile with CXRS and the He density profiles in reversed shear mode with ●: He beam injection and □:He gas puff.

In the case of He beam injection, the He density inside the ITB was steeply higher than the He density outside the ITB when the ITB was formed. The He density profile was peaked as well as n_e profile. The He density inside the ITB increased fast as compared with the He density outside the ITB.

On the contrary, in the case of He gas puff, the He density inside the ITB was lower than the He density outside the ITB. The He density profile became hollow steeply inside the ITB.

The He density inside the ITB increased slowly as compared with the He density outside the ITB. These He density profiles in reversed shear mode were clearly different from those in ELMy H-mode and L-mode[1].

This result indicates that it is difficult to penetrate He particles into the ITB and to purge He particles from the inside of the ITB. The result also indicates that the particle diffusivity in the ITB region is much less than that in the other region. When mini-collapse occurred after the formation of the ITB, the ITB disappeared and He particles inside the ITB was expelled like ELM events.

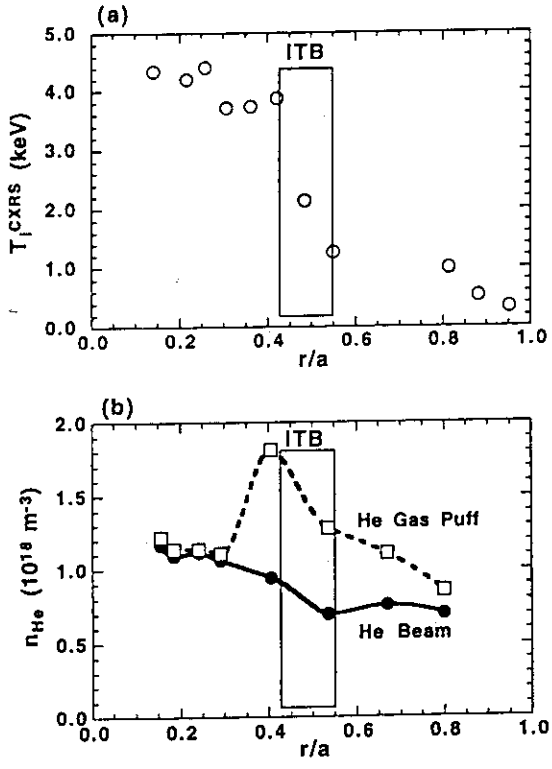

Fig. 1. (a): The ion temperature profile with CXRS and (b): comparison of the helium density profiles between ●: He beam injection and □: He gas puff in reversed shear mode.

4. Conclusions

Helium transport of reversed shear plasmas has been studied using He beam injection and He gas puff. The He density profiles in reversed shear mode were clearly different from those in ELMy H-mode and L-mode. The enhancement of the He particle confinement and low diffusivity were found in reversed shear mode. When mini-collapse occurred, He particles inside the ITB was expelled at the same time of the disappearance of the ITB. Therefore the mini-collapse and safety factor q(r) control in reversed shear mode are expected to reduce He ash content in the core plasma.

Reference

[1] A. Sakasai et al., Journal of Nuclear Materials 220-222 (1995) 405.

2.6 Radiative divertor in negative shear plasmas

K. Itami, N. Hosogane and N. Asakura

1. Introduction

In JT-60U, improved particle and energy confinement inside the internal transport barrier are obtained in the discharges with negative magnetic shear in the center region of the plasmas with the intense beam heating [1]. In this paper, the initial results of the radiative divertor experiment during the hydrogen discharges of the negative shear plasmas are presented.

2. Experimental results

Neon has large radiative cooling rate of ions. Neon gas puff works as seeding gas which effectively enhance the radiative cooling and the particle recycling at the divertor with the aid of the fuel gas puff [2]. The compound gas puff effectively promotes radiative divertor plasmas. Compound gas puff of Neon and Hydrogen was applied to the negative shear plasmas with Ip= 1.2MA, BT=3.5T and PNB=15MW where the plasma temperature and density profiles were peaked inside the transport located at r/a = 0.5. Negative magnetic shear in the center were formed by PNB=7MW of the pre-heat beam during the ramp-up phase of the plasma current in these discharges. The plasma density was also ramped during the pre-heat beam by the feedback control. As a result of Neon and Hydrogen gas puff, radiative divertor plasmas were obtained while the internal transport barriers are sustained for the first time. (See Fig. 1(a)) The most part of the heat flux to the divertor are dissipated for the most part by radiation loss and charge exchange loss. Thus only 20% of the beam power was deposited to the divertor plates from the measurement with infrared TV camera. (See Fig. 1(b)) At the strike point of the separatrix, heat and particle fluxes vanished and the detached state was produced. The increment of the radiation loss from the main plasma after the compound gas puff was very small, compared with the increment of that from the divertor plasma. This indicates Neon ions are effectively shield against the main plasma and confined in the divertor plasma. The electron density increase from $1 \times 10^{19} m^{-3}$ to $2 \times 10^{19} m^{-3}$ at the plasma edge. (See Fig. 1(c)) This trend is preferable from the points to increase particle recycling at the divertor and to shield impurity ions, resulting to assist radiative divertor plasmas. The transport barrier was sustained after the radiative divertor formation until t = 7.6 s and the central plasma density increases from $3 \times 10^{19} m^{-3}$ to $4 \times 10^{19} m^{-3}$, while the radius of the transport barrier was reduced.

It was found from the soft X-ray measurement that the transport barrier shrinks in time with repetitive mini collapses in the discharges without the compound gas puff. In the discharges with the compound gas puff, the pressure gradient near the transport barrier was reduced and the transport barrier shrunk without repetitive mini collapses in time scale of the resistive diffusion time given by the central electron temperature. (See Fig. 2)

It was found that the particle recycling condition during the ramp-up phase affected the

formation of the transport barrier. Fig. 3 shows wave forms of Φmain / Nmain and Te0. Te0 is the electron temperature at the center form ECE measurement. Here Φmain is the total particle recycling around the main plasma that was obtained from Hα detectors viewing the main plasma and Nmain is total number of electrons, the product of the line averaged density at the U2 port and the plasma volume. Thus Φmain / Nmain is a reciprocal of particle confinement time around the main plasma. In all of the discharges shown in the figure, the plasma densities were ramped up from ne= 1 x$10^{19}m^{-3}$ (at t= 4.2 s) to ne = 2 x $10^{19}m^{-3}$ (at t= 4.9 s) by the density feedback and the neutral beams were programed to the same power during the whole heating phase. The transport barriers were formed in #25364 and #25368 and no barriers were formed in #25366, #25367 and #25370 where the particle recycling level, Φmain / Nmain , were slightly high. Especially, there was no significant differences of Te profile and the polarization angles on the MSE measurement in #25366 from #25364 and #25368 except the recycling level. The establishment of the remote radiative divertor by the neon and hydrogen gas puff should be also noted from the point of the particle recycling control. In contrast to the constraint during the ramp-up phase, the particle recycling around the main plasma is allowed to be a factor of three larger and the divertor particle recycling a factor of five larger once after the transport barrier has established.

3. Summary

In JT-60U, radiative divertor plasma was obtained while the transport barrier of the negative magnetic shear plasma was maintained for the first time. Heat flux to the divertor plates was almost removed and divertor detachment at the separatrix, This was obtained by compound gas puffing of Neon and D2 gas which was initiated at the low particle recycling conditions.

References

[1] T. Fujita et. al see 2.1 of this issue

[2] K. Itami et al. Plasma Phys. Control. Fusion 37 (1995) A235-A265.

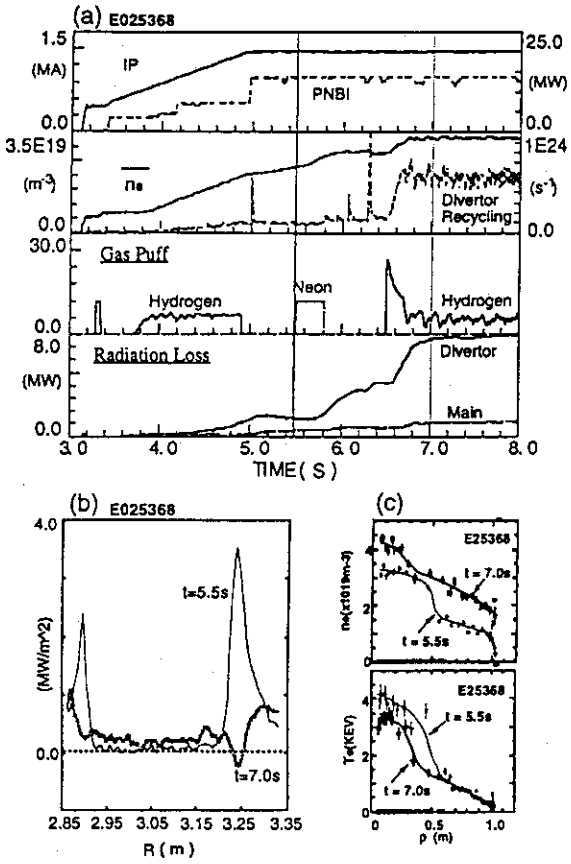

Fig. 1
(a) Wave forms of the negative shear discharge with Neon & Hysrogen gas puff.
(b) Heat flux density profiles before (T=5.0s) and during (T=7.0s) the radiative divertor phase.
(c) Electron density and temperature profiles before (T=5.0s) and during (T=7.0s) the radiative divertor phase.

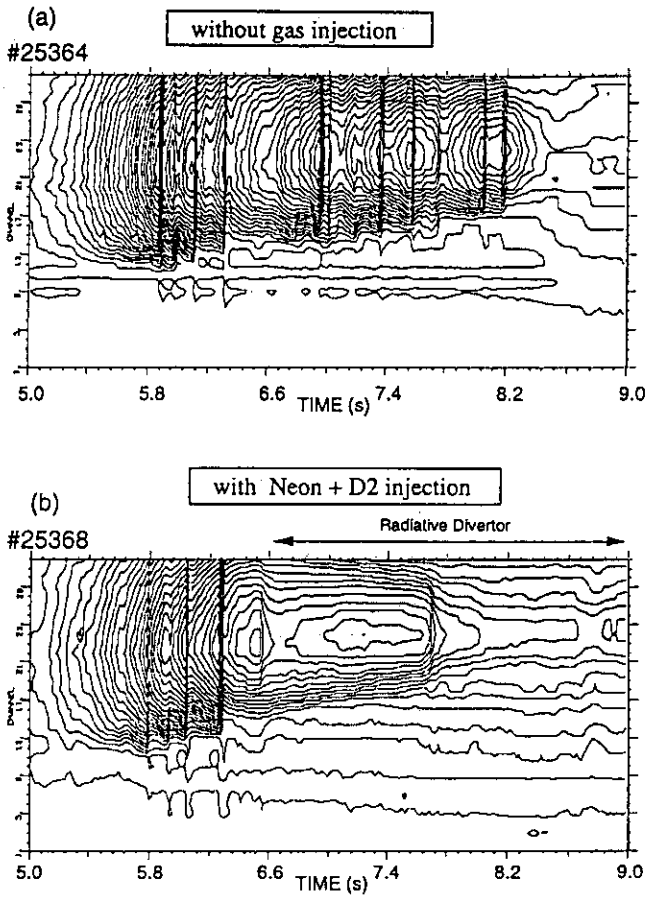

Fig. 2
(a) Soft X-ray contour of the negative shear without gas puff
(b) Soft X-ray contour of the negative shear with neon and hydrogen gas puff

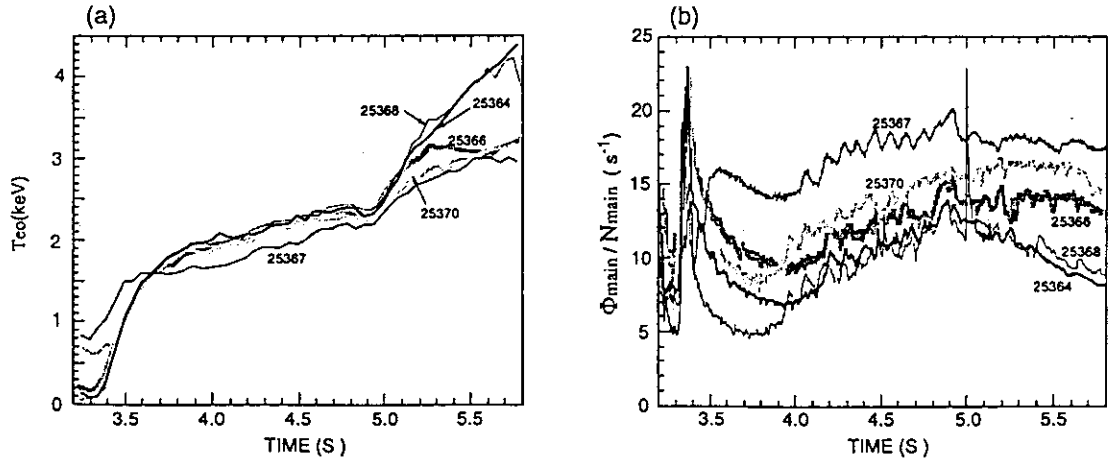

Fig. 3
Time evolution of (a)Te0 and (b) Φmain/Nmain during ramp-up phase of negative shear plasmas.

3. High Triangularity Plasma

3.1 Configuration Control for High Triangularity Plasma

M. Matsukawa, R. Yoshino, K. Ushigusa, S. Takeji

1. Introduction

Triangularity is one of important configuration parameter, and its beneficial effect on the energy confinement has been demonstrated in DIII-D[1]. However there are many unresolved triangularity effects on the plasma performance (especially the density limit on ELM appearance [2]), which are a part of ITER Physics R&D issues. Thus in JT-60U high triangularity plasma with δ of 0.4~0.5 has been studied. Owing to the limit of the coil power supply, the plasma current (I_p) has been raised with two steps; 1 MA in 1995 as the 1st step, and 2MA in 1996 as the 2nd step. Furthermore I_p of 2.5 MA is now under consideration as the 3rd step, according to the experimental results with 2.0 MA.

2. Rearrangement of Poloidal Field Coil

To raise a triangularity, a vertical magnetic field coil system has been rearranged in two groups (VR-coil with 46 turns, VT-coil with 32 turns) as shown in Fig.1. VT-coil (series connection of V3 ~ V6) is mainly used for triangularity-control, and VR-coil (series connection of V1 and V2) is mainly used for the control of the plasma horizontal position. This reconnection has been realized by changing the connection at the connection-box settled in a torus hall. Power supply for VT-coil could generate + 24 kA / ± 0.55 kV in the 1st step, and + 40 kA / ± 1.0 kV in the 2nd step. The negative excitation of VT-coil with a current of -8.6 kA can reverse the triangularity up to -0.1.

3. Range of Triangularity

Triangularity increases with a ratio of VT-coil current and the plasma current as shown in Fig.3(a) obtained from experimental data. Here the maximum triangularity of ~0.5, which is investigated from a fast boundary identification code, has been achieved at the outermost flux surface. Increasing the poloidal beta and internal inductance may affect on δ. Then feedback control of δ is also required during NB heating and I_p-ramp-down phases. There is a dependence between the plasma elongation and triangurality as shown in Fig.3(b), which should be considered for improving the plasma performance.

4. Plasma Configuration Control Variables

For the plasma configuration control, five control variables are selected as shown in Fig.2; the plasma current (I_p), horizontal plasma position of the geometrical plasma center (R_p), vertical position of the plasma current center (Z_J), height of null point from the divertor plate (X_p), triangularity at the outermost flux surface (δ).

Latter four control variables are calculated in real time (computation cycle of 250 μsec) from magnetic probe signals, plasma and coil currents using the statistical method[3]. Figure 4 compares each configuration control variable between the output of statistical method and the one of an equilibrium fitting code performed as a post processing. It shows that reasonable agreement has been achieved for all control variables. Here use of X_p and δ is limited for divertor plasmas, and cannot be applied for limiter plasmas. The statistical equation for X_p has been improved from the standard eq.(1), which was used in 1st step, to eq.(2) to include the effect of VT-coil current on triangularity as shown in Fig.3 (a).

$$X_p^{cont.}=X_{p0}+\sum_{i=1}^{8}\left[\alpha_{1i}\frac{B_{ti}}{I_p}+\alpha_{2i}\left(\frac{B_{ti}}{I_p}\right)\left(\frac{I_d}{I_p}\right)\right]+\sum_{k=1}^{8}\left[\beta_{1k}\frac{B_{nk}}{I_p}+\beta_{2k}\left(\frac{B_{nk}}{I_p}\right)\left(\frac{I_d}{I_p}\right)\right] \tag{1}$$

$$\begin{aligned}X_p^{cont.}=X_{p0}&+\sum_{i=1}^{8}\left[\alpha_{1i}\frac{B_{ti}}{I_p}+\alpha_{2i}\left(\frac{B_{ti}}{I_p}\right)\left(\frac{I_d}{I_p}\right)+\alpha_{3i}\left(\frac{B_{ti}}{I_p}\right)\left(\frac{I_{VT}}{I_p}\right)\right]\\&+\sum_{k=1}^{8}\left[\beta_{1k}\frac{B_{nk}}{I_p}+\beta_{2k}\left(\frac{B_{nk}}{I_p}\right)\left(\frac{I_d}{I_p}\right)+\beta_{3k}\left(\frac{B_{nk}}{I_p}\right)\left(\frac{I_d}{I_p}\right)\right]\end{aligned} \tag{2}$$

5. Noninteracting Multivariable Control

Five control variables are controlled by five independent power supplies according to the multivariable noninteracting control method[4]. A matrix gain is used for this method, but a complete matrix gain of 5x5 is impossible to calculate within one control cycle due to the limitation of computation capability. Each element of gain matrix was estimated from the state equation of each control variable[4]. To test a validity of gain matrix, each control variable has been swung with 10 Hz as shown in Fig.5. A deviation of δ is relatively large, but a reasonable decoupling has been demonstrated.

6. Plasma Breakdown

To apply a enough loop voltage at the plasma initiation position (inboard-up in the vacuum vessel), VT-coil power supply must produce the higher voltage. In the 1st step, the maximum loop voltage was 20 V, then a stable plasma breakdown could not be obtained without LHRF assistance [5] especially for the low toroidal magnetic field. Then the voltage rating of VT-coil power supply was increased up to 1.0 kV from a 0.55 kV with a rearrangement of power supply system. As a result, the loop voltage could be raised up to 30 V, and then the plasma breakdown has been largely stabilized. PSEX-power supply (1kV-10kA) has been connected with the VT-coil power supply, then it has been switched on just before the breakdown (at t = 0.0 sec), but any destabilizing effect on the breakdown has never been observed.

7. 2.5 MA Discharge

According to the experimental results of 2 MA, plasma current of 2.5 MA is planned as the third step. Here the power supply for VT-coil can generate + 55 kA / ± 1.0 kV at present,

thus the following items should be checked systematically; 1) temperature of VT-coil feeder in a torus hall, 2) stress on the toroidal magnetic field coils, 3) stress on the poloidal magnetic field coils.

References

[1] T. Taylor, et al., 14th IAEA Wurtzburg (1994) IAEA-CN-56/A-3-1.

[2] Y. Kamada, et al., section 3.2 in this paper

[3] M. Matsukawa, et al., Plasma Phys. and Control. Fusion, **34** (1992) 907.

[4] R. Yoshino, et al., Fusion Engineering and Design, **24** (1994) 375.

[5] R. Yoshino, et al., section 11.6 in this paper.

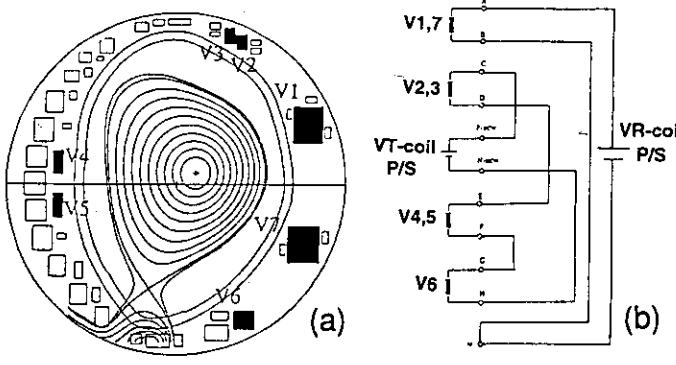

Fig.1 VR-coil(V1,V7) and VT-coil(V2~V6).

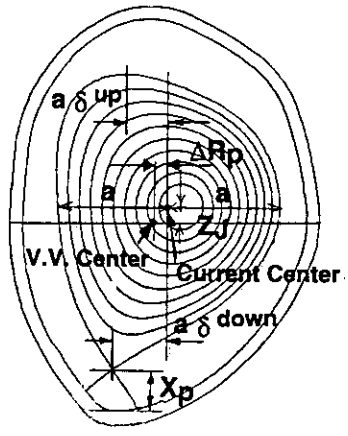

Fig.2 Control variables.

δ is defined as $(\delta^{up}+\delta^{down})/2$.

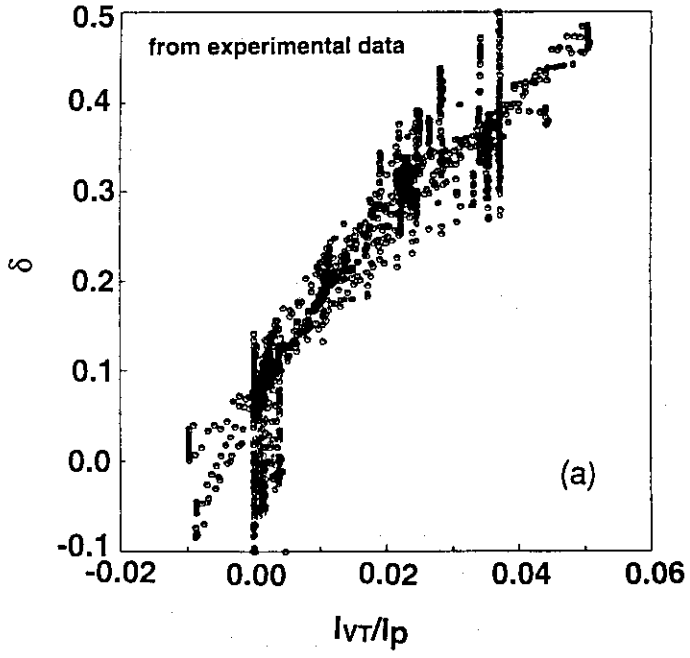

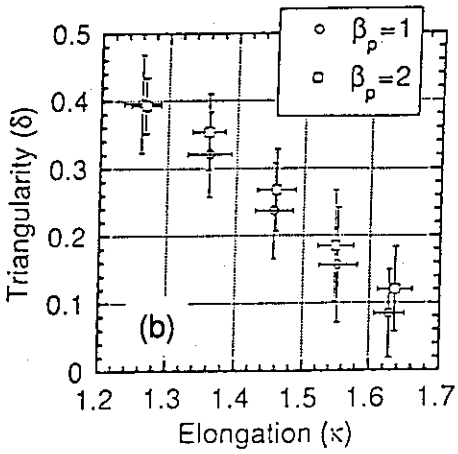

Fig.3 Plasma Triangularity.

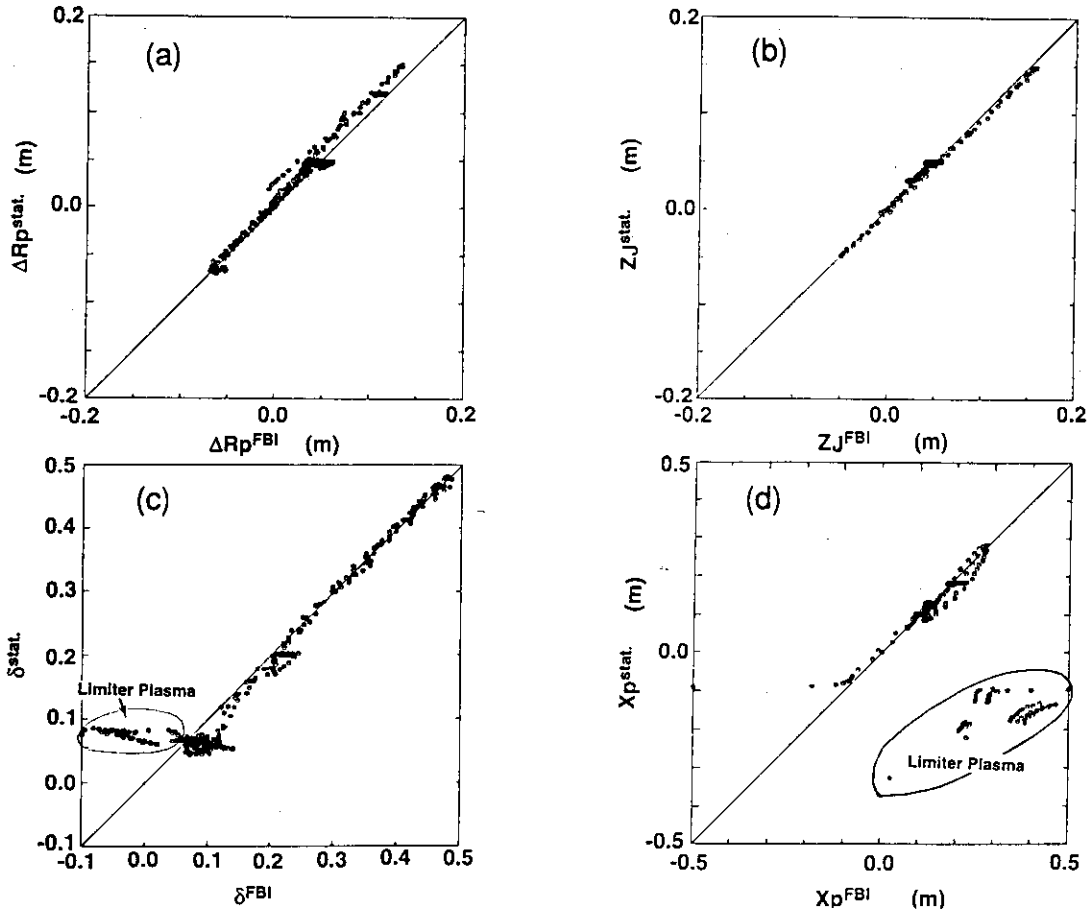

Fig.4 Fitting accuracy of control variables. *(a)ΔRp, (b)Zj, (c)δ, (d)Xp*

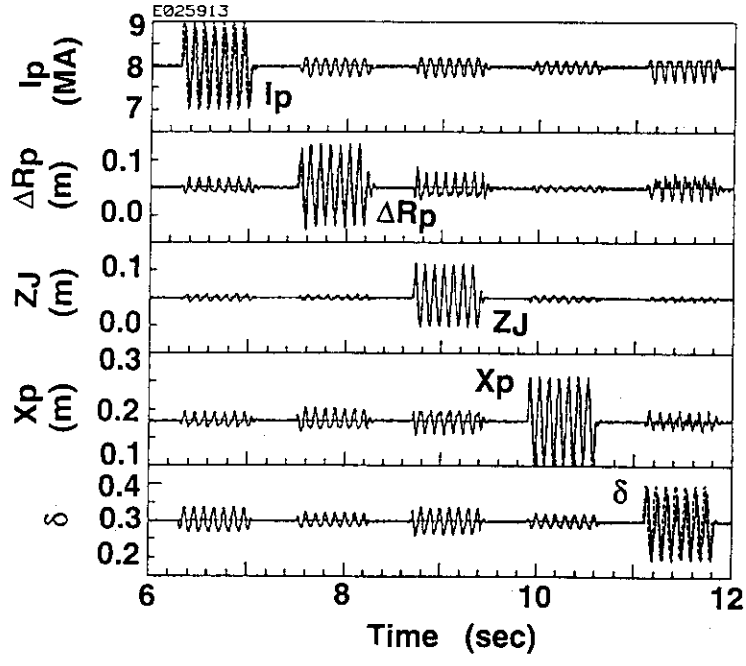

Fig.5 10Hz swing of each control variables.

3.2 Improved Edge Density and Pressure Limits for Onset of Giant ELMs in High Triangularity Discharges

Y. KAMADA, R.YOSHINO, Y. NEYATANI, M. SATO, S. TOKUDA, M.AZUMI, S.TAKEJI, K.USHIGUSA, T. FUKUDA, M. MORI, T.TAKIZUKA and JT-60U Team

1. Introduction

Control of ELM behaviors is one of the most important issues for sustainment of plasmas with the high integrated performance required in the steady-state fusion reactors. To contribute to establish control scenarios of ELMs, this paper identifies the onset conditions of giant ELMs and emphasizes effects of plasma shape such as triangularity δ and elongation κ. Appearance of giant ELMs limits the achievable edge density and edge pressure and also restricts core plasma performances through profile-effects on stability and transport. In particular, in H-mode plasmas with broad pressure profiles, the edge pressure limit directly determines the global β_N limit [1]. This edge pressure limit also affects the ELM frequency f_{ELM}. At a given heating power, f_{ELM} increases with decreasing pressure limit, which results in poor confinement in a ELMing steady-state.

For the typical shapes of JT-60U plasmas with δ~0.1, two types of ELMs have been observed. The first is dithering ELMs observed when heating power P_{net} is around the threshold power for the L-H transition. The second is giant ELMs observed when the edge pressure reaches a critical value. When both δ and β_p are high (δ>~0.3, β_p>~2), the third type is observed; the wave form is minute-grassy and the edge n_e, T_i and T_e can continuously increase during the grassy ELMs. (The behaviors of these three types are similar to those observed in DIII-D [2].) The dependence of f_{ELM} on P_{net} is different among these three types. With increasing P_{net}, dithering ELMs appear at first, $f_{ELM\text{-}dither}$ decreases quickly, then giant ELM appears after a ELM-free period and $f_{ELM\text{-}giant}$ increases almost linearly with P_{net}[3]. The frequency $f_{ELM\text{-}giant}$ also increases with decreasing $B_t^2/(Rq^2)$, decreasing l_i and increasing n_e [3]. On the other hand, the minute-grassy ELMs have higher f_{ELM} than giant ELMs and no clear dependence on P_{net} has been observed.

2. Effects of Plasma Shape on the Onset Conditions of Giant ELMs

In JT-60U, an ELM-free phase appears only when is lower than a threshold value $\bar{n}_e^{th}$, which increases with I_p or $B_t^2/(Rq_{eff}^2)$ (a measure for the ballooning stability) [3]. The values of $\bar{n}_e^{th}$ are ~$1\times10^{19}m^{-3}$ at I_p=1MA and ~$3\text{-}4\times10^{19}m^{-3}$ at 4MA. Since values of edge n_e and edge T_i (or T_e) are roughly proportional in JT-60U ELM-free H-modes, the onset condition of giant ELMs is given by a function of edge n_e or edge pressure. To obtain higher plasma performance at higher n_e, we started to study effects of plasma shape on the onset condition. Recently a new connection of the poloidal field coils enabled us to scan triangularity δ from the original value of ~0.1 up to δ~0.4 (limited at I_p<1.2MA so far) and also down to a negative value δ~ -0.06. Figures 1. a)-c) compare the typical cross sections at I_p=1MA. Figure 1 d) shows the operation region of d and k for our study on ELMs: the δ-scan at fixed κ, the κ-scan at fixed δ and negative δ.

Figure 2 shows effects of δ at I_p=1MA. From Figs.2 a) and b), higher δ has higher $\bar{n}_e$ at the first giant ELM. In addition, the ELM free period (from H-transition to the first giant ELM) was increased from ~0.05 sec to 0.9 sec. (Note: The length of the ELM-free period is a rough measure of improvement, because the length is also a function of density

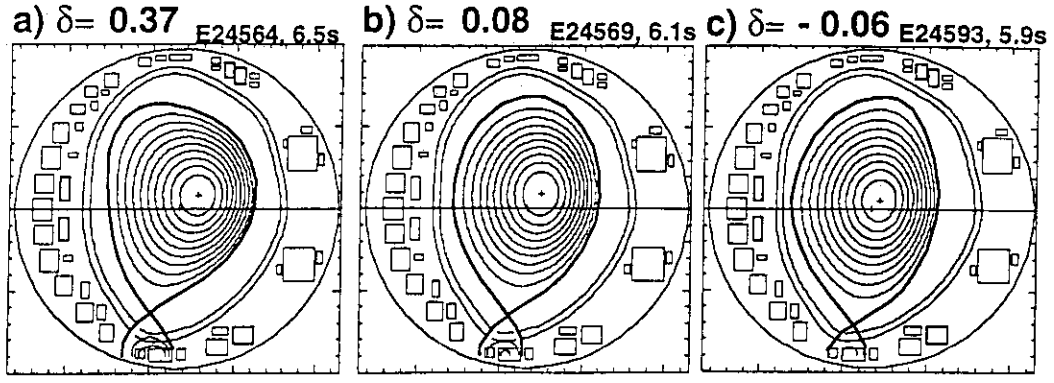

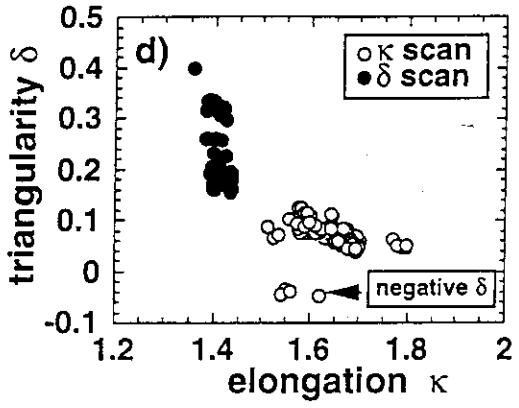

Figure 1.
Typical plasma shapes at Ip=1MA:
a) high triangularity,
b) standard,
c) negative triangularity.
d) Region of elongation κ and triangularity δ used in the ELM study.

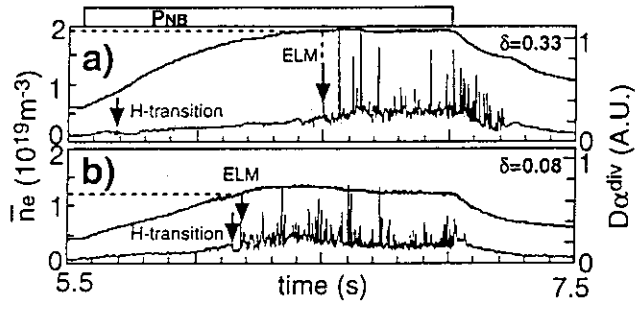

Figure 2. a)&b): time traces of $\overline{n}_e$ (center) and Dα signal for high-δ (P_{NB}=25MW) and low-δ (P_{NB}=20 MW) plasmas at I_p=1MA, B_t=2.5T.
c)&d): Increasing $\overline{n}_e$ (center), $\overline{n}_e$(0.7a), T_e(r/a=95%) and T_i(r/a=95%) with δ at the onset of giant ELMs.

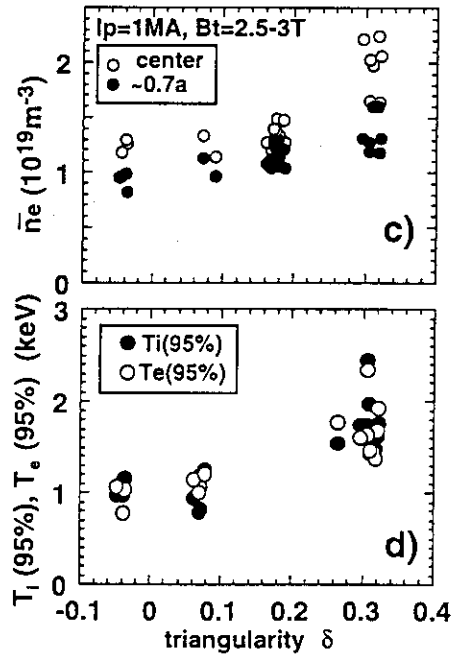

rise affected by NB power, recycling etc.) Figures 2 c) and d) show that edge density and edge temperatures at the onset of giant ELMs increase with δ. The improvement from δ~ 0.08 to δ~0.33 are 30-40% for $\overline{n}_e$ and ~80% for T_e(r/a=95%) and T_i(r/a=95%). The edge pressure limit (nxT) increases roughly linearly with δ.

The onset condition of giant ELMs is given by a clear proportionality -grad-p^{th}_{edge} ~ $B_t^2/(2\mu_0 R q_{95}^2)$ over wide ranges of I_p (0.4-4MA) and B_t (1-4T) (Fig.3 (b)), where p^{th}_{edge} is a measure of thermal pressure given by (~0.7a)x(fT_i(95%)+T_e(95%)) and f is a function of Z_{eff}. (In this paper, we assumed Z_{eff}(95%)=3.5 and carbon impurity.) The pressure gradient

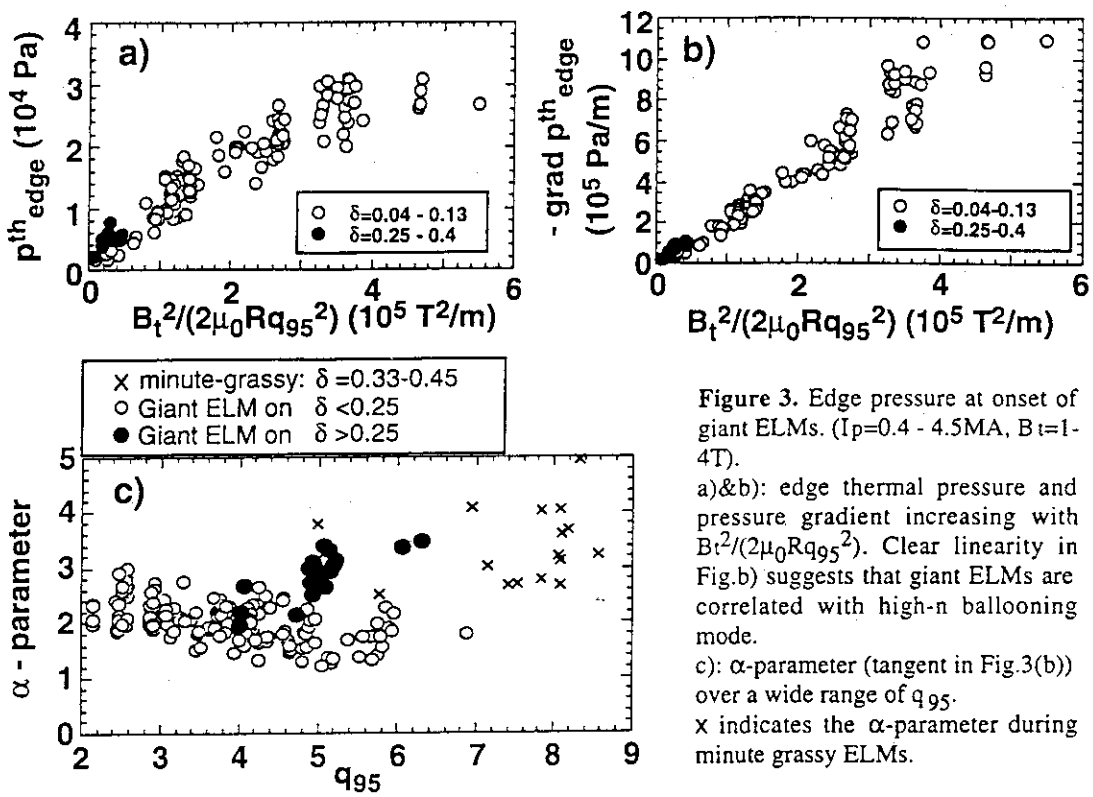

Figure 3. Edge pressure at onset of giant ELMs. (Ip=0.4 - 4.5MA, Bt=1-4T).
a)&b): edge thermal pressure and pressure gradient increasing with $B_t^2/(2\mu_0 R q_{95}^2)$. Clear linearity in Fig.b) suggests that giant ELMs are correlated with high-n ballooning mode.
c): α-parameter (tangent in Fig.3(b)) over a wide range of q_{95}.
× indicates the α-parameter during minute grassy ELMs.

grad-p^{th}_{edge} is given by p^{th}_{edge}/Δ, where Δ is width of the edge pressure pedestal. We assume that $\Delta = 4\varepsilon^{0.5}\rho_i$ based on JT-60U experiment 4), where ε is the inverse aspect ratio and ρ_i is the poloidal gyro radius of thermal ions: $\rho_i \sim T_i(95\%)0.5/B_p(a)$. The normalized pressure gradient $\alpha=(-\text{grad-}p^{th}_{edge})/(B_t^2/(2\mu_0 R q_{95}^2))$) (= tangent in Fig.3 b)) is almost constant over a wide range of q_{95} (=2-7) at low-δ (open circles in (Fig.3 c)). This result suggests that the giant ELM is triggered by high-n ballooning mode. A time dependent analysis including bootstrap current supports this result [5]. Whereas, high-δ plasmas (closed circles) have higher values of α. In Fig.4 a), the α-parameter at the onset of giant ELMs increases with δ (closed circles: the δ-scan at fixed κ). This tendency may be saturated around δ~0 because the data with δ~0.08 and -0.05 at κ~1.5 have similar values of α (see open circles in Figs. 4 a) and 5 a)). Another important result is that the β_N value at the onset of giant ELM increases with δ (Fig.4 b)). In JT-60U H-mode at δ~0.1, β_N was lower than 1.8 limited by giant ELMs [1]. The results obtained here shows that the H-mode performance in JT-60U is increasing with δ. Figure 5 a) shows the α-parameter also increases with κ for κ=1.5-1.8 at a fixed δ (=0.06-0.13) (open circles). Finally, at the fixed κ (=1.5-1.6) and δ (= 0.06-0.13) the α-parameter increases with l_i (Fig.5 b)), which suggests that the giant ELMs in this low-δ region is triggered in the first stability region for the high-n ballooning mode.

Because the local edge measurement is not sufficient for all plasma configurations, we simply assumed the width Δ is given by $\Delta = 4\varepsilon^{0.5}$ri and $Z_{eff}(95\%)=3.5$, which should be studied in detail. Contribution of the fast ion pressure gradient is another issue. Concerning effects of the current profile, the region of li in the high-δ (>0.3) cases in Fig.4 is 0.8-1.6 and almost in the same range of l_i in the low-δ cases. The study on edge shear at high-δ is our future work including the access to the second stability regime. The minute grassy ELMs appear at high values of α (~3-5) as shown in Figs.3-5, which may be related to access to the second stability regime.

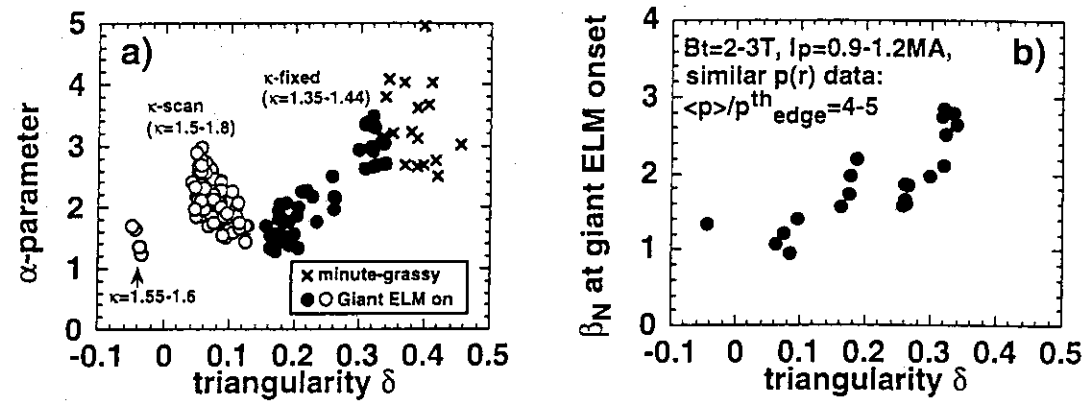

Figure 4. Dependence of α-parameter and β_N on triangularity at onset of giant ELMs

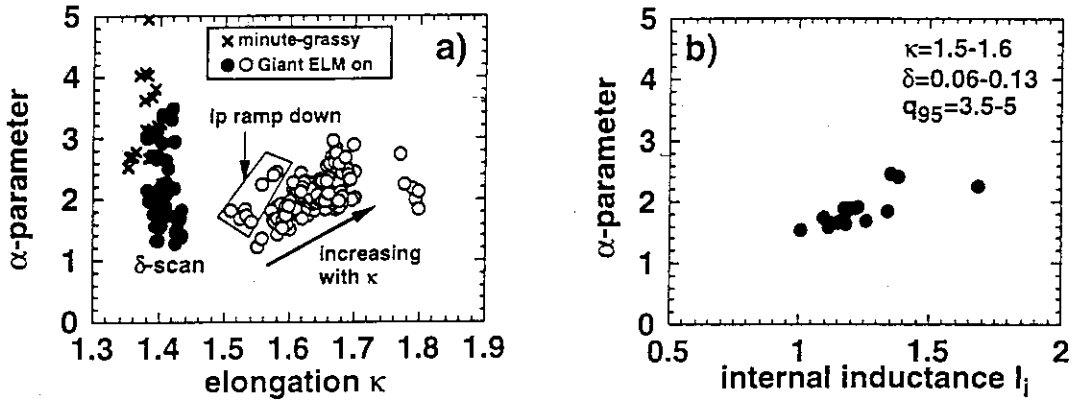

Figure 5. Dependence of α-parameter on elongation and l_i at onset of giant ELMs

3. Conclusion

For the standard shape of JT-60U at low triangularity δ (~0.1), the onset condition of giant ELMs is clearly correlated with the high-n ballooning limit in the first stability regime over wide ranges of plasma parameters (I_p, B_t, q_{95}..). The limit of the normalized edge pressure gradient (α-parameter) increases with elongation κ (1.5-1.8) and internal inductance l_i. Recently a new connection of the poloidal field coils enabled us to scan triangularity δ from the original value of ~0.1 up to δ~0.4 (limited at I_p<1.2MA so far). The δ-scan (-0.05 ~0.4) showed that the limit of edge density, edge pressure and the α-parameter increase with δ. When both d and β_p are high (δ>~0.3, β_p>~2), minute-grassy ELMs appear. The edge α-parameter during the minute grassy ELMs can be higher than that for the onset of giant ELMs.

Acknowledgement. The authors gratefully acknowledge contribution by Dr. T. S. Taylor to establish the high triangularity shape in JT-60U.

References

1) Y.Kamada et al., in Plasma Phys. Cont. Nucl. Fusion Res. Proc.15th Int. Conf., Seville, 1994, IAEA-CN-60/A-5-I-5, see also Y. Kamada et al., Nucl. Fusion **34** 1605 (1994).
2) E. J. Doyle et al., Phys. Fluids B **3** (1991)
3) Y. Kamada et al., Plasma Phys. Cont. Fusion **36** Suppl (7) A123 (1994).
4) T. Hatae et al., 37th Ann. Meeting, APS Div. Plasma Phys. 1995, Louisville, 5R.13.
5) M. Sato, et al.,in Plasma Phys. Cont. Nucl. Fusion Res. Proc.15th Int. Conf., Seville, 1994, IAEA-CN-60/A2-II-4

3.3 Confinement, β-limit and Current Drive Characteristics in High Triangularity Discharges

Y. KAMADA, K.USHIGUSA , R.YOSHINO, Y. NEYATANI, S. TOKUDA, M.AZUMI, S.TAKEJI, and JT-60U Team

1. Introduction

The most important mission in tokamak development is the simultaneous achievement of i) high confinement (high H-factor = $\tau_E/\tau_E^{ITER89PL}$), ii) high power density (high β_N), iii) high bootstrap fraction (high β_p), iv) full non-inductive current drive and v) high efficiency of heat and particle exhaust in the steady-state. The tokamak operation should satisfy the integrated performance at a high level [1]. For the core plasma performance i)-iv), the JT-60U device has produced i) high values of fusion product $1.2\times10^{21}m^{-3}skeV$ in ELM-free high-β_p H mode [2] and $4\text{-}5\times10^{20}m^{-3}skeV$ in quasi-steady ELMy high-β_p H mode [3], ii) β_N up to 4.8 [3], iii) bootstrap fraction up to ~80% [4] and iv) 3.6MA full non inductive current drove with LHCD [5]. For the integration of i)-iv), we demonstrated feasibility of the SSTR concept in a quasi steady ELMy H-mode with I_p=1MA and B_t=3T where high values of H-factor~2.5 and β_N~2.9 were sustained for ~0.7sec under the fully noninductive current drive condition (bootstrap=74%, NBCD=37%)[3]. However this result demonstrates only an integration of core plasma performances in a time scale shorter than the current diffusion time. The remaining issues in approaching the final goal are A) combination of a high core plasma performance and a high divertor plasma performance and B) sustainment in a steady-state longer than the current diffusion time. Concerning A), we have to increase the density range. However, energy confinement is decreasing with increasing density. This is because high confinement usually requires low recycling. For B), the β-limit in a quasi-steady state is lower than that obtained transiently. To overcome these difficulties, we are trying three modifications: new equilibria with high triangularity δ (from 1995), the negative ion source NB injection (from 1996) and the closed divertor (from 1997). Out of these modifications, Sec. 3. introduces the initial results of high δ experiments in JT-60U where the main purposes are to obtain high confinement at high density and high β-limit with high confinement. Concerning the high density operation, the most critical issue in JT-60U is the onset condition of giant ELMs. We demonstrated that the density and pressure limit for the onset of giant ELMs is increasing with increasing δ in sec.3.2. This section 3.3 treats characteristics of confinement, β-limit and current drive.

2. Energy confinement

In JT-60U, attainable values of H-factor and β_N are affected by plasma position (major radius) R_p because NB-heating profiles and loss of fast ions by toroidal field ripple are functions of R_p. Firstly, the discharge regions of the high-δ (closed circles) and low-δ (open circles) experiments are introduced by Fig.1(a) and (b). In this section, the ripple loss is not subtracted in estimating H-factor. Figure 1(a) shows attainable value of H-factor is strongly decreasing with increasing R_p: Degradation of attainable H-factor $\Delta H/\Delta R_p$ ~ 0.6 / 10cm. This is mainly because, at smaller R_p, the heating profile is more peaked and ripple loss is smaller. On the other hand, the maximum β_N-limit is obtained at medium R_p (3.2-3.4m) because medium-peaked pressure profiles have the highest β-limit concerning both internal low-n kink-ballooning modes and ELMs 2). In Fig.1(b), β_N at smaller R_p is limited mainly by the low-n modes and that at larger R_p is limited by ELMs. From Fig.1, the high-δ discharges have higher values of H-factor and β_N than the low-δ discharges at the same position R_p. Figure 2 (a) shows dependence of H-factor of ELM-free H-mode on δ at almost fixed values of I_p, V_p and R_p. With increasing δ, H-factor tends to be improved. This tendency may become stronger when the difference of R_p between high-δ and low-δ discharges (Fig.2 (b)) is taken into account: The high-δ data have larger R_p than the low-δ data by 5-10cm.

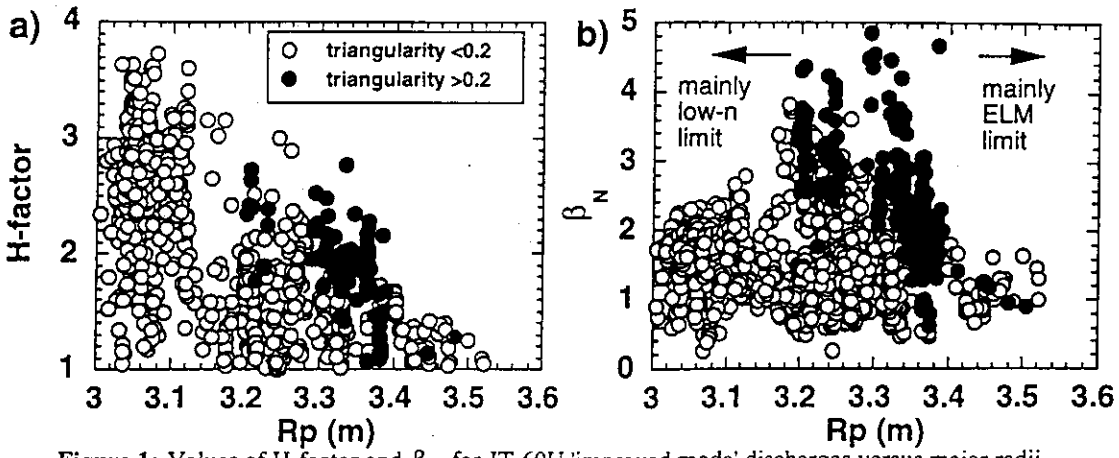

Figure 1: Values of H-factor and β_N for JT-60U 'improved mode' discharges versus major radii. Open and closed circles indicate low δ (<0.2) and high δ (>0.2) discharges, respectively.

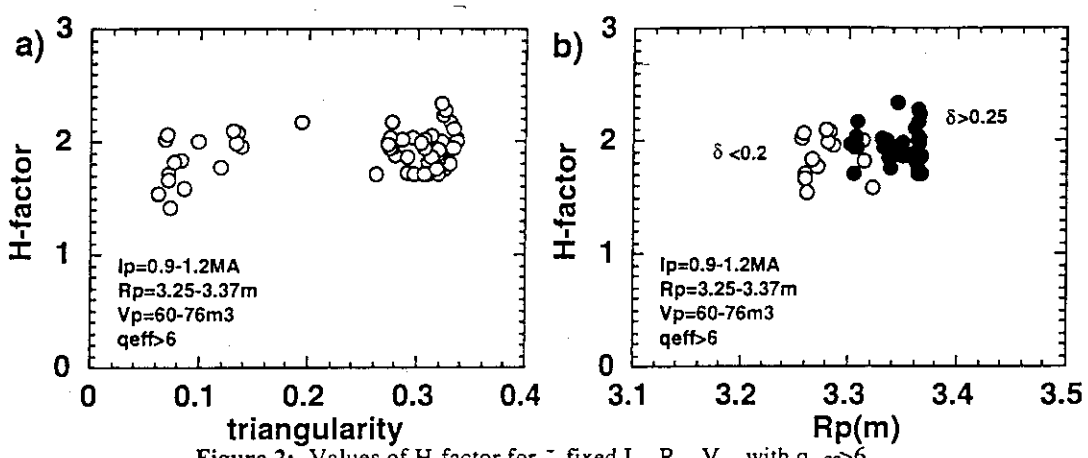

Figure 2: Values of H-factor for ˜ fixed I_p, R_p, V_p with q_{eff}>6.

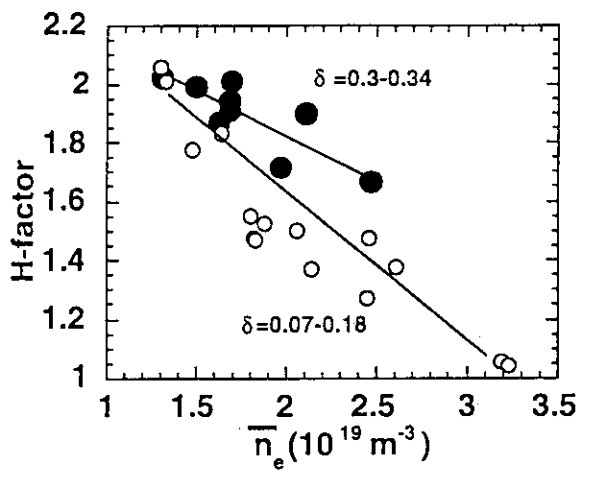

Figure 3: Dicreasing H-factor with increasing electron density. The degradation for high-δ discharges is weaker for low-δ discharges. (I_p=0.9-1MA, B_t=2T, Vp=64-75m^3 P_{NB}=14-23MW, l_i(target)=1.4-1.7)

Concerning energy confinement in ELMy H-mode, improvement in high-δ discharge is clearer. Figure 3 shows dependence of H-factor on ne for low-δ (0.3-0.34: open circles) and high-δ (0.07-0.18: closed circles). The degradation in H-factor with increasing n_e is weaker for high-δ discharges. This result seems to be partly related to that the n_e-limit for onset condition of giant ELMs is higher for higher δ.

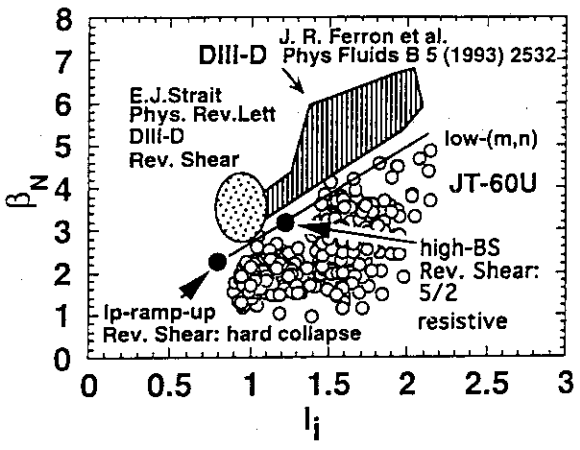

Figure 4: β_N vs. l_i in JT-60U compared with DIII-D. The upper boundary of β_N is almost limited by low-(m,n) pressure driven modes.

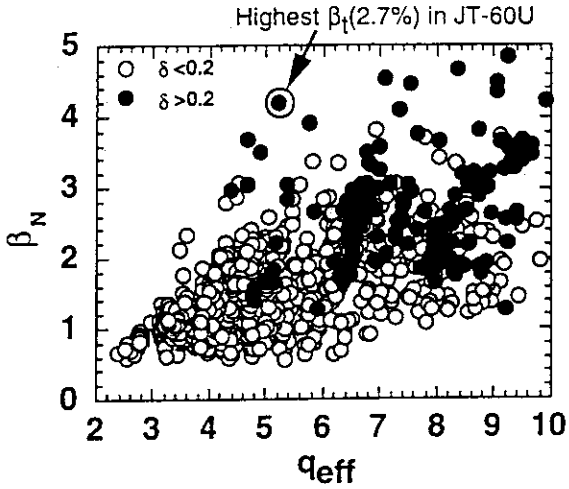

Figure 5: β_N vs. q_{eff} in JT-60U. Open and closed circles correspond to low-δ and high-δ discharges, respectively. The discharge ◎ has the highest β_t (2.7 %) in JT-60U at δ=0.34, B_t=1.5T, I_p=0.9MA, q_{95}=3.9.

3. β-limit

It is known that the β_N-limit increases with the internal inductance l_i 6-8). Figure 4 shows this tendency for DIII-D[6] and JT-60U. For each li value the maximum β_N tends to be limited by low-n modes. In case of the reversed magnetic shear experiment with fast I_p-ramp in JT-60U [9], the β_N limit obtained so far is almost on the expected line of the l_i-scaling. Therefore the global shear across entire volume seems to be the key factor for these low-n mode with a global displacement. The higher β_N limit in DIII-D than that in JT-60U may be caused by difference in the plasma shape (triangularity, elongation, aspect ratio), plasma rotation, rotation shear, location of the resistive wall or difference in collisionality.

The β-limit related to low-n pressure driven mode seem to be improved with increasing δ. Figure 5 shows the relation between β_N and q_{eff} in JT-60U where closed and open circles correspond to δ>0.2 and δ<0.2, respectively. The upper boundaries of β_N for both δ>0.2 and δ<0.2 are limited by low-n modes. The β_N-limit for high-δ discharges is systematically higher than that for low-δ. The arrowed point in Fig.5 has the highest β_t (2.7%) in JT-60U at δ=0.34, B_t=1.5T, I_p=0.9MA, q_{eff}=5.2, q_{95}=3.9 and H-factor=2.8. Based on Fig.5, the improvement in β_N seems to be larger at lower q_{eff}. The high-δ discharges tends to have higher l_i than low-δ discharges, which seems to be one of the reasons of high β-limit.

4. Non Inductive Current Drive with Bootstrap Current and NB Driven Current

Concerning full non-inductive current drive, a favorable integrated performance with I_{NBCD}/I_p~0.4, I_{BS}/I_p~0.6, H-factor =2-2.6, β_N~3.1 was sustained for ~2sec (>10xτ_E) at δ= 0.32, I_p=1MA, B_t=3T and n_e~2.3x$10^{19}m^{-3}$ (Fig.6). The life time of the full CD at I_p=1MA with the original shape in JT-60U was 0.7s at δ~0.2 3). In addition, the ELM behavior in Fig.6 is much weaker than usual giant ELMs observed at low-δ. Although the heating profile of this discharge is relatively broad, a clear internal transport barrier in T_i and n_e profiles is produced like the high-β_p mode. In this discharge, degradation in stored energy seems to be correlated with slowly growing n=1 mode.

The optimization of both confinement and stability should be demonstrated with the final equilibrium in the steady-state where the current profile has been fully diffused. The stability limit in the steady-state is different from that obtained transiently. Another important point is that the β_N-values tend to be limited by resistive instabilities in the quasi-steady state rather than ideal modes. In JT-60U, the maximum β_N sustainable in the quasi-steady state with high bootstrap fraction is ~3 which is much smaller than that obtained transiently (up to 4.8) [3]. For example, ref.8) showed a quasi steady high-β_p ELMy

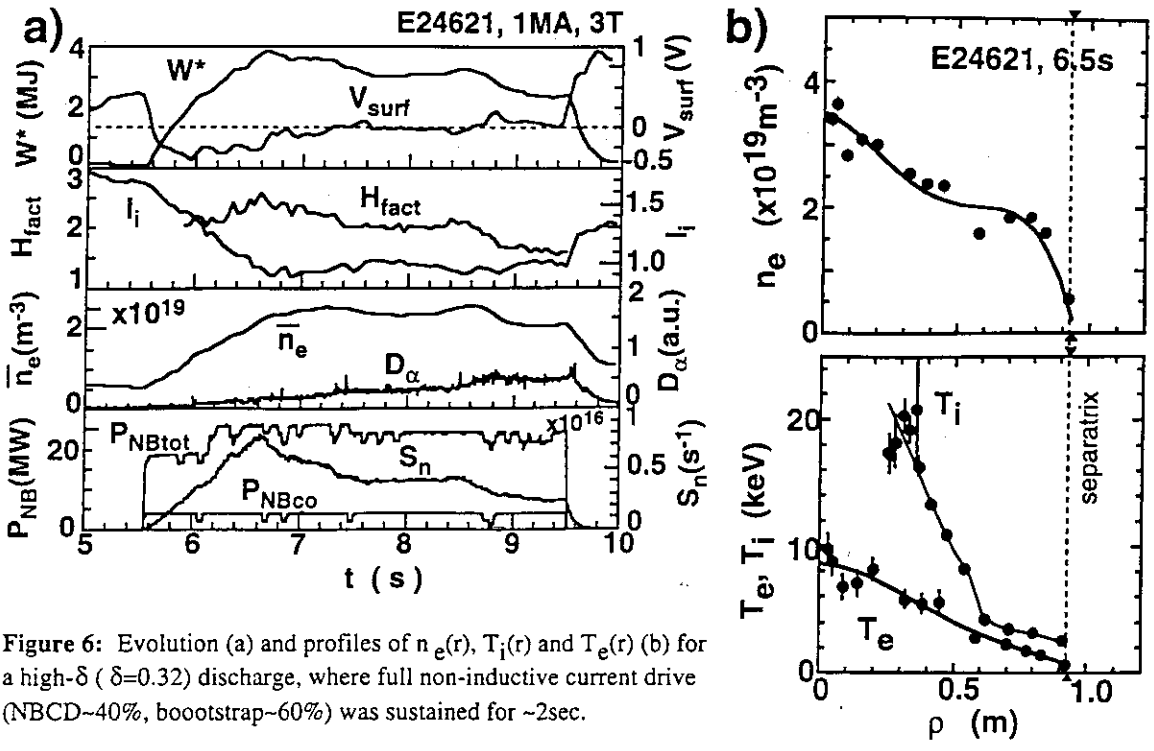

Figure 6: Evolution (a) and profiles of $n_e(r)$, $T_i(r)$ and $T_e(r)$ (b) for a high-δ (δ=0.32) discharge, where full non-inductive current drive (NBCD~40%, boootstrap~60%) was sustained for ~2sec.

discharge with reversed shear in which confinement was degraded by a resistive pressure driven low-n mode destabilized when the q-profile has a pitch minimum at q~2.5 (calculation) in the later phase of the NB heating.

5. Summary

The high-δ (~0.3-0.35) discharges seem to have better performances for confinement, β-limit and non-inductive current drive than low-δ (~0.07-0.2) discharges, which suggests high-δ shape is favorable for high integrated performance in the steady-state. The high-δ discharges have higher values of H-factor than the low-δ discharges at the same position R_p. In ELMy H-mode, the degradation in H-factor with increasing n_e is weaker for high-δ (~0.3-0.34) discharges than low-δ (0.07-0.18). The β_N-limit related to low-n pressure driven mode for high-δ discharges is systematically higher than that for low-δ. At δ=0.34, the highest β_t (2.7%) in JT-60U was obtained (q_{eff}=5.2, q_{95}=3.9). Concerning full non-inductive current drive, a favorable integrated performance with I_{NBCD}/I_p~0.4, I_{BS}/I_p~0.6, H-factor =2-2.6, β_N~3.1 was sustained for ~2sec (>10xτ_E) at δ=0.32, I_p=1MA and B_t=3.

References

1) Y. Kamada et al., 'Characteristics and Issues of the Combined H-modes' to appear in Plasma Phys. Control. Fusion
2) M. Kikuchi and JT-60Team, in Plasma Phys. Control. Nucl. Fusion Research. Proc.15th Int. Conf., Seville, 1994, A-1-I-2
3) Y. Kamada et al., in Plasma Phys. Control. Nucl. Fusion Research. Proc.15th Int. Conf., Seville, 1994, A-5-I-5
4) M. Kikuchi, et al., Nucl. Fusion **30**, 343 (1990)
5) Y. Ikeda et al., in Plasma Phys. Control. Nucl. Fusion Research. Proc.15th Int. Conf., Seville, 1994, A-3-I-1
6) J. R. Ferron et al., Phys. Fluids B **5** , 2532 (1993)
7) S. A. Sabbagh et al., Phys. Fluids B **3** , 2277(1991)
8) Y. Kamada et al., Nucl. Fusion **34**, 1605 (1994)
9) T. Fujita et al., in preparation

3. 4 LH coupling property with triangle-shaped plasma

M. Seki

1 introduction

Highly triangle-shaped plasma are used not only to improve its confinement, but also to simulate high triangularity configuration expected after modification of divertor in 1997. LH power is injected into the highly-triangle shaped plasma, in order to obtain coupling property of LH and to examine current drive performance. Because it is difficult to bring plasma close to LH antenna for good coupling in closed divertor configuration of JT-60U.

2 experimental results

Effect of triangularity on coupling is investigated during one shot as shown in Fig. 1. Upper side of the figure represents poloidal cross-section at t = 9, 10, and 11 sec. Injected power P and reflection coefficient R of antenna A and B are illustrated in lower side. Plasma current is 1 MA in this shot, toroidal magnetic field and line averaged density 4 T and 0.6 x $10^{19}m^{-3}$, respectively. LH antenna is flushed with the first wall, distance between plasma and the wall δ_0 keeps quasi-constant of 14 cm. Reflection coefficient R does not change so much, while triangurality Δ changes from 0.26 to 0.16 in LH injection of 4 seconds.

Dependence of reflection coefficient on plasma-wall distance δ_0 is studied with triangle-plasma of Δ = 0.26~0.29. Experimental results show that low reflection coefficient is obtained up to δ_0 = 18 cm as drawn in Fig. 2. This good coupling is consistent with SOL measurement using a fast reciprocating probe as indicated by LH coupling code. Reflection coefficient decreases with increasing radiated LH power. These characteristics suggest that peripheral plasma in front of LH antenna may be produced by LH power and allows long distance coupling [1]. On the other hand, this long distance coupling up to 15-18 cm disappears when q_{eff} is less than 4 for Ip = 1 MA due to short connection length of field lines near LH antenna. Therefore high toroidal field up to 3.5-4 T might be required for good coupling of $\delta_0 > 15$ cm with Ip = 2MA in closed divertor.

Current drive efficiency is examined with triangle-plasma of Δ = 0.26~0.29. Plasma current Ip is 0.9-1 MA, line averaged plasma density is relatively low as 0.6-0.8 x 10^{19} m^{-3}, and input LH power is 1-1.7 MW with parallel refractive index $N_{//}$ of 1.6. Serious degradation in current drive efficiency is not observed even though plasma-wall distance δ_0 is extended up to 18 cm with triangle-plasma as shown Fig. 3. This drive

efficiency η_{CD} of ~1.7 x 10^{19} $m^{-2}AW^{-1}$ is somewhat low, but η_{CD} will increase with increasing Ip.

3 conclusion

It seems that triangularity does not affect coupling property and current drive performance of LH, peripheral plasma around LH antenna may govern LH waves even with highly triangle-shaped plasma. Simulations using triangle-plasma suggest that good coupling is expected when plasma is approached to LH antenna as δ_0 ~ 15 cm after modification of divertor configuration. Unfortunately, effect of baffle panel of closed divertor is well not unknown in this simulation. The baffle panel may affect on coupling property due to short connection length of field line. In this case LH antenna should be protruded into vacuum vessel for good coupling with monitoring heat load on LH antenna mouth.

Reference

1) M. Seki et al. ; in this JAERI research, sec. 7. 1

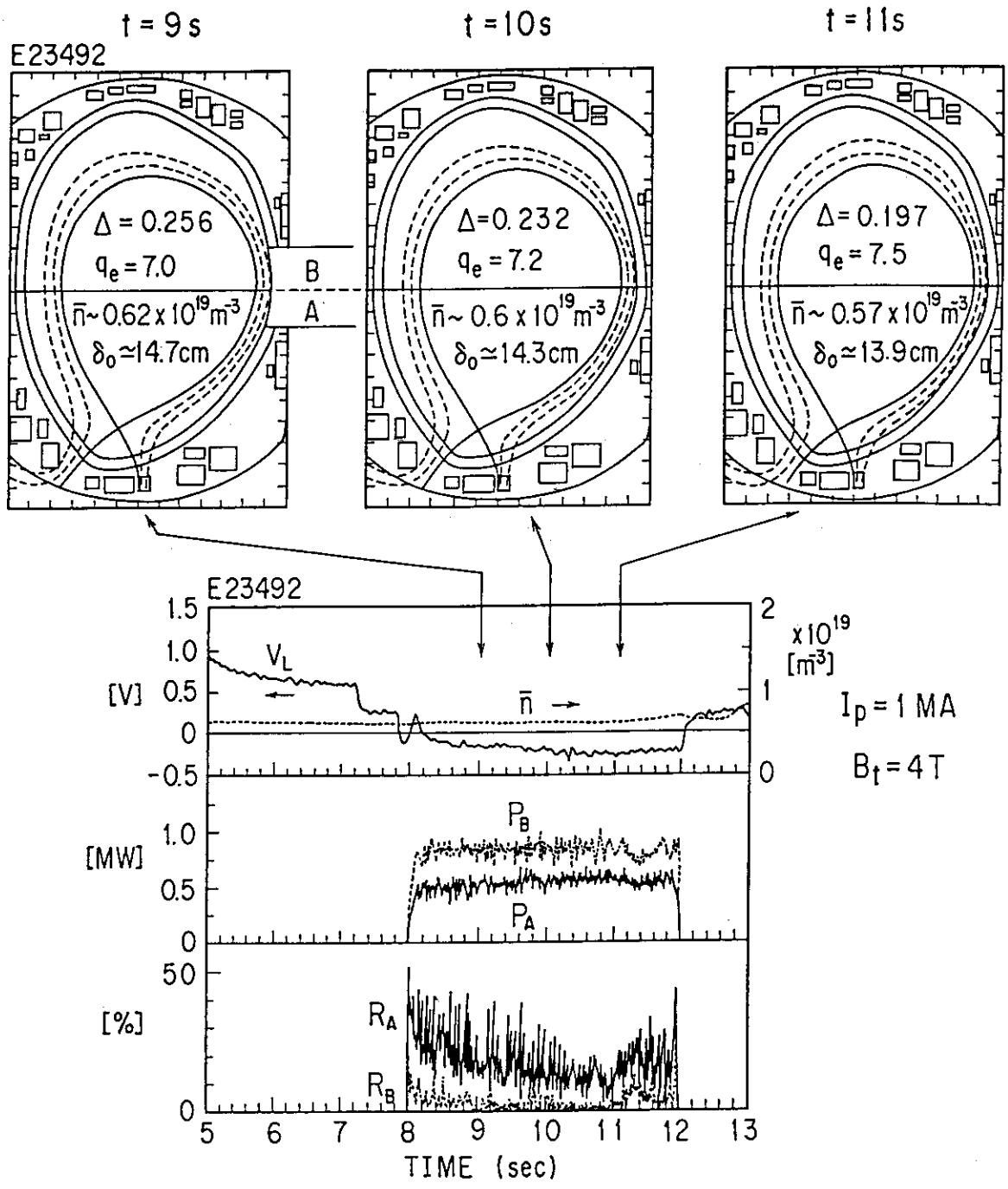

Fig. 1

Time trajectories of input power and reflection coefficient are shown for antenna A and B in lower side. Loop voltage and line average density are also drawn. Poloidal cross-sections are illustrated at t = 9, 10, 11 sec in upper side. Plasma current Ip is 1 MA toroidal magnetic field Bt 4 T, line averaged density n ~0.6 x 10^{19} m^{-3}. Plasma-wall distance is quasi constant of 14-15 cm during LH injection of 4 sec.

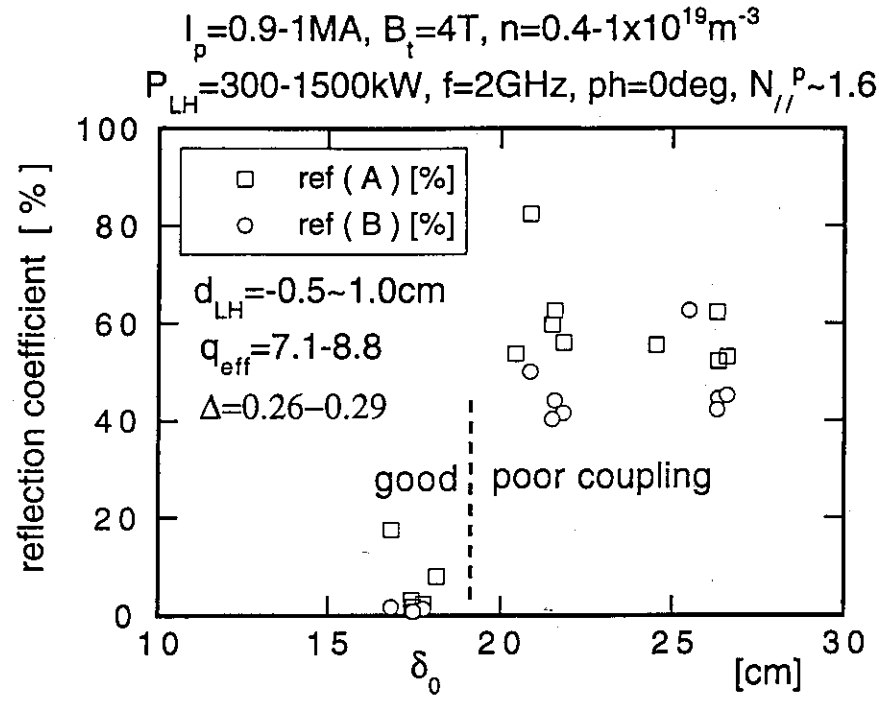

Fig. 2

Averaged reflection coefficient in input waveguides as a function of plasma-wall distance δ_0. Reflection of antenna A is presented by open square and reflection of antenna B open circle. Triangularity is relatively high of 0.26-0.29, plasma current 0.9-1 MA Bt = 4 T. Good coupling is obtained with long distance of δ_0~15-18 cm.

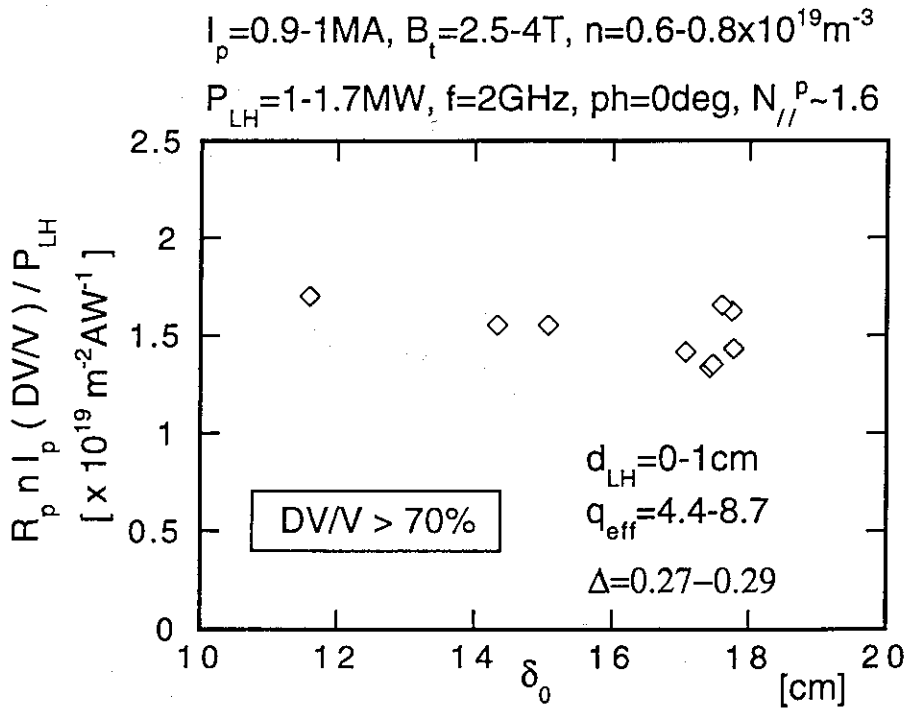

Fig. 3

Current drive efficiency vs plasma-wall distance δ_0. The efficiency is estimated using drop in loop voltage as DV/V. Δ = 0.27–0.29 Ip = 0.9-1 MA, Bt = 2.5-4 T, n = 0.6-0.8 x 10^{19} m^{-3}. Injected LH power is 1-1.7 MW with parallel refractive index of ~1.6.

3.5 ICRF Coupling to High Triangularity Plasma

Moriyama, Saigusa, Fujii, and Kimura

1. Introduction

It is important to confirm applicability of ICRF heating to high triangularity plasma after divertor modification. Antenna coupling resistance was measured to estimate the capable ICRF power with the high triangularity plasma assuming baffle plates of closed divertor. Heating of high triangularity plasma was checked.

2. Optimization of the plasma configuration for ICRH

A high triangularity plasma configuration is optimized for ICRF coupling at I_P = 0.9 ~ 1.0 MA, triangularity = 0.27 ~ 0.3. Clearance to the planned baffle plate of closed divertor was kept. As shown in Fig. 1, curvature in front of the antenna was not so different from the "standard RF configuration"

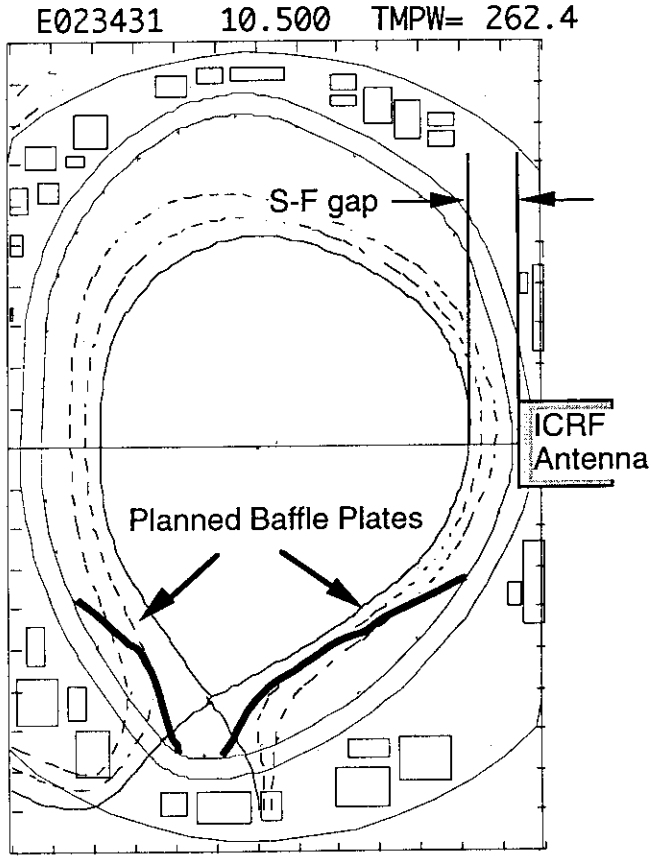

Fig. 1 High triangularity configuration optimized for ICRF heating keeping a clearance to the planned baffle plate for the closed divertor.

3. Measurement of antenna coupling resistance

Antenna coupling resistance is measured to estimate how much power can be coupled to the high triangularity plasma, changing the gap between separatrix and Faraday shield of the ICRF antenna (S-F Gap) from 16 cm ~ 31 cm for (π, 0), (0, 0) and (135°, 0) phasing.

As shown in Fig. 2, R_C = 3 Ω was obtained for S-F gap = 28 cm in (π, 0) phasing. 5 ~ 7 MW will be coupled for 35 ~ 40 kV of antenna voltage limit. R_C for the high triangurality plasma in this experiment is not so different from standard RF configuration in I_P = 1.0 MA case, probably because the shape of the outer separatrix in front of the antenna is similar to the "standard RF configuration."

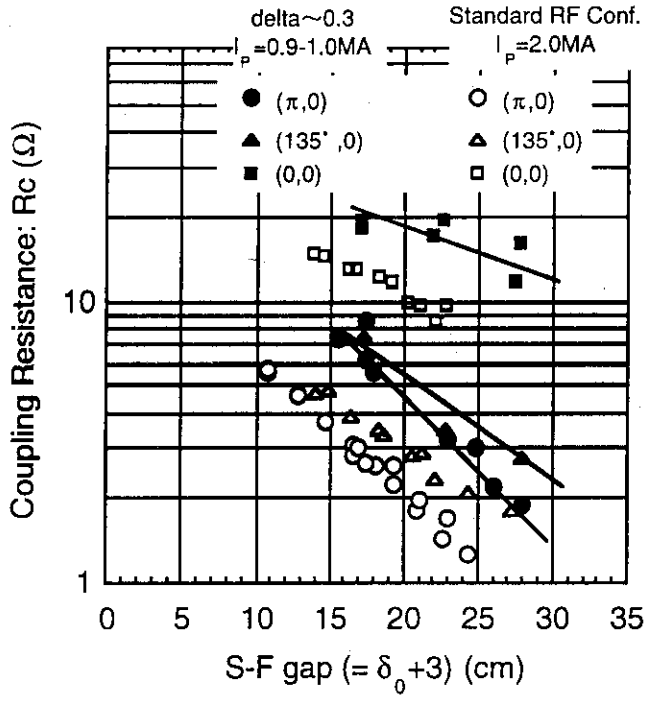

Fig. 2 Coupling resistance to high triangularity plasma

4. Confirmation of heating for (π,0) phasing

Heating was confirmed in both IC only and NB + IC cases for 18 ~ 21 cm of S-F gap at I_P = 1.0 MA. Increment of electron temperature, ΔT_e, is 0.7 keV for 1.6 MW of ICRF power for 1 sec without NBI. Increment of stored energy, ΔW_{dia}, is 450 kJ (including effect of increment of n_e) for P_{IC} = 3.2 MW with P_{NB} ~ 10 MW.

Heating will be more effective with high concentration of hydrogen which is necessary for $2\omega_{CH}$ heating.

5. Conclusion

Enough coupling resistance is obtained to be able to couple 5 ~ 7 MW of ICRF power to the high triangularity plasma with 25 cm of S-F gap simulating the configuration after divertor modification. Heating for high triangularity plasma is also confirmed.

4. High β_p mode

4.1 Threshold Heating Power for ITB Formation

Y. Koide, T. Takizuka, S. Takeji, S. Ishida, M. Kikuchi, Y. Kamada,
T. Ozeki, Y. Neyatani, H. Shirai, M. Mori and S. Tsuji-Iio*

1. Introduction

High confinement in the JT-60U High-β_p H-mode[1, 2] is attributed to the formation of internal transport barrier (ITB) at $r/a \leq 0.7$[3] which is followed by the edge transport barrier formation ($r/a \sim 1$): An intense central heating produced high plasma pressure inside the ITB; the subsequent H-mode transition was triggered by a transient relaxation phenomena accompanied with an energy flow across the ITB; the resultant plasma pressure was high from the central to the edge regions and normalized beta β_N ($\equiv \beta_t(\%)/(I_p(MA)/a(m)B_t(T))$) reached 2.4. Study of the internal transport barrier is, therefore, as important as that of the edge transport barrier from the viewpoints of the understanding of the improved confinement and of pressure-profile control.

The following phenomena were shown in previous papers[2, 3]: (I) The ion temperature T_i and the toroidal rotation velocity V_t increased inside ITB where the causality between them has not been made clear. (II) The electron temperature T_e also increased during ITB formation, however, it was not so significant as compared with T_i. (III) Ion thermal diffusivity was dramatically reduced at ITB position. (IV) We often observed that the location of ITB stagnated at a certain radial position which moved inward with increase in safety factor on the plasma surface. (V) In some cases, the improved confinement region was initiated near the plasma center and expanded outwards.

In this review, recent results of further study on ITB are presented. It was proved that ITB is produced when heating power exceeds a certain value. The threshold heating power is studied in this section.

2. Threshold heating power for ITB formation

We investigated the threshold heating power (P_{th}) for ITB formation. Plasma parameters for this study are as follows: plasma current and toroidal magnetic field were in the ranges of I_p=0.7-1.4 MA and B_t=2.2-4.4 T, respectively. The effective safety factor was kept almost constant (q_{eff}=6.5-7.1) in order to fix the ITB location after its stagnation[3]; the plasma volume was V_p=50m^3 and the beam energy was E_{NB}=85 keV. Plasma configuration, projected NB trajectories and some diagnostic fields of view (visible bremsstrahlung, line integrated n_e and D_α measurement) are shown in Fig. 1. In this experiment, perpendicular NB was primarily used and tangential NB was used as a reference because the power of former beams can be easily controlled from 2 MW to 20 MW with the step of ~2 MW by changing the number of

NB units. Electron density was controlled by short gas puffing (e.g. 50 Pam^3/s for 100 ms) just before or during NB injection; this gas-puffing technique is effective to change $\overline{n_e}$ with little effect on the internal inductance of plasma column.

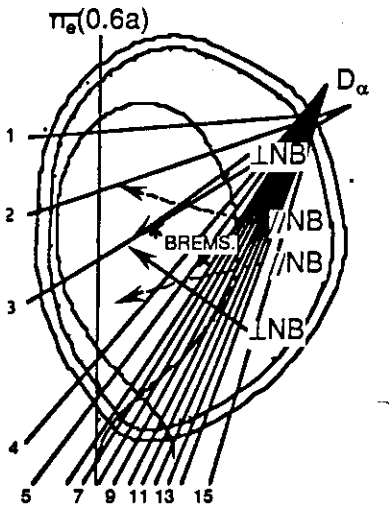

FIG. 1. Plasma configuration for threshold-power study. Projected neutral beam trajectories of perpendicular beams (⊥NB : solid arrows) and of tangential beams (//NB : dotted arrows) are shown. Line of sight of FIR interferometer along 60% of tangent minor radius is shown with a vertical solid line ($\overline{n_e}$(0.6a)). Two crosses are projected tangential radii of visible bremsstrahlung measurement used in this discussion. Fifteen viewing chords of D_α measurement are shown with thin lines.

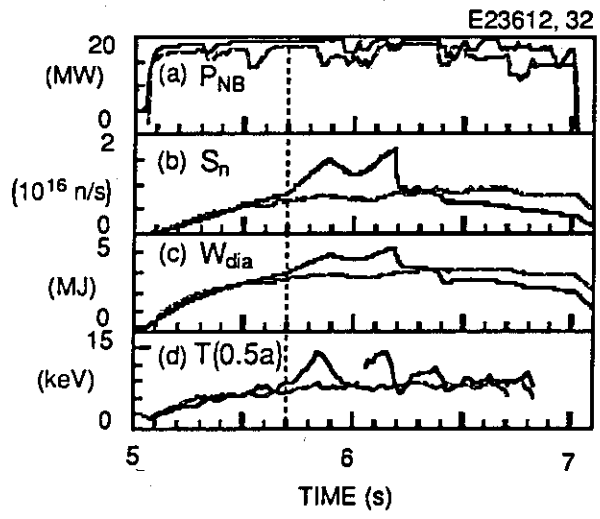

FIG. 2. Criterion for the presence of ITB. Two discharges with ITB (thick lines) and without ITB (thin lines). (a) Injected neutral beam power (P_{NB}), (b) neutron emission rate (S_n), (c) diamagnetic stored energy (W_{dia}), (d) ion temperature at r/a=0.5 (T_i(0.5a)). P_{NB} is a little bit lower in the case without ITB (thin lines). Vertical dotted line shows the onset time of ITB formation.

Our criterion for the presence of ITB is explained in Fig. 2, where two discharges with and without ITB are compared. In a discharge shown with thick lines, ITB was produced at t=5.7 s (shown by a vertical dotted line in this figure), when ion temperature at a half radius (T_i(0.5a)) started increasing (Fig. 2(d)). A clear increase in the neutron emission rate (S_n) and the stored energy (W_{dia}) accompanied with it (Figs. 2(b) and 2(c)). In this discharge, a minor collapse occurred at t=5.9 s and ITB was recovered soon, resulting in a harder collapse at t=6.2 s. Thin traces show a discharge with lower heating power, resulting in no appearance of ITB. Data points shown in the following were taken at the onset of ITB formation. As for the discharges without ITB, data were taken at nearly the same times as those in discharges with ITB.

Figure 3 (a) shows the absorbed heating power (P_{NB}^{abs}) against $\overline{n_e}$(0.6a), where P_{NB}^{abs} was defined as injected NB power subtracted by the shinethrough power measured with thermocouples. Closed symbols designate discharges with ITB and open symbols discharges without ITB. In the case of I_p=1.4 MA and B_t=4.4 T (●,○), $\overline{n_e}$ was scanned from 0.6 to 1.0

$\times 10^{19}$ m^{-3}. P_{th} was linearly increased from 5 to 10 MW within experimental accuracy (shown by a shaded region).

Figure 3(b) shows B_t-dependence of P_{th} in the density range of $\overline{n_e}$=0.4-0.65$\times 10^{19}$ m^{-3}. Since data at different B_t were taken at different $\overline{n_e}$ as seen in Fig. 3(a), the observed slight increase in P_{th} with B_t can be affected by the $\overline{n_e}$-dependence. Taking the linear dependence on $\overline{n_e}$ into consideration, $P_{NB}^{abs}/\overline{n_e}$ is plotted against B_t in Fig. 3(c). The resultant independence of B_t suggests the importance of the power density per a particle for ITB formation. The independence of P_{th} from B_t is different from the threshold power of H-mode transition[4].

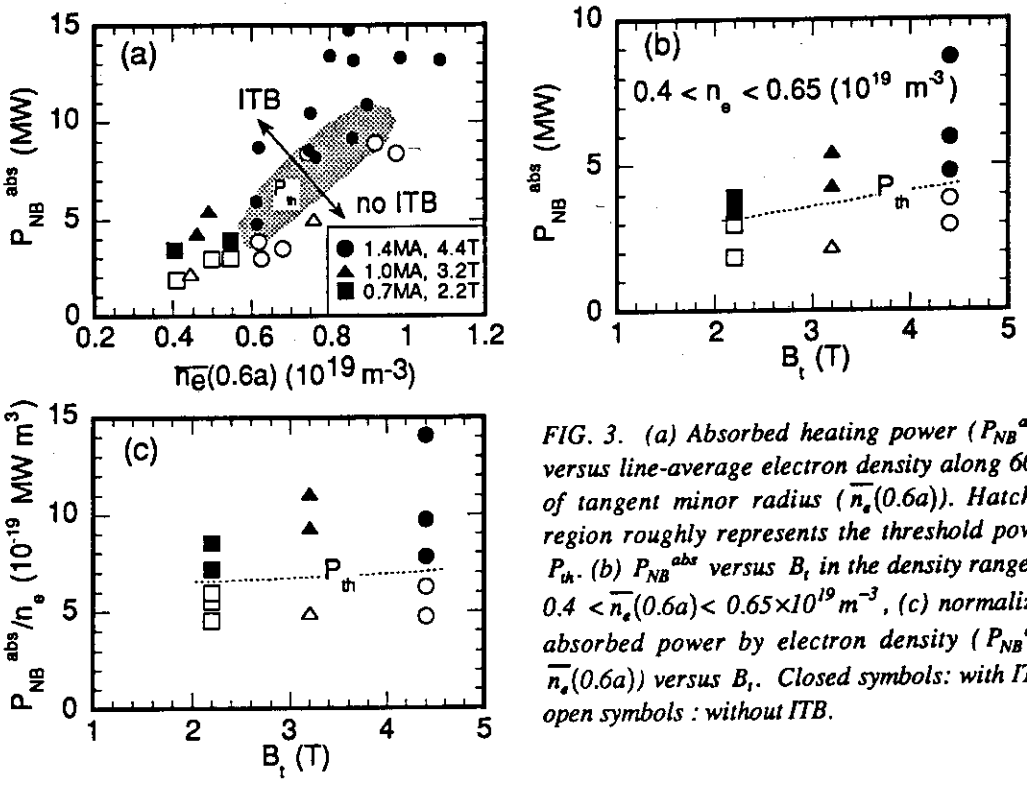

FIG. 3. (a) Absorbed heating power (P_{NB}^{abs}) versus line-average electron density along 60% of tangent minor radius ($\overline{n_e}$(0.6a)). Hatched region roughly represents the threshold power P_{th}. (b) P_{NB}^{abs} versus B_t in the density range of 0.4 < $\overline{n_e}$(0.6a)< 0.65×10^{19} m^{-3}, (c) normalized absorbed power by electron density (P_{NB}^{abs}/ $\overline{n_e}$(0.6a)) versus B_t. Closed symbols: with ITB, open symbols : without ITB.

References

1) Mori M. et al., Nucl. Fusion, 34 1045 (1994).

2) Koide Y. et al., Plasma Physics and Controlled Nuclear Fusion Research 1994 vol 1 (International Atomic Energy Agency, Vienna) 199 (1995).

3) Koide Y., Kikuchi M. et al., Phys. Rev. Lett., 72, 3662 (1994).

4) Sato M. et al., IAEA Technical Committee Meeting on H-Mode Physics, Princeton, (1995).

4.2 Measurement of q-profile during ITB Formation

Y. Koide, S. Ishida, M. Kikuchi

1. Introduction

Radial location of internal transport barrier (ITB) was investigated in connection with the local safety factor q ($\equiv (r/R)(B_t/B_p)$). Before showing recent results, we will describe, in this section, the background of this study.

The relation between them has been discussed since JT-60 experiments. Hot-ion mode in JT-60 ($T_i(0)$~10 keV, H^0beam into H^+ plasma of 30 m^3) exhibited peaked profiles of ion temperature, $T_i(r)$, and toroidal rotation velocity, $V_t(r)$. In Fig. 1, radial location of ITB is plotted against the location of q=1, 2, 3 surfaces deduced from of m=1 (●), 2, (△) 3 (○) mode oscillations, respectively (m: poloidal mode number). Phenomenologically, ITB location was explained by the integer rational surfaces such as q=1, 2 and 3 surfaces[1]. However the effect of magnetic island was left unsolved and there was no direct measurement of q-value.

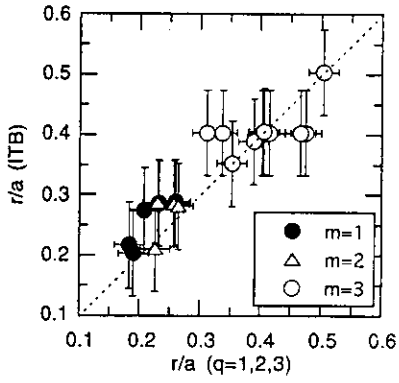

FIG. 1. Correlation of ITB location and the locations of q=1, 2 and 3 surfaces inferred from m=1, 2 and 3 oscillations, respectively (from Ref. [1]). Quantities are normalized by the minor radius. Vertical and horizontal error bars are defined by the spatial resolution of the CXRS and SXR measurements, respectively.

In JT-60U High-β_p H-mode[2], the formation of ITB at $r/a \leq 0.7$ was followed by the edge transport barrier formation (r/a~1). The H-mode transition was triggered by a sudden release of energy across the ITB[3] (see ECE signals in Fig. 2(a)); the instability was a pressure-driven type because the fluctuation level was larger on the bad-curvature side; magnetic fluctuations were detected simultaneously with the MHD phenomena in this discharge (Fig. 2(b); three reversal of sign was recognized, e.g. m=3, however, time and spatial resolutions of this measurement were poor and m can be 4 or 5). In later measurements, most likely toroidal-mode number was proved to be n=1[4]. We considered that the plasma pressure, which built up just inside the ITB, reached a stability limit of ballooning-type instability; the location of ITB may be characterized by the local safety factor $q=m/n$. In order to

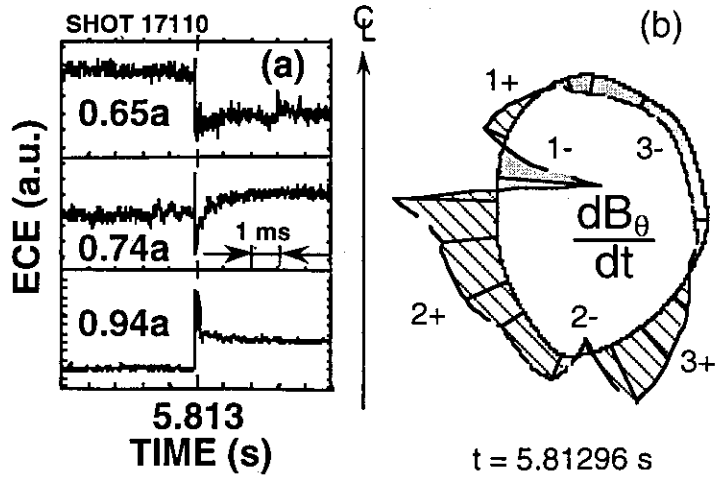

FIG. 2. (a) MHD event detected in ECE signals (from Ref. [3]) and (b) poloidal pattern of the time derivative of poloidal magnetic field.

check this hypothesis on the role of rational surfaces, direct measurement of q-value is indispensable.

2. q-profile and ITB location

Plasma configuration and typical evolution of this experiment are shown in Figs. 3 and 4: plasma current and toroidal field were varied in the ranges of I_p=0.43-1.45MA and B_t=3.47-4T, respectively, leading to the coverage of effective safety factor of q_{eff}=5.6-21.2; neutral beam heating power was P_{NB}^{TOT}=11.2-22.5MW, where tangential beams of P_{NB}^{TAN}=7.7 MW were always injected; triangularity was increased at need from δ=0.2 to 0.3 in order to suppress vertical instability (Figs. 3 and 4(d)).

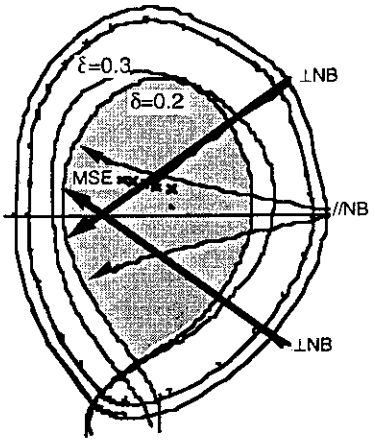

FIG. 3. Plasma configuration and neutral beam trajectories. MSE field of view is shown by crosses.

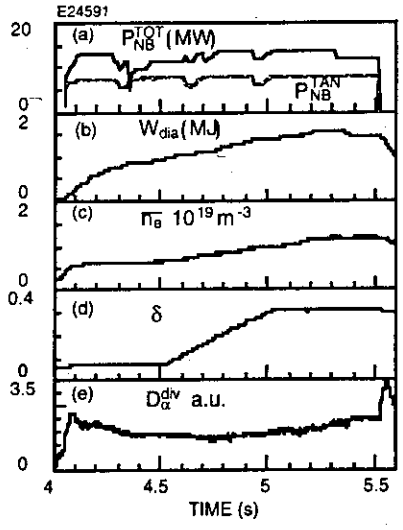

FIG. 4. (a) Total injection power P_{NB}^{TOT} and beam power of tangential beams P_{NB}^{TAN}, (b) diamagnetic stored energy W_{dia}, (c) line-average electron density $\overline{n_e}$, (d) triangularity δ, (d) D_α emission in divertor region D_α^{div}.

Fig. 5 shows the relation of ITB location and q_{eff}. Open circles are data taken for 50 m^3 plasma on the inner side of vacuum vessel in order for the intense central heating, where MSE diagnostics has not been put into operation yet; we can see that ITB location was a monotonic function of q_{eff}. Based on this result, we built up the working hypothesis that a certain q-value was related to the ITB location.

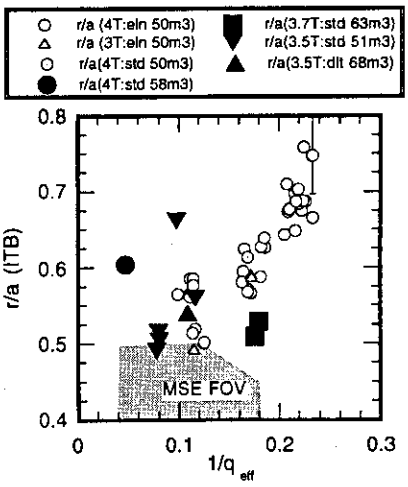

FIG. 5. ITB-location vs. inverse of q_{eff}. Open symbols: intense central heating into small volume plasmas. Closed symbols: outward-shifted configuration for MSE measurement. Shaded region shows its field of view.

New data with MSE measurement are shown by closed symbols in the same figure. In contrast to the old data, no systematic dependence on q_{eff} was observed. In Fig. 6, profiles of T_i, q and magnetic shear s ($\equiv (r/q)(dp/dr)$) at q_{eff}=12.6, 9.2 and 5.6 are compared at a time when ITB has been fully established (Data at ITB-onset is not readily available at

present). Monotonic q-profile was observed at q_{eff}=12.6 and q-value at ITB was between 2 and 3 (Fig. 6(a)); when q_{eff} was decreased down to 9.2, q was around 3 inside the ITB, i.e. s ~0; magnetic shear was reversed when q_{eff} was further decreased down to 5.6 and ITB was located at pitch minimum of q~2 (Fig. 6(c) (T_e showed no barrier-structure unlike reversed-shear mode (see paper 2.3 in this review)).

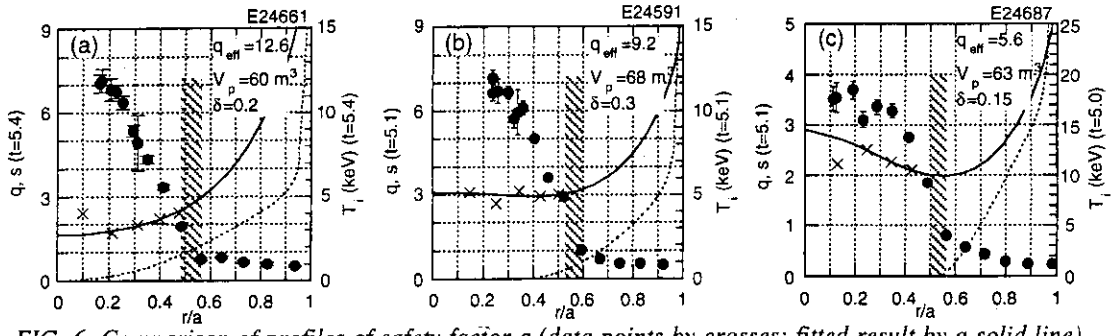

FIG. 6. Comparison of profiles of safety factor q (data points by crosses; fitted result by a solid line), magnetic shear (r/q)(dq/dr) (a dotted line) and T_i (closed circles). (a) q_{eff}=12.6, (b) q_{eff}=9.2, (c) q_{eff}=5.6.

It should be noted that the q-value at ITB was around q=2-3 while q_{eff} was changed by a factor of 2 (Fig. 7). This result may be interpreted several ways: 1) ITB was formed on q=2 and 3 surfaces, which was consistent with the above-mentioned hypothesis on the role of rational surfaces; 2) low or negative s is a key mechanism of reduced transport as predicted by Fukuyama et al.[5]; 3) the $E \times B$ velocity shear induced by unknown mechanisms can be a candidate because velocity shear usually accompanied with ITB. Two of these candidates 1) and 3) are difficult to be checked due to the insufficient space and time resolutions of MSE and CXRS measurements. Preliminary assessment of the Fukuyama's theory is described in the next section.

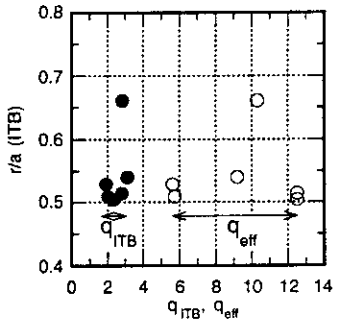

FIG. 7. ITB location vs. qeff (○), the local q at ITB of which is shown by ●.

3. Comparison with theory of self-sustained turbulence

The theory of Itoh et al.[6, 7] of self-sustained turbulence driven by current diffusivity was successful to explain the power-degradation of energy confinement time. This is the first theory which explains the experimentally observed profile of thermal diffusivity (χ increasing toward the edge). Fukuyama et al. reported[5], based on this theory, that thermal diffusivity is improved as a result of the cooperative effect between the current profile and the pressure profile and that the improved confinement in high-β_p mode, i.e. ITB formation, can be explained by this model. In fact, ITB was formed in weak-s regions ($s \leq 2$) as seen in Fig. 6. Here we compare the threshold power of ITB formation and ITB location with predicted ones.

The theory predicts that threshold power scales as $P_{th} \propto I_p^{2.27}$. Experimental results are shown in Fig. 8(a), the data set of which is identical to that shown in Fig. 4(c) in the paper 4.1

in this review. In this data set, B_t was changed with I_p in order to keep q_{eff}~6.7. This parameter coupling seems not be a problem for the assessment of this theory because the predicted thermal diffusivity ,

$$\chi_{TB} = F(s,\alpha,k)|\alpha|^{3/2}\frac{c^2}{\omega_{pe}{}^2}\frac{v_A}{qR} \qquad (\alpha \equiv -q^2 R\, d\beta/dr,\ k \equiv -(r/R)(1-q^{-2})), \qquad (1)$$

is not sensitive to B_t: B_t-dependence in κ might be weakened by the constraint of q_{eff}. The observed no strong I_p-dependence of absorbed power P_{NB}^{abs} was in contrast to the prediction.

The theory also predicts that the radial location of ITB at its onset scales as $r_{ITB} \propto P^{0.44}/I_p{}^{0.85}$. Experimental results are shown in Fig. 8(b). The data with fixed I_p (=1.4MA) and $\overline{n_e}$=0.75-0.9$\times 10^{19}$ m^{-3} are chosen from Fig. 4(a) in the paper 4.1 in this review. Irrespective of the change in P_{NB}^{abs} by a factor of 1.8 (change in $P^{0.44}$ by 29%), r_{ITB} was almost constant. I_p dependence of r_{ITB} is shown in Fig. 8(c), where absorbed power was almost constant as P_{NB}^{abs}=4-4.8 MW. Results showed a slight decrease in r_{ITB} with I_p, however, the predicted strong dependence as $r_{ITB} \propto I_p{}^{-0.85}$ was not recognized. Detailed comparison must be carried out using the complete set of profile data such as $p(r)$ and $q(r)$, which allows the evaluation of the factor F in eq. (1).

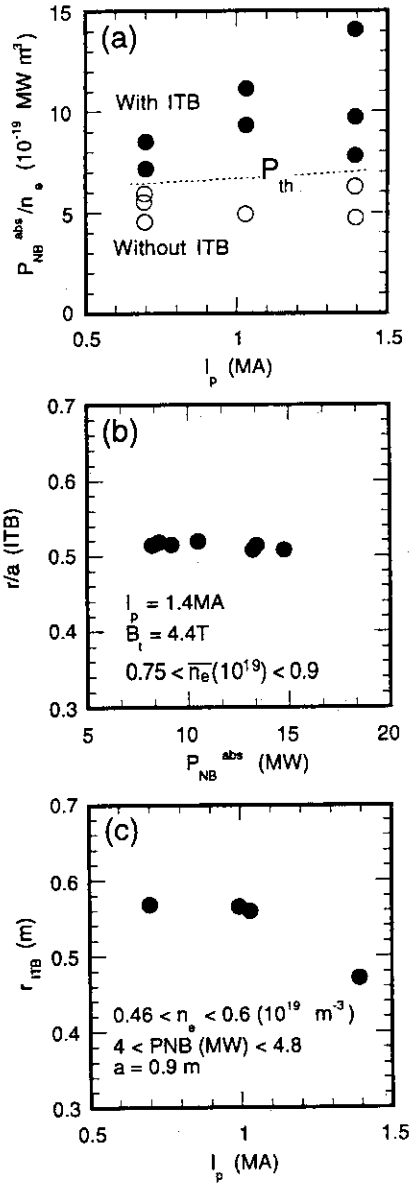

FIG. 8. (a) Absorbed heating power normalized by $\overline{n_e}$ for ITB formation vs. I_p, (b) ITB location vs. absorbed power, (c) ITB location vs. I_p.

References

1) Koide Y. et al., Nucl. Fusion, 33 251 (1993).
2) Koide Y. et al., Plasma Physics and Controlled Nuclear Fusion Research 1994 vol 1 (International Atomic Energy Agency, Vienna) 199 (1995).
3) Koide Y., Kikuchi M. et al., Phys. Rev. Lett., 72, 3662 (1994).
4) Takeji S. et al., Proc. 22nd European Conf. on Controlled Fusion and Plasma Physics (Bournemouth) 1995.
5) Fukuyama A. et al., Plasma Phys. Control. Fusion, 37 611 (1995).
6) Itoh K. et al., Phys. Rev. Lett., 69 1050 (1992).
7) Itoh K. et al., Plasma Phys. and Control. Fusion, 35 543 (1993).

4.3 MHD Analysis of Instabilities Associated with ITB

S. Takeji, Y. Kamada, T. Ozeki, S. Ishida, T. Takizuka, Y. Neyatani, S. Tokuda

1. Introduction

High poloidal beta (β_p) operation is required for a steady state tokamak reactor, in which avoidance of pressure-driven instabilities is crucially important to achieve a high performance plasma. In this review, we report pressure-driven magnetohydrodynamic (MHD) activities in the high-β_p mode; (1) the β_p-collapse which terminates the improved confinement abruptly [1-3] and (2) the minor collapse which does not result in the degradation of the improved confinement. We refer to the minor collapse as the "barrier localized mode (BLM)", since it is associated with a significant pressure gradient generated around the internal transport barrier (ITB) [4]. Experimental observations and stability analysis of the BLM are described here in comparison with the β_p-collapse.

2. MHD Characteristics of Barrier localized Mode

Time evolution of typical high-β_p mode discharges with the β_p-collapse and the BLM are shown in Fig. 1. The two discharges have almost the same experimental conditions as the plasma current (I_p) of 2 MA, the toroidal field (B_T) of 4.4 T and the neutral beam injection power (P_{NBI}) of about 28 MW. The β_p-collapse becomes more disruptive with increase in plasma current and the BLM often occurs in such large current discharges. One of the obvious differences between the β_p-collapse and the BLM is the effect on the stored energy (W_{dia}). Reduction of W_{dia} by the BLM is quite smaller than that by the β_p-collapse. The line-averaged electron density ($\bar{n}_e$) and the edge ion temperature (T_i) increase after the BLM and the high-β_p mode is changed to the high-β_p H-mode.

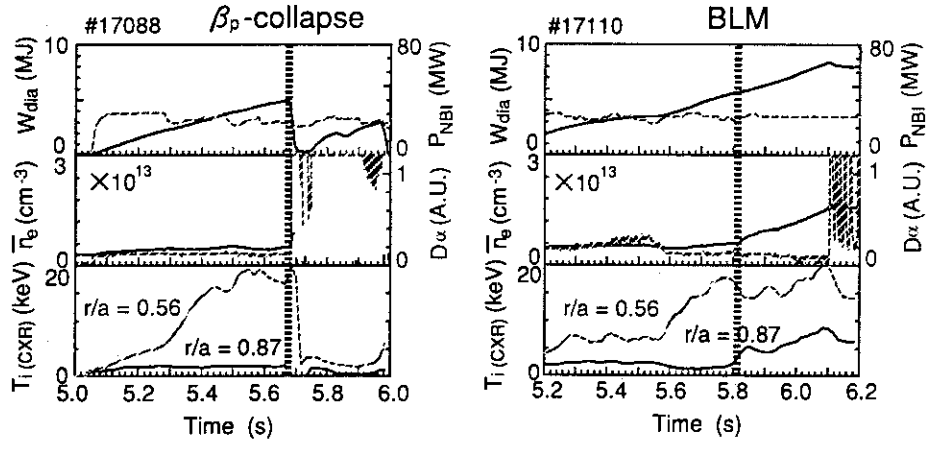

Fig.1 *Typical MHD behavior of the β_p-collapse and the BLM.*

Figure 2 shows the radial profile of relative change of the electron temperature (T_e) by

the collapses. In case of the β_p-collapse (dotted line), the change of T_e is observed in the whole plasma region. On the other hand, the BLM (solid line) does not changes T_e at the central region and the inversion radius of the change of T_e is near the ITB, which implies that the BLM is a localized mode occurring near the ITB. The BLM releases energy from inside the ITB to the outer region to trigger the L-H transition.

Typical magnetic fluctuations during the BLM is shown with the electron cyclotron emission (ECE) signal in Fig. 3. No clear precursor of the BLM was observed. The amplitude of the ECE changed in the time duration of about 100μs, which is the time scale of the ideal MHD. The magnetic fluctuations with low toroidal mode number (n) were excited during the BLM. The largest mode was the n = 1 kink mode. Just after the BLM, the postcursor of the BLM was sometimes observed, of which poloidal mode number (m) was $3 \leq m \leq 5$.

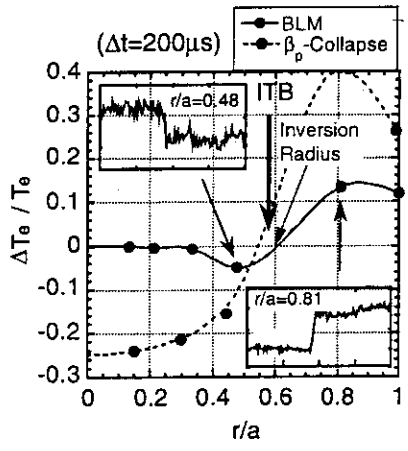

Fig.2. *Radial profiles of change of the electron temperature by the BLM and the β_p-collapse. Time period of the change is 200μs.*

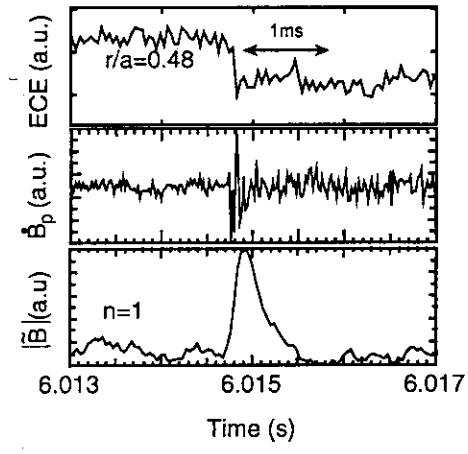

Fig.3. *Time evolution of ECE and magnetic fluctuations.*

We searched for the parameter region occurring the β_p-collapse and the BLM. Figure 4 shows $\beta_p - \bar{n}_e \nabla T_i$ region where we observed the β_p-collapse and the BLM in the same discharge parameters (I_p=2 MA, B_T=4.4 T, internal inductance $\ell_i \sim$ 1.0 and q_{eff} = 4.7) The parameter $\bar{n}_e \nabla T_i$ indicates the local pressure gradient near the ITB. The BLM occurs in the lower β_p region ($\beta_p \leq 1.1$) than the β_p-collapse ($\beta_p \geq 1.2$) with the same local pressure gradient near the ITB. Time trajectorys to the β_p-collapse and the BLM suggest that the BLM occurs when $\bar{n}_e \nabla T_i$ grows relatively faster than the growth of the β_p, and $\bar{n}_e \nabla T_i$ reaches to certain boundary of instabilities associated with the local steep pressure gradient.

3. Stability Analysis of Barrier Localized Mode

Numerical analysis was done to study the effects of the local steep pressure gradient at ITB on the ideal MHD stability. We used BETA code and ERATO-J code for the stability analysis of infinite n ballooning modes and low n kink-ballooning modes, respectively. At first, we considered only the effect of the pressure profile. Figure 5 shows a stability boundary on

$\beta_p - \nabla p_{(ITB)}$ plane for the $n = 3$ kink mode and the infinite n ballooning mode with the typical experimental data, where $\nabla p_{(ITB)}$ is the local pressure gradient at the ITB and the $n = 3$ is the most unstable low n mode in the situation (Detail of the stability analysis were described in Ref. 5). We found that the stability boundary against the low n kink-ballooning modes is $\beta_p \approx 1.3$ and is a weak function of $\nabla p_{(ITB)}$, while the stability of the infinite n ballooning modes depend on $\nabla p_{(ITB)}$. The stability boundary against $n = 3$ mode corresponds to that for β_p-collapse. The width of the experimental data is due to uncertainty of the gradient of T_i and the n_e profile near the ITB. The local pressure gradient $\nabla p_{(ITB)}$ can reach to the stability boundary of infinite n ballooning modes, while low n kink modes are stable.

We investigated the effect of the current profile with the pressure profile. Current profile may be changed locally by $\nabla p_{(ITB)}$ through the bootstrap current, which weaken the local magnetic shear near ITB. Then, we found that low n kink modes are destabilized with the relatively localized displacement distribution near ITB (Fig. 6). On the other hand, infinite n ballooning mode is stabilized due to the weakened magnetic shear near ITB. Figure 7 shows a dependence of growth rate of the $n = 1$ kink mode on the q value at the weak (negative) magnetic shear near ITB. The low n mode has positive growth rate only when the q value at the weak (negative) magnetic is close to integer. The plausible integer q value near ITB is 2 in our employed equilibrium.

4. Summary and Conclusions

This review paper reported pressure-driven instabilities in the high-β_p mode in JT-60U. A localized mode (BLM) is destabilized at the ITB. The BLM results in a non-disruptive collapse to induce the high-β_p H-mode. The BLM is accompanied by the low n magnetic fluctuations and grows in the time scale of the ideal MHD, which suggests that the BLM is an ideal low n kink mode. Ideal MHD stability analysis showed that low n kink modes with the relatively localized displacement distribution can be destabilized when the magnetic shear is locally weakened by the bootstrap current driven near ITB and the q value is close to integer at the weakened magnetic shear. The result of the stability analysis is consistent with the present experimental one.

Results of the stability analysis depend on the employed equilibrium, i.e. current and pressure profiles. Details of the BLM will be revealed by measurement of the current profile in the situation in near future.

References

[1] S Ishida et al, *Phys. Rev. Lett.* **68** 1531 (1992)

[2] Y Neyatani et al, *Plasma Phys. Control. Fusion* **37** 741 (1995)

[3] T Ozeki et al, *Nucl. Fusion* **35** 861 (1995)

[4] Y Koide et al, *Phys. Rev. Lett.* **72** 3662 (1994)

[5] S Takeji et al, in *Control. Fusion and Plasma Phys.* (Proc. 22th Eur. Conf. Bournemouth, 1995) Vol. 19C, Part IV, European Physical Society, Geneva (1995) IV-033

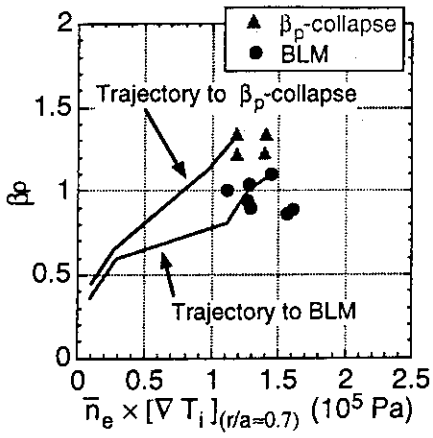

Fig.4. *Comparison of $\beta_p - (n_e \nabla T_i)$ region between the β_p-collapse and the BLM.*

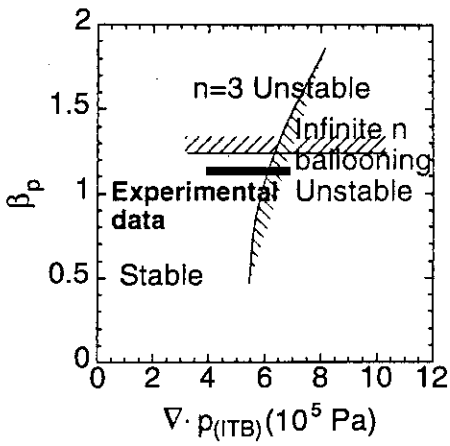

Fig.5. *Stability boundary on $\beta_p - \nabla p_{(ITB)}$ plane of $n = 3$ kink-ballooning mode and the infinite n ballooning mode.*

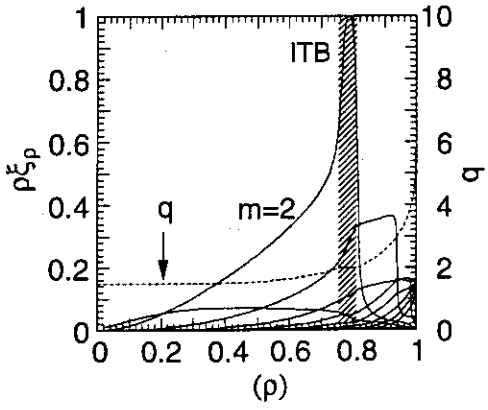

Fig.6. *Radial profiles of normalized $\rho\xi_\rho$ (solid line) and q (broken line) for the $n = 1$ kink mode.*

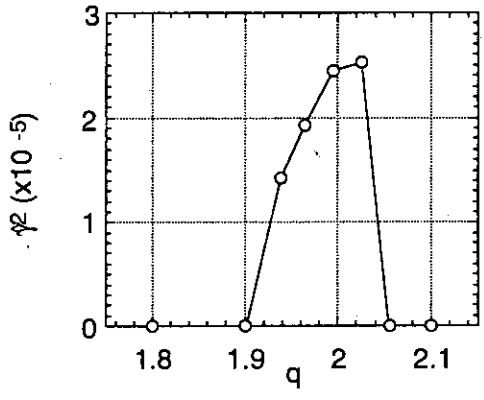

Fig.7. *Square of growth rate of the $n = 1$ kink mode versus q at the weak (negative) shear region near the ITB.*

5. H-mode, L-mode Confinement

5.1 Confinement of High Current Hot-Ion H-mode Discharges

S. Ishida, Y. Kamada, A. Isayama, H. Kimura and Y. Neyatani

1. Introduction

The development of a high current low-q regime is an important issue to determine whether it will be workable for ignition devices such as ITER. As the confinement improvement appears to be lowered with decreasing the safety factor or increasing the plasma current [1], it has become necessary to assess an optimal q for future tokamaks. In 1995, the hot-ion H-mode regime was extended up to 4.5 MA in JT-60U, which allowed us to investigate a low-q regime down to q_{95}~2.0 with high performance plasmas including a nominal q value in ITER, q_{95}~3. This paper is discussing the achievement and limitation of confinement and stability performance for the high current hot-ion H-mode discharges in JT-60U.

2. Experimental conditions

The hot-ion H-mode discharges in JT-60U have been produced with intense neutral beam injection (P_{NBI}≤30 MW) and/or second harmonic ICRF heating (P_{IC}≤5 MW): for the standard configuration with 3.0≤I_p≤4.5 MA, B_t~3.85 T, R_p~3.5 m, a~1.0 m, an elongation of κ~1.4, a triangularity of δ~0.2, and q_{eff}=2.4-3.5; and for the high elongation configuration with 3≤I_p≤4.5 MA, B_t~4.2 T, R_p~3.2 m, a~0.85 m, κ~1.7, δ~0.06, q_{eff}=2.5-4.0. It is noted that the combined heating of NBI and ICRF was done only for the standard configuration experiment because of the antenna coupling. The experiments were aimed at improving the fusion performance such as the fusion triple product. While the target plasma was accompanied with sawtooth oscillations, the sawtooth period was prolonged by the central beam injection and more effectively by ICRF heating. The avoidance of locked modes at low density was necessary for producing a stable and robust target plasma. A relatively high internal inductance around ~1.1 was obtained by increasing the plasma bore during the plasma current ramp-up phase for improvement in confinement and stability.

Figure 1 shows the waveforms of a typical high current hot-ion H-mode discharge obtained at 4 MA with neutral beam and ICRF heating in the standard configuration. Effective sawtooth stabilization by 5 MW ICRF heating was achieved as shown in the electron

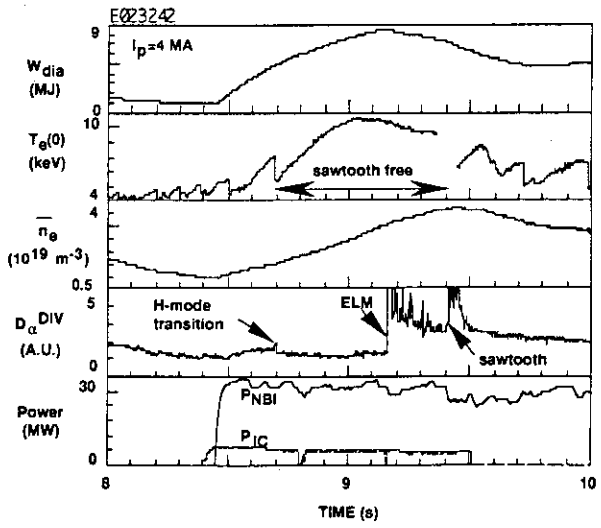

Fig. 1 Waveform of a typical hot-ion H-mode discharge at 4 MA

temperature evolution. Following the ELM free phase of ~0.5 s, a large ELM (Edge Localized Mode) occurs and degrades the confinement improvement. Because of the large bore plasma, the fast ion loss fraction to the total beam injection power due to the toroidal field ripple reaches ~40% for a standard configuration and ~20% for a high elongation configuration. While this enhanced loss of the injection power is not taken into account in this paper unless otherwise noted, the influence of the ripple-induced fast ion loss on confinement is discussed in a separate paper [2].

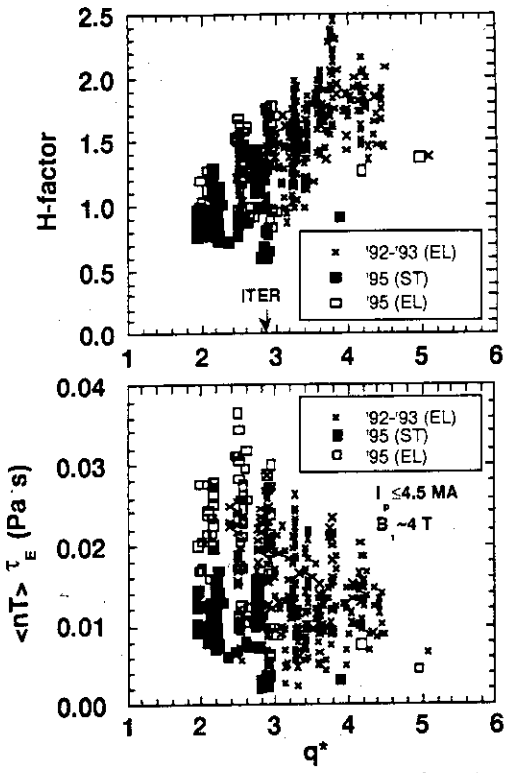

Fig.2 H-factor and <nT> τ_E as a function of q for the hot-ion H-mode regime*

3. Safety factor dependence

Although the confinement improvement (H-factor against the ITER89-P L-mode scaling) is substantially decreased, the fusion product continues to increase with the plasma current. However, the further degradation of confinement would result in a decline of the fusion product with decreasing the safety factor. This tendency appears to be seen as the upper envelop for the data in Fig.2 where the H-factor and the volume-averaged fusion product are plotted as a function of the cylindrical safety factor defined as $q^*=\pi a^2 B_t[1+\kappa^2(1+2\delta^2-1.2\delta^3)]/(\mu_0 I_p R_p)\sim q_{95}$ for the hot-ion H-mode discharges obtained in 1992-1995. Here, an optimal q for the fusion product appears to be q*~2.5 in this regime.

As discussed in Ref.[3], the ratio of H-factor to the safety factor, H/q, is a useful figure of merit for ignition margin as the value of $(H/q)^2$ is proportional to the fusion product, where $H/q_{95}\geq 0.6$ is required for sustained ingnition. Figure 3 shows the $H_{ITER89\text{-}P}/q^*$ as a function of q* for the hot-ion H-mode regime in 1992-1995 and the high-β_p H-mode regime in 1992-1993 where the cross symbols indicate the fast ion ripple-loss corrected

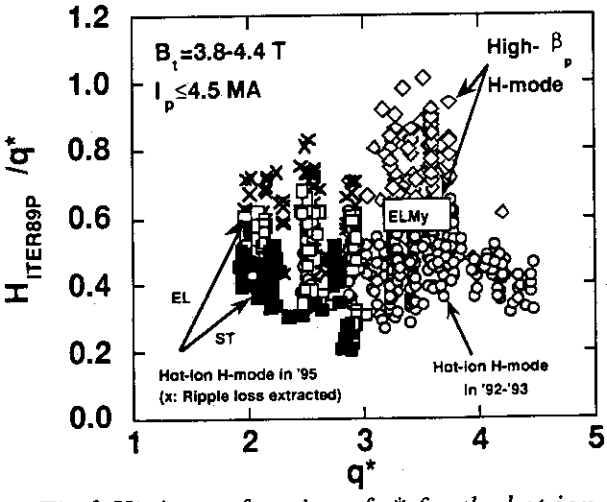

Fig.3 H/q as a function of q* for the hot-ion H-mode regime as compared with the high-β_p H-mode regime*

values for the hot-ion H-mode data in 1995. It is found that both high performance regimes in JT-60U are closely approaching the domain of H/q_{95}~1 at q_{95}~3 required for ITER.

4. Stability degradation

The most obvious concern appears to be the significant stability degradation with the plasma current. Figure 4 shows the diamagnetic stored energy as a function of $I_pB_tV_p/a$ for the hot-ion H-mode regime in comparison with the high-β_p regime where the gradient represents the normalized beta defined as $\beta_N=\beta_t[\%]aB/I_p[MA]$. In contrast to the high-β_p regime, the attainable β_N value tends to be decreased in the hot-ion H-mode regime with a broad pressure profile consisting of a low pressure gradient in the core region and a high pressure gradient at the edge.

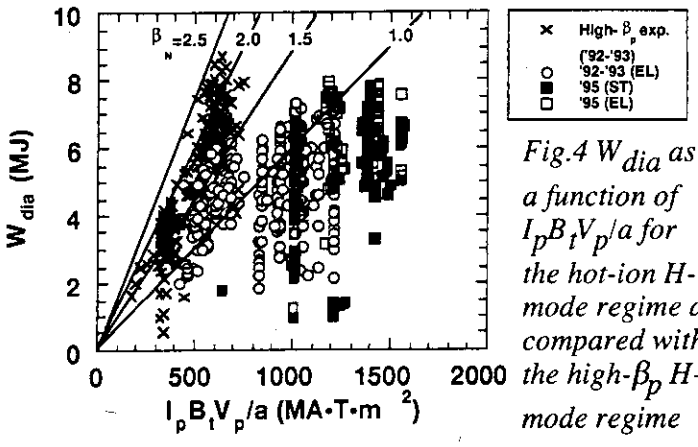

Fig.4 W_{dia} as a function of $I_pB_tV_p/a$ for the hot-ion H-mode regime as compared with the high-β_p H-mode regime

The stability improvement has so far been addressed mainly for a high q region above q*~3 in JT-60U as shown in Fig.5 where the β_N is plotted as a function of q* for the hot-ion H-mode regime in comparison with the high β_N at low B_t, the high-β_p H-mode and the ITER regimes. The hot-ion H-mode regime shows that the stability tends to be degraded with decreasing q*. The demonstration of stability improvement around q*~3 becomes crucial to determine whether the low-q regime is workable.

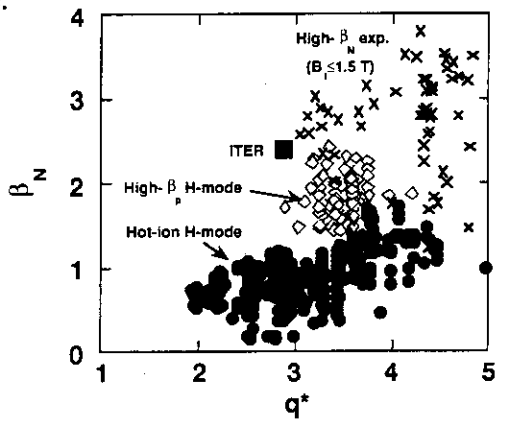

Fig.5 β_N as a function of q fior the hot-ion H-mode regime compared with the high-β_p H-mode regime and high-β_N regime*

In the high current regime, the confinement and stability limitation was most often caused by a large ELM event following a ELM free phase, suggesting that the edge stability limit is a primary cause of the observed stability degradation with increasing the plasma current. Figure 6 shows the β_N as a function of $B_t^2/(2\mu_0R_pq^{*2})$ where the $B_t^2/(2\mu_0R_pq^{*2})$ value is a measure of edge pressure gradient limited by ballooning modes [4]. The result indicates that the beta limit tends to be degraded with increasing the edge pressure gradient. It should be remarked that the pressure gradient development during an ELM-free phase reaches a critical value for the edge stability before the core pressure develops sufficiently in high current hot-ion H-mode discharges.

Therefore, the further profile optimization in the core plasma would be possible for improving the stability performance by enhancing the central heating and hot-particle fueling from NBI in JT-60U [5]. High triangularity configurations would be also effective for the prolongation of the ELM free phase and the suppression of ELM activities [4].

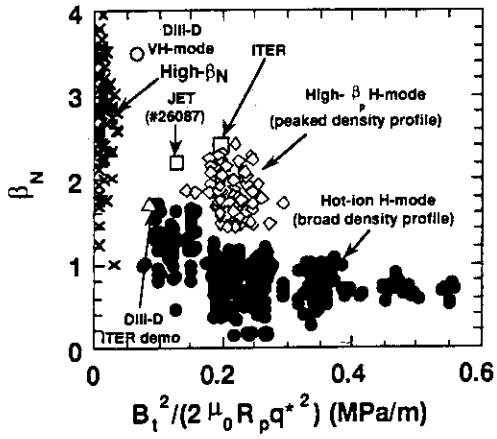

Fig.6 β_N as a function of $B_t^2/(2\mu_0 R_p q^{*2})$ for the hot-ion H-mode regime as compared with the high-β_p H-mode regime, the high-β_N regime, a typical JET discharge and the ITER regim

5. Conclusions

The hot-ion H-mode discharges up to 4.5 MA were achieved so that a low-q regime down to q*~2 was explored for the high performance plasmas in JT-60U. As the plasma current is increased, the confinement improvement is substantially decreased so that the fusion performance was maximized around q*~2.5. While the stability degradation with increasing the plasma current is clarified in association with the edge stability, the further improvement in performance would be possible with the enhancement of the central heat and hot particle deposition and the application of the triangular plasma shaping.

Reference:

[1] Sato M. et al., in Plasma Physics and Controlled Nuclear Fusion Research 1994 (Proc. 15th Int. Conf. Seville, 1994), IAEA, paper IAEA-CN-60/A-2-II-4.

[2] Isayama A. et al., Section 5.2 in this report.

[3] Perkins F. et al., in Plasma Physics and Controlled Nuclear Fusion Research 1994 (Proc. 15th Int. Conf. Seville, 1994), IAEA, paper IAEA-CN-60/A2/E-1-I-3.

[4] Kamada Y. et al., Section 3.2 and 3.3 in this report.

[5] Park H. et al., in Plasma Physics and Controlled Nuclear Fusion Research 1994 (Proc. 15th Int. Conf. Seville, 1994), IAEA, paper IAEA-CN-60/A2/4-P-1.

5.2 Effects of Ripple Loss of Fast Ions on High I_p H-mode Plasma Confinement

A. Isayama, S. Ishida, H. Shirai, Y. Kamada

1. Introduction

In a Tokamak, toroidal field is made by toroidal coils, whose finiteness causes ripple in the toroidal field. It is known that charged particle trapped in the toroidal ripple is lost outside of plasma within much shorter time than confinement time of the plasma. In JT-60U, the number of toroidal coils is 18, and about 70% of input power is supplied by perpendicular NB injection for full power NB injection. Thus the effects of ripple loss is not ignorable in large volume operation and it is important to include the effects of ripple loss in confinement study.

The ripple loss power and the effects of it on high current(low safety factor) plasma confinement in the standard configuration(plasma volume V_p=90m^3) and the high elongation configuration (V_p=70m^3) is investigated by using OFMC(Orbit Following Monte Carlo) code[1].

2. Assumption in calculation and plasma parameters in analysis

Particles orbits of neutral beam are traced by OFMC code until they are thermalized or lost outside of the bulk plasma. In calculation, effective charge number is assumed spatially uniform and set to 2.5. Particle confinement time is assumed 0.5sec. Observation time is just before the degradation of stored energy W_{dia} caused by the occurrence of ELM or sawtooth oscillation. Plasma shapes and beam lines in the high elongation configuration and the standard configuration are shown in Fig.1. Ranges of plasma parameters in analysis are as follows: plasma current I_p=3.0-4.5MA, toroidal field B_t=3.8-4.3T, effective safety factor q_{eff}=2.4-3.8, NB injection power=16-28MW, averaged electron density=1.8-4.2x10^{19}m^{-3}.

3. Results of calculation

The V_p dependence of ion heating power and electron heating power and ripple loss power are shown in Fig.2. Each value is normalized by input NB power. The larger V_p becomes, the smaller ion heating power becomes: the ion heating power is 50% of input NB power in the high elongation configuration and 35% in the standard configuration. The reverse is the case for the ripple loss power: in the high elongation configuration, it is 20% and comparable to electron heating power; in the standard configuration, it becomes as large as 35% and comparable to ion heating power. The increment of ripple loss power is as large as the reduction of ion heating power, which means that larger ripple loss impedes efficient ion heating. As for the ratio of shine-through power and charge exchange loss power to total NB power, they are small(<10%). It should be noted that shine-through loss power has a strong correlation with electron density as shown in Fig.3.

4. Discussion

Energy confinement time is defined by W_{dia}/P_{net}, where P_{net} is net input power. Upper limit and lower limit of energy confinement time are obtained as follows.

$\tau_E^{upper}=W_{dia}/(P_{tot}-\dot{W}_{dia}-P_{ST}-P_{CX}-P_{RPL})$: for upper limit,

$\tau_E^{lower}=W_{dia}/(P_{tot}-\dot{W}_{dia}-P_{ST})$: for lower limit,

where P_{tot}, P_{ST}, P_{CX}, P_{RPL} are total NB power, shine-through loss power, charge exchange loss power and ripple loss power, respectively. The V_p dependence of H-factor is shown in Fig.4. In this figure, shots are selected so that the plasma parameters, such as electeron density, q_{eff}, net NB input power and internal inductance, show almost same value. The shot numbers and plasma parameters used in this analysis are listed in Table1. The H-factor of thermal component(discussed later) is also plotted. Even if the ripple loss power is extracted from NB injection power, degradation of H-factor is observed. One of the reasons is thought to be the difference of NB deposition profile. Typical deposition profiles for the high elongation configuration and the standard configuration are shown in Fig.5. The peak position for the standard configuration locates outer region than that for the high elongation configuration. Thus fast ions are more easily lost out of the plasma before they are fully thermalized. Or there may be some other effects of the ripple loss on confinement. It was shown that V_p dependence of H-factor becomes small by extracting the ripple loss power from NB injection power in lower I_p(=2MA) plasmas[2]. The discrepancy may be attributed to q_{eff}, averaged electron density and V_p. Since q_{eff} is higher(>5) and averaged electron density is lower($\leq 2\times10^{19}$ m^{-3}) and V_p is smaller($<80m^3$) in Ref.2, the degradation may not be obvious.

Next, we consider the thermal energy confinement. W_{dia} can be thought to be sum of the stored energy of thermal energy W_{th} and that of fast ion component W_{fast}. Since the energy of injected NB is 90keV, the slowing down time of fast ions is comparable to global energy confinement time. By assuming $\dot{W}_{fast}/\dot{W}_{dia}=W_{fast}/W_{dia}$ the energy confinement time of thermal component $\tau_E^{th(H)}$ is expressed as follows:

$$\tau_E^{th(H)}=W_{th}/(P_{tot}-(W_{dia}-W_{fast})\dot{W}_{dia}/W_{dia}-P_{ST}-P_{CX}-P_{RPL}) \ .$$

The scaling of thermal energy confinement time of L-mode plasma $\tau_E^{th(L)}$ is given by Takizuka and Shirai,

$$\tau_E^{th(L)}=0.047\exp(-1.2\mu)M^{0.15+0.3\mu}\kappa^{1.10-0.45\mu}R_p^{1.07+0.73\mu}a_p^{1.15-0.45\mu}I_p^{1/2}B_t^{(5+4\mu)/18}n_{19}^{1/2}P_{net}^{-2/3} \ ,$$

where M, κ, R_p, a_p and n_{19} are ion mass number, elongation, plasma major radius, plasma minor radius and electron density in unit of $10^{19}m^{-3}$, respectively[3-5]. μ takes from 0 to 1. By using these parameters, H-factor of thermal component H_{th} can be defined by $\tau_E^{th(H)}/\tau_E^{th(L)}$. The R_p dependence of H_{th} is show in Fig.4. In this figure, μ is set to 0.5. Unlike the H-factor including fast ion component, H_{th} does not change significantly, which means thermal component is less sensitive to ripple loss.

5. Summary

The ripple loss power and the effects of it on high current(I_p=3.0-4.5MA) plasma confinement in the standard configuration and the high elongation configuration is investigated by using the OFMC code. The ripple loss power is as large as ion heating power in the standard configuration. Even if the ripple loss power is extracted from NB input power, degradation of H-factor is found.

References

[1] TANI K., AZUMI M., KISHIMOTO H., and TAMURA S.: J. Phys. Soc. Japan, 50, 1726 (1981).

[2] VAN BLOKLAND, AZUMI M., KIKUCHI M., TANI K. and TOBITA K.: Plasma Phys. control. Fusion, 36, 925 (1994).

[3] TAKIZUKA T., Proc. 19th EPS Conf. on Cntr. Fusion and Plasma Phys. (1992) Vol. 16C, Part I, 51.

[4] SHIRAI H. et al., Plasma Phys. Contr. Nucl. Fusion Reserch 1994 (IAEA-CN-60/A-2-III-6).

[5] SHIRAI H.et al., J. Phys. Soc. Japan, 64, 4209 (1995).

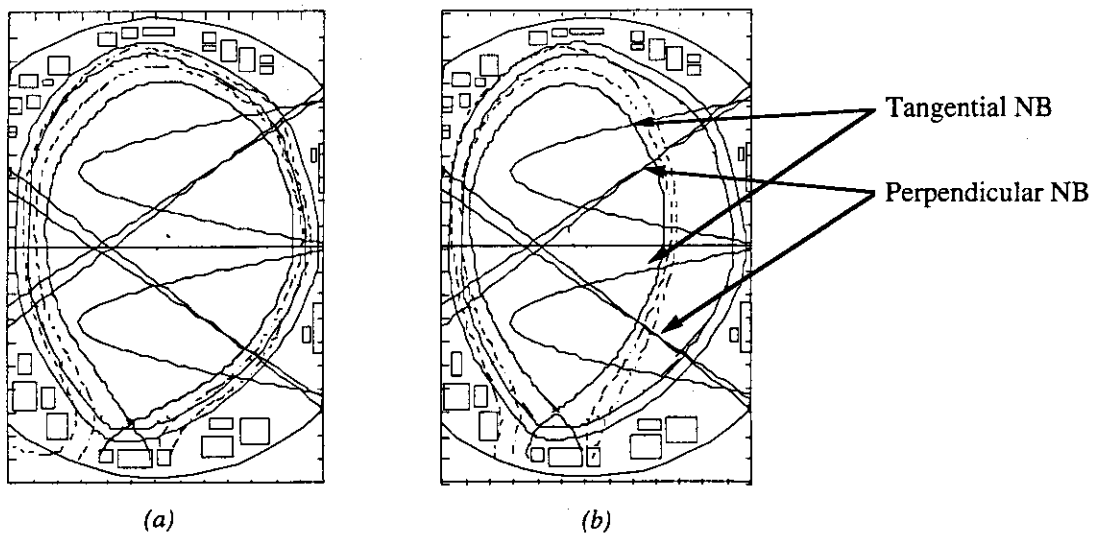

Fig.1: Typical plasma shape and NBI beam line for (a)the standard configuration and (b)the high elongation configuration.

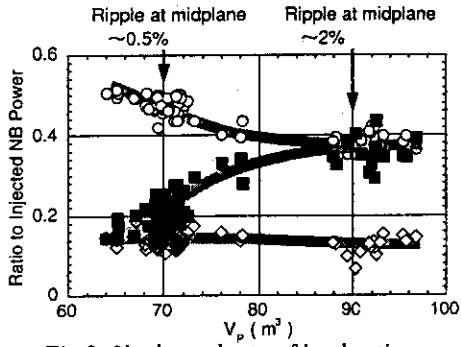

Fig.2: Vp dependence of ion heating power (○), ripple loss power(■) and electron heating power(◇).

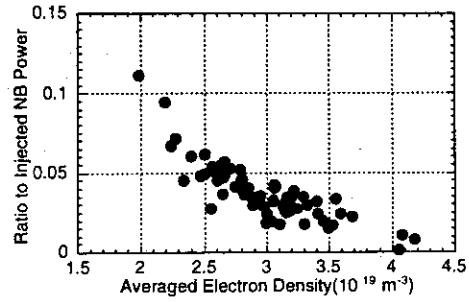

Fig.3: Electron density dependence of shine-through loss power.

Table 1: Shot numbers and plasma parameters used in analysis.

Shot No.	Configuration	Ip(MA)	Bt(T)	Rp(m)	qeff	Vp(m^3)	li	$\overline{ne}$ (m^-3)	PNBI(MW)	Pnet(MW)
23142	Standard	3.0	3.8	3.4	3.5	88	1.1	2.3E+19	19	10
23143	Standard	3.0	3.8	3.4	3.4	88	1.1	2.6E+19	22	12
23969	High Elogation	3.4	4.2	3.2	3.4	69	1.1	2.6E+19	26	10
23979	High Elogation	3.5	4.2	3.2	3.3	67	1.1	2.6E+19	26	11
23996	High Elogation	3.5	4.2	3.2	3.3	65	1.1	2.8E+19	26	11

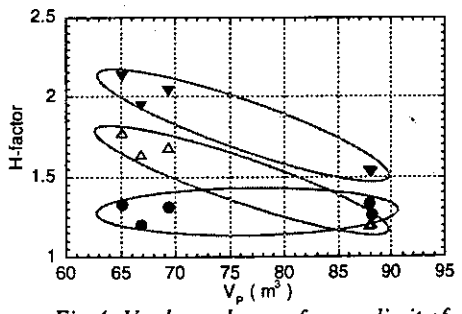

Fig.4: Vp dependence of upper limit of H-factor(▼), lower limit of H-factor(△) and H-factor of thermal energy confinement(●).

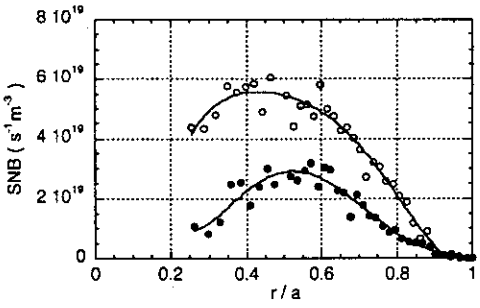

Fig.5: Typical NB source profile for the standard configuration (●) and the high elongation configuration (○).

5.3 Recent Results on H-mode Confinement Studies in JT-60U (Contributions to the 5th H-mode Workshop)

T. Fukuda, T. Takizuka, Y. Kamada, H. Shirai, K. Tsuchiya, H. Takenaga, M. Sato, M. Kikuchi, S. V. Neudatchin, N. Isei, Y. Koide, M. Azumi, S. Ishida, M. Mori, O. Naito, Y. Kawano, T. Hirayama, R. Yoshino, K. Ushigusa, S. Tokuda, Y. Neyatani and S. Takeji

Improvement of the energy confinement is admittedly one of the most crucial issues to realize thermonuclear fusion reactors. On the basis of L-mode confinement, a tokamak reactor would require a large value of A x I_p of more than 100 MA, where A is the aspect ratio and I_p is the plasma current. This value is too large in terms of the economic constraints and engineering difficulties. Therefore, improved confinement is indispensable in the fusion plasmas. Various kinds of improved confinement modes have been found out and developed on many tokamaks in the world. Among them, ubiquitously observed H-mode is one of the excellent improved confinement modes. This mode is characterized by the formation of edge transport barrier. Features of improved core confinement are often combined with that of H-mode, which often leads to further enhancement of fusion performance. From the viewpoint of steady-state operations, ELMs (Edge Localized Modes) are useful for the particle control, although the energy confinement is slightly degraded. The ELMy H-mode is therefore considered to be a principal operational scheme in ITER. For the engineering design of ITER, there still remain issues to be clarified on the H-mode characteristics, such as energy confinement time scaling, H-mode power threshold scaling, non-dimensional transport, ELM model and so on. These issues are required to be studied on the present tokamaks as ITER physics research needs [1].

In order to fulfill the requirement above, a series of experiments on the H-mode confinement was undertaken on JT-60U. Recent results of the H-mode confinement study in JT-60U during the period from April to September, 1995 are published in Ref. 2, and this chapter therefore only summarizes the result of individual work in this report. The authorship for each study lies on the authors of each chapters in Ref. 2, and there is no particular authorship for this chapter. Subsection headings in Ref. 2 are as follows: (1) the scaling of high T_i H-mode confinement, (2) time behaviour of heat diffusivity during L-H-L transitions, (3) time evolution of transport properties in H-mode plasmas with improved core confinement, (4) non-dimensional transport experiment, (5) threshold power scaling, (6) parametric study of edge local quantities at the transition, (7) effect of edge neutrals on the transition criteria, (8) phenomenology of H-L back transition, and (9) the onset condition of ELMs.

1. Scaling of High T_i H-mode Confinement

Comparative studies among the JT-60U confinement data of ELM-free high T_i H-mode, L-mode scaling law (ITER-89 power law) and ELM-free H-mode scaling laws were carried out. The average of H-factor for the present data is about 1.8, which is much smaller than that expected from the ELM-free H-mode scaling ($H \approx 3$). Scatter from the fitted function, $\tau_E = 1.8 \times \tau_E^{ITER89P}$, is rather large. In order to clarify the effect of high T_i, we have carried out a preliminary analysis of the data, and found for the first time that values of H-factor are fitted well by a formula, $H^{fit} = 1+(T_{io}/T_{eo} - 1)\, n_e^{1.5}/I_p^2$.

2. Time Behaviour of Heat Diffusivity during L-H-L Transitions

L-H-L transitions for high field pulses in JT-60U were analyzed. The simultaneous T_e response (with uncertainty of 10 ms) has been clearly observed during L-H-L transitions over $0.2 < \rho < 0.9$ in JT-60U plasmas similarly in JET. This evolution of $T_e(\rho, t)$ is difficult to be explained as the result of HPP from the periphery, but is reasonable to be described as the result of the fast χ_e jump (reduction at L-H transitions and increment at H-L transitions) over $0.2 < \rho < 0.9$. The simultaneous T_i response (with uncertainty of 20 ms) was also observed similarly to the T_e response. The fast variation of χ (at least 20-40 times less than τ_E) inside almost all the plasma volume is a heuristic feature of the L-H-L transition in JT-60U. The T_e response in the central region ($\rho \sim 0.3$) often delays, compared with that in the outer region ($\rho \sim 0.5$) seen, and the role of HPP could be important similarly to JET results. Values of χ_e jump, $\delta\chi_e$, were obtained for $0.5 < \rho < 0.7$, whose absolute values were $0.6\ m^2/s < |\delta\chi_e| < 0.9\ m^2/s$. They usually increase with radius. Values of $\delta\chi_i$ were also obtained for $0.4 < \rho < 0.7$. Their absolute values, $|\delta\chi_e|$ and $|\delta\chi_i|$, usually increase with radius. In high I_p pulses ($I_p > 3$ MA/B_t = 4.2 T), values of $|\delta\chi_i| \approx 0.5\ m^2/s$ are almost the same as or a little smaller than those of $|\delta\chi_e|$, while in a low I_p pulse (2 MA/4.2 T), values of $0.6\ m^2/s < |\delta\chi_i| < 1\ m^2/s$ are almost the same or a little larger than $|\delta\chi_e|$. In a low field pulse (1.5 MA/2.5 T), values of $|\delta\chi_i|$ are rather large as 2 m^2/s at $\rho \approx 0.60$.

Values of $\delta\chi$ are consistent with the change of τ_E during transitions. The dependence of $\delta\chi_i$ is negative on B_t or I_p like $1/B_t$ or $1/I_p$, while the B_t or I_p dependence of $\delta\chi_e$ is weak. These I_p dependencies agree qualitatively with the result of power balance analysis for JT-60U L-mode plasmas.

3. Temporal Evolution of Transport Properties in JT-60U H-mode Plasmas with Improved Core Confinement

Temporal evolution of the global confinement and local transport properties in ICC H-mode plasmas with $T_i(0) \geq 20$ keV was studied. At the first L-H transition when both T_e and

T_i keep increasing and the confinement continues to improve, TH factor and χ_i change in two different time scales: much smaller than τ_E^{th} at the L-H transition and the succeeding slow change is on the time scale of τ_E^{th}. At the repetitive L-H-L transitions, when the confinement improvement is well developed, TH factor and χ change on a much smaller time scale than τ_E^{th}.

We continue the transport study of ICC H-mode plasmas to clarify the mechanism of fast and slow changes in the global confinement and local transport properties. Difference of χ_e behaviour in shot E16168 (small change between L- and H-phases) and in shot E16107 (remarkable change) is not resolved. The evolution of χ in the edge barrier was not studied here because of lack of edge profile data. These are future problems to be clarified.

4. Non-dimensional Transport Experiment in JT-60U

Non-dimensional transport experiment for the ELMy H-mode plasmas was carried out under the ITER relevant conditions. The obtained results show that the confinement property of the ELMy H-mode is a Bohm type. When B_T increases with constant β and decreasing ρ_*, an index of ELM activity, β/ρ_*, increases and ELMs become more vigorous. We suppose that this enhanced ELM activity suppresses the degree of H-mode confinement in plasmas with smaller ρ_*. This suppression can be well the cause of the Bohm type confinement for the ELMy H-mode discharges in JT-60U.

In order to reduce the ELM activity, the increase of the triangularity δ of a plasma cross section can be efficient. We will perform the non-dimensional transport experiments in the high δ configuration of JT-60U.

5. Threshold Power for H-mode Transition in JT-60U Plasma

In order to reasonably reduce the influence of wall conditions as much as possible, power threshold data was obtained from the consecutive tokamak discharges in a single series of experiment with a fixed equilibrium configuration. P_{NB}^{th} is scaled as $n_e^{0.5}\ B_T^{1.0}$ in the region $\overline{n_e} \geq 1.2 \times 10^{19} m^{-3}$. The density dependence of P_{th} was weaker than P_{th}^{ITER}, and the threshold power significantly increases with decreasing density in the range $\overline{n_{e19}} \leq 1.2 \times 10^{19} m^{-3}$. This is congenial to the $ne^{0.75}B_TS$ scaling produced by the ITER H-mode database working group. The quality of database compiled, thus having been remarkably improved, Ip dependence of P_{NB}^{th} was not resolved. It can be deduced from the JT-60U scaling that P_{th} for ITER is less than 100 MW. Further analysis is in progress for the better scaling with other tokamaks, regarding the role of aspect ratio which is related to the ion orbit width.

6. Parametric Study of Edge Local Quantities across the H-mode Transition

We have herewith clearly documented that the low density limit for the H-mode transition does exit, and it can be scaled with q_{eff} or the edge neutral density. Therefore, it was suggested

that the density limit can be machine dependent. We have also shown that increase of the edge neutral density reduces the value of ion collisionality required to induce the transition, which significantly increase the necessary NB heating power. In the region where the ion collisionality at the transition is remarkably below unity, the ratio of charge exchange frequency divided by the bounce frequency, as evaluated by the DEGAS code, is significantly large. It can be deduced from the results above that the ion collisionality is not the sole necessary condition for the H-mode transition, and we are urged to seek for the full set of criteria.

7. Effect of Edge Neutrals on the Condition of H-mode Transition Effect of neutral density on the H-mode transition was experimentally studied in JT-60U. The neutral density near the separatrix was evaluated with the DEGAS code. We have obtained the result which indicates strong correlation between $\nu_i^*{}_{eff}$ and n_o^{95}/n_e^{95}. This means that the edge neutrals have a substantial influence on the condition of H-mode transition, and it is also consistent with the transition theory, which is based on the ion orbit loss.

8. H-L Back Transitions

The H to L back transitions observed in JT-60U were categorized into three species, depending upon their phenomenological features; i.e., the one which occurs (1) after the end of the NB heating phase, (2) during the density increasing phase due to the strong gas-puffing, and (3) when the wall conditioning is insufficient , which is related to the high recycling factor and or a large amount of the impurities generation at the first wall and the divertor plates.

The first phenomena is often observed after the robust ELM activities, whilst in the second case, H-L back transitions are not obvious. This is consistent with the theoretical predictions, which concerns the edge neutral density. The third case represents repeated L to H and H to L transitions.

9. Onset Condition of ELMs

For the standard shape of JT-60U at low triangularity δ (~0.1), it was confirmed that the onset condition of the giant ELMs is clearly correlated with the high-n ballooning limit in the first stability regime over wide ranges of plasma parameters (I_p, B_t, q_{eff}..). The edge pressure limit increases with elongation κ (1.5-1.8) and internal inductance l_i. The δ-scan (-0.05 ~ 0.4) experiment showed that the limit of edge density, edge pressure and edge pressure gradient increases with δ.

References

[1] ITER Physics Committee: ITER Physics Committee Meeting, Naka, 1994 .

[2] H-mode Study Group: JAERI-Research 95-075 (1995).

5.4 Edge Pedestal Width of H-mode Plasmas in JT-60U

T. Hatae, S. Ishida, Y. Kamada, T. Fukuda, T. Takizuka, M. Kikuchi,
H. Yoshida, O. Naito and Y. Koide

1. Introduction

Quantitative investigation of edge transport barrier formed at the H-mode transition is an important issue for the understandings of H-mode phenomena. In JT-60U, the pedestal width in H-mode observed in T_e, T_i and n_e profiles, are studied and compared with the theory [1)-4)]. Recently, the peripheral profiles of T_e, n_e and T_i in JT-60U are measured with significantly improved spatial resolution with the Ruby laser Thomson scattering system and the charge exchange recombination spectroscopy system (CXRS). In this study, we carried out NBI experiments with a wide range of plasma current from 1MA to 4.5MA in order to investigate the poloidal gyroradius dependence.

2. Edge Pedestal Width and Edge Parameter Dependence

We introduce a quantity, of which we refer to as the pedestal width. The pedestal width is defined as length from appearance point of temperature and density steep gradient to plasma surface (separatrix) at the periphery of plasma. A peripheral electron temperature profile and its pedestal width (Δr) are shown in Fig.1. In this study, we are concerned with T_e and T_i pedestal width. Both pedestal widths are almost comparable in the ELM free H-mode plasma.

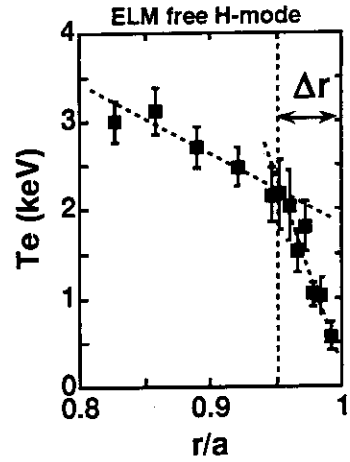

Fig.1 Peripheral electron temperature profile in ELM free H-mode plasma(E023956). Plasma current is 3.5MA, toroidal field is 4T. Pedestal width Δr is 3.9±1 cm.

Shaing proposed the theoretical edge radial electric field layer width in H-mode as follows [5)],

$$\Delta r = \sqrt{\varepsilon}\left(\rho_{Pi}/\sqrt{S}\right),$$

$$S = \left|1 - \frac{1}{B_P \Omega_P}\frac{dE_r}{dr}\right|,$$

where ρ_{Pi} is poloidal gyroradius of thermal ions and S is squeezing factor. In a 3.5MA H-mode plasma, E_r is estimated -79±34kV/m at v_θ~-6km/s by the CXRS diagnostic. As the pedestal width is 3.8cm, dE_r/dr can be estimated -2.1×10^6V/m^2. At this time, the squeezing factor is 1.08 (I_p=3.5MA with Bp=0.72T). Hence the squeezing factor is in the range of about 1-1.2 in JT-60U. We can say that squeezing factor is almost 1. As the term of $\sqrt{\varepsilon}\rho_{Pi}$ is a banana width, the theoretical width Δr could be comparable to the banana width in JT-60U.

The new data set of the pedestal width was obtained with wide temperature ranges of peripheral T_e and T_i profiles in the ELM free H-mode plasma. From this data set, we have proved that the pedestal width did not simply be expressed by the inverse poloidal field ($1/B_P$) in contrast to the previous results [2] (Fig.2).

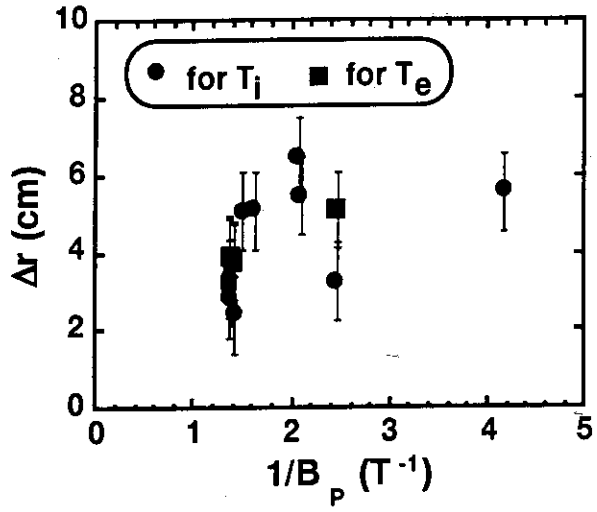

Fig.2 Relation between pedestal width and inverse poloidal field ($1/B_P$). Circle symbols show pedestal widths for T_i profile. Square symbols show pedestal widths for T_e profile. The pedestal width does not simply be expressed by $1/B_P$.

At fixed T_i, the pedestal width is inversely proportioned to poloidal field dependence. The pedestal width normalized by $1/B_P$ shows a linear dependence of the square root edge ion temperature suggesting the poloidal gyroradius dependence of the pedestal width (Fig.3).

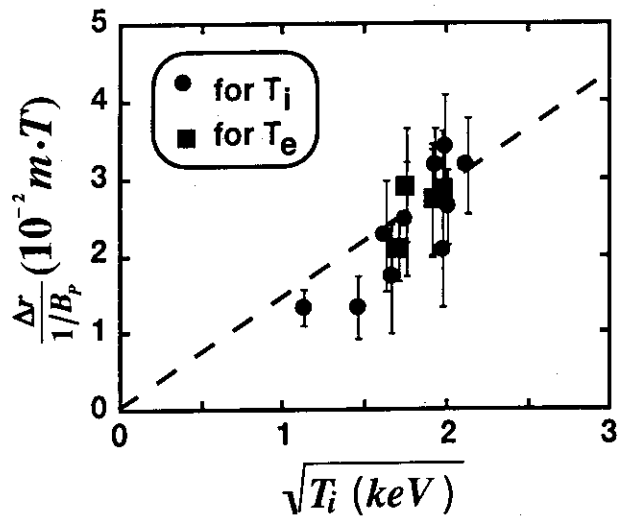

Fig.3 Clear T_i dependence of the pedestal width. Circle symbols show pedestal widths for T_i profile. Square symbols show pedestal widths for T_e profile. Pedestal width normalized by $1/B_P$ shows a linear dependence of the square root edge temperature.

Measured pedestal width of T_e and T_i range from 2.4cm to 6.5cm showing a clear dependence on $\sqrt{\varepsilon}\rho_{Pi}$ (Fig4). The pedestal width are found to be a factor ~4 larger than the theoretical prediction.

3. Discussion

We discuss here that the pedestal width is a factor ~4 larger than the banana width. It is possible to refer to following two hypotheses about the factor, (1) Fast ion, (2) Perpendicular viscosity.

(1) Fast ion

Provided that an effective edge ion temperature by fast ion is 50keV, banana width of fast ion is comparable to order of experimental results [3)-4)]. As the energy of injected beam ion is kept constant, the banana width of fast ion can be proportional to $1/B_P$ uniquely. However, this hypothesis based on the banana width of fast ion can not explain T_i dependence of the pedestal width. Effect of the radial electric field due to ripple enhanced beam ion loss is not taken into account in this study. It needs further consideration.

(2) Perpendicular viscosity

Itoh et al.* proposed the theoretical pedestal width in H-mode as follows,

$$\Delta r \sim \sqrt{\frac{\mu_\perp}{\nu_i} + \rho_{Pi}^2}\,.$$

Where $\mu_\perp$ is perpendicular viscosity. Assuming the following equation,

$$\Delta r = \sqrt{\frac{\mu_\perp}{\nu_i} + \rho_{Pi}^2}\,,$$

experimental results are compared with this theory with various $\mu_\perp$ values. In the case of $\mu_\perp$=0.1m^2/s, the theoretical pedestal width is comparable to order of experimental width, but the $\sqrt{\varepsilon}\rho_{Pi}$ dependence becomes weaker than linear (Fig.5).

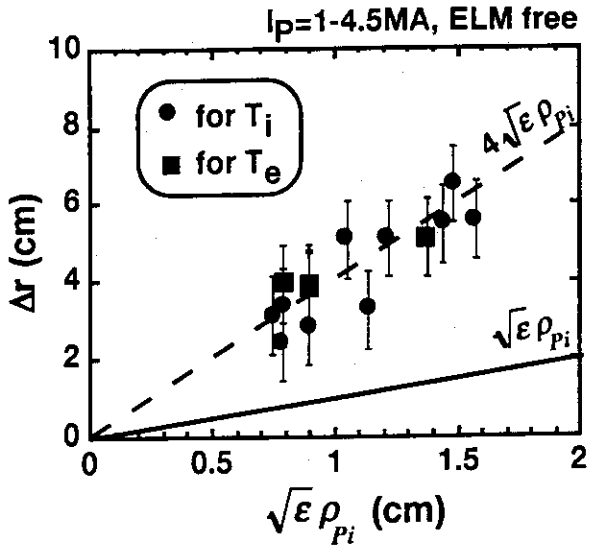

Fig.4 Clear Banana width dependence of the pedestal width. Circle symbols show pedestal widths for T_i profile. Square symbols show pedestal widths for T_e profile. Measured pedestal widths show a clear dependence on banana width $\sqrt{\varepsilon}\rho_{Pi}$.

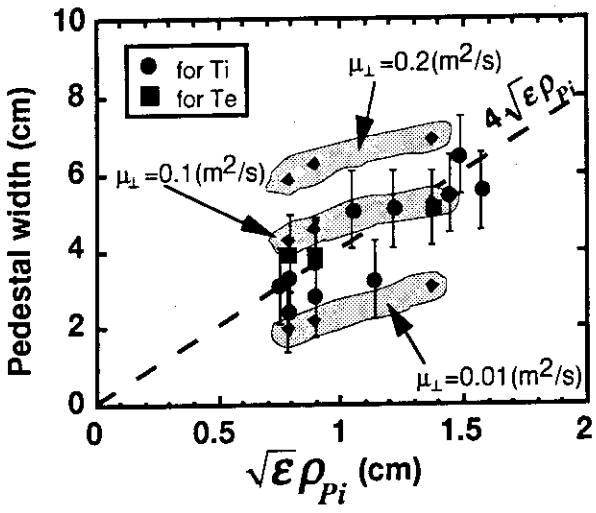

Fig.5 Comparison with experimental results assuming possible perpendicular viscosity $\mu_\perp$. Diamond symbols show theoretical pedestal widths with various $\mu_\perp$. The $\sqrt{\varepsilon}\rho_{Pi}$ dependence of theoretical pedestal width becomes weaker than linear.

---

* *Itoh K., Itoh S-I., Fukuyama A., Yagi M.,"Pressure Gradient at H-mode Pedestal", presented at 'ITER Expert Meeting for Confinement Data Base and Modeling' Oct. 1995*

4. Summary

Edge pedestal width was measured for a wide range of I_p=1-4.5MA in the JT-60U ELM free H-mode plasmas, where $\sqrt{\varepsilon}\rho_{Pi}$ was varied from 0.7cm to 1.6cm. The pedestal width does not simply be expressed by $1/B_p$. However, the pedestal width normalized by $1/B_p$ shows a linear dependence of the square root edge ion temperature. Pedestal width clearly shows the $\sqrt{\varepsilon}\rho_{Pi}$ dependence with a factor of ~4 larger than theoretical prediction.

The pedestal width was discussed from the viewpoints of fast ion and viscosity. Both hypotheses are not fully consistent with experimental results.

References

1) Kikuchi M., Shirai H., Takizuka T., et al. 1993 Proc. 14th Int. Conf. on Plasma Physics and controlled Nuclear Fusion Research, Würzburg Vol.1 (Vienna:IAEA) 219
2) Kikuchi M., Sato M., Koide Y., et al. 1993 Proc. 20th EPS conf., Lisboa I 179
3) JT-60 team 1993 'Review of JT-60U Experiment Results from January to October, 1992' (JAERI Report JAERI-M 93-057) 21-24
4) Mori M., the JT-60 Team, and the JFT-2M Team 1994 Plasma Phys. Control. Fusion 36 A39
5) Shaing K. C., 1992 Phys. Fluids B4 290

5.5 Nondimensional Transport Study of JT-60U L-mode Plasmas

H. Shirai, T. Takizuka, O. Naito, M. Sato, N. Isei, Y. Koide, T. Hirayama and M. Azumi

1. Introduction

Regression analyses of confinement and transport properties by using nondimensional plasma parameters [1,2] have been carried out in various tokamaks [3-5]. Important nondimensional parameters related to the plasma confinement and transport are the aspect ratio, $A=R/a$, the elongation, κ, the triangularity, δ, the safety factor, q, the shear parameter, $s=\left(r/q\right)dq/dr$, the normalized Larmor radius, $\rho^* = \rho_L/a = \sqrt{2mT_e}/eBa$, the thermal component of beta value, $\beta_{th} = 2\mu_0\left(n_eT_e+n_i^{th}T_i\right)/B^2$, the normalized collision frequency, $\nu^* = \nu_{ei}/\left(\nu_b\varepsilon^{1.5}\right)$, the ratio of the electron to the ion temperature, T_e/T_i, the ratio of the electron to the ion mass, $\mu = m_e/m_i$, and so forth. Here n_i^{th} is the thermalized ion density, $\varepsilon = r/R$ is the local inverse aspect ratio, ν_{ei} is the electron-ion collision frequency, and $\nu_b = V_{th}/qR$ is the electron bounce frequency.

The thermal diffusivity, χ, is expressed by nondimensional plasma parameters as,

$$\chi = \chi_{Bohm}\left(\rho^*\right)^X G\,(q, s, \beta_{th}, \nu^*, T_e/T_i, A, \kappa, \delta\cdots), \qquad (1)$$

where $\chi_{Bohm} = T_e/eB$ denotes the Bohm diffusion coefficient. A nondimensional function G should be clarified by the systematic experiments of nondimensional parameter scan. The ρ^* dependence of χ is especially extracted as eq.(1) and the special cases of X=0 and X=1 are called "Bohm type diffusion" and "gyroBohm type diffusion", respectively. The gyroBohm type diffusion is considered to have a short wave length structure, $k_\perp\rho_i \sim 1$, where $k_\perp$ is the perpendicular wave number of the dominant turbulence and ρ_i is the ion Larmor radius. On the other hand, the Bohm type diffusion is considered to have longer wave length structure, $k_\perp\rho_i << 1$.

If we compare values of nondimensional parameters between ITER and the present large tokamaks, q, s, β_{th}, ν^* and so forth are similar between them. However, ρ^* value of ITER is much smaller than that in large tokamaks. Therefore the ρ^* dependence of χ is important for the prediction of transport properties of ITER plasmas. In this subsection we summarize the study the ρ^* dependence of χ in NBI heated L-mode plasmas [6], which is the first step of nondimensional transport study.

2. Numerical Calculation Method

The profiles of effective thermal diffusivity, χ_{eff}^{exp}, electron and ion thermal diffusivities, χ_e^{exp} and χ_i^{exp}, are calculated by the steady-state power balance equation of electron and ion by using the profile data of JT-60U experiment. The power deposition profile of NBI is calculated by OFMC (Orbit Following Monte-Carlo) code [7] in order to evaluate the ripple

loss of fast ions. In order to clarify the ρ^* dependence of χ^{exp}, we will compare χ^{exp} with the three types of thermal diffusivity models as follows,

$$\chi_B^{model} = \chi_{Bohm}\left(\rho^*\right)^0 G_B \tag{2}$$

$$\chi_{WGB}^{model} = \chi_{Bohm}\left(\rho^*\right)^{0.5} G_{WGB} \tag{3}$$

$$\chi_{GB}^{model} = \chi_{Bohm}\left(\rho^*\right)^1 G_{GB} \tag{4}$$

The function G_k (k=B, WGB, GB) appears in eq.(1). In this subsection, a B_t=2.4 T plasma and a B_t=4.0 T plasma, which have the similar profiles of nondimensional parameters except for ρ^*, are compared. We can assume that the profiles of G_k are almost the same between two shots. Therefore by taking the ratio of χ_k^{model}(2.4T) / χ_k^{model}(4.0T), we can eliminate the effects of G_k and highlight the ρ^* dependence of the thermal diffusivity. Comparing this ratio with χ^{exp}(2.4T) / χ^{exp}(4.0T) obtained from local transport analysis, we will find out the best model to describe the properties of thermal diffusivity. Now we introduce following indexes of conformity,

$$F_{eff}(r) = \frac{\chi_k^{model}(2.4\mathrm{T}) / \chi_k^{model}(4.0\mathrm{T})}{\chi_{eff}^{exp}(2.4\mathrm{T}) / \chi_{eff}^{exp}(4.0\mathrm{T})} \tag{5}$$

$$F_e(r) = \frac{\chi_k^{model}(2.4\mathrm{T}) / \chi_k^{model}(4.0\mathrm{T})}{\chi_e^{exp}(2.4\mathrm{T}) / \chi_e^{exp}(4.0\mathrm{T})} \tag{6}$$

$$F_i(r) = \frac{\chi_k^{model}(2.4\mathrm{T}) / \chi_k^{model}(4.0\mathrm{T})}{\chi_i^{exp}(2.4\mathrm{T}) / \chi_i^{exp}(4.0\mathrm{T})} \tag{7}$$

for each model (k=B, WGB, GB). The model with which F_{eff}, F_e and F_i become close to 1 is the conformable model to describe the type of thermal diffusivity.

3. Results of Nondimensional Transport Study

We have examined a pair of NBI heated L-mode shots with q_{eff}=4.5; shot E21795 (B_t=2.4 T) and shot E21810 (B_t=4.0 T) with R=3.33 m, a=0.95 m, a_V (volume averaged minor radius)=1.09 m, κ=1.4, δ=0.16, V=77 m^3. We adjusted the density and the temperature as $n \propto B^{4/3}$ and $T \propto B^{2/3}$ by changing the NBI heating power and the gas puffing and set $I_p \propto B$ in order to get the same profile of nondimensional parameters such as q, s, ν^*, β_{th} and so forth except for ρ^*.

Figure 1 shows the comparison of the measured profiles of n_e, T_e, T_i, and the calculated ohmic and NBI heating profiles of Q_{OH}, Q_{NBI}^e and Q_{NBI}^i between 2.4 T shot (solid lines and closed symbols) and 4.0 T shot (broken lines and open symbols). The n_e profile is considerably flat in JT-60U L-mode plasmas. Temperature profiles are fairly similar between these shots, and T_e/T_i is 0.8±0.05 in the region $a/3 \le r \le 2a/3$ for both shots. The deposition profile of NBI is rather off-axis. In this configuration the ripple loss of fast ions is evaluated about 20 % of injected power. Therefore the Q_{NBI} rapidly tends to zero in the plasma outer region.

The point of maximum Q_{NBI}^i in 2.4 T shot locates slightly near the plasma central region comparing with that in 4.0 T shot due to the different density. The total heating

power of electrons is almost the same as that of ions. Profiles of β_e, β_i^{th} and ν^* in shots E21795 and E21810 are compared in Fig. 2. They show fairly good agreement.

The values of W_f/W_{tot}, however, are different between for 2.4 T case and for 4.0 T case as shown in Table I; W_f/W_{tot}=0.38 for 2.4 T and W_f/W_{tot}=0.25 for 4.0 T. As the same as the previous works [3-5], we assume that this nondimensional parameter affects little the thermal transport in L-mode plasmas. The heat and loss power integrated from the plasma center to a magnetic surface at r, $P(r) = \int_0^r Q(r)\,dV$, in shots E21795 and E21810 are compared in Fig. 3 ((a) electrons and (b) ions). Each power is normalized by the total absorbed power, $P_{abs} = P_{OH} + P_{NBI}$ The conduction loss is the dominant energy loss channel in both electrons and ions. The convection loss, the radiation loss, and the charge exchange loss are negligibly small in the region $a/3 \le r \le 2a/3$. All the normalized powers, $P(r)/P_{abs}$, are almost the same between for B_t=2.4 T (solid line) and for B_t=4.0 T (broken line). Profiles of χ_e^{exp} and χ_i^{exp} are also presented in Fig. 3. The values of χ_i^{exp} is larger than χ_e^{exp}, and both increase from the plasma central region toward the outer region. These are the typical L-mode features.

The profiles of F_{eff}, F_e and F_i for a pair of shots E21795 and E21810 are shown in Fig. 4. The solid line, the broken line and the dotted line correspond to the Bohm type diffusion, the weak gyroBohm type diffusion and the gyroBohm type diffusion, respectively. Comparing three F_{eff} values, we find that χ_{eff}^{exp} property is between the weak gyroBohm type diffusion (X=0.5) and the Bohm type diffusion (X=0) in the region of $a/3 \le r \le 2a/3$. Around $r = 2a/3$ χ_{eff}^{exp} is almost the weak gyroBohm type, which is consistent with the results of the global confinement study [8]. The properties of electron and ion transports are a little different. The profile of F_e shows that χ_e^{exp} is almost the weak gyroBohm type diffusion in the region $a/3 \le r \le 2a/3$. On the other hand, we find from the F_i profile that χ_i^{exp} is almost weak gyroBohm around $r = 2a/3$ and tends to be Bohm like diffusion around $r = a/2$.

The q_{eff}=6.0 case has been also analyzed. The results are almost the same as those of q_{eff}=4.5 case.

References

1) B. B. Kadomtsev : Sov. J. Plasma Phys. **1** (1975) 295.
2) J. W. Connor and J. B. Taylor : Nucl. Fusion **17** (1977) 1047.
3) F. W. Perkins, C. W. Barnes, D. W. Johnson, et al. : Phys. Fluids B **5** (1993) 477.
4) J. P. Christiansen, P. M. Stubberfield, J. G. Cordey, et al. : Nucl. Fusion **33** (1993) 863.
5) C. C. Petty, T. C. Luce, R. I. Pinsker, et al. : Phys. Rev. Lett. **74** (1995) 1763.
6) H. Shirai, T. Takizuka, O. Naito, et al. : J. Phys. Soc. Jpn. **64** (1995) 4209.
7) K. Tani, M. Azumi and H. Kishimoto : J. Phys. Soc. Jpn. **50** (1981) 1726.
8) H. Shirai, T. Takizuka, M. Kikuchi, et al. : *Proc. 15th Conf. on Plasma Phys. and Controlled Nucl. Fusion Research, Seville, 1994*, (IAEA, Vienna, 1995) Vol. 1, P. 355.

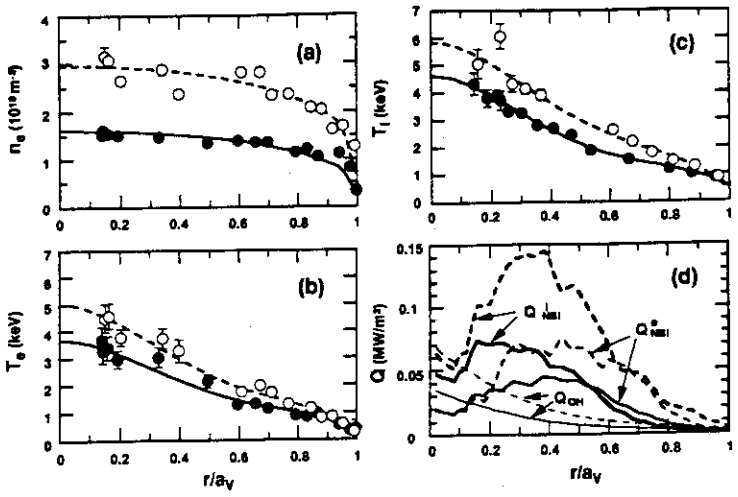

Fig. 1 Comparison of (a) n_e, (b) T_e, (c) T_i and (d) heating profile for q_{eff}=4.5 case. The solid line and the broken line correspond to B_t=2.4 T and B_t=4 T, respectively.

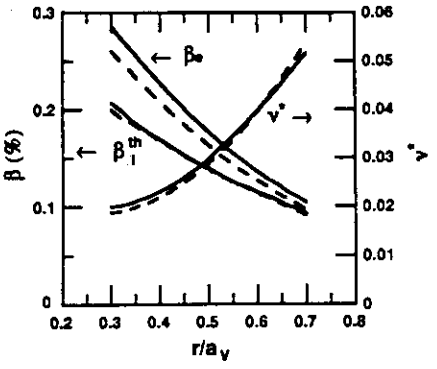

Fig. 2 Comparison of β_e, β_i^{th} and ν^* for q_{eff}=4.5 case. The solid line and the broken line correspond to B_t=2.4 T and B_t=4 T, respectively.

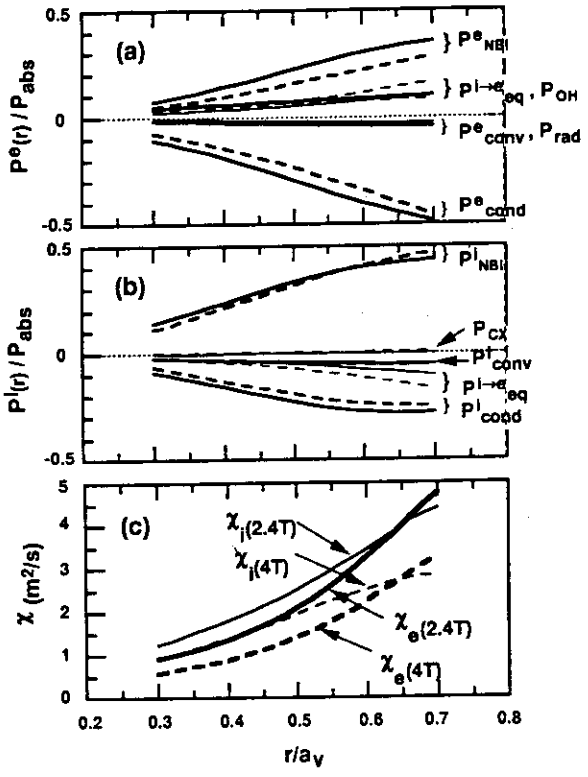

Fig. 3 Comparison of (a) P_e, (b) P_i and (c) thermal diffusivities, χ_e and χ_i, for q_{eff}=4.5 case. The integrated power is normalized by P_{abs}. The solid line and the broken line correspond to B_t=2.4 T and B_t=4 T, respectively.

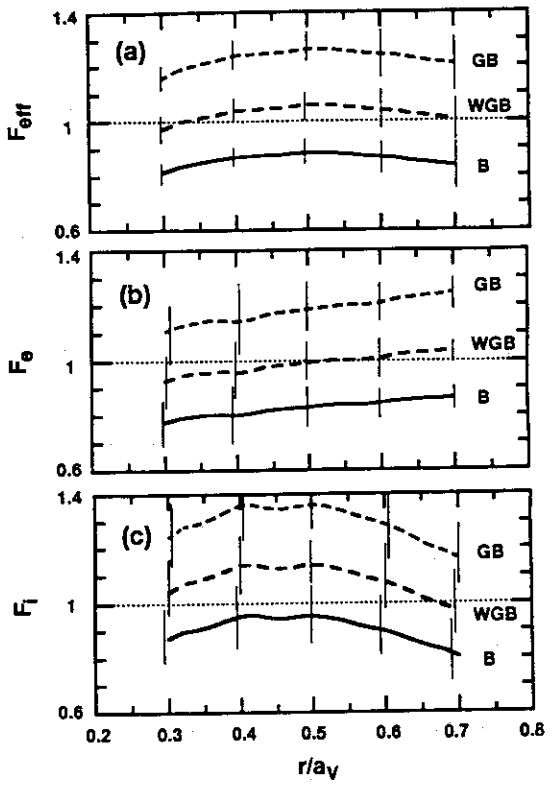

Fig. 4 Profiles of F_{eff}, F_e and F_i for q_{eff}=4.5 case.

5.6 Confinement Scaling for Thermal Energy Based on Database of JT-60

T. Takizuka, H. Shirai, M. Kikuchi, T. Hirayama

1. Introduction

Scaling laws of energy confinement time in tokamak plasmas have been used to design new devices. They have also been utilized to guess the transport property of tokamak plasmas. One of them called ITER89P law for the energy confinement time τ_E of L-mode plasmas is given as [1)]

$$\tau_E^{ITER89P} = 0.048\, M_i^{0.5}\, \kappa^{0.5}\, R^{1.2}\, a^{0.3}\, I_p^{0.85}\, B_t^{0.2}\, (n_e/10)^{0.1} / P^{0.5} \qquad (1)$$

where M_i is ion mass number, κ is ellipticity, and the units of parameters are; τ_E in s, major radius R and minor radius a in m, toroidal magnetic field B_t in T, plasma current I_p in MA, line averaged electron density n_e in $10^{19}m^{-3}$, and heating power P in MW.

In a intensely heated tokamak plasma with low density, several ten percent of high energy component is sometimes included in the stored energy. Therefore above scaling does not directly show the characteristics of the transport of thermal energy. In order to study the energy transport property, it is necessary to clarify the parametric dependence of the confinement time for thermal energy component. Bartiromo presented a scaling for thermal energy confinement time τ_{th} in L-mode plasmas of the form [2)],

$$\tau_{th}^{B} = 0.019\, M_i^{0.3}\, \kappa^{1.0}\, R^{1.7}\, a^{0.55}\, I_p^{0.75}\, B_t^{0.2}\, n_e^{0.55} / P^{0.75} \ . \qquad (2)$$

This scaling shows the rather strong n_e dependence of τ_{th} and strong power degradation. thermal energy confinement. Takizuka also presented a τ_{th} scaling [3)] based on the kinetic database of JT-60 L-mode plasmas [4)];

$$\tau_{th}^{T0} = C\, (I_p\, B_t\, n_e)^{1/2} / P^{2/3} \ . \qquad (3)$$

Here he pointed that B_t dependence is not clear compared with other dependencies because of narrow variation of B_t value.

In this paper, we give a scaling law including size dependence, which fits well the experimental data of τ_{th} in L-mode plasmas as well as in Ohmic plasmas.

2. Dimensionally correct scaling

At first we compare the experimental database of L-mode and Ohmic discharges [4)] in JT-60 with above scalings. Figure 1 shows the scattering of the ratio ($\tau_{th}^{exp} / \tau^{fit}$) for (a) ITER89P scaling, (b) Bartiromo scaling, and (c) Takizuka scaling. Density dependence of τ_{th} is clearly stronger than that of $\tau_E^{ITER89P} \propto n_e^{0.1}$, and I_p dependence is weaker than that of $\tau_{th}^{B} \propto I_p^{0.75}$. The scattering for τ_{th}^{T0} with C = 0.096 is remarkably small.

Next we study the size scaling. On the basis of the dimensionally correct analysis [5], we assume the following relation between τ_{th} and the effective heat diffusivity χ_{eff} ; $\tau_{th} \propto a^2/\chi_{eff}$. This relation is actually seen from Fig. 2, where $<\chi_{eff}>$ denotes the spatially averaged one in the region of $1/2 < r/a < 2/3$. We also assume that χ_{eff} can be described as

$$\chi_{eff} \propto (T/eB)\, \rho_*^{\mu}\, \beta^x\, \nu_*^y \ , \tag{4}$$

where T denotes the plasma temperature, (T/eB).is the Bohm diffusion coefficient, $\rho_* \propto T^{1/2}/RB$ the normalized Larmor radius, $\beta \propto n_eT/B^2$ the beta value, and $\nu_* \propto nR/T^2$ is the collisionality. The "gyro-index" μ classifies the type of diffusion; μ=0 represents to the Bohm type diffusion and μ=1 to the gyro-Bohm type one. Since the confinement time is defined by $\tau_{th} = W/P \propto R^3\, n_eT\, /\, P$ and the relation, $\tau_{th} \propto a^2/\chi_{eff}(T)$, holds, we can express τ_{th} of a function of P without using T.

Assuming that he dependence of τ_{th} on I_p, n_e, and P is given as Eq. (3), while B_t dependence is uncertain, we obtain a dimensionally correct scaling with the "gyro-index" μ;

$$\tau_{th} \propto I_p^{1/2}\, B_t^{(5+4\mu)/18}\, n_e^{1/2}\, R^{(40+5\mu)/18}\, /\, P^{2/3} \ . \tag{5}$$

The powers to β and ν_* in Eq. (4) are determined as $x = (4-\mu)/6$ and $y = (\mu-1)/6$.

3. Shape and mass dependencies

We found the size scaling as mentioned above. In order to determine the shape and mass dependencies, we analyze other data of JT-60 with lower X-point configuration (JT-60/LX), of JT-60U with elongated configuration (JT-60U/E), and of JT-60U with standard configuration (JT-60U/S). Figure 3 shows stored thermal energy W_{th} vs $W_0 = 0.096\, I_p^{1/2}\, B_t^{(5+4\mu)/18}\, n_e^{1/2}\, (R/3)^{(40+5\mu)/18}\, P^{1/3}$ with $\mu = 0.5$. From these data, we obtain the following scaling with shape (ellipticity κ and inverse aspect ratio ε) and mass M_i dependencies.

$$\tau_{th}^{T}(\mu) = 0.047 \exp(-1.2\mu)\, M_i^{0.15+0.3\mu}\, \kappa^{1.10-0.45\mu}\, \varepsilon^{1.15-0.45\mu}$$
$$\times\ I_p^{1/2}\, B_t^{(5+4\mu)/18}\, n_e^{1/2}\, R^{(40+5\mu)/18}\, /\, P^{2/3} \ . \tag{6}$$

As an example of the analysis using N = 458 data points, the standard deviation σ ($\sigma^2 = N^{-1}\Sigma (\tau^{exp}/\tau^{fit} - 1)^2$) is shown in Fig. 4, which becomes the smallest when the power of κ, α_κ, is about 0.875 for $\mu = 0.5$, $\alpha_{Mi} = 0.3$, and $\alpha_\varepsilon = 0.925$.

The validity of this scaling is checked by using the database of Ohmic discharges on ASDEX. The ASDEX τ_{th} data have a little stronger dependence on n_e, $\tau_{th} \sim n_e^{0.56}$, but their values and other parametric dependencies are well fitted by the above scaling for various μ values. Introducing a factor f_μ called "μ factor";

$$f_\mu \equiv (M_i^{0.3}\, R^{0.728}\, B_t^{0.222})\, /\, (3.32\, \kappa^{0.45}\, a^{0.45}) \ , \tag{7}$$

Eq. (6) is rewritten as $\tau_{th}^{T}(\mu) = \tau_{th}^{T}(0) \times f_{\mu}^{\mu}$. The values of f_{μ} are nearly unity for above all data points. Therefore the fitting accuracy is unchanged by the change of μ value.

The value of μ can be given from other experimental results on the mass dependence; $\tau_{th} \propto M_i^{0-0.5}$. Especially in JT-60U, the dependence is considered as $\tau_{th} \propto M_i^{0.2-0.4}$. We present here a scaling $\tau_{th}^{T} = \tau_{th}^{T}(\mu=0.5)$ called "weak gyro-Bohm type" scaling [6,7] for L-mode confinement as well as for Ohmic confinement in tokamak plasmas. This scaling fits well the experimental data as shown in Fig. 5, where $W_{th}^{T} = \tau_{th}^{T} P$.

4. Conclusion

We presented a dimensionally correct scaling called "weak gyro-Bohm type" scaling,

$$\tau_{th}^{T} = 0.0258\, M_i^{0.3}\, \kappa^{0.87}\, I_p^{1/2}\, B_t^{0.39}\, n_e^{1/2}\, R^{1.44}\, a^{0.93} / P^{2/3},$$

which fits well the experimental data of thermal energy confinement not only in L-mode plasmas but also in Ohmic plasmas. Parametric dependencies are determined on the basis of the results from JT-60, JT-60/LX and JT-60U. This scaling will be checked in near future by using new ITER L-mode database [8].

Acknowledgment We are indebted to members of the JT-60 team for their contributions to the database. We also thank the members of the ASDEX team for the permission to use the ASDEX data.

References

1) P.N. Yushmanov, T. Takizuka, K.S. Riedel, et al., Nucl. Fusion 30 (1990) 1999.
2) R. Bartiromo, Controlled Fusion and Plasma Physics (Proc. 18th Eur. Conf. Berlin, 1991), Vol. 15C, Part I (European Physical Society, 1991) 73.
3) T. Takizuka, Proc. 1992 Int. Conf. on Plasma Physics, Innsbruck, 1992 (19th Eur. Conf.), Vol. 16C, Part I (European Physical Society, 1992) 51.
4) M. Kikuchi, K. Kikuchi, T. Aoyagi, K. Tani, "Kinetic Database of the JT-60 Tokamak during 1985-1987 Experiments", JAERI-M 91-057 (1991).
5) J.W. Connor, J.B. Taylor, Nucl. Fusion 17 (1977) 1047.
6) H. Shirai, T. Takizuka, M. Kikuchi, et al., Plasma Physics and Controlled Nuclear Fusion Research 1994, Vol. 1 (IAEA, Vienna, 1995) 355.
7) H. Shirai, T. Takizuka, O. Naito, et al., J. Phys. Soc. Japan 64 (1995) 4209.
8) H-mode working group, presented at Third Meeting of ITER Confinement Database and Modelling Expert Group, Naka (1995).

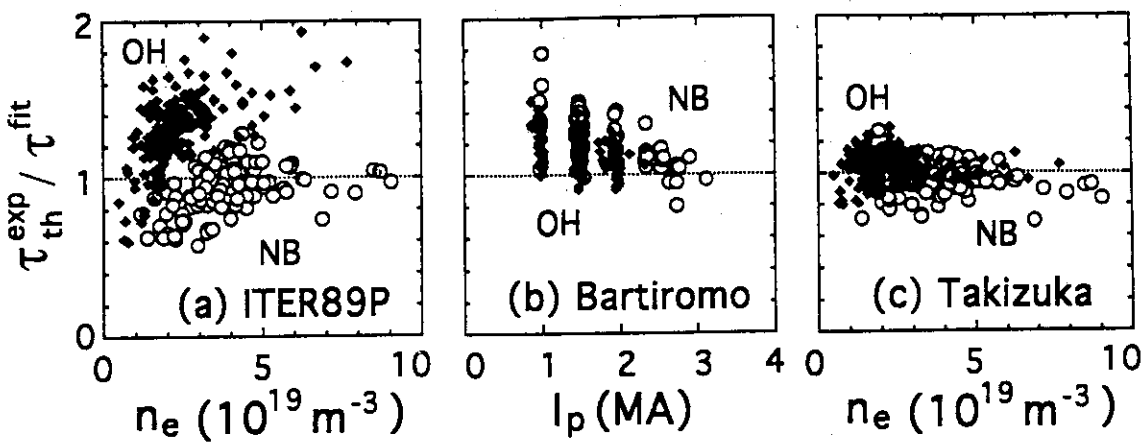

Fig. 1 Comparison of JT-60 data with scalings. Scattering in $\tau_{th}^{exp}/\tau^{fit}$ is large for ITER89P scaling and for Bartiromo scaling, while it is remarkably small for Takizuka scaling.

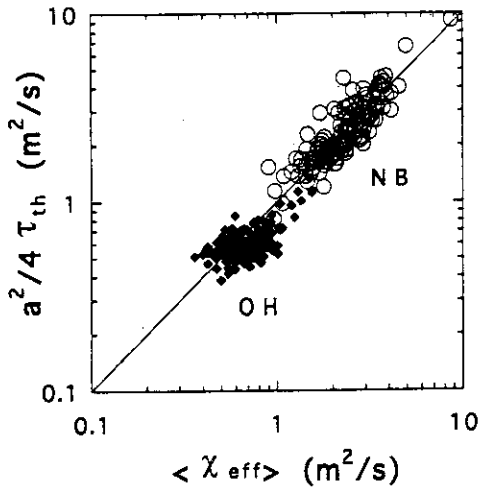

Fig. 2 Relation between τ_{th} and $<\chi_{eff}>$.

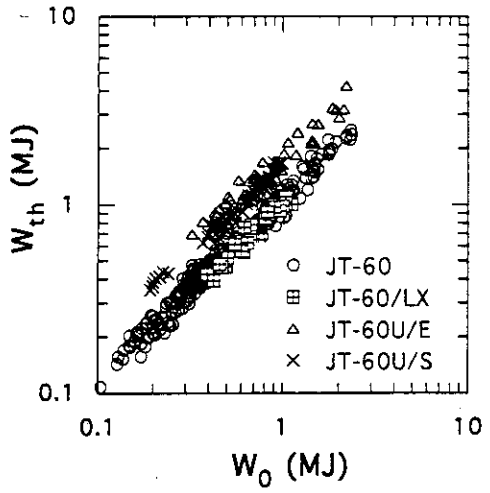

Fig. 3 W_{th} vs W_0 for various configurations.

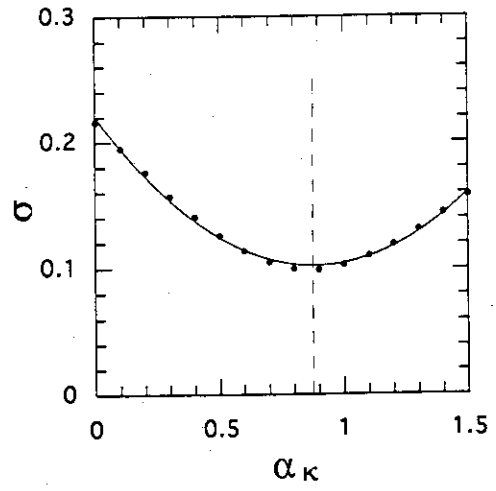

Fig. 4 Standard deviation σ vs α_κ.

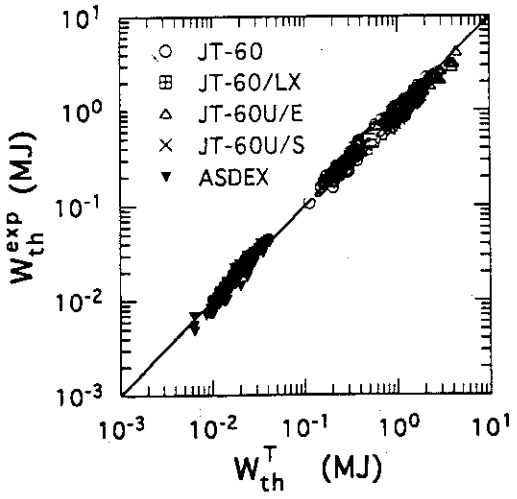

Fig. 5 Comparison of W_{th} scaling law with experimental data.

5. 7 Effects of Central Fuelling and Edge Fuelling on Particle Confinement in JT-60U

H. Takenaga, N. Asakura, K. Shimizu, K. Nagashima, H. Kubo and A. Sakasai

1. Introduction

In order to understand the particle confinement properties, the task to establish the scaling law of the particle confinement time started for ITER physics R&D. In JT-60U, the particle confinement time has been estimated based on the analysis of neutral particle behavior.[1),2)] It is crucial for the particle confinement study to understand systematically database which has the various particle fuelling methods and their distributions. In this section, the effects of central fuelling by NBI and edge fuelling by wall recycling and gas-puffing on the particle confinement were investigated.

2. Particle balance

The particle balance equation can be expressed using the particle confinement time (τ_p) as follow.

$$\frac{dN_e}{dt} = -\frac{N_e}{\tau_p} + S_R + S_{GP} + S_{NB}, \quad (1)$$

where N_e is the total electron number inside the main plasma, S_R, S_{GP} and S_{NB} are the particle fuelling rate due to wall recycling, gas-puffing and NBI, respectively.

The values of S_R and S_{GP} were estimated though the calculation of the neutral particle penetration rate into the main plasma using the neutral particle transport simulation code DEGAS. Dα emission profiles calculated using DEGAS was fitted to the measured profile in order to determine the absolute value of S_R. The absolute value of S_{GP} was determined from the gas flow rate though the gas-puffing port. The value of S_{NB} was estimated based on the Orbit Following Monte-Carlo (OFMC) code.

Furthermore, we consider the particle balance for the particle supplied by NBI (central fuelling) and by wall recycling and gas-puffing (edge fuelling), separately, as follows.

$$\frac{dN_e^C}{dt} = -\frac{N_e^C}{\tau_p^C} + S_{NB}, \quad (2)$$

$$\frac{dN_e^E}{dt} = -\frac{N_e^E}{\tau_p^E} + S_R + S_{GP}, \quad (3)$$

$$N_e = N_e^C + N_e^E, \quad (4)$$

where N_e^C and N_e^E are the electron number supplied by central fuelling and edge fuelling, respectively. τ_p^C and τ_p^E are the confinement time of the central fuelled particle and the edge fuelled particle, respectively. This separation is very important for a design of a future machine. In the steady state without gas-puffing, the recycling coefficient (R) can be

expressed as $R=S_R/(S_R+S_{NB})$, therefore, N_e can be expressed as $N_e=(\tau_p^C+R/(1-R)\tau_p^E)S_{NB}$ using Eqs. (2)-(4). Because R is determined from the divertor conditions such as divertor configuration and pumping speed, it is difficult to control the value of R. Therefore, it is preferable that τ_p^C is comparable to $R/(1-R)\tau_p^E$ in order to obtain the large controllability for the plasma density.

During steady state, Eqs. (2)-(4) are rewritten as $N_e=\tau_p^E(S_R+S_{GP})+\tau_p^C S_{NB}$. This equation means that when there are some data points with the same values of τ_p^E and τ_p^C, a straight line fitted to the data plots of $N_e/(S_R+S_{GP})$ against $S_{NB}/(S_R+S_{GP})$ gives τ_p^C from its gradient and τ_p^E from its y-intercept.

3. Numerical simulation of particle transport

In order to imagine the effect of particle source distribution on the particle confinement, the particle transport was simulated using following equations.

$$\frac{\partial n_e}{\partial t} = -\nabla\cdot\Gamma + s \qquad (5)$$

$$\Gamma = -D\cdot\nabla n_e - v\cdot n_e \qquad (6)$$

$$v = D\cdot C_v\cdot\frac{2r}{a^2} \qquad (7)$$

Where Γ is the particle flux across the magnetic surface, s is the particle source, D and v are the particle diffusion coefficient and the inward pinch velocity, respectively. The inward pinch velocity can be expressed as Eq.(7) using C_v. The values of D and C_v were assumed to be spatial constant values of $0.4m^2/s$ and 2.0, respectively. The source distribution was assumed as follow.

$$s(r/a)=s_{edge}\exp(-((r/a)-1.0)^2/0.07^2) + s_{central}\exp(-((r/a)-0.5)^2/0.7^2) \qquad (8)$$

Figures 1(a) and (b) show the electron density profile and the particle source distribution during steady state phase for the case of s_{edge}=1.0 and $s_{central}$=0.0 (case1) and for the case of s_{edge}=0.0 and $s_{central}$=1.0 (case2). The value of τ_p was estimated to be 0.14s and 0.73s for case1 and case2, respectively, and was different for the same transport coefficients and the different source distribution. In fig. 2, the plus symbols and the open circles show τ_p and N_e/S_{edge}, respectively, as a function of $S_{central}/S_{edge}$, where S_{edge} and $S_{central}$

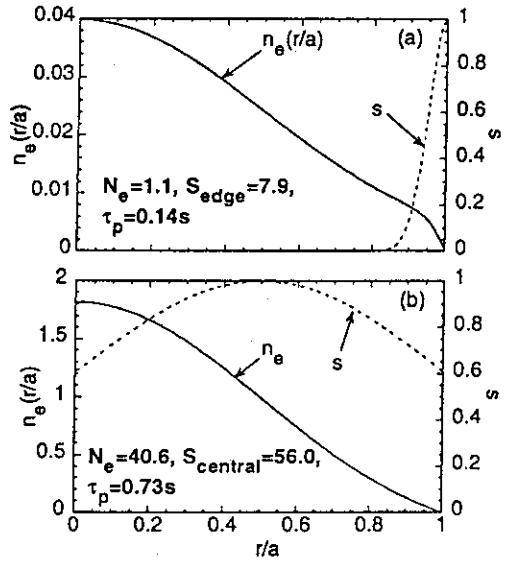

Fig. 1 Calculated electron density profiles for case1 (a) and for case2 (b).

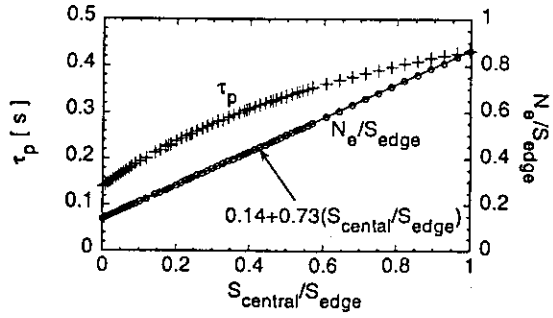

Fig. 2 (N_e/S_{edge})-$(S_{central}/S_{edge})$ plot.

are the volume integrated values of first and second term in Eq. (8). The value of τ_p increased with $S_{central}/S_{edge}$, and the gradient of the straight line fitted to the data of N_e/S_{edge} expresses τ_p for case2, and y-intercept expresses τ_p for case1.

4. Experimental results and discussion

In order to understand the effect of source distribution, the experiment that fuelling rates of NBI and gas-puffing were systematically scanned was performed at I_p=2MA and B_T=3.5T. The calculated Dα emission profile agrees well with the measured one in the divertor region for the case of $n_e=2\times10^{19}m^{-3}$, P_{NB}=6MW and without gas-puffing as shown in fig. 3. In region far from the divertor, the measured intensities are larger than calculated profile, because the neutral particle was released only at the divertor plates in the calculation. However, this difference does not affect S_R, because the Dα emission intensity in region far from the divertor is much smaller than that in the divertor region. Figure 4 shows the particle source distributions. Fuelling rate of wall recycling was substantial in the peripheral region of r/a>0.95, while, fuelling rate of NBI was relatively flat, and was dominant in the central region of r/a<0.4 compared with fuelling rate of wall recycling. The ratio of NBI fuelling rate to wall recycling rate was estimated to be less than 0.1, and the particle confinement time was estimated to be about 0.24s.

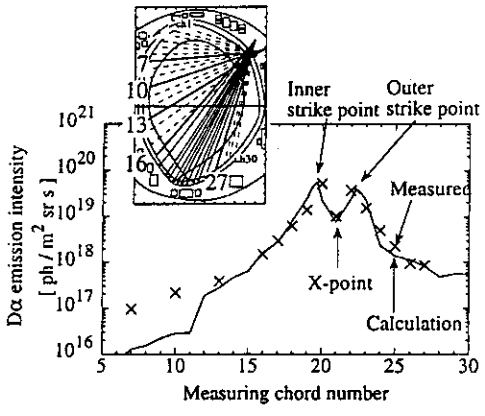

Fig. 3 Dα emission profile as a function of measuring chord number.

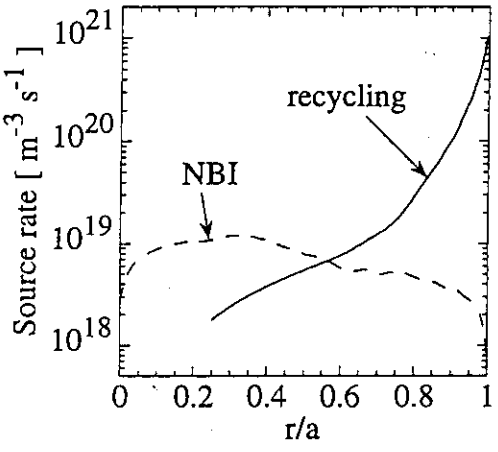

Fig. 4 Source rate distribution.

By changing the NBI power (6-10MW) and the gas-puffing rate (0-4Pam^3/s), $S_{NB}/(S_R+S_{GP})$ was scanned from 0.06 to 0.6 during $n_e=1\text{-}4\times10^{19}m^{-3}$ as shown in fig. 5. The error bar shown in this figure comes from the ambiguity of S_R, S_{GP} and S_{NB} calculations. The correlation of τ_p and $S_{NB}/(S_R+S_{GP})$ was shown in fig. 6. It can be seen from this figure, τ_p increases with $S_{NB}/(S_R+S_{GP})$. This correlation suggests that τ_p^C is larger than τ_p^E as mentioned in section 3.

Next, we try to separate τ_p^C and τ_p^E. Figure 7 shows a $[N_e/(S_R+S_{GP})]$-$[S_{NB}/(S_R+S_{GP})]$ plot for the data where S_{NB} is two times larger than dN_e/dt. The line fitted to the data gives 0.75s for τ_p^C and 0.16s for τ_p^E, and the ratio of τ_p^C/τ_p^E is estimated to be about 5. In the

discussion of section 3, the edge electron density was assumed to be zero, however, for the experimental data, the edge electron density is not zero and tends to be proportional to N_e. When the edge electron density is not zero, the electron density become some value determined by C_v without the particle source. Therefore, the term of the electron number due to edge density must be add in Eq. (4). In this case, because the edge electron density is proportional to N_e, the ratio of τ_p^C/τ_p^E is not changed, however, the values of τ_p^C and τ_p^E become smaller by 20% for C_v=0.0 and by 60% for C_v=2.0, respectively.

In the data analyzed here, the penetration depths of the central fuelling and the edge fuelling are changed from 0.5a to 0.6a and from 0.03a to 0.08a, respectively, because the electron density is not constant. Furthermore, the analysis was performed not only the steady state but also the density increasing phase. Therefore, it is necessary to perform the same analysis during steady state at the constant density in future work.

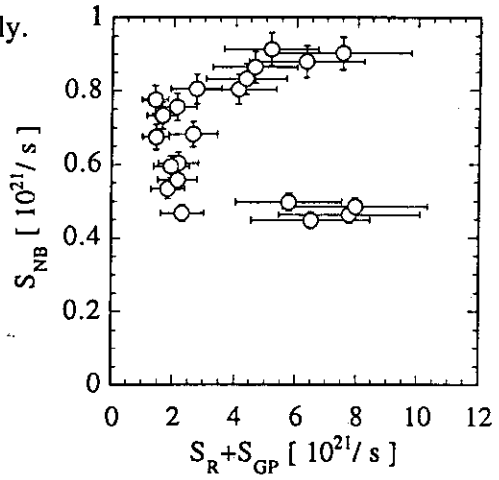

Fig. 5 Relationship S_{NB} and S_R+S_{GP}.

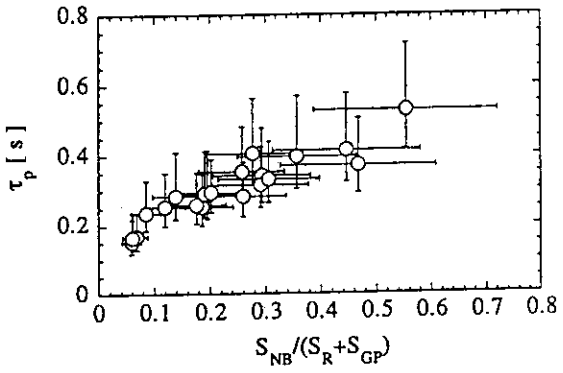

Fig. 6 Correlation of τ_p and $S_{NB}/(S_R+S_{GP})$.

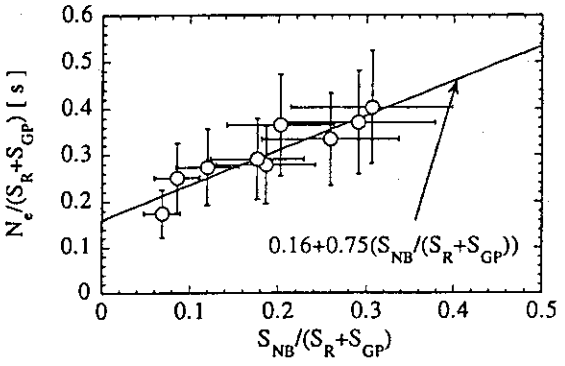

Fig. 7 $(N_e/(S_R+S_{GP}))$-$(S_{NB}/(S_R+S_{GP}))$ plot.

5. Conclusions

The effect of edge and central fuelling on the particle confinement was investigated. It was found that the particle confinement time increased with the ratio of NBI fuelling rate to wall recycling and gas-puffing fuelling rate. The confinement times of edge fuelled particle and central fuelled particle were firstly separated, and it was also found that the confinement time of central fuelled particle was five times longer than that of edge fuelled particle.

References

1) H. Takenaga, et. al., J. Nucl. Mater. 220-222 (1995) 429-432.

2) H. Takenaga, et. al., Nucl. Fusion, Vol. 35, No 7 (1995) 853.

6. Impurities and Divertor
6.1 MARFE Operations and Density Limit

N. Asakura, N. Hosogane, K. Itami, S. Higashijima, S. Sakurai, A. Sakasai

1. Introduction

High density operation with maintaining the good energy confinement is essential requirement for a tokamak reactor to produce enough fusion power. For example, ITER is temporally designed to operate at $\bar{n}_e$ of 1.3×10^{20} m^{-3}, which is by the factor of 1.5 higher than an empirical scaling "Greenwald density limit" ($n^{\rm Gr}[10^{20}\ {\rm m}^{-3}] \equiv I_p/\pi a^2[{\rm MA\ m}^{-2}]$, where a is a minor radius at the midplane), with relatively high enhancement factor (H-factor) of the energy confinement time (more than 2). However, there are few database for such high density operations of the existing tokamaks. In this section, high density operation limit, radiation power fraction in the divertor and the degradation of the H-factor are summarized, in particular, for the ELMy H-mode discharges. An occurrence of the high density disruption in the divertor discharges is also discussed. Divertor plasma detachment and divertor MARFE appear in the high density operation. Details about the divertor plasma and radiation profiles were described in Refs 1 and 2.

2. Divertor MARFE operation

Density limit scaling on net input power P_{net} (or power into the scrape-off layer, $P_{SOL} \equiv P_{net} - P_{rad,main}$) is the most important issue in order to decide the ITER performance and the operation scenario, in which the density limit should be increased with input power to obtain such a high density discharge. At the same time, density at the divertor MARFE onset, $\bar{n}_e^{\rm M}$, is investigated to determine the operation window of the divertor detachment condition, under which the heat flux to the divertor target is significantly reduced. During 1995, wide range scans of NBI power P_{NBI} have been performed in L-mode discharges with P_{NBI} = 2−23 MW (I_p = 1.2−2.5 MA, B_t = 2−4 T), and in ELMy H-mode discharges with P_{NBI} = 6−25 MW (I_p = 1.2 MA, B_t = 2 T) at high $\bar{n}_e$ up to $n^{\rm Gr}$. Deuterium gas is supplied and wall baking temperature is 300°C.

Figure 1 shows a typical ELMy H-mode discharge at high density. The divertor MARFE occurs at 9.1 s, which is found by rapid increases in the radiation power near the divertor X-point and $\bar{n}_e$, decreasing the plasma stored energy, and change in an asymmetry in the recycling profile at the divertor to a symmetric profile. The plasma detachment starts at the divertor separatrix a few 100 ms before the MARFE occurrence. The similar characteristics are observed in L-mode discharges [1,2].

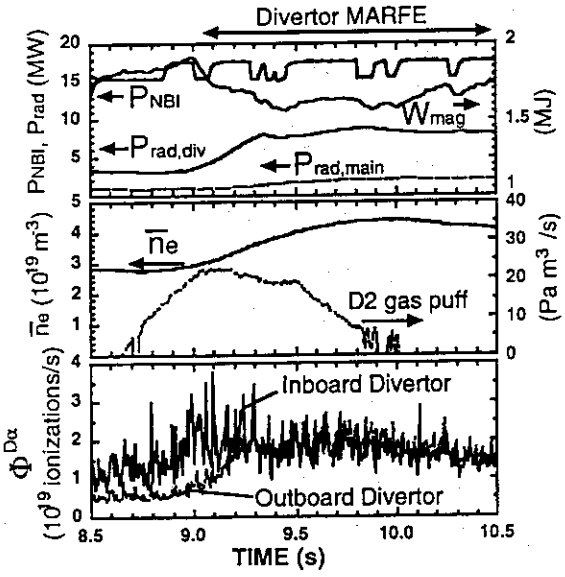

Fig. 1: *Time evolution of the high density ELMy H-mode discharge with P_{NBI} = 16 MW. Divertor MARFE starts at 9.1 s just after break-down of a NB unit.*

Figure 2 shows P_{NBI} dependence of $n_e^{\rm M}$ normalized by $\bar{n}_e^{\rm Gr}$ for the L-mode (I_p = 1.2 MA, B_t = 3.5−4 T, q_{eff} = 7−7.5), and the ELMy H-mode (I_p = 1.2 MA, B_t = 2−2.1 T, q_{eff} = 4.2−4.6). Here, the ion ∇B drift direction for all discharges is towards the divertor.

Open circles represent $\bar{n}_e$ before the MARFE occurrence, where the plasma detachment is proceeding at the inboard divertor separatrix. On the other hand, closed circles shows $\bar{n}_e$ during the divertor MARFE. The maximum $\bar{n}_e$ is limited by the gas puff rate small enough to cause the plasma disruption except for a few cases with low P_{NBI} (triangles).

For the L-mode discharges, $\bar{n}_e^{\rm M}/n_e^{\rm Gr}$ is increased from 0.45 at P_{NBI}= 2 MW to 0.6 at P_{NBI}= 8 MW. There are a few disruptive discharges at $\bar{n}_e^{\rm M}/n_e^{\rm Gr}$ = 0.7−0.9 with P_{NBI}= 2−8 MW. On the other hand, the ratio is increased very weakly from 0.60−0.65 at high P_{NBI} of 8−22 MW. Similar ratio of $\bar{n}_e^{\rm M}/n_e^{\rm Gr}$ (0.55 − 0.65) are observed for the low q_{eff} discharges such as I_p = 1.8 MA (q_{eff}=4.7) and I_p = 2.5 MA (q_{eff}=3.5) cases. When the ion ∇B drift direction is away from the divertor [1,2], $\bar{n}_e^{\rm M}/n_e^{\rm Gr}$ ranges between 0.55 − 0.60 at P_{NBI} = 7 − 15 MW, which are slightly lower than or comparable to the normal B_t results. However, the MARFE operation with completely detached divertor plasma condition can be maintained up to $\bar{n}_e^{\rm Gr}$ without a high density disruption.

ELMy H-mode is obtained with $P_{NBI} \geq$ 6−7 MW at B_t = 2 T. $\bar{n}_e^{\rm M}/n_e^{\rm Gr}$∼0.7 is slightly large compared to that for the L-mode. ELM activities are observed during a MARFE as long as $\bar{n}_e/n_e^{\rm Gr}$ is less than 1 (0.85 for P_{NBI}= 6 MW). Since the energy confinement time is reduced further less, it may be difficult to operate the discharge at $\bar{n}_e$ higher than $\bar{n}_e^{\rm Gr}$. As the results, P_{NBI} dependence of $\bar{n}_e^{\rm M}$ is weak at high $P_{NBI} \geq$ 7 MW, and Greenwald density limit is fairly valid scaling of the high density limit (the latter is not concluded).

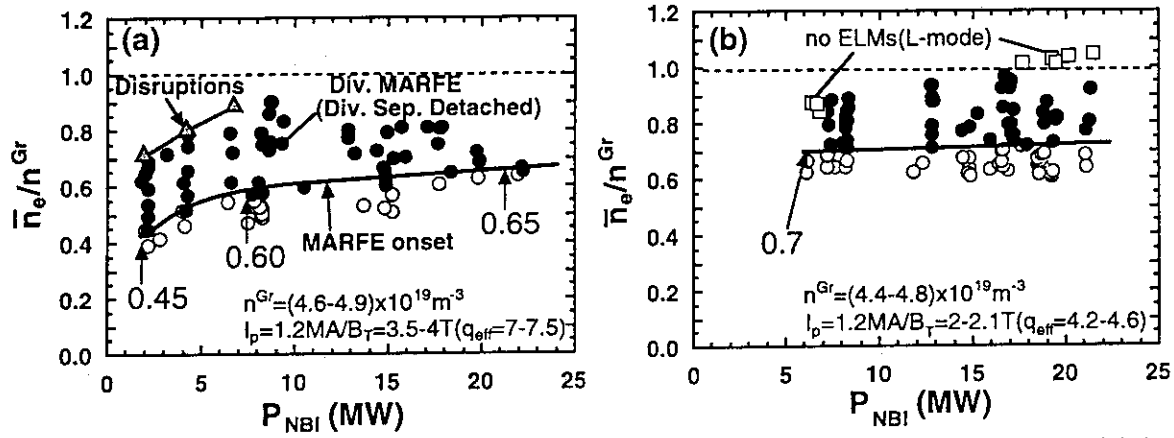

Fig. 2: *P_{NBI} dependence of $\bar{n}_e$ at the divertor MARFE onset: (a) for L-mode and (b) for ELMy H-mode. ELM activities disappear at high $\bar{n}_e$ (squares).*

3. Radiation power in the divertor

Figure 3 shows the fraction of radiation power loss in the divertor, $P_{rad,div}/P_{SOL}$. Database of the ELMy H-mode with P_{NBI} = 10−22 MW is used. When $\bar{n}_e/n^{\rm Gr} \geq$ 0.5, the divertor radiation power fraction raises rapidly from 10% due to a decrease in the electron temperature of the divertor plasma and an increase in the density. At the same time, radiation power fraction of carbon ions (C^{3+}) in $P_{rad,div}$ raises rapidly. At the MARFE onset, $P_{rad,div}/P_{SOL}$ is about 0.4 with varying P_{NBI}, and this is because of an increase in the number of carbon impurities with P_{NBI} increasing.

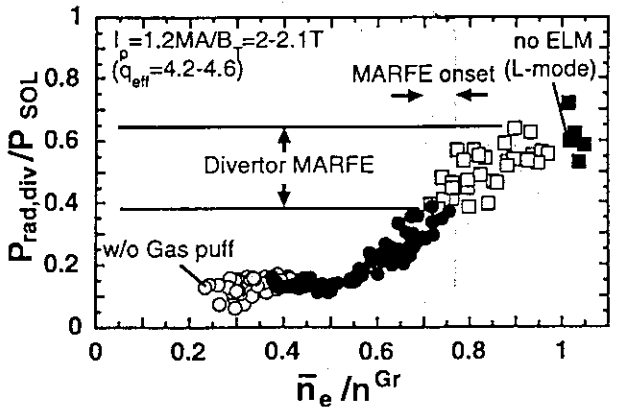

Fig. 3: *Radiation power fraction in the divertor as a function of $\bar{n}_e/n^{\rm Gr}$ with varying P_{NBI} = 10−20 MW for ELMy H-mode discharges: squares represent during MARFEs.*

During the MARFE, the radiation power fraction in the divertor is increased up to 55−65%, and it is finally saturated when $\bar{n}_e/n^{Gr} = 0.9-1$. The bolometer array measurement shows that the radiation region is moving from the divertor region into the main plasma near the X-point, causing the reduction of the electron temperature inside the last closed magnetic flux surface (LCFS). Shrinking of n_e and T_e profiles inside the LCFS is measured with the Thomson scattering. However, a mechanism to generate the large pressure gradient in the plasma boundary (causing the ELM activities) is still maintained.

4. Energy confinement degrading

Degradation of the energy confinement at high $\bar{n}_e$ is the most unpredictable problem to determine the reactor performance [1]. It may be caused by increasing the neutral density in the plasma boundary. The effect is not included in existing confinement scalings. Figure 4 shows the H-factor of the ELMy H-mode from the ITER89 L-mode power scaling. With increasing the gas puff rate, neutral recycling in the divertor is enhanced substantially and $\bar{n}_e$ is increased. The H-factor is reduced with $\bar{n}_e$ from 1.9 to 1.2 for the high P_{NBI} case, and from 1.7 to 1.0 for the low P_{NBI}. This is correlated with the reduction of T_i at the plasma edge (inside LCFS), degrading the transport barrier in the boundary plasma.

Figure 4(b) shows that the H-factor is reduced with increasing the neutral recycling in the main plasma boundary, $\Phi^{D\alpha}_{main}$. Whereas $\Phi^{D\alpha}_{main}$ is an order of magnitude smaller than the neutral recycling in the divertor, $\Phi^{D\alpha}_{main}$ is by the factor of 7−12 larger than the deuterium fuelling rate (maximum value of 1.3×10^{22} s^{-1}). Thus, large number of neutrals in the plasma boundary are provided from the divertor chamber. Baffle plates and tilted divertor target of JT-60U W-type divertor are designed to reduce the neutral backflow.

When the divertor MARFE occurs, the H-factor is further reduced to 1−1.1. Finally, it is decreased to 0.8 when the ELM activities disappear at around the Greenwald density. This caused by the reduction of the edge plasma temperature due to penetrating the MARFE inside LCFS and by deterioration of the impurity shielding effect of the divertor/SOL plasma. Installing the private dome in the W-type divertor is also an important requirement to maintain the MARFE in the divertor chamber by suppressing the carbon ion penetration near the X-point.

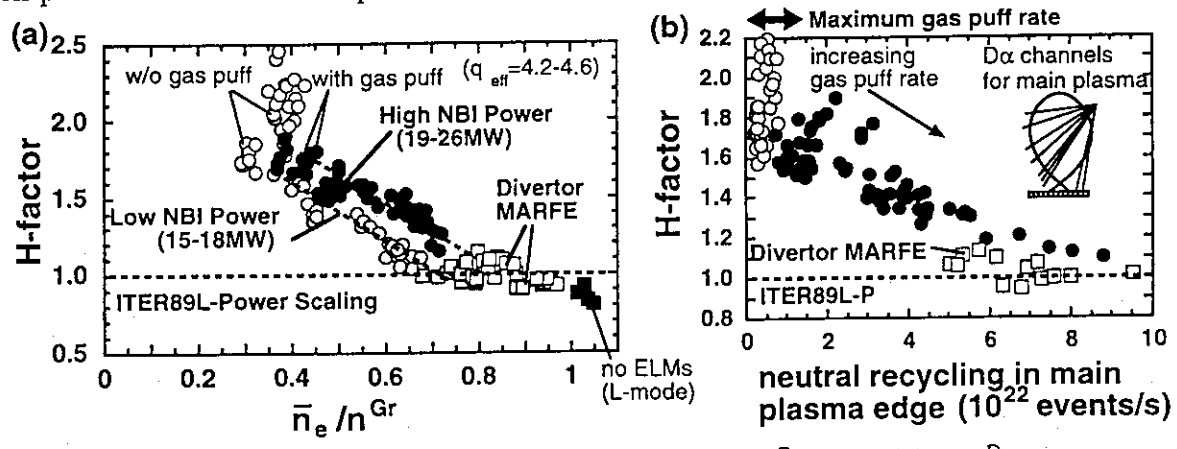

Fig. 4: *H-factors for ELMy H-mode discharges (a) vs* $\bar{n}_e/n_e^{Gr}$ *, and (b) vs* $\Phi^{D\alpha}_{main}$.

5. High density disruption

High density disruptions are observed in low P_{NBI} L-mode discharges at less than n_e^{Gr}. Figure 2(a) shows that $\bar{n}_e/n_e^{Gr} = 0.7$, 0.8 and 0.9 for $P_{NBI} = 2$, 4 and 8 MW, respectively.

Density limit tends to rise with heating power up to 8 MW. Common behaviour of the edge plasma preceding the disruption is described.

During the divertor MARFE, the edge plasma is shrinking inside the LCFS. Figure 5 shows that the edge pedestal of n_e profiles measured with the Thomson scattering moves inward from $r/a = 0.98$ to 0.90 and that n_e at the LCFS is reduced. At the same time, n_e in the core plasma ($r/a \leq 0.6$) is increasing, and n_e profile becomes peaked. Plasma internal inductance l_i is raised from 1.3 to 1.42. They are caused by the MARFE penetrating into the main plasma (inside the LCFS), degrading the edge confinement.

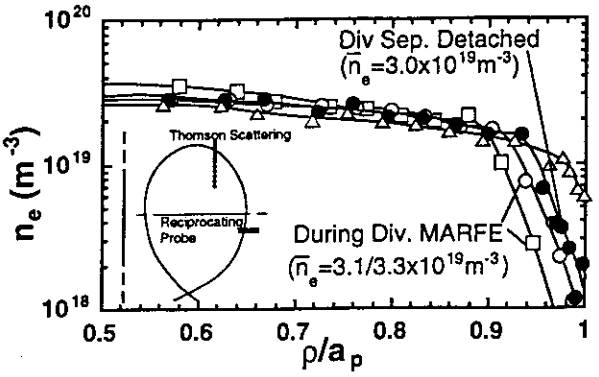

Fig. 5: *Electron density profiles during the divertor MARFE for L-mode discharges with P_{NBI}= 4 MW.*

Figure 6 shows expanded waveforms just before a high density disruption, where P_{NBI} = 8 MW. Thermal collapse starts at 9.44 s. It occurs even when the fraction of $P_{rad,main}$ is still much smaller than P_{NBI} (e.g. about 20% of P_{NBI}), and total radiation power in the divertor and main plasma is maintained at 60−80% of P_{NBI}. Thus, the trigger of the disruption can not be explained by the collapse of the power balance at the plasma boundary, which was reported in JT-60 limiter discharges.

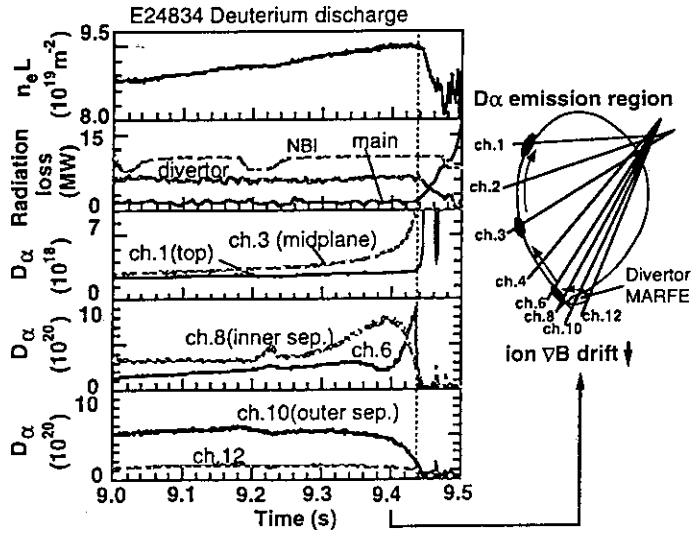

Fig. 6: *Time evolution of $\bar{n}_e$, $P_{rad,main}$, $P_{rad,div}$ and D_α signals for 0.5 s before the high density disruption. P_{NBI} = 8 MW.*

Before the thermal collapse occurs, maximum ionization region, measured with D_α scope, moves quickly from the outboard divertor through the X-point to the high field side. It reaches plasma's top before $P_{rad,main}$ suddenly rises larger than P_{NBI}. These suggests that a poloidal asymmetry in the radial or parallel transport of the boundary plasma changes before the collapse of the power balance due to the edge cooling.

6. Summary

Density limit and $\bar{n}_e^{\mathrm{M}}$ are increased with P_{NBI} up to 8 MW. However, it will not survive so far above n_e^{Gr} at high P_{NBI} (8−22 MW) for the open divertor configuration, since the energy confinement is degraded less than L-mode level and the edge plasma is shrinking inside the LCFS. Density limit study for the high P_{NBI} will be done in 1996.

References:

1) Asakura N., *et al.*: Proc. 15th Int. Conf., 1994, Vol. I, IAEA, Vienna (1995) 515.
2) Asakura N., *et al.*: "Field reversal effects on divertor plasmas under radiative and detached conditions in JT-60U", to be published in Nucl. Fusion.

6.2 SOL Profile Study in High Density Discharges

N. Asakura, S. Tsuji-Iio[1], K. Itami, N. Hosogane, S. Sakurai

1. Introduction

Database of scrape-off layer (SOL) plasma profiles in the high density discharges is essential to design the ITER divertor, and to understand the mechanism of the divertor plasma detachment along the magnetic field line. The SOL plasma profiles between the last closed magnetic flux surface (LCFS) and the first wall at the midplane have been measured with a fast reciprocating probe system [1]. The characteristic lengths (e-folding length) of the profiles and parallel temperature and density gradients under the high density and detached divertor conditions are summarized. Details of the divertor plasma and radiation profiles under the detached divertor condition and during the divertor MARFE were described in Ref. 2. Results of the SOL profile measurements during ohmic heating were presented in Ref. 3.

2. SOL profiles

The fast reciprocating probe measurements were performed in the L-mode discharges with $P_{NBI} = 4$MW, and line-averaged density $\bar{n}_e$ was varied on a shot by shot basis. A series of high safety-factor discharges ($q_{eff} = 7.2$–7.7, $I_p = 1.2$ MA, $B_t = 3.5$–4 T and the plasma volume of 80 m^3) were used for the detail $\bar{n}_e$ scan. Profiles were also measured in the low q_{eff} discharges such as $I_p/B_t = 1.2$ MA/2.1 T ($q_{eff} = 4.3$) and $I_p/B_t = 1.8$ MA/3.5 T ($q_{eff} = 4.7$). Results of the high q_{eff} discharges are presented in this section.

The probe head is inserted horizontally at 36 cm below the equatorial plane. Double probe method is used for the profile measurement, and a triangle-waveform voltage with the period of 3 ms is applied. Fig. 1 shows the electron density, n_e, and temperature, T_e, profiles, and Fig. 2 explains the change in the n_e profile with $\bar{n}_e$ increasing. Two (i.e. inner and outer) SOL regions with different characteristic lengths are observed both in the T_e and n_e profiles. The inner SOL extends up to a few cm outside the LCFS, and the n_e and T_e profiles have small e-folding lengths: λ_{n_e} and λ_{T_e} of 2 cm and 3 cm, respectively. They are approximately constant with increases in $\bar{n}_e$ and the local density at the magnetic separatrix $n_{e,sep}$.

On the other hand, for the outer SOL region, large λ_{n_e} (3-10 cm) and λ_{T_e} (6-15 cm), which are increased with an increase in $\bar{n}_e$, are observed. At the same time, the outer SOL region extends to the LCFS, and the inner SOL is shrinking as shown in Fig. 2. Density dependence of the e-folding lengths on $\bar{n}_e$ is shown in Fig. 3.

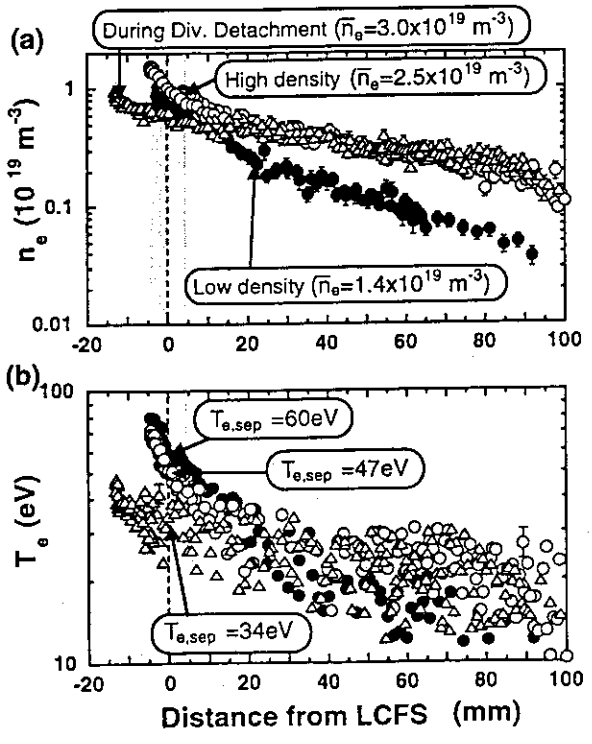

Fig. 1: *(a) n_e and (b) T_e profiles for the high q_{eff} (= 7.2) discharges with $\bar{n}_e$ increasing.*

[1]Present address: Research Laboratory for Nuclear Reactors, Tokyo Institute of Technology.

Fluctuations of $\tilde{n}_e/n_e$ and $\tilde{T}_e/T_e$ are measured with the triple probe method. Fluctuation levels are different in the inner and outer SOL regions. In particular, low frequency components ($1 \leq f \leq 10$ kHz) $\tilde{n}_e/n_e$ and $\tilde{T}_e/T_e$ are 20−40% in the inner SOL. They are smaller than those in the outer SOL ($\tilde{n}_e/n_e$ and $\tilde{T}_e/T_e \geq 50\%$). Large scatter of data in the outer SOL, using the double probe method as shown in Fig. 1, is affected by the large fluctuation level in the low frequency components.

When the plasma detachment occurs at the divertor separatrix, the local density, $n_{e,sep}$, and temperature, $T_{e,sep}$, are reduced. While n_e and T_e profiles in the outer SOL stay at the same levels. Thus, the n_e and T_e profiles have large λ_{n_e} (10cm) and λ_{T_e} (15 cm) between the LCFS and the first wall.

With $\bar{n}_e$ increasing, a MARFE occurs near the divertor X-point ("Divertor MARFE"). During the divertor MARFE, shrink of the edge plasma inside the LCFS is observed. Thomson scattering results (Fig. 5 in Sec. 6.1) show that the edge pedestal of n_e profile moves inward from $r/a = 0.98$ to 0.90, and $n_{e,sep}$ is reduced. While, n_e in the core plasma region ($r/a \leq 0.6$) is increasing, n_e profile becomes peaked. It is presumably caused by the divertor MARFE penetrating into the main plasma (inside LCFS), and degrading the edge plasma confinement in $r/a \geq 0.90$.

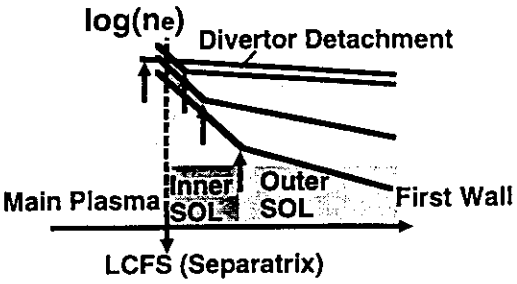

Fig. 2: *Illustrating the change in n_e profile with $\bar{n}_e$ increasing.*

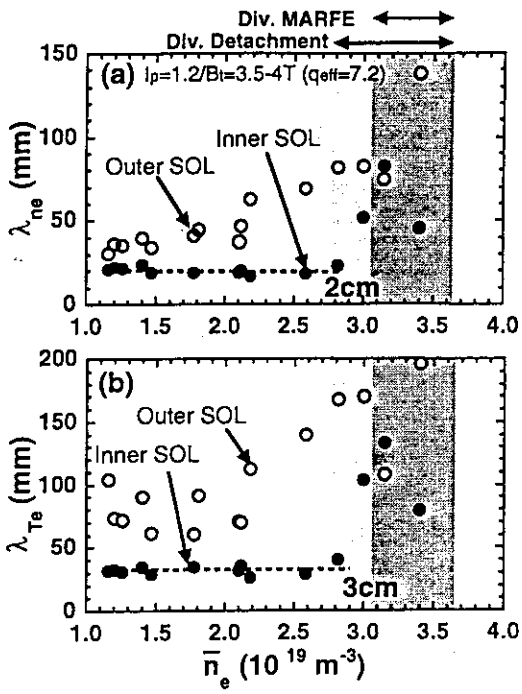

Fig. 3: *e-folding lengths of (a) n_e and (b) T_e profiles in the inner and outer SOLs as a function of $\bar{n}_e$.*

At the same time, cross-field transport is enhanced in the SOL region. The fast reciprocation probe measurements show that n_e and T_e in the SOL region ($d \leq 40$ mm) are reduced, and that λ_{n_e} and λ_{T_e} in the region ($10 \leq d \leq 40$ mm, and they plotted as the outer SOL) are increased to 14 cm and 20 cm, respectively. While, local λ_{n_e} and λ_{T_e} near the separatrix (plotted as the inner SOL) are decreased.

3. q_{eff} dependence of e-folding length

In this section, λ_{n_e} and λ_{T_e} for the low q_{eff} discharges are compared to those for the high q_{eff} discharges. Different combinations of I_p and B_t (I_p/B_t = 1.2 MA/2.1 T and 1.8 MA/3.5 T) are chosen for the low q_{eff} discharges. Figure 4 shows λ_{n_e} and λ_{T_e} in the inner SOL region as a function of $T_{e,sep}$. Squares, circles and triangles correspond to the discharges for I_p/B_t = 1.2 MA/3.5−4 T, 1.2 MA/2.1 T and 1.8 MA/3.5 T, respectively.

When $T_{e,sep} \geq 45$ eV, e-folding lengths stay at the relatively constant levels. For the case of the low q_{eff} discharges, λ_{n_e} and λ_{T_e} range between 1.0 − 1.3 cm and between 1.7−2.5 cm, respectively. These values are by the factor of 1.5−2 smaller than those for the high q_{eff} discharges, which is explained by the shorter connection length along the magnetic field line.

Both λ_{n_e} and λ_{T_e} increase below $T_{e,sep}$ = 45 eV, and the plasma detachment is proceeding near the divertor strike point below $T_{e,sep} \sim 40$ eV independent of q_{eff}. The divertor MARFE occurs below $T_{e,sep}$ $\sim$ 30 eV for the high q_{eff} case. During the divertor MARFE, the local e-folding length at the separatrix is decreased due to large reduction of n_e and T_e in the SOL region rather than those inside LCFS. For the case of the low q_{eff} cases, data was not obtained in the series of experiments.

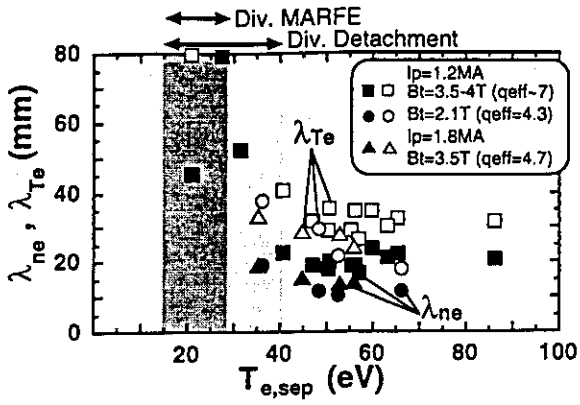

Fig. 4: *λ_{n_e} and λ_{T_e} in the inner SOL region as a function of $T_{e,sep}$.*

4. SOL and divertor plasmas

Electron pressure profiles at the midplane ($p_{e,mid} = n_{e,mid}T_{e,mid}$) are compared to those measured at the outboard divertor target ($p_{e,div} = n_{e,div}T_{e,div}$) measured with the divertor dome-type probes. Figure 5 shows the profiles of $p_{e,mid}$ and $p_{e,div}$, which are plotted on the same magnetic flux surfaces.

When the divertor plasma attaches the target plate (a), electron pressure is approximately constant along the magnetic field lines within the error bars of the fitting. Electron temperature and density are also constant for the low density case ($\bar{n}_e$ = 1.8 × 10^{19}m^{-3}). The electron pressure is kept approximately constant in the high density discharges, where $T_{e,div}$ is lower than $T_{e,mid}$ and $n_{e,div}$ is higher than $n_{e,mid}$.

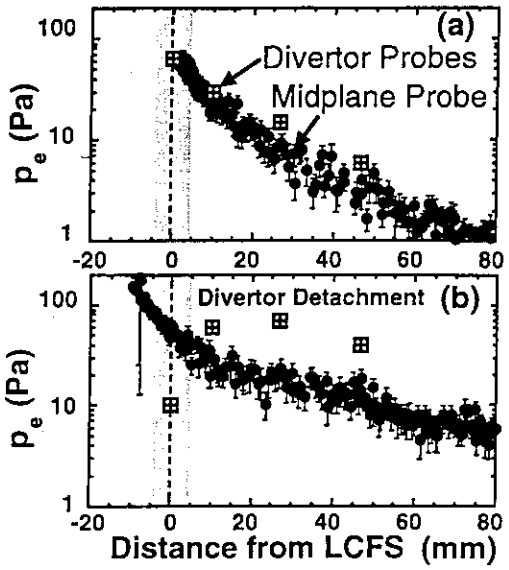

Fig. 5: *Electron pressure profiles at the midplane (circles) and at the outboard divertor target (squares); under (a) attached and (b) detached divertor plasma conditions.*

Here, the dynamic pressure due to the sound-speed flow near the divertor target, which increases total plasma pressure by a factor of two, is not considered. Assuming that T_i at the midplane is by a factor of 3 larger than T_e, and that they become comparable at the divertor target due to the large collisionality of the ions in the parallel transport, total plasma pressure balance is satisfied.

Figure 5(b) shows that the divertor plasma is detached at the divertor separatrix. This is due to large reduction of $n_{e,div}$ rather than $T_{e,div}$. On the other hand, the electron pressure on the outer flux surfaces is increased significantly, due to an increase of $n_{e,div}$. These facts clearly violating constant pressure along the magnetic field lines. Increases rates of charge exchange events and elastic collisions between the plasma ions and the recycled neutrals are an acceptable candidate to explain the momentum loss at the divertor target. Since mean-free-path of the neutral ionization is about 10 cm for $T_{e,div}$ = 10 eV and $n_{e,div}$ = 3 × 10^{19}m^{-3}, re-ionization of the neutrals lost from the inner flux surfaces through charge exchange process may occur in the divertor, causing the increase in the ion flux at the outer magnetic surfaces.

Figure 6 shows the evolution with $\bar{n}_e$ of electron temperature, density and pressure at the divertor target and midplane near the separatrix. Since it is difficult to identify that the divertor probe is located on the separatrix due to the error of the magnetic equilibrium

calculation (~5 mm), two values for the divertor plasma parameters are plotted; one is an average value measured with two probes close to the separatrix, and another is with the first probe outside the separatrix.

At low density, $\bar{n}_e \leq 1.5 \times 10^{19}\mathrm{m}^{-3}$, electron temperature, density and pressure are constant along the magnetic field line. Neutral recycling and radiation power in the divertor are small. At moderate density, $2.0 \times 10^{19} \leq \bar{n}_e \leq 2.7 \times 10^{19}\mathrm{m}^{-3}$, $T_{e,div}$ falls relative to high $T_{e,mid}$, while $n_{e,div}$ rises rapidly. At the same time, the ratio of the neutral ionization rate in the divertor, $\Phi^{D\alpha}_{div}$, to that in the main plasma, $\Phi^{D\alpha}_{main}$, which corresponds approximately to the flux amplification factor in the divertor, is enhanced from 2 to 4. The flux amplification factor is relatively small due to the low input power of 4 MW.

At high density, $\bar{n}_e \geq 2.8 \times 10^{19}\mathrm{m}^{-3}$, the temperature gradient along the magnetic field line is increased, and the divertor MARFE occurs when $T_{e,mid} = 30$ eV and $T_{e,div} = 10$ eV. During the divertor MARFE, where the plasma detachment extends from the divertor separatrix to the outer flux surfaces, both $p_{e,mid}$ and $p_{e,div}$ are reduced. The critical $T_{e,mid}$ and $T_{e,div}$ at the MARFE onset are similar for the lower q_{eff} discharges (shorter connection length). This is not explained simply by 1D parallel transport model.

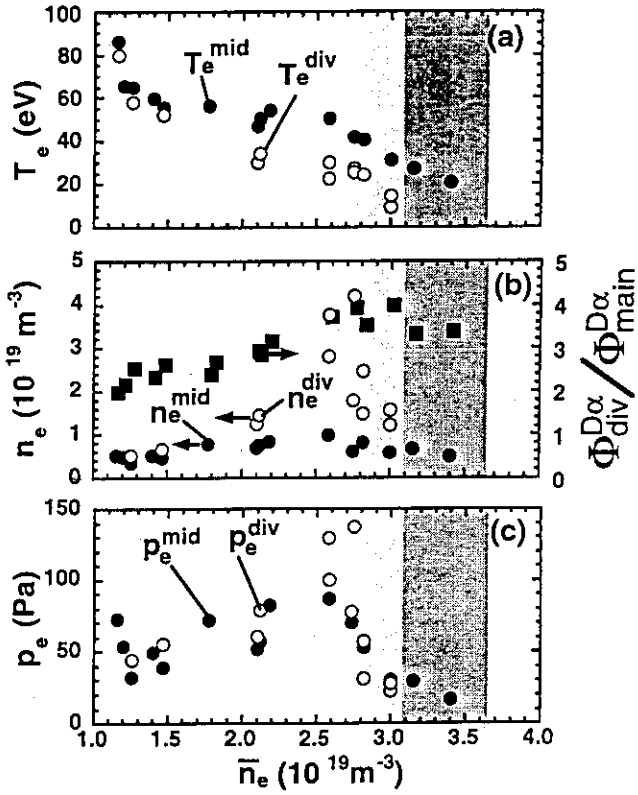

Fig. 6: *Electron temperature, density and pressure at the midplane (open circles) and at the outboard divertor target (closed circles) for I_p= 1.2 MA, B_t= 3.5−4 T. Ratio of neutral ionization rate in the divertor and that in the main plasma is plotted by squares.*

5. Summary

The SOL plasma profiles were investigated in NBI L-mode discharges. Inner and outer SOL regions with different e-folding lengths are observed both in the T_e and n_e profiles. Common behaviours of the SOL profiles are found. (1) the outer SOL is extending to the LCFS with $\bar{n}_e$ increasing, and e-folding lengths of the profiles are increased. Candidates which cause the broadening of the SOL plasma such as density/potential fluctuations and interaction with increasing neutrals are under investigation. (2) p_e profiles at the midplane and at the divertor target are comparable. (3) $T_{e,mid}$ and $T_{e,div}$ at the MARFE onset are similar for the different q_{eff} discharges. Total plasma pressure balance and heat transport along the magnetic field line are analyzed using a simple divertor code.

References:

1) Asakura N., *et al.*: Rev. Sci. Instrum. **66**, 5428 (1995), and Sec. 12.8 in this report.
2) Asakura N., *et al.*: "Field reversal effects on divertor plasmas under radiative and detached conditions in JT-60U", to be published in Nucl. Fusion.
3) Asakura N., *et al.*: Abstracts of the 50th meeting of the Physical Society of Japan, Yokohama, Part 4 p.140 (1995) in Japanese.

6.3 Active Control of Helium Exhaust on ELMy H-mode

A. Sakasai, H. Kubo, S. Sakurai, S. Higashijima, N. Asakura

1. Introduction

Helium (He) exhaust has been studied on ELMy H-mode using He beams and a short pulse He gas puff. Helium and deuterium recycling flux profiles in the divertor was measured with a divertor visible spectrometer to investigate the in-out asymmetry with He flux. Active He removal with ICRF heating and ripple loss was tried in the hydrogen operation for the first time.

For the He exhaust, it is desirable that fueling particle and He ash can be selectively exhausted and He ash can be effectively exhausted from the outboard divertor. The divertor operation with higher He pressure in the outboard divertor is very beneficial because of longer toroidal length and more space for pumping system. The selective exhaust between fuel and ash is very important from a viewpoint of the burning control.

2. In-out asymmetry of He flux

The D flux on the inner target in the divertor was larger than one on the outer target and the in-out asymmetry was studied in L-mode and ELMy H-mode on JT-60U[1]. However, the asymmetry with He flux has not been investigated in JT-60U and the other devices yet . It is an important issue to control He ash exhaust. The in-out asymmetry with He flux in the divertor was investigated and controlled by changing of NB power and Ip.

Recycling influx profiles of deuterium and helium ions in the divertor region were measured with spectroscopic diagnostics viewing a wide divertor area which was composed of a 60-channel optical fiber array modified from a 38-ch array in JT-60U. It is possible to measure He and D flux in ELMy H-mode discharges with high X-point configuration(Xp=20 cm) to study the in-out asymmetry of He flux in the divertor.

2.1 Normal B_T with He gas puff

Helium exhaust experiment was carried out in ELMy H-modes with H-factor=1.7 - 1.4. The discharge conditions were I_P=1.0MA/B_T=2.5T(q_{eff}=6.2), 1.4MA/3.5T(q_{eff}=6.0), 1.7MA/2.5T(q_{eff}=3.5), 1.5MA/2.5T(q_{eff}=3.9), 1.7MA/3.5T(q_{eff}=4.8) and Vol=60 m^3 with P_{NB}=18 MW and He gas puff 5 Pa.m^3/s x 0.2 s to obtain the dependence of q_{eff}, I_P and B_T. The Helium exhaust experiment was also carried out in L-mode with the same configuration and high n_e under the condition of 1.7 MA/3.5 T, (q_{eff}=4.8) and P_{NB}=10 MW.

Figure 1 shows the He I (728.1 nm) brightness (He flux) and Dα brightness (D flux) profiles in the divertor in the cases of (a): I_P=1.0 MA, B_T=2.5 T, P_{NB}=18 MW and (b): I_P=1.7 MA, B_T=3.5 T, P_{NB}=18 MW. The He flux on the outer target in the divertor was

larger than one on the inner target as shown in Fig.1 (a). On the other hand, the He flux on the inner target in the divertor was larger than one on the outer target in the case of high I_P as shown in Fig.1 (b). The in-out asymmetry with the outboard enhanced He flux was remarkable in ELMy H-mode with high NB power heating.

It was found that the asymmetry with the outboard enhanced He flux occurred near the condition of I_P=1.0 MA, B_T=2.5 T, P_{NB}=18 MW and β_P=1.8 from the result of I_P and B_T scan. The asymmetry seems to depend on β_P (including edge parameters: n_e, T_e, T_i et al.). In the condition of β_P<1.8, the asymmetry was marginal or changed to the asymmetry with the inboard enhanced He flux.

2.2 Reversed B_T with He gas puff

The effect of the ion grad-B drift direction on the in-out asymmetry with the He flux was investigated in the condition of reversed B_T and I_P with He gas puff. Figure 2 shows the He I brightness and Dα brightness profiles in the divertor in the cases of I_P=1.0 MA, B_T=2.5 T, P_{NB}=18 MW with the reversed B_T and I_P. The inner He flux was larger than the outer flux with only this condition in ELMy H-mode. On the other hand, the inner He flux was less than the outer flux with other conditions. The reversed effect on the in-out asymmetry with the He flux profiles was not observed. This result indicates that the asymmetry with the He flux profiles do not depend on the ion grad-B drift direction.

However, the in-out asymmetry with the D flux was changed in the reversed B_T and I_P. The outer D flux was larger than the inner flux with the above all conditions in ELMy H-mode. The reversed effect on the in-out asymmetry with the D flux was clearly observed[1]. The He flux profiles were very narrow as compared with D flux profiles. This result of B_T and I_P reversal was interested in the causality and mechanism.

2.3 Normal B_T with ^{4}He Beam injection

The in-out asymmetry with He flux was investigated using 60 keV ^{4}He beams (P_{HeNB}=2.4 MW) with the normal B_T in ELMy H-mode.

The I_P scan was performed in the condition of 1.0 MA/2.5 T, 1.2 MA/3.0 T, 1.3 MA/3.25 T, 1.4 MA/3.5 T to make clear the dependence of I_P on the asymmetry with the same q_{eff}. The He flux towards the outboard target was gradually decreased and the He flux towards the inboard target was gradually increased in the case of higher I_P than 1.0 MA. And the scan of NB power was also performed in the condition of P_{NB}=18, 14, 12, 10 MW (1.0MA/2.5T) to make clear the dependence of P_{NB} on the asymmetry.

Figure 3 shows the comparison of the He I brightness and Dα brightness profiles in the divertor between (a): I_P=1.0 MA, B_T=2.5 T, P_{NB}=18 MW (b): I_P=1.3 MA, B_T=3.25 T, P_{NB}=18 MW and (c): I_P=1.0 MA, B_T=2.5 T, P_{NB}=10 MW in ELMy H-mode in the case of He beam injection. The asymmetry with the outboard enhanced He flux was observed with P_{NB}=18 MW as shown in Fig.3 (a). In the case of P_{NB}=10 MW, it changed to the asymmetry with the inboard enhanced He flux as shown in Fig.3 (c). The He flux towards

the outer target was gradually decreased with the lower NB power from the result of NB power scan.

The He concentration, He flux and the He pressure reduced to 1/2, 1/10 and 1/3 respectively with the He removal by wall pumping due to a Solid Target Boronization discharge (STB)[2]. STB means that the outer divertor strike point hits 300-μm thick B_4C converted CFC (Carbon Fiber Composite) tiles and B_4C layers evaporate and deposit in the discharge. Helium ash could be effectively exhausted in combination with the control of the asymmetry and the He removal due to the STB.

3. Helium Exhaust with ICRF

Active He removal with ICRF heating and ripple loss was performed on the first trial in the hydrogen operation. The operation condition is I_P=1.1 MA/B_T=3.244 T, Vol=83 m^3, P_{NB}=13 MW (or No H-NB), P_{HeNB}=1.6 MW, P_{IC}=3.8 MW and $6\omega_{CHe}$ IC resonance layer was located on R=4.21 m. In this experiment, the IC resonance layers of $\omega_{CHe} = \omega_{CD} = 0.5\omega_{CH}$ were very complicated to obtain the ^{4}He acceleration. This problem was a matter of concern.

Actually, the ^{4}He acceleration could not be observed with a charge exchange neutral particle analyzer. However, the H acceleration was observed well. It seem that the IC power is almost absorbed for H acceleration ($3\omega_{CH}$). Because He recycling flux was increased with ICRF heating, the He density in the core and edge plasma was increased. Active He removal with ICRF heating and ripple loss in the D operation phase is planned in the deuterium opeartion with no hydrogen and low He recycling in 1996.

4. Conclusions

In-out asymmetry with He influx in the divertor has been controlled by changing of neutral beam (NB) power and plasma current (Ip). The effect of the ion grad-B drift direction and Ip and BT (q_{eff}) dependence on He exhaust was investigated in ELMy H-mode and L-mode. The asymmetry with the He flux profiles do not depend on the ion grad-B drift direction. The asymmetry seems to be determined by β_P (including edge parameters: n_e, T_e, T_i et al.) and not be explicitly determined by NB power and I_P. Helium ash exhaust could be actively controlled in combination with the control of the asymmetry with He flux and He removal due to the STB. This result suggests that the selective exhaust, for example He ash removal from the outboard and fueling particle removal from the inboard, is possible to control the burning of core plasma in future reactors.

References

[1] N. Asakura et al. et al.., IAEA Seville 1994, IAEA-CN-60/A-4-I-3.

[2] A. Sakasa et al. et al.., IAEA Seville 1994, IAEA-CN-60/A-2/4-P-12.

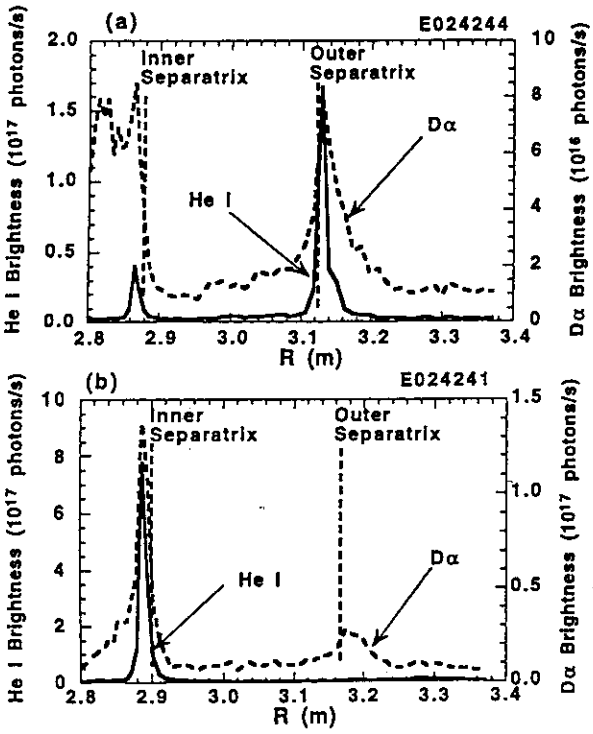

Fig. 1. Comparison of the He I brightness (He flux) and Dα brightness (D flux) profiles in the divertor between
(a): Ip=1.0 MA, B_T=2.5 T, P_{NB}=18 MW and
(b): Ip=1.7 MA, B_T=3.5 T, P_{NB}=18 MW.

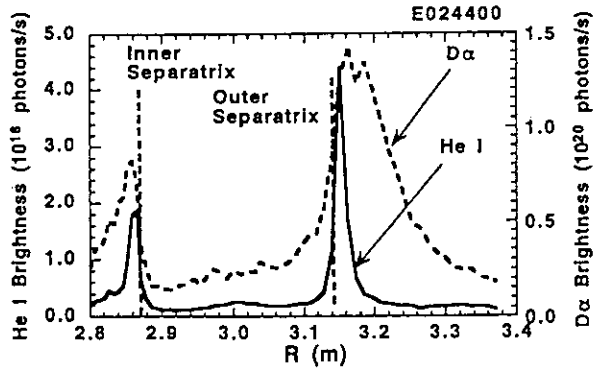

Fig. 2. The He I brightness and Dα brightness profiles in the divertor in the cases of Ip=1.0 MA, B_T=2.5 T, P_{NB}=18 MW with the reversed B_T and Ip.

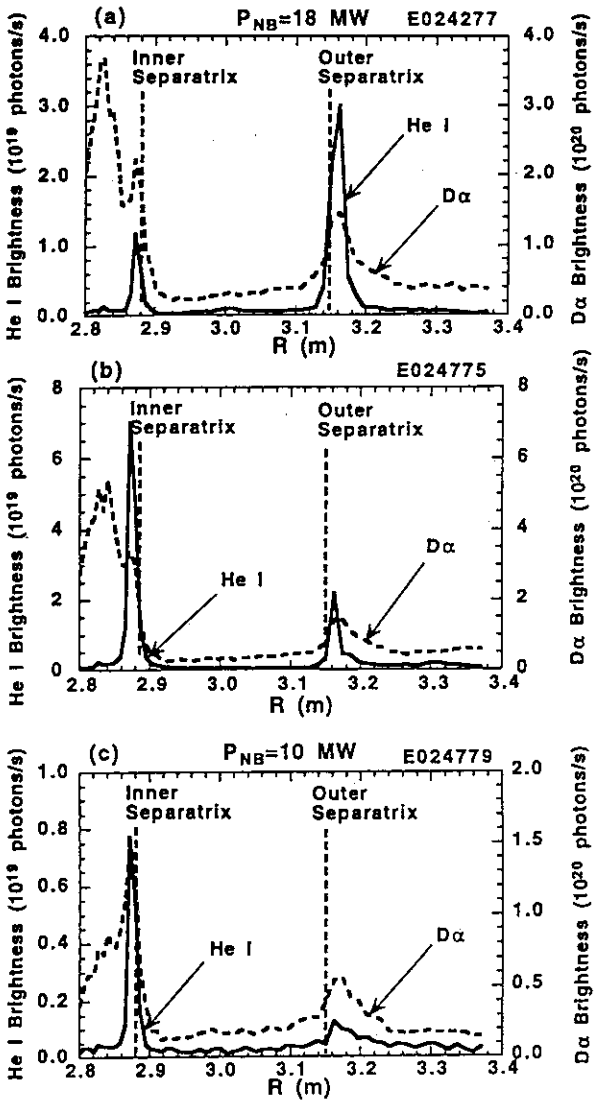

Fig. 3. Comparison of the He I brightness and Dα brightness profiles in the divertor between
(a): Ip=1.0 MA, B_T=2.5 T, P_{NB}=18 MW,
(b): Ip=1.3 MA, B_T=3.25 T, P_{NB}=18 MW and
(c): Ip=1.0 MA, B_T=2.5 T, P_{NB}=10 MW
in ELMy H-mode.

6.4 Radiative divertor plasma with Neon injection

K. Itami, N. Hosogane, N. Asakura, A. Sakasai

1. Introduction

In order to obtain the core plasmas with high ion temperature, it is important to suppress particle recycling to low revel around the main plasma , as well as operating plasmas in improved confinement mode. It is becoming difficult to produce cold, dense and radiative divertor plasmas due to high heat flux density to the divertor and high temperature in the scrape off layer under sucn conditions. Major part of efforts in divertor study in recent tokamak devices are recently devoted to the radiative divertor experiment by impurity gas puff. In ASDEX Upgrade tokamak, complete detachment at the divertor plasma was obtained during ELMy H-mode without degradation of the core plasma confinement. Demonstration of significant reduction of heat flux at the divertor due to the enhanced radiation loss from the boundary attracted attentions and the concept of radiative divertor by impurity puffing is recognized as an alternative of gas target divertor concept of ITER. Radiative divertor experiments by impurity gas puffing were carried out in March, July and September, in 1995. A part of the results was presented at the 22nd EPS conference at Bounemouth, UK.[1].

2. Experimental results

The purpose of this study is to investigate the compatibility of high ion temperature in ELMy H-mode plasmas that are produced at the low particle recycling conditions and the radiative divertor plasmas by utilizing neon as seed impurity to enhance radiation loss from the plasma. In order to compare effecs on divertor plasma parameters by a various Neon gas and D_2 gas puff sequences, ELMy H-mode plasmas with Ip = 1.2MA, B_T = 2T and P_{NB} = 15MW were produced at the low particle recycling conditions as target discharges. A synagistic effect of the neon gas puff followed by deuterium gas puff was found on the enhancement of radiation loss and particle flux at the divertor . In Fig.1(a), the increment of the radiation loss from the main and divertor plasmas after four kinds of the gas puff sequences is shown. after the . These sequences indexed as "Neon Only", "D_2 Only", "Neon + D_2" and "D_2 + Neon" in the figure mean neon gas puff, deuterium gas puff, neon gas puff followed by deuterium gas puff and deuterium gas puff followed by neon gas puff, respectively. Total injection of neon gas and deuterium gas were 1.2Pam^3 and 9.6Pam^3, respectively. As shown in the figure, the increment of radiation loss by "Neon + D_2" gas puff is much larger than the sum of the radiation loss by the "Neon Only" gas puff and that by "D_2 Only" gas puff from both the main and divertor plasmas. Such a synagistic effect is not seen for the "D_2 + Neon" gas puff. In Fig. 1(b) and Fig. 1(c), the increment of deuterium particle flux to the divertor and the increment of the electron density in the main plasma by the same gas puff sequences are shown, respectively. While the synagistic effect was again observed for the "Neon + D_2 " gas puff, no synagistic effect was observed for "Neon + D_2" gas puff. In other words, the effect of the "D_2 + Neon" gas puff on the divertor particle flux and electron density is the same with or less than the sum of the effect by the "Neon

Only" gas puff and that by "D_2 Only" gas puff. It was clearly demonstrated that the "Neon + D_2" gas puff was effective to produce the radiative divertor plasmas.

With the synagistic effect of neon and deuterium gas puffing, radiative divertor plasma was obtained in ELMy H-mode plasma with P_{NB} = 23MW while the H-factor was maintained to 1.5. The discharge was produced at the low particle recycling condition (Φ_{main}= 2 x 10^{22}/s) and particle recycling was increased by a factor of five and radiation loss was increased by a factor of two at the divertor. Change of Z_{eff} due to Neon was about 1 and total dilution of Deuterium due to impurity ions was estimated to be 50%. This discharge is compared with the reference plasma of ELMy H-mode which was produced at the high particle recycling condition in Table 1. Since the high T_{i0} that produced at the low recycling phase was maintained in the case 1 until the radiative divertor phase, neutron rate was even larger than the case 2, irrespective of the dilution of deuterium due to neon in the case 1.

By increasing radiation loss at the divertor further, the radiative divertor plasma which dissipates 80% of incoming heat flux was produced in ELMy H-mode plasmas with P_{NB} = 20MW. (See Fig. 2. In such a discharge, the total radiation loss from the plasma increased from 6MW to 14MW of the NB power. Profiles of heat flux density to the divertor at the initial phase and at the radiative divertor phase are shown in Fig. 2(b). Detachment at the strike point of the separatrix occurred when the heat flux density vanished at t = 9.0 s. The detachment was maintained for two seconds until the end of the NB heating. Degradation of the main plasma confinement due to the radiation enhancement is shown in Fig. 3. H-factor of the main plasma is ploted against P_{TOT}/P_{ABS} . Data points are taken from ELMy H-mode plasmas with P_{NB} < 23MW. Here P_{TOT} is the total radiation power plasma and P_{ABS} is NB absorption power.

Summary

A synagistic effect of the neon gas puff followed by deuterium gas puff was found on the enhancement of radiation loss and particle flux to the divertor . With the synagistic effect, radiative divertor plasma were obtained with relatively high ion temperature in the main plasma.

Reference

[1] K. Itami et al. Plasma Phys. Control. Fusion 37 (1995) A235-A265.

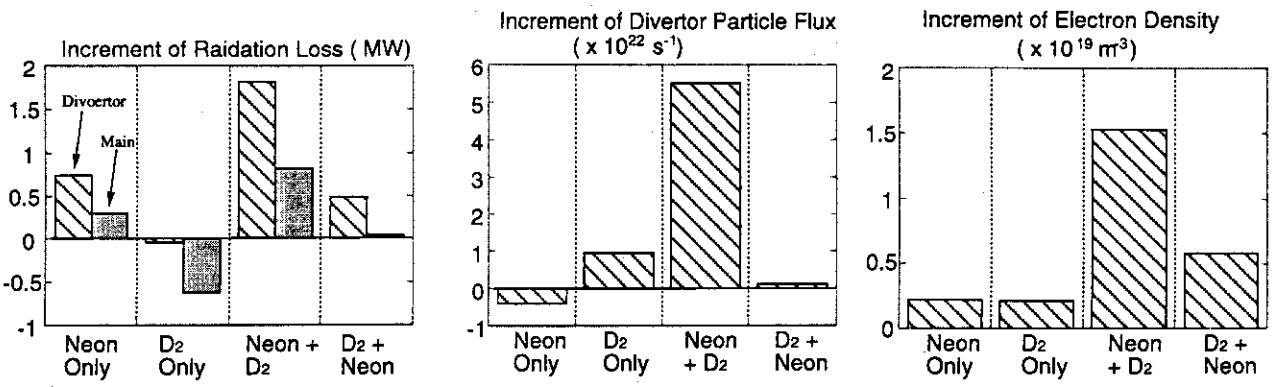

Fig. 1
(a) Increment of the radiation loss from the main and divertor plasmas
(b) Increment of Divertor Particle Flux
(c) Increment of Electron Density
after four kinds of the gas puff sequence

	conditions	Φ_{MAIN} (s^{-1})	$\overline{n_e}$ (m^{-3})	Prad/PNB	Ti0 (keV)	$n_{DD}(s^{-1})$
case 1	Low Recycling + Ne & D2 puff	5×10^{22}	3.2×10^{19}	50%	7	3.8×10^{15}
case 2	High Recycling + No gas puff	2×10^{22}	2.8×10^{19}	30%	5	3.1×10^{15}

Table. 1

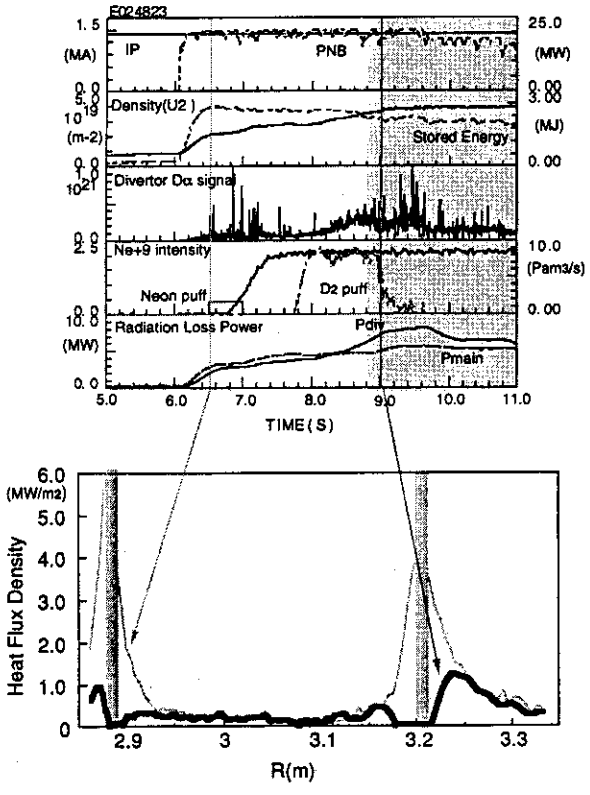

Fig. 2
(a) Waveforms of ELMy H-mode discharge with radiative divertor
(b) Heat flux density profiles.
(Before and after the radiative divertor .)

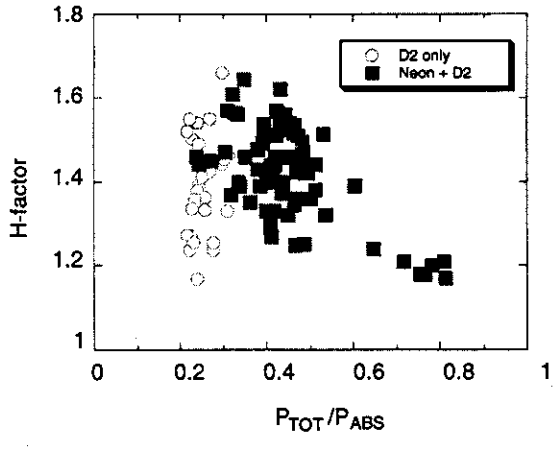

Fig. 3
H-facrot vs P_{TOT}/P_{ABS} in ELMy H-mode plasmas with neon and deuterium gas puff.
(P_{NB}<23MW)

6.5 Particle and Heat Fluxes on the Divertor and Carbon Generation during ELMy Phase

S. Sakurai, N. Asakura

1. Introduction

ELMy H-mode is considered as a steady-state operation mode in a tokamak reactor. Divertor tiles will be periodically exposed huge particle and heat fluxes at ELM events, and the surface temperature of them will exceed the endurance limit of materials, if the heat load toward divertor is not effectively reduced and removed. Therefore, it is very important to study the effect of particle and heat fluxes and divertor tile temperature on carbon generation during ELMy phase.

2. Carbon Burst in Quasi-steady State high βp ELMy H-mode Discharge

Figure 1 shows the typical waveform of a quasi-steady state high βp ELMy H-mode discharge in JT-60U. Good energy confinement state (H-factor ~2) was sustained by high power (~30MW) NB heating under the low recycling condition. Emission profile from carbon impurities in divertor region was measured with the optical fiber array for divertor spectroscopy, and emission from highly ionized carbon impurity in edge plasma was also measured by the VUV spectrometer viewing across the main plasma. These signals abruptly increase just after the rising of the Dα signal and the surface temperature of divertor tiles. Brightness of CII line reached to the same level of Dα radiation. On the contrary, a carbon burst was not observed in similar discharges, in which Dα radiation and the tile temperature were kept slightly lower. These results suggest that the increase of particle and/or heat fluxes toward the divertor causes a carbon burst. In addition, CII brightness increased strongly as the surface temperature of outboard divertor tiles went up in these discharges. Since the inner strike point of these discharges was located outside the viewing area of divertor diagnostics, we can not determine the place of a dominant carbon source. Furthermore, the effect of the huge particle and heat fluxes at ELM event on the carbon impurity generation has

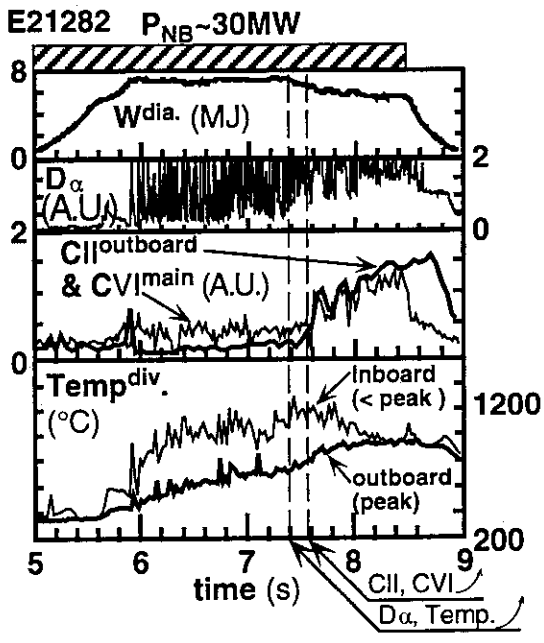

Fig.1 Typical waveform of quasi-steady state high βp ELMy H-mode discharge. Ip =2.3MA, B_T =4.4T. CII(658nm) at outboard divertor and CVI(3.37nm) at main were measured with the 38ch optical fiber array and VUV spectrometer, respectively. Surface temperatures of divertor tiles were measured with IRTV. The peak value at inboard divertor was not obtained due to the limit of sight.

not been clear, because the time resolution of divertor diagnostics (>20ms) was insufficient to resolve each ELM event (~a few ms).

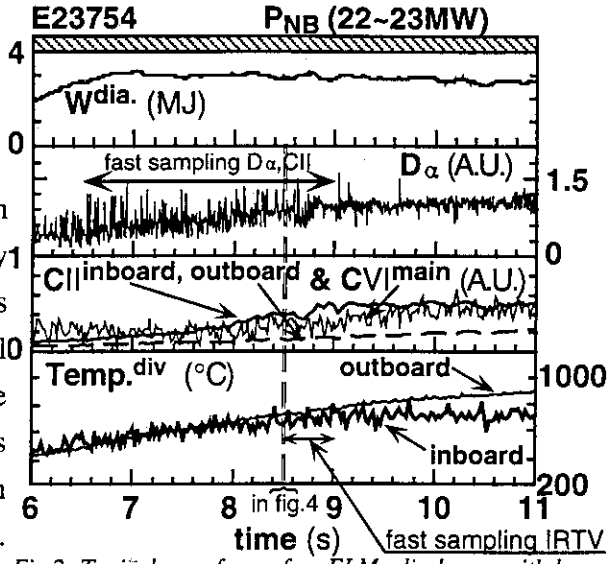

Fig.2 Typical waveform of an ELMy discharge with long pulse NB heating. Ip =1.5MA, B_T =3T. Signals from PMT array for CII at inboard divertor and poloidal profile of Dα were sampled at each 20μs from 6.5s to 9s. Surface temperature of divertor tiles were measured with fast sampling (250μs) IRTV.

3. Behavior of Carbon Impurities during ELMy Phase

In order to study the behavior of carbon impurities during ELMy phase with strongly heated divertor tiles, an ELMy discharge was sustained by long pulse NB heating. The typical waveform is shown in Fig. 2. Although the surface temperature of outboard divertor tiles reaches the same level at which the carbon burst is observed in the discharge shown in Fig. 1, no carbon burst is observed in these discharges. The plasma configuration was adjusted to divertor diagnostics, and the whole profile of CII radiation in divertor region was shown in Fig. 3. The surface temperature of outboard divertor tiles is higher than that of inboard, but the ratio of the CII brightness to the Dα at the inboard target is larger than that at the outboard target. It should be noticed that CII line is emitted from not only directly sputtered carbon but also recycling one, still we consider the localized emission near the strike point as an effective indicator of carbon influx. In addition, fast sampling of IRTV and Dα PMT array showed that particle and/or heat fluxes to the inboard target at an ELM event were larger than outboard side in these discharges. Therefore, we consider that carbon generation rate dominantly depends on particle and/or heat fluxes at ELM event within tile temperature of 900°C.

Fig.3 Setup of the divertor diagnostics and radiation profile of Da(656nm) and CII(658nm) measured with the 38ch optical fiber array.

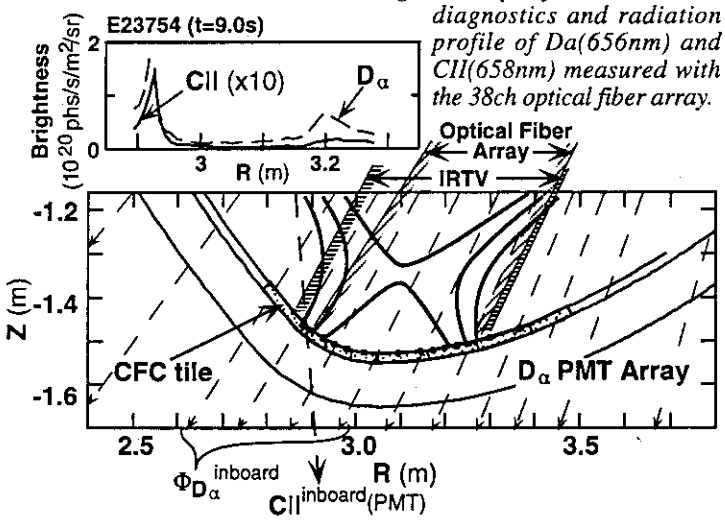

4. ELM Pulse Effect on Carbon Generation

Dα and CII radiation and tile temperature of the inboard divertor were measured by fast sampling of PMT array and IRTV as shown in Fig. 4. Increment of the surface temperature at an ELM pulse reaches several hundreds degrees, and peaks of CII radiation are much larger than

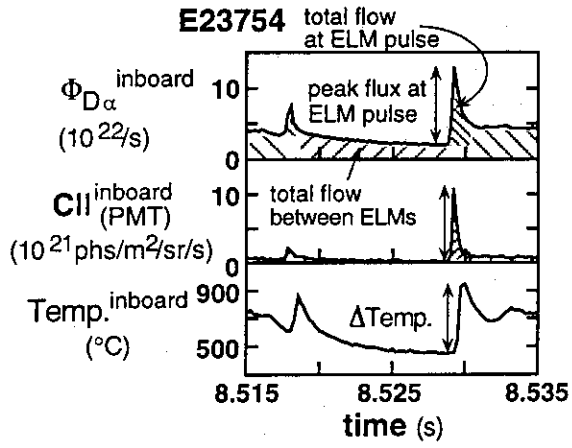

Fig.4 Typical waveform of ELMy phase shown in Fig. 2. Particle flux toward inboard divertor $\Phi_{D\alpha}$ was evaluated from Dα radiation. Brightness of CII (658nm) and Dα was sampled at each 20μs. Surface temperature of inboard divertor was measured with fast sampling (250μs) IRTV.

average value between ELMs. The relation between CII radiation and the particle flux, which evaluated from Dα radiation, was analyzed at each ELM pulse and between ELMs. CII radiation increased with the particle flux both at ELM pulse and between ELMs, but the ratio of CII radiation to the particle flux at ELM pulse is much larger than that between ELMs as shown in Fig. 5(a). These results show that the sputtering yield of carbon was enhanced at an ELM pulse. The time-integrated CII radiation due to an ELM pulse is compared with that of between ELMs in Fig. 5(b). They increase with the total particle flow toward inboard divertor at both situations. Although total particle flow at ELM events is much smaller than that between ELMs, total (time-integrated) CII radiation at ELM events is almost same amount of that between ELMs. Therefore, the effect of ELM pulses on carbon impurity generation are not negligible. It has been very difficult to distinguish the effect of heat flux and particle flux, because heat flux increased with particle flux in these discharges

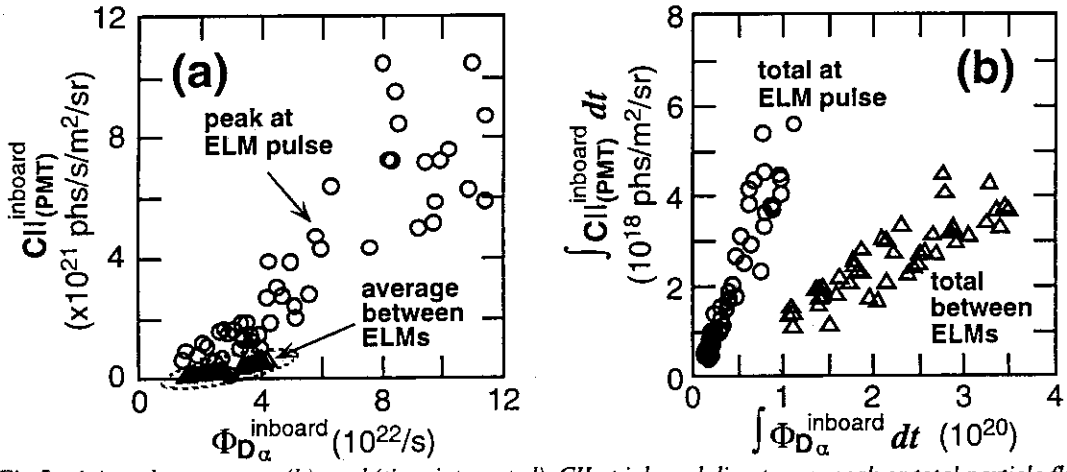

Fig.5 (a) peak or average (b) total (time-integrated), CII at inboard divertor vs. peak or total particle flux toward inboard divertor. Definitionsof peak and total were illustrated in Fig. 4. Circles indicate peak or total at ELM pulse. Triangles show average or total between ELMs.

5. Summary

The effect of particle and heat fluxes and divertor tile temperature on carbon generation during ELMy phase has been studied by fast sampling of PMT array and IRTV. Carbon burst from divertor tiles has been observed when maximum temperature of tiles exceeds 900°C at least. Radiation of carbon impurity strongly depends on particle and/or heat fluxes at ELM events, even if the tile temperature is kept lower than this temperature. Therefore, the effect of ELM pulses on carbon impurity generation are not negligible.

6.6 In-out Asymmetry of Divertor Heat Flux in High βp Plasma

K. Nagashima, K. Itami

For the development of steady state tokamak reactor, a stable operation with high poloidal beta (β_p) plasma is one of the most important issues. Plasma characteristics with high β_p have been extensively examined in several tokamaks[1, 2]. On the other hand, adequate control of divertor heat load and particle exhaust is also an indispensable issue for the tokamak development. However, divertor characteristics with high β_p plasma have not been studied enough. In the high β_p plasma, the Shafranov shift is large and the magnetic flux becomes dense in the outer region and sparse in the inner region. The same situation exists in the divertor region, that is, adjacent flux surfaces are close in the outer divertor and they are away from each others in the inner divertor. Therefore, the large Shafranov shift influences the divertor characteristics, in particular, the in-out asymmetry of heat and particle flux densities. It is inferred that the widths of heat and particle flux become narrow in the outer divertor and broad in the inner divertor.

The in-out asymmetry of divertor heat flux was examined for ELMy H-mode plasmas with $\beta_p \leq 1.7$. In high density plasmas, divertor radiation becomes large and the heat flux are dissipated before reaching the divertor plates. Hence, the data were obtained from low density plasmas with $\bar{n}_e/n_{GW} \leq 0.4$ (where $\bar{n}_e$ and n_{GW} are the line averaged density and the Greenwald limit). It was observed that the asymmetry is strongly dependent on the β_p value and the heat flux width is broader in the outer divertor. It is in contradiction to the above inference. The heat flux profile was measured on the divertor plates (Fig.1(a)). The measured position is transferred to the equatorial plane on the same flux surface and the measured profile is projected on the equatorial plane (Fig.1(b), (c)). Then, the heat flux profile may be compared on the flux coordinate between the inner and the outer divertors. Ratio of the outer width over the inner width increases with increasing the β_p value, as shown in Fig.2, and the ratio becomes over 2 for $\beta_p \geq 1.5$. The in-out asymmetry of particle flux seems to have the similar tendency.

This in-out asymmetry is a considerably important problem for the divertor design of the high β_p tokamak machine and further investigation is necessary.

References

1) Y. Kamada et al., Proc. 15th Int. Conf. Plasma Physics and Controlled Nuclear Fusion Research, Seville, Spain (1994), A-5-I-5
2) The JET Team, Proc. 15th Int. Conf. Plasma Physics and Controlled Nuclear Fusion Research, Seville, Spain (1994), A-5-I-3

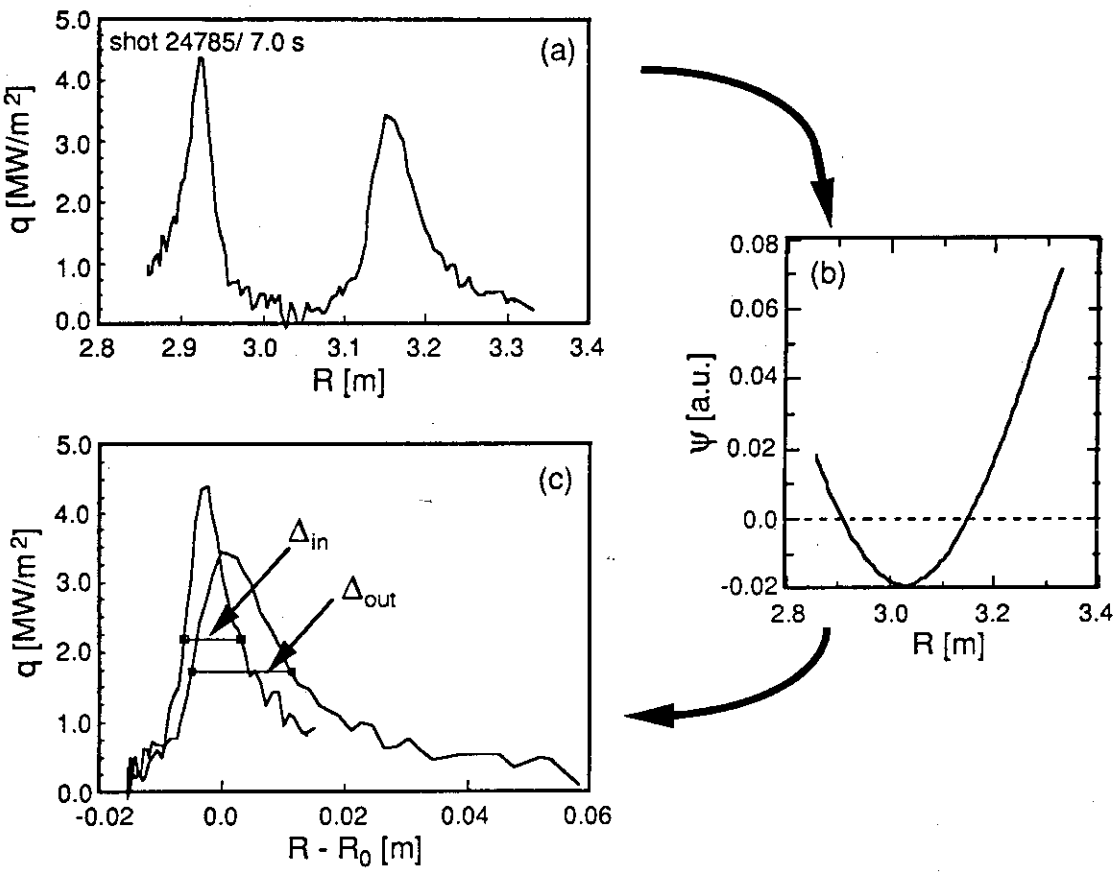

Fig.1 (a) Heat flux profile measured on the divertor plates.
(b) Relation between the flux function and the measured position.
(c) Heat flux profile projected on the outer equatorial plain.

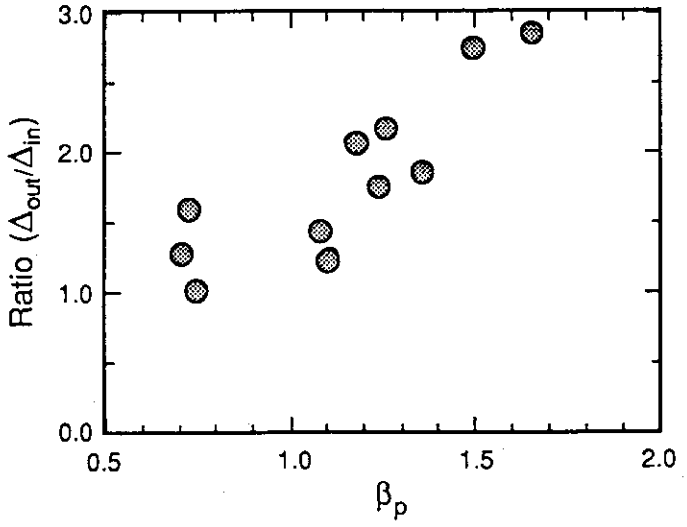

Fig.2 Poloidal beta vs. ratio between the inner and the outer heat flux widths on the equatorial plane.

6.7 Measurement of Electron Temperature and Density in Divertor Plasmas Using Intensity Ratios of He I Spectral Lines

H. Kubo, S. Higashijima, A. Sakasai, T. Sugie and N. Asakura

1. Introduction

Electron temperature and density in divertor plasmas has usually been measured with Langmuir probes located at divertor plates so far. However high heat flux damages the probe and then it is difficult to measure the density. On the other hand, the method using line intensity ratios does not suffer such a problem. To use He line emission is favorable, because He injection has little effect on fusion plasma performance and He atoms are produced by the nuclear reaction in fusion reactors. In TEXTOR, He I lines: 2p ^{1}P - 3s ^{1}S (728 nm), 2p ^{3}P - 3s ^{3}S (706 nm) and 2p ^{1}P - 3d ^{1}D (668 nm), from an injected He-atom beam have been used to measure the temperature and density profiles in the plasma edge[1]. This paper describes the spatial profile measurement of the temperature and density in the JT-60U divertor using the line intensities.

2. Experiment

Figure 1 shows diagnostics for this investigation in a schematic diagram of the JT-60U divertor. We have simultaneously measured the three He I line emissions from the divertor plasmas with a spatial resolution of 1 cm using a 38-channel optical fiber array[2]. The temperature and density at the divertor plates are measured with Langmuir probes and the radiative losses are measured with bolometers.

Figure 2 shows time evolution of a discharge for this study. During NB heating, He gas was puffed for 300 ms and the electron density was raised by a continuous H_2 puff. From the increase in the electron density, the ratio of the helium ion density to the hydrogen ion density was estimated to be 0.34 and 0.068 at 6.5 s and 10 s, respectively. A MARFE occurs in the vicinity of the null point at 9.1 s and the radiative losses measured with the bolometer viewing the null point increases drastically. Then the outboard divertor was partially detached.

3. Results and Discussion

The intensity ratios around the outboard strike point are compared with those calculated by TEXTOR group[1] and Kyoto group[3] in Fig. 3. In the calculations, the electron density was assumed to be 1×10^{19} m^{-3} for the temperature measurement and the electron temperature is assumed to be 50 eV for the density measurement. The error bar in Fig. 3(a) indicates the change in the calculated intensity when the density changes from 0.2 to 5×10^{19} m^{-3}. And the

error bar in Fig. 3(b) indicates the change in the calculated intensity when the temperature changes from 10 to 100 eV. We cannot identify the discrepancy between the two calculations. Kyoto group has recently updated the atomic data and considered more energy levels than TEXTOR group. The scattering of the measured data is ascribed to the error in the probe measurement. For the temperature measurement, although the measured intensity ratio increases with the temperature as expected, it is smaller than calculated ones. The discrepancy cannot be ascribed to the assumption of the density in the calculations. The measured intensity is closer to that calculated by TEXTOR group than that calculated by Kyoto group. For the density measurement, the measured intensity ratio agrees with that calculated by TEXTOR group. The discrepancies between the measurement and the calculations might be attributed to ion collision effect, that was ignored in the calculations. It is expected that the ion collision effect decreases the intensity ratio for the temperature measurement and increases that for the density measurement.

The fifth and sixth rows in Fig. 2 show the time evolution of the temperatures and densities around the outboard strike point obtained by the probe measurement and spectroscopic measurement. Here the TEXTOR data were used to derive the temperature and density from the spectroscopic measurement. Although the temperature derived from the spectroscopic measurement decreases with the increase in the electron density in the main plasma as that measured with the probe, it is about half of that measured with the probe. The density derived from the spectroscopic measurement agrees with that measured with the probe.

Fig. 4 shows the spatial distributions of He I 728 nm intensity, the temperature and density derived from the spectroscopic measurement. We discuss the distributions between the outboard strike point and the null point. In the region, the angle between the viewing chords of the spectroscopic measurement and the separatrix surface is rather large and the viewing chords changes along the field line. Under the attached divertor condition, the intensity profile has a clear peak at the outboard strike point. The intensity profile becomes flat as a MARFE occurs. As the electron density in the main plasma increases, the temperature decreases and the density increases in the divertor. During the MARFE, the temperature decreases down to 10 eV and the profile becomes flat. Then the density near the divertor plates to that the plasma is attached is two times higher than that around the null point.

The optical fiber viewing the strike point observes the line emission from the vicinity of the strike point where He atoms recycle dominantly. It is expected that the temperature and density at the strike point are reliably derived from the intensity ratios. Assuming that the electron density is 1×10^{19} m^{-3} and the energy of the He atoms is 600K, the ionization length of the He atoms is estimated to be 20 and 1.4 cm at electron temperatures of 10 and 50 eV, respectively. Under the attached divertor condition, it is expected that the He atoms cannot penetrate the scrape-off layer because the temperature is high. Then the line emission measured with the fibers viewing the range between the strike point and the null point comes from two

boundaries of the scrape-off layer: the outboard boundary and the private-region boundary. Therefore it is difficult to obtain the correct profiles of the temperature and density between the strike point and the null point from the spectroscopic measurement. As the density increases and the temperature decreases, the He atoms penetrates deeper into the scrape-off layer, and the density obtained by spectroscopy increases and the temperature obtained by spectroscopy decreases. When the MARFE occurs and the temperature is low, the measurement is useful to derive the temperature and density profiles because the He atoms penetrate the scrape-off plasma and the peripheral region of the main plasma.

4. Summary

It is estimated that the intensity ratios of the He I spectral lines are available to estimate the electron temperature and density profiles in divertor plasmas, although more precise atomic data are necessary. Around the strike point, the temperature and density derived from the spectroscopic measurement agreed with those measured with probes within a factor of two. On the other hand, it is difficult to obtain the correct profiles of the temperature and density between the strike point and the null point. However, when a MARFE occurs and the temperature is low, the measurement is useful to derive the temperature and density profiles. Then the spectroscopic measurement suggested that the temperatures around the divertor plates to that the divertor plasma attached and the null point were about 10 eV .

Acknowledgment

The authors are grateful to Dr. M. Goto and Prof. T. Fujimoto of Kyoto university for providing the atomic data.

References

1) B. Schweer et al.; J. Nucl. Mater. 196 - 198 (1992) 174.
2) H. Kubo et al.; Plasma Phys. Control. Fusion 37 (1995) 1133.
3) M. Goto et al.; private communication.

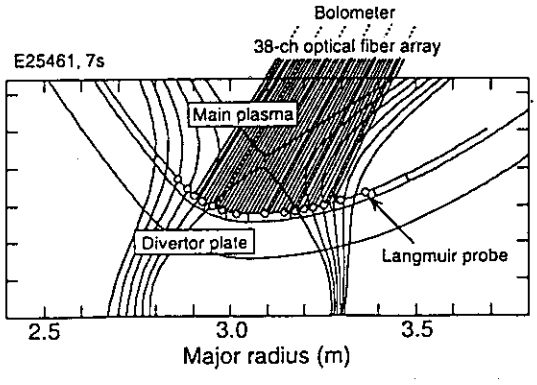

Fig.1 Schematic diagram of the JT-60U divertor.

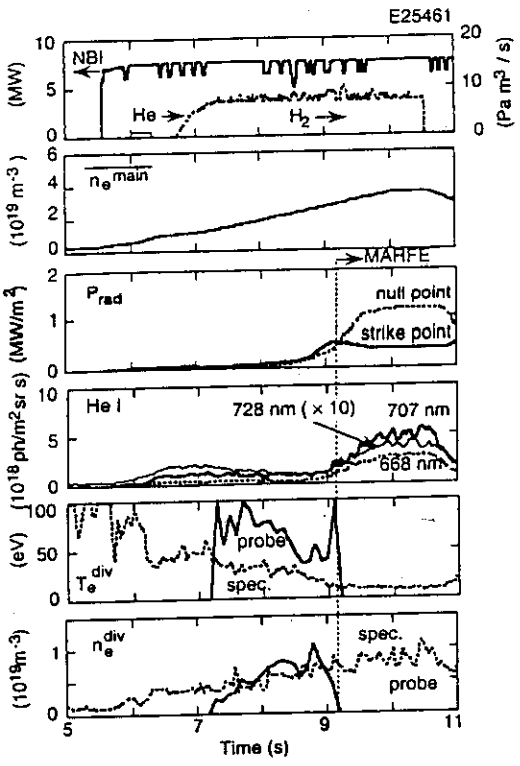

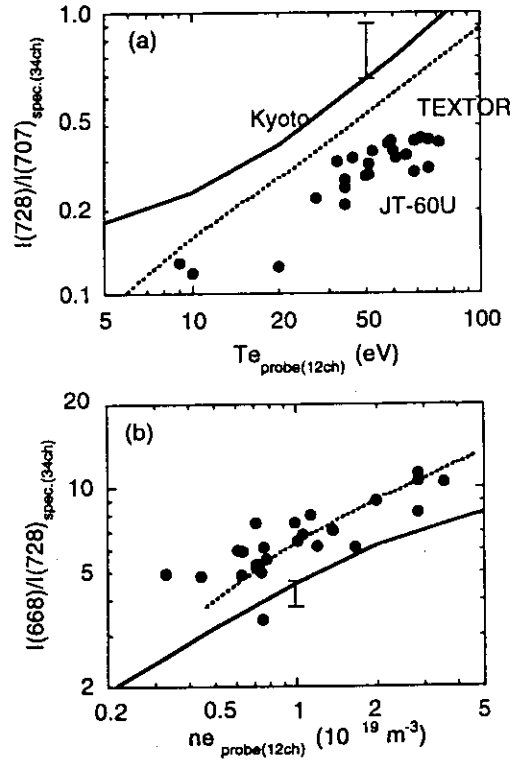

Fig. 3 Intensity ratios for (a) the temperature measurement and (b) the density measurement. The solid points indicate the ratios measured around the outboard strike point in JT-60U and the lines indicate those calculated by TEXTOR group and Kyoto group.

Fig. 2 Time evolution of a discharge with a He puff. The NBI power and the puff rates of He and H_2 are shown in the first row. The line-averaged electron density in the main plasma is shown in the second row and the radiative losses measured with the bolometers viewing the null point and the outboard strike point are shown in the third one. The forth row shows line intensities of He I 728 nm, 707 nm and 668 nm around the outboard strike point. The fifth and the sixth shows the temperatures and densities around the outboard strike point obtained by the probe measurement and spectroscopic measurement.

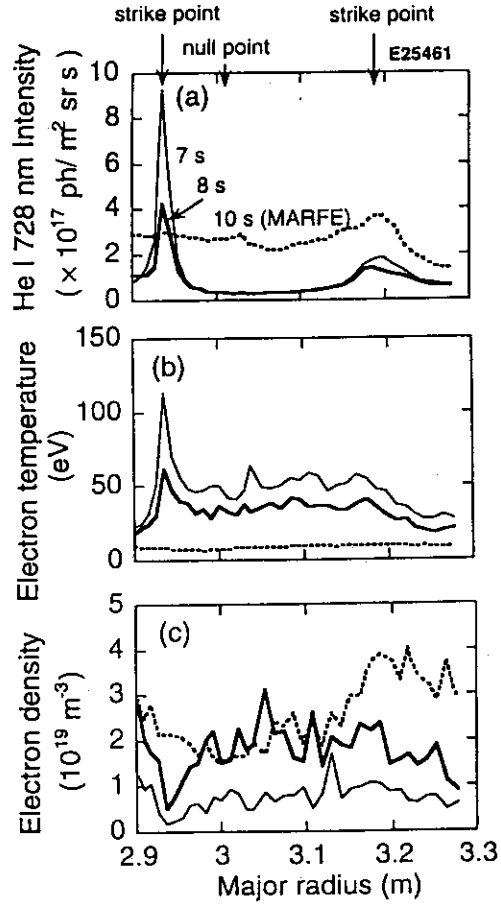

Fig. 4 Spatial distributions of (a) He I 728 nm intensity, (b) the temperature and (c) density derived from the spectroscopic measurement using the TEXTOR data.

7. LHRF

7. 1 LH coupling property at large plasma-antenna distance

M. Seki, N. Asakura

1. Introduction

It is very important to obtain good coupling for Lower Hybrid current drive (LHCD) performance, because optimized spectrum for high efficiency is launched under the condition of low reflection coefficient. In order to realize good coupling, thin plasma more than cut-off density is required in front of LHCD antenna. This means that outer plasma must be close to LHCD antenna so as to obtain enough density for good coupling. Severe controllability of plasma position is needed. Situation will be worse in ITER like machine, since operational frequency raised up to 8 GHz leads higher density for good coupling. On the other hand a large clearance between the separatrix and the first wall should be kept for enough low erosion level. Therefore active method must be established for good coupling at a large plasma-antenna distance. This long distance coupling allows wide flexibility in LHCD operation. Moreover undesirable heat load on LH antenna may be avoided.

Large clearance could be maintained by using a gas feed at low reflection in ASDEX [1]. The distance was extended up to 11.5 cm with pellet injection. In JT-60U, efficient coupling was observed with distance of 10 cm in LH injection alone using 24 x 4 multi-junction antenna [2]. Increase in density was measured by a double probe during good coupling phase. The probe was located in the same field line of ray trajectory of LH waves. It was pointed out that neutral gas near antenna was a key item for good coupling [3]. In this section, coupling property of LH waves is reviewed using 48 x 4 multi-junction antenna at a large plasma-antenna distance. Especially, active coupling method is mentioned and SOL measurements using a fast reciprocating probe are also presented [4].

2. Experimental results

Coupling code taken into account of multi-junction effect in divided waveguides shows that reflection coefficient in input waveguide is acceptable low as < 10 % when edged density n_{edge} in front of LH antenna exceeds cut off density n_{co} of operational frequency. Namely n_{edge} is required higher than 5×10^{19} m^{-3} corresponding of n_{co} for 2 GHz. If peripheral density can be raised by some active methods, good coupling is expected.

Typical shot of distant coupling of LH using ICRF injection is shown in Fig. 1. At beginning of LH injection, reflection coefficient is high due to a large clearance δ between plasma and LH antenna. By applying of ICRF power, reflection coefficient in

input waveguides suddenly decreases from 45 to a few % with δ ~15 cm. ICRF power of 1MW with 116 MHz is injected into 1.2 MA plasma with 2.5 T. Loop voltage degreases to zero with increasing input power of LH. It should be pointed out that good coupling still continues after switching off ICRF power. Loop voltage keeps constant until LH power stops. In order to investigate a difference in density profile during good coupling due to ICRF injection, SOL measurements is carried out by a fast reciprocating probe located below LH antenna in poloidal direction. Figure 2 shows density profile near LH antenna during LH injection with / without ICRF power. Density during ICRF exceeds cut off one, but density decrease to a level of LH only case after injection of ICRF power.

Previous experimental results shows possibility to control coupling property by regulation of gas puffing. However the mechanism of good coupling using gas puff is not well understood. For example, ionization using neutral gas by LH power and / or fast electrons should play important role in good coupling, but where ionization is performed. Does ionization lead degradation in current drive efficiency through energy loss ? To solve these questions, active coupling with gas puff is carried out at a large distance. Time trajectories of active coupling by gas puff are shown in Fig. 3. Reflection coefficient is reduced due to gas puffing. Gas puff near to LH antenna is more effective than that from far port side. Line averaged density normally increases by gas puffing. Even though density gradually decreases, low reflection is lasting. After obtainment good coupling, input power is raised up to ~1.7 MW. Current drive efficiency is estimated to be ~2 x 10^{19} $m^{-2}AW^{-1}$, degradation in efficiency is not observed until plasma-wall distance of ~15 cm. Figure 4 illustrates edge density with / without gas puff. Density really increase by 40% during gas puffing in compared with no gas puff. However density measured by the probe recovers LH only level after gas puff. On the other hand good coupling continues. This situation is the same with long distance coupling by ICRF injection.

These results suggest that LH power produces a tenuous plasma for propagating by itself just around LH antenna using neutral gas. Area of ionization should be localized, and is orientated in the same field line of LH waveguides. Because density increase was observed in toroidal direction as mentioned in ref 2), in contrast with in no-sufficient increase in poloidal one. This means energy loss should be negligible because LH power is used to ionize just near antenna mouth. This is consistent with non-degradation in current drive efficiency.

3. Summary

Good coupling property is obtained by applying ICRF power and gas puff at a large distance between plasma-antenna up to δ~15 cm. Low reflection maintains after stopping ICRF and / or gas feed. Mechanism of this long distance coupling seems that

LH power produces plasma in front of antenna using neutral gas with small energy loss. Current drive efficiency does not degrade up to δ~15 cm.

This long distance coupling leads high flexibility in operation of LHCD, moreover reduction in heat loads on the first wall and LH antenna. In a next generation LH antenna, coupling will be actively controlled by using gas puffing near LH antenna.

References

1) F. Leuterer, et al.; Plasma Physics and Contr. Fusion 33 (1991) 169
2) M. Seki, et al. ; 19th EPS Conf. on Controlled Fusion and Plasma Physics II-985
3) Y. Ikeda, M. Seki et al. ; 17th Symp. on Fusion Tech. (Rome, 1992) 534
4) N. Asakura, et al. ; in this JAERI Research, sec. 12. 8

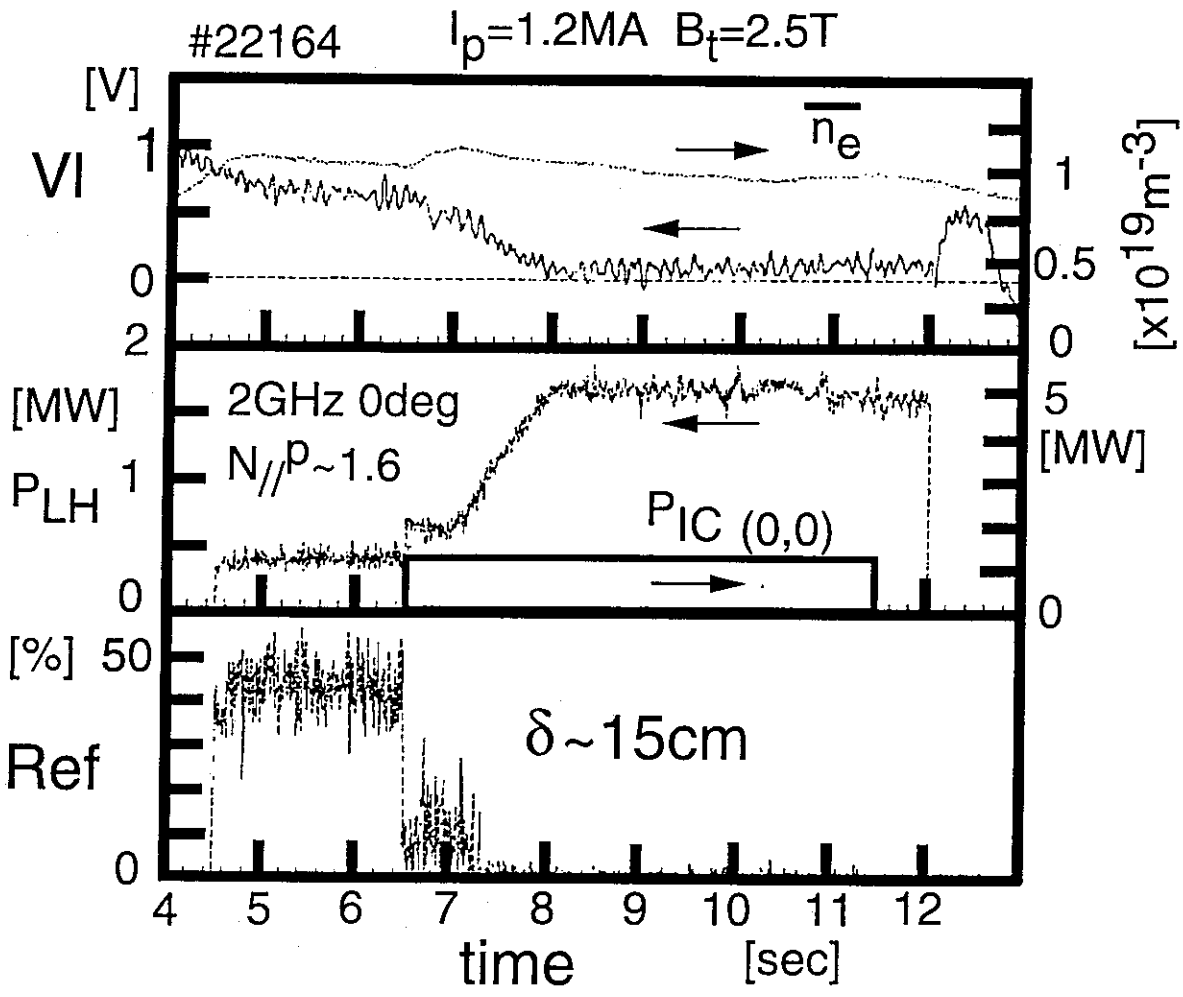

Fig. 1 : Typical shot of distant coupling of LH using ICRF injection. Reflection coefficient in input waveguides suddenly decreases by applying of ICRF power with plasma-antenna distance of 15 cm.

Fig. 2 : Density profile near LH antenna during LH injection with / without ICRF power. SOL measurements is carried out by a fast reciprocating probe located below LH antenna in poloidal direction. Density during ICRF exceeds cut off one, but density decrease to a level of LH only case after injection of ICRF power.

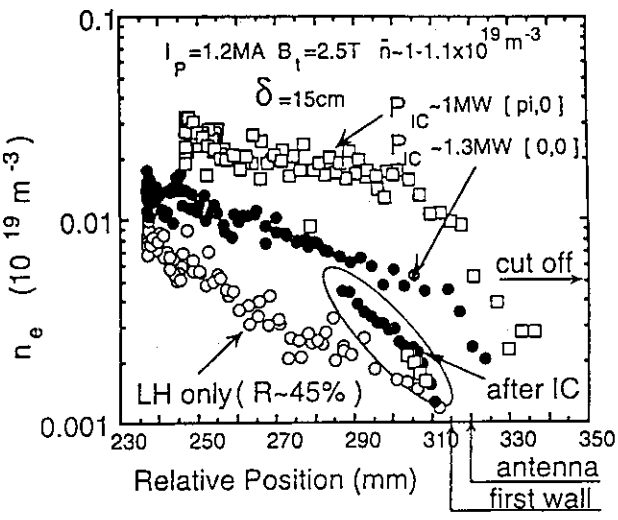

Fig. 3 : Time trajectories of active coupling by gas puff are shown. Reflection coefficient is reduced due to gas puffing. Line averaged density normally increases by gas puffing. Even though density gradually decreases, but low reflection is lasting. Current drive efficiency is estimated to be ~2 x 10^{19} $m^{-2}AW^{-1}$, degradation in efficiency is not observed until plasma-wall distance of ~δ~15 cm.

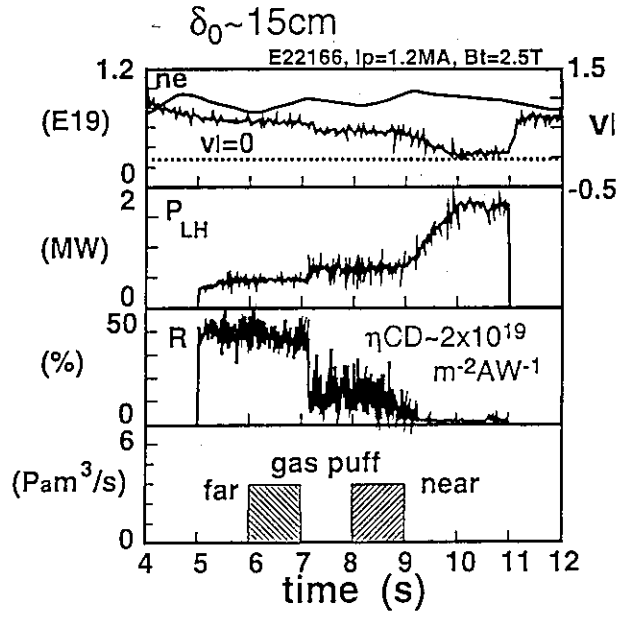

Fig. 4 : Edge density with / without gas puff. Density really increases by 40% during gas puffing in compared with no gas puff.

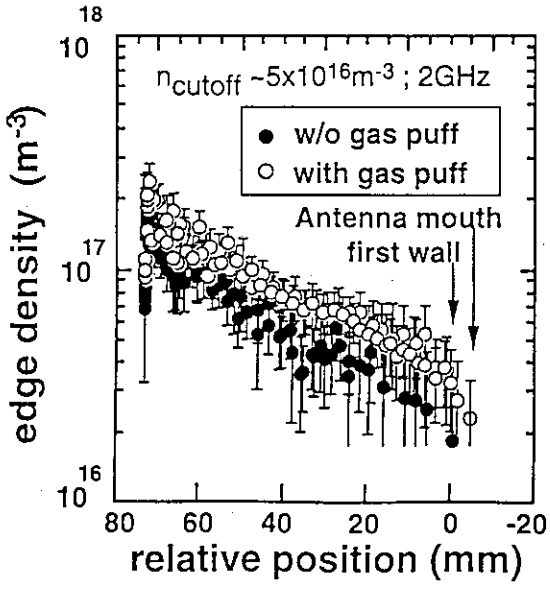

7.2 Effect of Lower Hybrid Current Drive on ELM Activities

O. Naito, S. Ide, M. Seki, T. Kondoh, K. Ushigusa

7.2.1 Introduction

To make the enhanced confinement property of the H-mode compatible with a steady-state operation of tokamak reactor, permitting some amount of Edge Localized Mode (ELM) activities is a possible candidate for preventing the impurity accumulation in the plasma core and allowing heat exhaust. In neutral beam (NB) heated plasmas, injection power, for instance, is one of the key parameters which govern the characteristics of ELMs, i.e. increases in power leads to increase in ELM frequency. In order to decouple the ELM activities from the heating power or other global parameters, some active method to control ELM may be useful. Since ELMs are thought to be a manifestation of ballooning instabilities in the plasma periphery, edge current drive can be a possible tool to control the ELM activities. In this section, a preliminary result of applying Lower Hybrid Current Drive (LHCD) to plasmas with ELMs is reported.

7.2.2 Experiment condition and results

The experiments were done on plasmas with I_p = 0.85–0.92 MA, B_t = 1.9–2.2 T, q_{eff} = 4.4–6.4, $\bar{n}_e$ = 1–1.3×10^{19} m^{-3}, V ≈ 80 m^3. ELMy plasmas were produced by 10 MW of deuterium neutral beam injection, where only tangential beams were used to reduce the loss of ripple trapped particles. When the electron density built up by NB and ELMs with regular frequencies appeared, 1 MW of LH was applied. To see the effects of current modification by LH more clearly, experiments with reverse ohmic current (i.e. counter-LHCD) were also carried out. The LH waves were launched from multijunction launcher ("Unit C") with wave refractive index parallel to the static field ($N_{\parallel}$) ranging from 1.4 to 3.3. Typical waveforms of D_α signals during NB heating with and without LHCD are shown in Fig. 1 for the case of counter-LHCD. The period of LH injection is shown by bold-lined box. For the case of fast wave injection (e.g. $N_{\parallel}$ = 1.4), ELM activities did not change

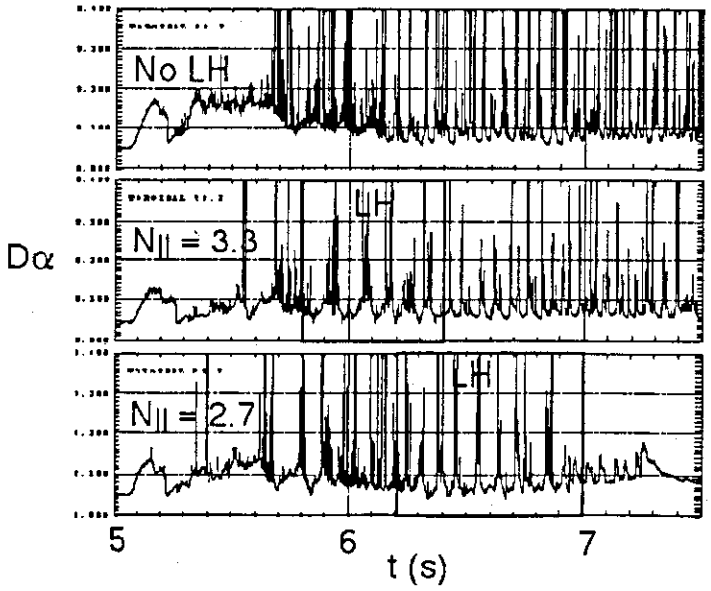

FIG. 1. Waveforms of Da signals during NB heating for the case of reverse ohmic current. LH injection (Nll = 3.3, 2.7) is shown by bold-lined box.

significantly from the case without LH. However, as shown in Fig. 1, ELM-free period tended to prolong when LH with slow wave phase velocities were injected. During ELM-free period, plasmas were in the H-phase as observed from the increase in the plasma stored energy. The response time of ELM activities on LHCD was typically around 0.2 s. This is relatively short compared to the current diffusion time which is at least a few seconds for the target plasmas of this experiment. Moreover, the effect of LHCD on ELMs were almost the same for the case of co-LHCD (i.e. LHCD in the direction of ohmic current). The interval between each starting time of ELM-free period is shown in Fig. 2 as a function of injected wave refractive index. Squares show the counter-LHCD case and circles show the co-LHCD case. For comparison, case without LH is plotted at $N_{\parallel} = 1$. The frequency of ELMs for NB only case is 20–100 Hz which is consistent with the previous results [1]. By injection of large $N_{\parallel}$ waves, the interval between ELM-free period prolonged by a factor of 2–3. This tendency is almost the same both for co- and counter-LHCD.

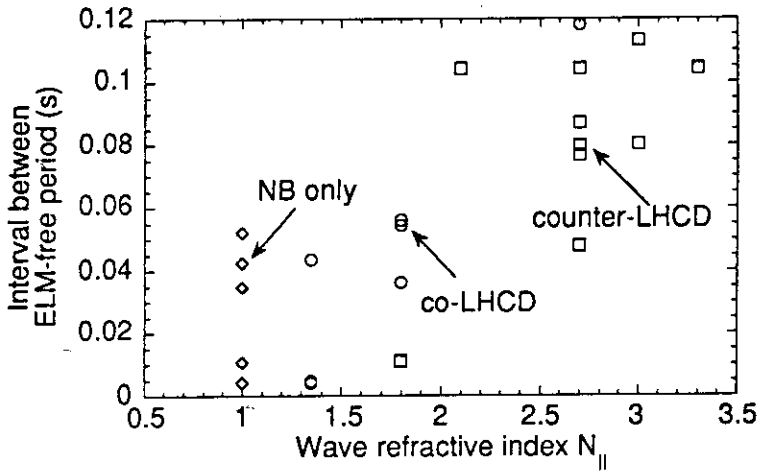

FIG. 2. Interval between each ELM-free period as a function of injected wave refractive index Nll.

7.2.3 Discussion

The facts that the response time of ELM activities to LHCD was sufficiently shorter than the current diffusion time and that the characteristics of ELMs were not affected by the current reversal indicate that the current modification by LHCD is not the major cause of the change in ELM activities. This has to be, however, further examined by using "Units A and B" launchers which have better directivity than "Unit C". The change in the total input power and density due to LH injection were not so large and may not be the major cause either. In the old JT-60, ELM-free H-mode was obtained by simultaneous injection of different-frequency waves. In that case, H-mode was obtained with ~ 1 MW of LH power for I_p = 1.5 MA, B_t = 4.5 T, $\bar{n}_e \sim 2\times10^{19}$ m^{-3}, but was spoiled by NB injection. Effects of fast electrons may be a possible cause, however, it should be clarified in the future study.

References

[1] Kamada Y. *et al.*, JAERI-M 93-057, "Review of JT-60U Experimental Results from January to October, 1992", p. 13 (1993).

[2] Tsuji S. *et al.*, Phys. Rev. Lett. **64**, 1023 (1990).

7.3 Measurement of Safety Factor Profile during Lower Hybrid Current Drive

O. Naito, S. Ide, T. Fujita, T. Kondoh, M. Seki, K. Ushigusa

The lower hybrid current drive (LHCD) experiments on JT-60 have demonstrated the effectiveness of LH wave as a current profile controller in a large tokamak [1]. It has been shown that the plasma current profile can be either peaked or broadened by selecting the phase velocity of the injected wave. In the experiments, the change in the global current profile is inferred from the magnetic measurement. The validity of this measurement has been partially supported by a calculated time evolution of plasma internal inductance (ℓ_i) assuming that the LH-driven current is similar to the observed hard X-ray profile [2]. Recently, a direct measurement of local safety factor ("q") profile using Motional Stark Effect (MSE) is available on JT-60 [3]. In this section, a preliminary result of MSE measurement during LHCD is reported.

Plasma parameters of the measured targets were: I_p = 1.2 MA, B_t = 3.5 T, $\bar{n}_e = 0.4\times10^{19}$ m^{-3}. The LH waves (1 MW) were injected from a multijunction launcher ("Unit C", number of subwaveguides: toroidally 24 × poloidally 4) with wave refractive indices parallel to the static field ($N_{\parallel}$) of 1.4 and 2.7. Time evolution of ℓ_i from magnetic measurement is shown in Fig. 1. Small spikes in ℓ_i are due to the injection of diagnostic beams for MSE. The current profile gradually peaked for the case of faster wave injection ($N_{\parallel}$ = 1.4, E24676) and broadened for the case of slower wave injection ($N_{\parallel}$ = 2.7, E24677). Although the hard X-ray signals are disturbed by neutrons when deuterium beams are injected, the LH-driven current profile inferred from the observed hard X-ray intensity profile (Fig. 2) was more peaked for faster wave injection, consistent with the magnetic measurement.

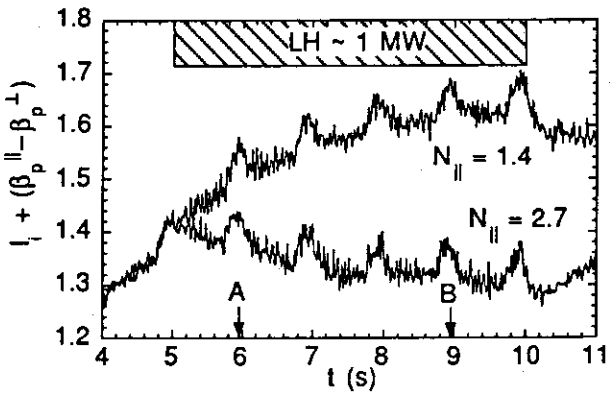

FIG. 1. Time evolution of plasma internal inductance for faster wave injection (Nll = 1.4) and slower wave injection (Nll =2.7).

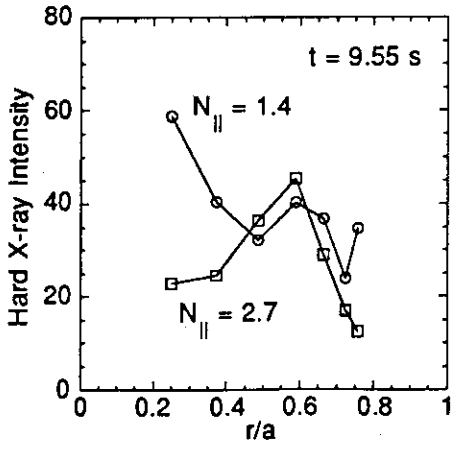

FIG. 2. Hard X-ray intensity profile during LHCD.

Measured q-profiles are shown in Fig. 3 for earlier phase (t = 5.95 s, "A" in Fig. 1) and

later phase (t = 8.95 s, "B" in Fig. 1). One second after the LH injection (t = 5.95 s), the q-value at the central- to mid-radius was smaller for the case of faster wave injection than that for slower wave injection, except for some scatters in the data. Accordingly the derived current density profile was rather flat near the plasma center and was more centrally weighted for the case of faster wave injection. Four seconds after LH injection (t = 8.95 s), the magnetic shear (r/q) (dq/dr) at the mid-radius increased for the case of slower wave injection whereas slightly decreased for the case of faster wave injection. The change in the q-profile in the inner region was small especially for the case of faster wave injection. Therefore the current profile in the inner region may settle in the rather early phase of LH injection.

In these experiments, an extra beam (#7B) was injected in addition to the diagnostic beam (#7A), which might reduce the signal to noise ratio of the data. Further study is necessary in the forthcoming campaign where more spatial measuring points of MSE diagnostics will be available.

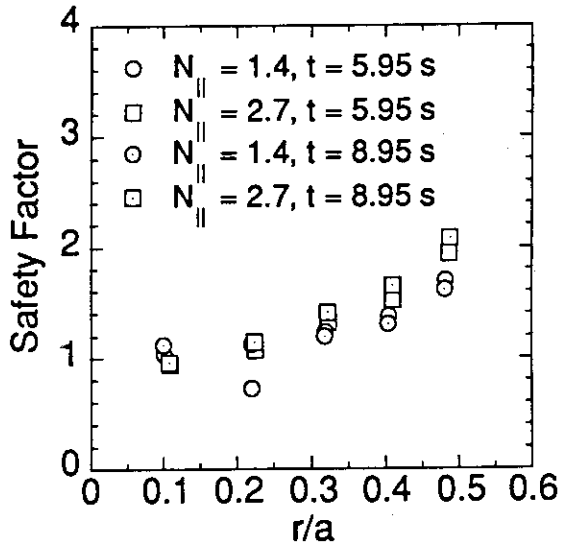

FIG. 3. Measured safety factor profile at points A and B in Fig. 1, for faster wave (Nll = 1.4) and slower wave (Nll = 2.7) injection.

References

[1] Ikeda Y. *et al.*, Fusion Engineering and Design **24**, 287 (1994).

[2] Kondoh T. *et al.*, Proc. 21th EPS Conference on Controlled Fusion and Plasma Physics, Monpellier, Part III, 1138 (1994).

[3] Fujita T. *et al.*, to appear in Fusion Engineering and Design (1996).

7.4 Investigation on Lower Hybrid Wave Absorption

S. Ide, O. Naito

1. Introduction

Realization of the absorption mechanism of lower hybrid wave (LHW) in a tokamak plasma is very important from a viewpoint not only of LHW physics itself but also of profile control in a reactor plasma. These days active control of profiles such as current, pressure and rotation profiles has been attracted large interest from a viewpoint of improved confinement. In this section two experiments related to LHW absorption done in JT-60U are reported. One of them is dependence of the wave deposition on the bulk electron temperature T_e, while the other is that on the wave propagation direction.

2. T_e dependence

It has been shown in many tokamaks that LHW deposition varies with the parallel ray refractive index $N_{//}$ of the injected waves. Simply speaking, lower $N_{//}$ waves tend to make a peaked power deposition profile while higher $N_{//}$ waves give a broad one. This can be understood taking distance between the wave spectrum and the bulk electron thermal speed in the phase space into account. From this point of view, changing T_e keeping $N_{//}$ constant would give a similar result.

In order to scan T_e the plasma current I_p and the toroidal field B_T were changed keeping the effective safety factor $q_{eff} \sim 7.9$. The scanned ranges were $0.45\ MA \leq I_p \leq 1.2\ MA$ and $1.5\ T \leq B_T \leq 4\ T$. The line averaged electron density $\bar{n}_e$ was adjusted almost identical as $5.5 \times 10^{18}\ m^{-3}$ for all the shots. The shape of n_e profile was kept almost the same as well. The LHW spectrum has a peak at $N_{//} = 2.44$ and the full width at the half maximum is about 0.5 and is injected from poloidal location at $\vartheta_{pol} \sim 45°$. The input power P_{LH} was tried to keep I_p/P_{LH} constant. However it was not completely successful, since the LHW power matching changes depending on the target plasma. In Fig.1, the T_e profiles measured by the Thomson scattering system are plotted. As shown in the figure, T_e increases with the increase of I_p. Hard X-ray (HX) emission is monitored by a multi-channel NaI scintillation tube array. The profiles of HX intensity I_{HX} are shown in Fig.2. Note that I_{HX} is a line integrated value and here ρ is the normalized flux radius. As

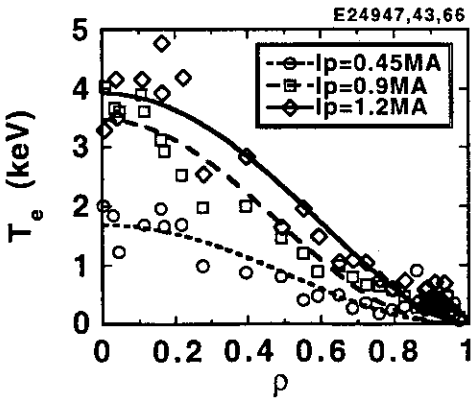

Fig.1 : T_e profiles for I_p = 0.45, 0.9 and 1.2 MA plasmas.

shown in the figure, the I_{HX} profile differs depending on I_P, in other words on T_e. As T_e (I_P) lowered, I_{HX} profile become peaked and lowered. Considering the wave spectrum, a resonant value of T_e is around 4.5 keV. Since the LHW were injected from $\vartheta_{pol} \sim 45°$ upshift of $N_{//}$ is expected. Although, no ray tracing calculation based on the experimental condition has been done yet, calculation results of other LHCD experiments suggests that $N_{//}$ can upshift by 0.1 or more. With an increase by 0.1 the resonant T_e can be 3.5 keV. Assuming the resonant T_e = 3.5 keV, a resonant position is around at $\rho \sim 0.3$ and 0.1 for I_P = 1.2 and 0.9 MA respectively. The change of I_{HX} profile at these I_P can be explained by this. In these cases absorption should be one pass absorption. A careful comparison between these data with calculation results would give a very important information about the wave-plasma interaction. That is to say, at which point does the wave interaction with the elections manifests in the velocity space, or if the toroidal effect can explain well the upshift of the spectrum and so on. By lowering I_P further, the absorption is expected to become multi pass absorption. Analysis of these data would give a clue to a question if the $N_{//}$ upshift due to the toroidal effect is still dominant in a multi pass situation. Anyway, in these cases more detailed ray tracing analysis based on the experimental condition are necessary.

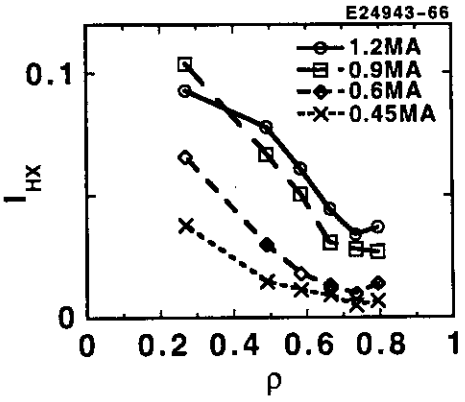

Fig.2 : I_{HX} profiles for different I_P

3. wave propagation direction dependence

Since LHWs propagate along the magnetic field line, the trajectory of the wave propagation can be changed by reversing the B_T direction. When LHWs are injected at $\vartheta_{pol} \sim 45°$ the ray trajectory projected in ρ space is different if the propagation direction is reversed. In Fig.3 schematic pictures of ray trajectories are shown. In the experiment the target plasma was of I_P = 1.2 MA, B_T = 3.5 T and the main working gas was hydrogen. The LHW spectrum used was the same as one mentioned in section 2, and P_{LH} was about 1.2 MW. Profiles of I_{HX} and HX temperature T_{HX} are shown in Fig.4. As is clear in the figure, both profiles are completely different between normal and reversed B_T direction cases.

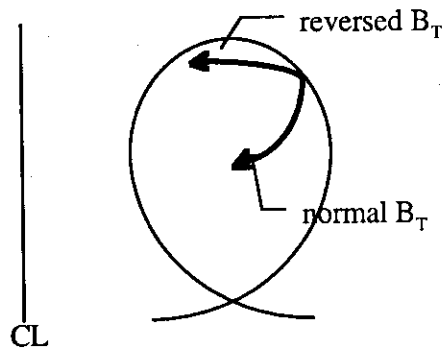

Fig.3 Schematic picture of ray trajectory depending on the direction of B_T

The difference can be explained as follows.

In the normal B_T direction case, the waves propagate towards the plasma center and along the trajectory $N_{//}$ upshifts as mentioned in section 2. On the contrary, the situation is different in the other case. At the first pass, the waves are not completely absorbed since the trajectory goes through the peripheral area. Therefore, the rest of the power is reflected at the plasma boundary and goes back into the plasma again. At this time, $N_{//}$ suffers downshift but not upshift in the experimental condition. Therefore, the actual spectrum inside plasma has lower $N_{//}$ component than the launched one. These lower $N_{//}$ waves accelerate the high energy electron tail to higher energy. This makes I_{HX} and T_{HX} higher in general.

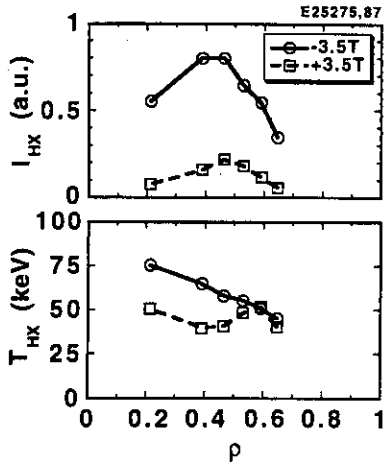

Fig.4 : I_{HX} and T_{HX} profiles in normal (broken lines) and reversed (solid lines) B_T cases.

3. Summary

In order to study the absorption mechanisms of LHW, LHW deposition has been investigated by changing T_e and the direction of B_T in JT-60U.

A systematic study of T_e dependence on wave absorption was carried out for the first time. In order to perform the experiment as correct as possible operation parameters, especially q, which is very important to the wave absorption, are kept as constant as possible. In the experiment a change of I_{HX} profile depending on T_e has been confirmed. At higher T_e cases, the change of I_{HX} profile consistent with a picture of one pass absorption. With more detailed analysis based upon a ray tracing calculation would give important information on LHW absorption mechanism such as, the manifestation limit of Landau damping.

An evident difference in both the I_{HX} and T_{HX} profiles is found when the direction of B_T is reversed. The difference can be explained by a difference in change of $N_{//}$ along the ray trajectory.

7.5 Effect of LHCD on particle confinement

S. Ide, K. Nagashima and O. Naito

1. Introduction

Particle confinement is one of the most important issues in a nuclear fusion research. In many radio frequency (RF) wave heated plasmas, such as electron cyclotron wave heating (ECH), ion cyclotron wave heating (ICH) and so on, changes of electron density n_e profile has been reported. In the other words, RF heating affects particle confinement. In JT-60U, effect of lower hybrid wave current drive (LHCD) on particle confinement has been investigated.

2. Experimental results

In the experiments the target plasma parameters, such as the plasma current I_p, the toroidal magnetic field B_T, n_e and so on, have been scanned to some extent. In Fig. 1, temporal traces of the line integrated n_e of a typical case of I_p = 0.45 MA and B_T = 1.5 T are plotted with different LHW spectrum injections. In these cases, the width of a spectrum is about 0.5 (the full width at the half maxima). As shown in the figure, decrease in n_e is clearest when the smallest $N_{//}$ waves are injected. The density profiles measured by the Thomson scattering diagnostics are show in Fig. 2. As is seen in the figure, the decrease in n_e is evident in the central region in the case of $N_{//}$ = 1.92 waves injection. Note that even in the higher $N_{//}$ waves injection case, n_e slightly decreases in the central region, although the line integrated n_e increases slightly. The increase in the line integrated n_e comes from the increase at the edge region. In the experimental condition, an increase in H_α signal has always been observed. This suggests release of neutral gas from the LHW launcher(s) or the wall. Therefore, in all the LHW injection cases n_e at the edge region increased. Although detailed analysis of the data is necessary, it is evident from the change the n_e profile itself that the change of the particle transport depending on the injection wave parameter .

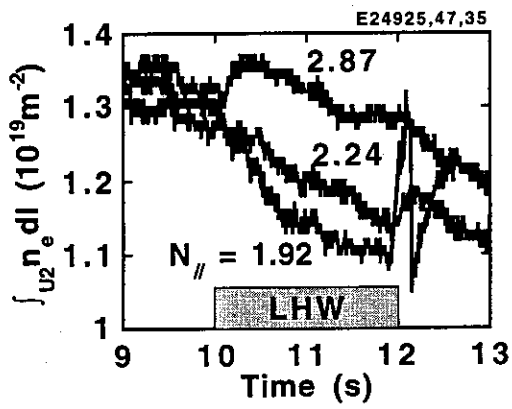

Fig.1 : Temporal evolution of line integrated density with the injection of LHW of various $N_{//}$

Within the range of plasma parameters scanned, the decrease in n_e seems to be clearer when ; I_P is lower, the target n_e is lower and the I_{HX} profile, or the wave deposition profile, is centrally peaked.

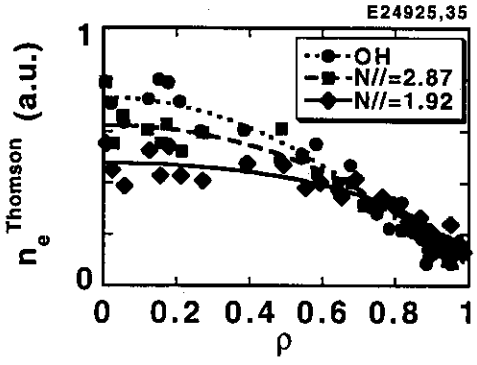

Fig.2 : n_e profiles of the target OH plasma and with the injection of LHWs of $N_{//}$ = 1.92 and 2.87.

The mechanism of this phenomenon is not understood yet. There might be some candidates such as, due to a current profile change, due to a bulk electron heating effect, due to a change of the high energy electrons distribution function, due to a change in the plasma potential or the radial electric field and so on. A change in the current profile seems plausible since one of the most significant effect of the LHW application is the current drive, of course. In order to check the effect of the current drive a similar experiment was carried out with a negative directional LHCD. That is, in the experiment the directions of both I_P and B_T were reversed. Since the phasing direction of LHW is fixed, LHW drives a current opposite to the OH current. Therefore, the total current profile should be in opposite tendency with respect to the injected LHW spectrum. That is, the total current profile is broaden when lower $N_{//}$ waves are injected. For a clear comparison, the target plasma was chosen that of I_P = 0.45 MA and B_T = 1.5 T. If a change in the current profile is dominate for the particle confinement, a result obtained in a negative directional LHCD should be in an opposite tendency to that in the normal LHCD case. However the result obtained in a negative directional LHCD is the same as the result in the normal LHCD case. In Fig.3 n_e profiles in the negative directional LHCD case are plotted. It is clear that n_e decreases in the plasma center when lower $N_{//}$ waves are injected. From the result, the modification of the current profile should be eliminated from the candidates.

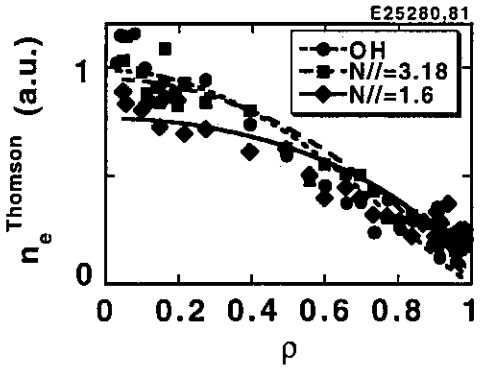

Fig.3 : n_e profiles in the negative directional LHCD cases.

In order to qualify the change of the particle confinement, a gas puff modulation experiment was also carried out[1]. The analysis shows that the particle diffusion

coefficient D is smaller in the OH plasma than that in LHCD plasma. Among LHCD plasmas, D is larger when lower $N_{//}$ waves are injected. The profile peaking factor C_V is larger in the OH plasma than that in LHCD plasma and smaller when lower $N_{//}$ waves are injected. Furthermore separating the plasma into inner and outer regions, it is found that D tends to be larger in the outer region.

3. Summary

In JT-60U an effect of lower hybrid wave current drive (LHCD) on particle confinement has been observed. Flattening of n_e profile, a decrease of n_e in the plasma central region, has been observed especially, when

1) lower $N_{//}$ waves are injected

2) operated at lower I_p

3) operated at lower target n_e.

The flattening should be attributed to a degradation of particle confinement. Results of the negative directional LHCD suggest that the degradation would not be attributed to the current profile modification by LHCD.

A qualitative analysis of a gas puff modulation experiment verifies the experimental observations.

Reference

1) K. Nagashima et.al. submitted to Plasma Phys. and Controlled Fusion

8. ICRF

8.1 Long Distance ICRF Coupling

S. Moriyama, H. Kimura, N. Asakura, T. Fujii, M. Saigusa

1. Introduction

It is important to study ion cyclotron range of frequency (ICRF) heating of H-mode plasma and with a large antenna-plasma gap for application to a future device such as ITER. In order to achieve heating with good confinement, H-mode plasma is preferable. On the other hand, to reduce heat load to the first wall and the ICRF antenna, lager S-F gap is preferable. However, the coupling resistance of the antenna, R_C, varies with L to H transition and decreases with increasing S-F gap. The change of the antenna coupling resistance requires adjustments of the impedance matching and the decrease in the resistance raise the RF voltage at the antenna. Consequently, they would be obstacles to continuous high power ICRF heating.

The second harmonic ICRF experiments have been performed by using a pair of phased antenna arrays since 1992. The scheme is minority proton heating in deuterium or helium majority plasma. The present operating frequency is 116 MHz which is the second harmonic proton cyclotron resonance frequency at a magnetic field of 3.8 T. The generator RF output power is 8 MW. The maximum coupled power with plasma is 7.0 MW for out-of-phase (π-phasing).

2. Coupling with H-mode plasma

High power of ~ 5 MW is coupled to ELM-free H-mode plasmas, and effective heating is observed in combination with NBI as shown in Fig. 1. The gap between the separatrix and the Faraday shield of the antenna (S-F gap) is 15 cm. The sawtooth is stabilized and highest level of the stored energy (~8MJ) among H-modes in JT-60U is achieved. Frequency Feedback Control (FFC) keeps good matching through L to H transition. Figure 2 shows that high power ICRF injection is rather difficult with smaller S-F gap which gives larger R_C and lower voltage at the antenna, possibly because fast ions escape from the plasma.

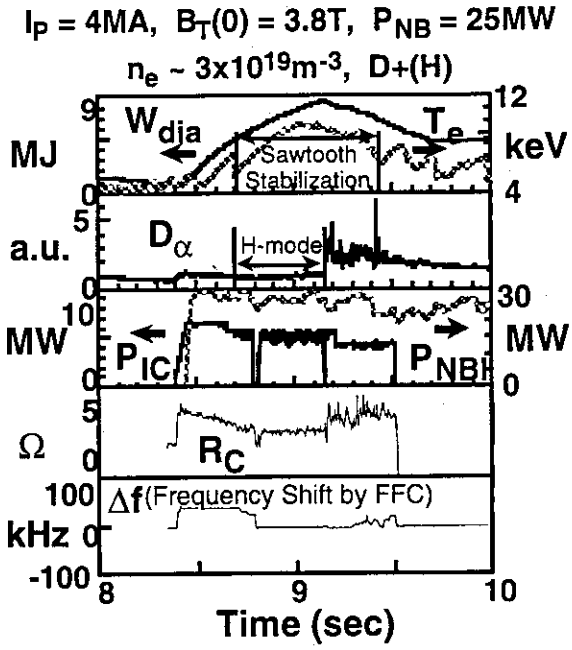

Fig.1 ICRF heating of H-mode plasma is successful with large plasma - antenna gap (=15 cm).

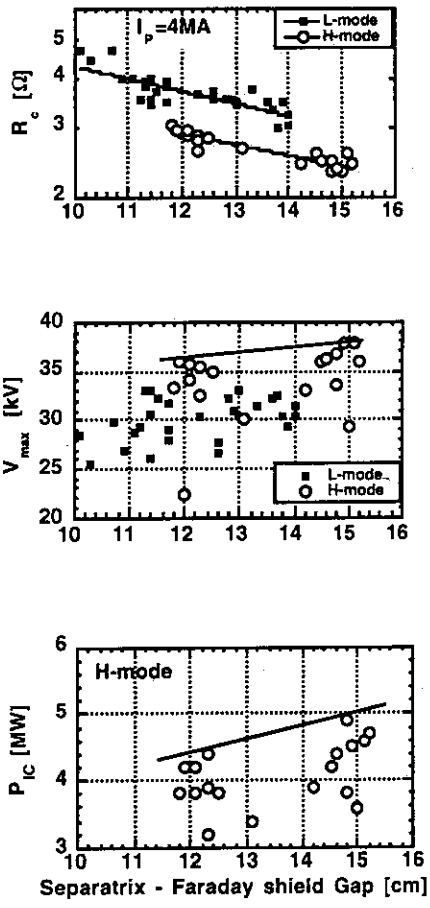

Fig. 2 High power ICRF injection is rather difficult with smaller S-F gap.

3. SOL Density Profile measurement during ICRF Heating

Density profile of the scrape off layer (SOL) plasma during ICRH is measured by a reciprocating probe. Relationship between the density profile and the antenna coupling resistance is examined. SOL plasma density and its decay length increase outside a point of ~3cm from the separatrix with ICRF heating as shown in Fig.3. If the increase of SOL density by ICRF is expected in ITER as observed in JT-60U, antenna design to obtain enough coupling resistance will be easier.

Using the measured SOL density profiles, antenna coupling resistance is calculated with a ICRF wave coupling code [2]. The coupling resistance calculated by the code including the 2nd slope in the SOL density profile shows good agreement with the measurement.

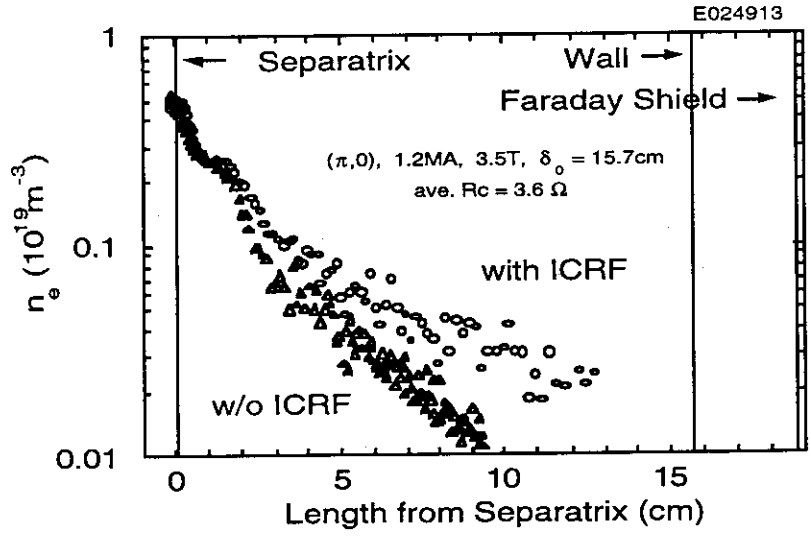

Fig. 3 Measured SOL density profile with and without ICRF heating. The second component of the profile produced in outer SOL region by ICRF heating. It helps higher coupling resistance.

4. Coupling Improvement with Large S-F Gap

A new trial for coupling with large S-F gap using low $n_{//}$ (135°-phasing) ICRF wave was further studied after the experiments in 1994 [1]. A peak value of the toroidal refractive index spectra is ~ 2.1 for the 135°-phasing, ~ 2.7 for the π-phasing. In the experiment in 1994, the coupling resistance was improved in the $n_{//}$ ~ 2.1 case, compared to the $n_{//}$ ~ 2.7 case as shown in Fig. 4. However, heating efficiency of $n_{//}$ ~ 2.1 is lower than that of $n_{//}$ ~ 2.7, especially at high density ($\bar{n}_e$ ~ $2.5 \times 10^{19} m^{-3}$) as shown in Fig. 5. Possible physical picture is as follows ; The wave scattered in the high field side SOL plasma at the cut off density heats a wide region of plasma because of low single-pass absorption in a low $n_{//}$ case. In the contrary, in high $n_{//}$ case, the wave absorption is concentrated in the plasma core because of high single-pass absorption. It is expected that absorption of low $n_{//}$ waves is improved by the high energy ion tail. Then, combined heating with hydrogen-NBI in helium majority plasma tried. Heating efficiency with the hydrogen-NBI for the $n_{//}$ ~ 2.1 heating was significantly improved as expected and is close to that for $n_{//}$ ~ 2.7 as shown in Fig. 6. Heating efficiency for $n_{//}$ ~ 2.7 and $n_{//}$ ~ 0 was also improved.

Coupling resistance at the S-F gap of 15 cm (a design parameter of ITER) for $n_{//}$ ~ 2.1 is ~ 5 Ω which is about two times higher than that for $n_{//}$ ~ 2.7.

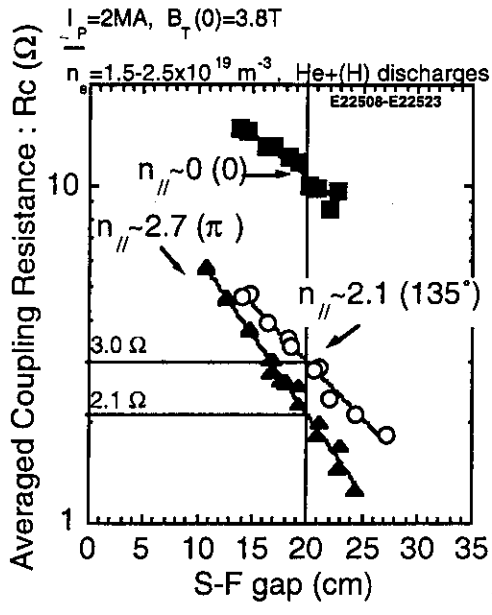

Fig. 4 Coupling resistance was improved in the $n_{//}$ ~ 2.1 case comparing to the $n_{//}$ ~ 2.7 case.

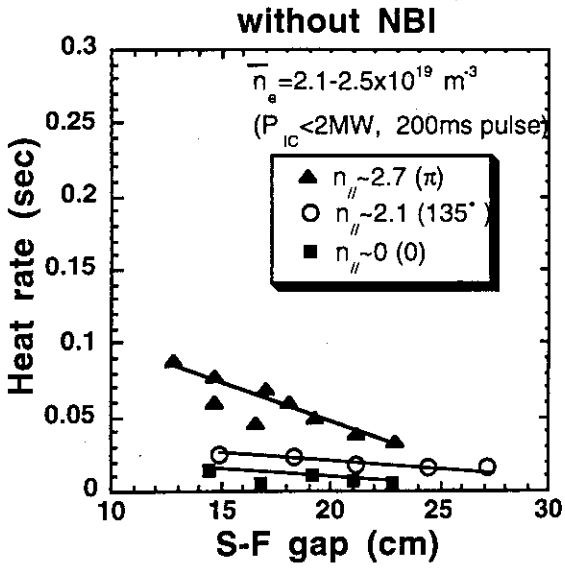

Fig. 5 Heating efficiency of $n_{//}$ ~ 2.1 is lower than that of $n_{//}$ ~ 2.7 especially at high density ($\bar{n}_e$ ~ 2.5x10^{19}m^{-3}).

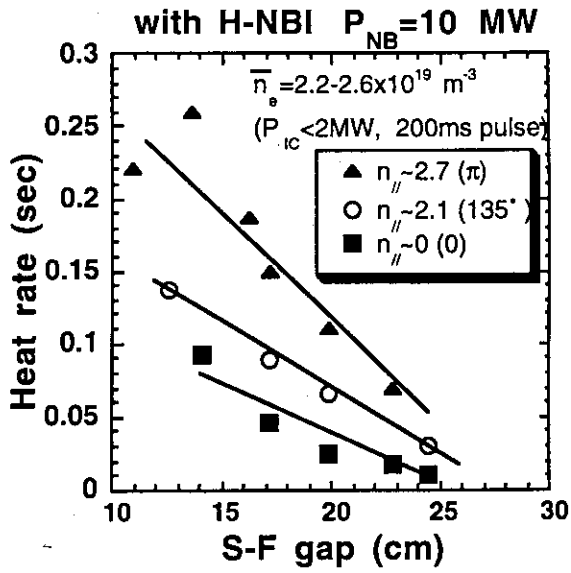

Fig. 6 Heating efficiency for the $n_{//}$ ~ 2.1 heating is significantly improved as expected and is close to that for $n_{//}$ ~ 2.7, by injecting hydrogen-NBI .

5. Summary

The long distance ICRF heating of H-mode plasma was successfully demonstrated. The ICRF power of 5MW was coupled with 15 cm (ITER designed value) of Separatrix-Faraday shield gap and effective heating was observed. The long distance coupling is effective to reduce heat load including the particle bombardment to the antenna.

It is found that the density profile at scrape off layer (SOL) plasma is changed by ICRF. The second slope in the SOL appears near the ICRF antenna and gives higher coupling resistance. This can make ITER antenna design easier.

Coupling was improved with low $n_{//}$ (~ 2.1) wave. 140% power can be coupled with 20 cm of S-F gap, compared to $n_{//}$ ~ 2.7 case. The heating efficiency is improved with lots of high energy ions, suggesting possibility of long distance ICRF heating in ITER.

References

1) Kimura H. et al.; Invited Paper for 11th Topical Conf. on RF Power in Plasmas (1995).

2) Kimura H. et al.; Proc. 4-th Joint Varenna-Grenoble Int. Symp. on Heating in Troidal Plasmas, **2**(1984)1128.

8.2 Study on Confinement Improvement for ICRF Heated Plasmas on Antenna-Plasma Gap and Plasma Volume

T. Fujii, H. Kimura, M. Saigusa, S. Moriyama, Y. Kusama, M. Nemoto, V. I. Afanassiev*

* A. F. Ioffe Physical-Technical Institute, St. Petersburg, 194021, Russia

1. Introduction

Ion cyclotron range of frequencies (ICRF) heating is one of strong plasma heating methods for reactor grade tokamaks. Second harmonic ICRF heating for minority ion has been carried out on JT-60U and its heating properties have been studied. Sufficient heating has been achieved in wide ranges of plasma parameters, especially in a line-average electron density range (1 - 5) x 10^{19} m^{-3}. By strong heating for the plasma core the sawtooth oscillation is stabilized[1], and then the plasma energy confinement is improved by 20 - 30%. Here another improvement mode on plasma confinement for ICRF heated plasmas is found on the plasma configuration with carefully adjusted the antenna-plasma gap and the plasma volume. Its improvement properties and mechanism are investigated.

2. Experimental Results

The ICRF heating experiment for study on confinement improvement is performed for helium plasmas with hydrogen ion minority at B_{t0} = 3.8 T and I_P = 2 MA. The concentration of hydrogen ion is estimated as 10% - 20% from the increase in the plasma density by hydrogen gas puffing before the ICRF pulse. ICRF phasing is (π,0) mode and injection power is in a range of P_{IC} = 1.5 MW - 7 MW.. Figure 1 shows the difference in plasma heating performance between two shots, E25140 and E25147. For these shots, the plasma density is similar ($\bar{n}_e$ = 3.2 x 10^{19} m^{-3} for E25140, $\bar{n}_e$ = 3.5 x 10^{19} m^{-3} for E25147) and the injection power is almost same (P_{IC} = 4.0 MW for E25140, P_{IC} = 4.5 MW for E25147). The heating performance, however, is quite different. The central electron temperature $T_e(0)$ rises from 2.2 keV to 5.4 keV and the stored energy W_{DIA}, measured by a diamagnetic loop, increases from 1.15 MJ to 2.28 MJ for E25147, while $T_e(0)$ from 2.4 keV to 4.7 keV and W_{DIA} from 1.06 MJ to 1.88 MJ for E25140. Therefore, the heating efficiency defined as $\Delta W_{DIA}/(P_{IC} + \Delta P_{OH})$ is larger by about 30% for E25147. The sawtooth oscillation is stabilized for both shots, further more, TAE mode[2, 3] is not observed. The high heating efficiency for E25147 is not caused by the sawtooth stabilization although the heating efficiency is normally improved by it. There is, however, much difference in tail temperature of atomic hydrogen flux as T_{tail} = 224 keV for E25147 and T_{tail} = 181 keV for E25140. Then this difference in T_{tail} is not a cause of high heating efficiency and rather a result due to different heating efficiencies.

What is different between the two shots is the plasma configuration, as shown in Figs. 2 (a) and (b) . The antenna-plasma gap (exactly separatrix-Faraday shield gap) δ_{S-F} is 12.6 cm for E25140 and 9.5 cm for E25147, which is a key parameter and further the plasma volume is

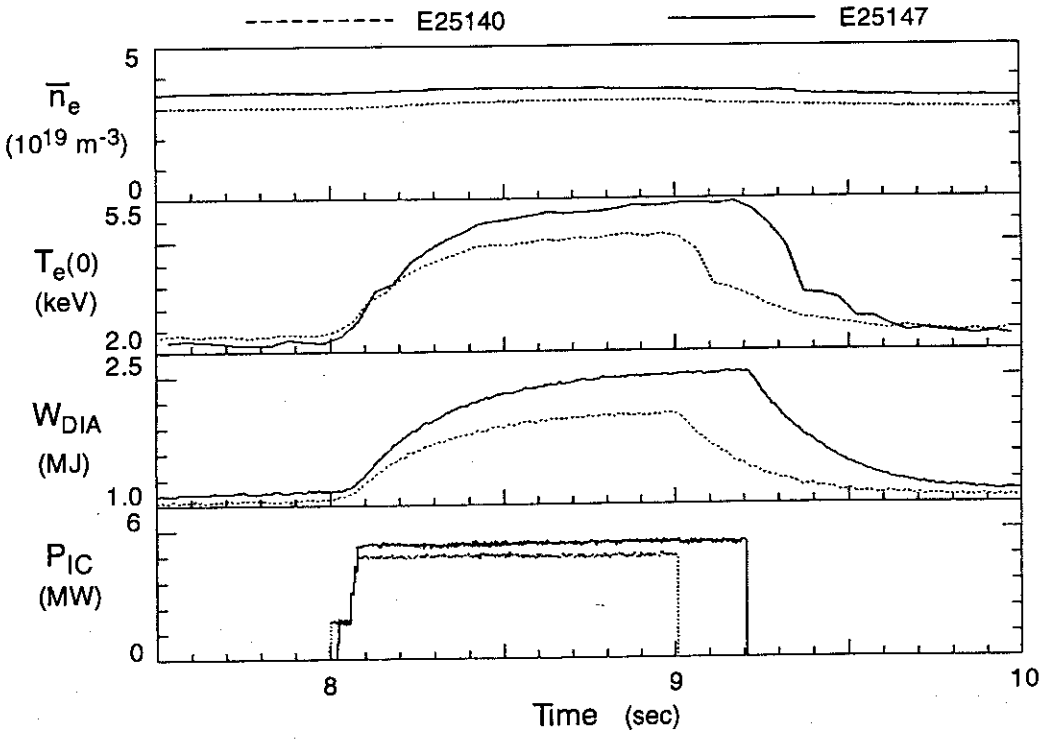

Fig. 1 Comparison of plasma heating between two shots, E25140 and E25147.

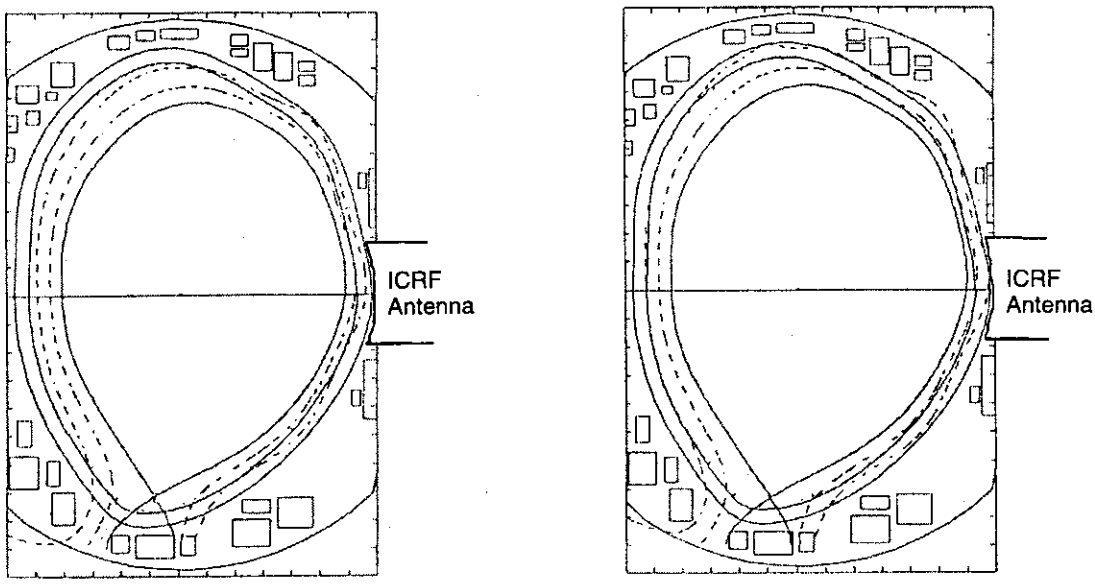

(a) E25140 (b) E25147

Fig. 2 Plasma configurations for the shots shown in Fig. 1.

slightly different as V_p = 91 m^3 for E25140 and V_p = 93 m^3 for E25147. It is noted that the plasma volume must be expanded in order to make the plasma close to the antenna. If the plasma with its volume < 88 m^3 is close to the antenna ($\delta_{S\text{-}F}$ < 11 cm) for this series, the breakdown at the antenna front, especially at the Faraday shield arises at power levels of 3 - 4 MW and the ICRF pulse length is limited to less than 0.8 sec. The relation of the confinement

improvement to the antenna-plasma gap is examined by shifting the plasma position for limited plasma parameters of V_p = 91 - 93 m^3, $\bar{n}_e$ = (3.2 - 3.6) x 10^{19} m^{-3} and P_{IC} = 4 - 5 MW. Figure 3 indicates the energy confinement improvement, H-factor as a function of δ_{S-F}. The H-factor is defined as $\tau_E/\tau_{E(ITER89)}$, where $\tau_{E(ITER89)}$ (sec) = 0.048 $I_p^{0.85}$(MA) $R_p^{1.2}$(m) $a_p^{0.3}$(m) $n_e^{0.1}$($10^{20}m^{-3}$) $B_t^{0.2}$(T) $(A_{eff}\kappa)^{0.5}$ $P_{abs}^{-0.5}$(MW), and in the estimation of $\tau_{E(ITER89)}$ the effective mass number for helium is assumed as A_{eff} = 1.8 because of 10% - 20% hydrogen concentration. It is found that the energy confinement is improved by about 20% for the condition of δ_{F-S} < 10 cm. The improvement mechanism has not yet been understood. However, varies changes in the edge plasma behavior are observed for the high efficiency mode which means the heating efficiency is higher as in the shot E25147 than normal shots ($\tau_E/\tau_{E(ITER89)}$ ~ 1). The one-turn loop voltage shifts up and down within 200 ms of the beginning of the ICRF pulse and the H_α signal drops during that time. Moreover, the antenna loading resistance decreases from a high value to a normal value, which is quite sensitive to the edge plasma density and its gradient. Then it is probably that the edge plasma density changes for the high efficiency mode, but any measurement of the edge plasmas density has not yet been performed during ICRF heating at high power levels.

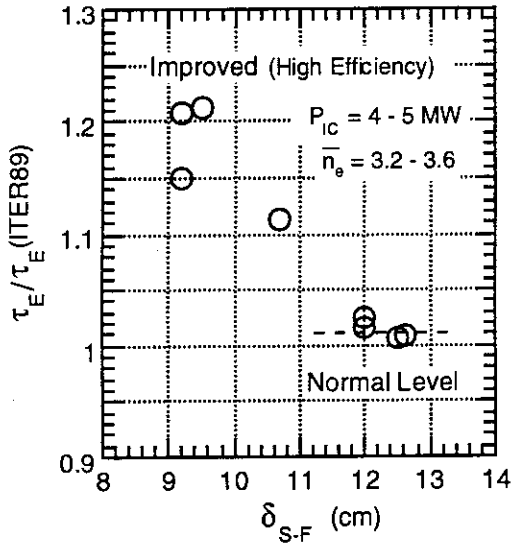

Fig. 3 $\tau_E/\tau_{E(ITER89)}$ as a function of δ_{S-F}.

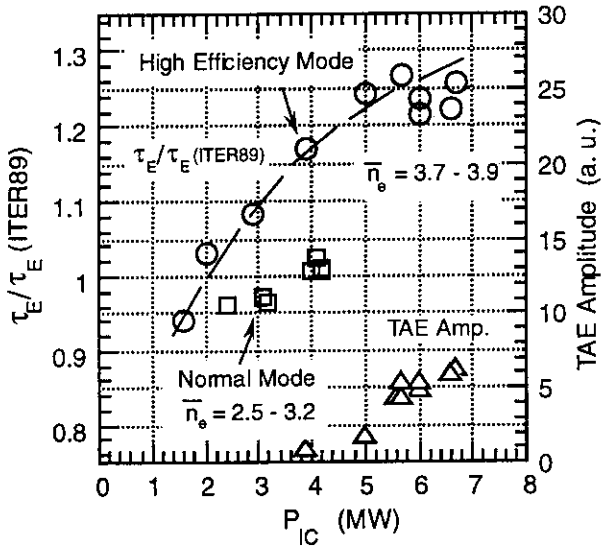

Fig. 4 $\tau_E/\tau_{E(ITER89)}$ and TAE mode amplitude versus P_{IC}.

Figure 4 shows the H-factor and the TAE mode amplitude versus P_{IC} at $\bar{n}_e$ = (3.7 - 3.9) x 10^{19} m^{-3} for the high efficiency mode and at $\bar{n}_e$ = (2.5 - 3.2) x 10^{19} m^{-3} for normal mod. The H-factor increases with P_{IC} and tends to be saturated to $\tau_E/\tau_{E(ITER89)}$ = 1.3 at power levels P_{IC} ~ 6 - 7 MW. The TAE mode is excited from P_{IC} ~ 5 MW and seems to correlate to the saturation of the H-factor. The stored energy, however, is quite slightly degraded and rather the central electron temperature is fairly affected by the TAE mode activities. At low power levels P_{IC} < 3 MW the power dependence of H-factor is similar to that for the normal

mode. Similar power dependence is also observed for the tail temperature as shown in Fig. 5. Thus it can be concluded that the power dependence of the H-factor at least for $P_{IC} < 3$ MW is caused mainly by the improvement of the power absorption by the energetic ions.

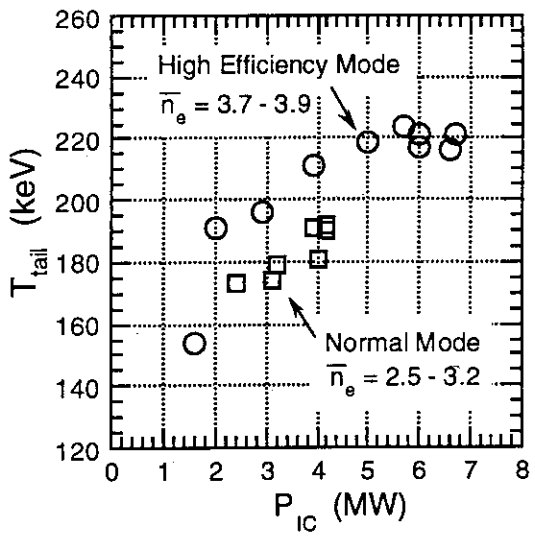

Fig. 5 Tail temperature T_{tail} versus P_{IC}.

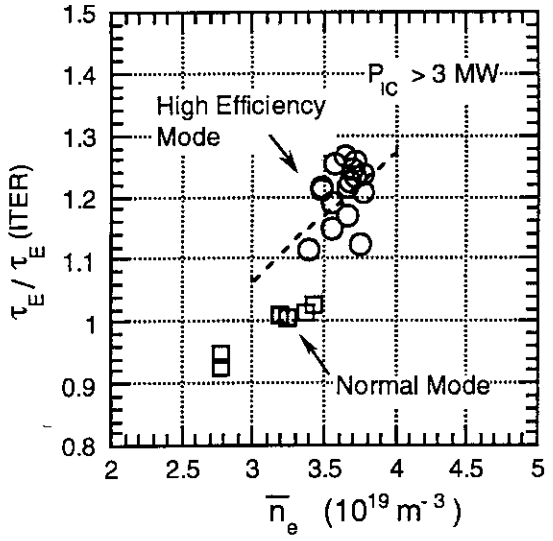

Fig. 6 τ_E/τ_E(ITER89) versus electron density.

Figure 6 shows the H-factor as a function of the electron density for $P_{IC} > 3$ MW. The H-factor tends to increase with the electron density for both modes. This means the energy confinement time has stronger density dependence than the ITER89 power low. Then it is important to examine the density dependence of the H-factor at higher densities and the H-factor for the high efficiency mode is expected to reach to 1.5 at densities $\bar{n}_e \sim 5 \times 10^{19}$ m^{-3}. But the H-factor at such high densities is not improved in this series, because the densities are close to the density limit for OH plasmas at $I_P = 2$ MA. Further studies on the confinement improvement for high densities are left.

3. Summary

The experiments are carried out to study the high efficiency mode for second harmonic ICRF heated plasmas on JT-60U. The following results are obtained. (1) The high efficiency mode is produced for the conditions of $\delta_{S-F} < 10$ cm and the plasma volume > 88 m^3 where the breakdown at the antenna front is suppressed. (2) The H-factor, τ_E/τ_E(ITER89) is improved by 20% - 30% . (3) The power dependence of the H-factor for $P_{IC} < 3$ MW is caused mainly due to the improvement of the power absorption by the energetic ions. (4) The H-factor tends to increase with the electron density up to τ_E/τ_E(ITER89) ~ 1.3.

References

1) H. Kimura et al. ; Fusion Engin. and Design, **26** (1995) 95.

2) H. Kimura et al. ; Phys. Letters A, **199** (1995) 86.

3) M. Saigusa et al. ; Plasma Phys. Control. Fusion, **37** (1995) 295.

8.3 Gamma-ray and neutron measurements in second harmonic minority ion ICRF heating

T. Kondoh, H. Kimura, M. Saigusa, T. Fujii, S. Moriyama, M. Nemoto,
K. Tobita, A. Morioka, K. Nagashima, T. Nishitani, and Y. Kusama

1. Introduction

Behavior of MeV-ions in tokamak plasma is important to investigate for the design of the fusion devices in which MeV-ions will be produced. In this paper, MeV-energy protons (2 - 6 MeV) were accelerated by Ion Cyclotron Range of Frequency (ICRF) heating in order to simulate fusion produced particles in DT reactors and characteristics of the fast ion were investigated with γ-ray and neutron measurements.

2. Experiments and measurements

Experiments were carried out by means of H-minority second harmonic ICRF heating[1] (f_{RF} = 116 MHz, $P_{RF} \leq 7$ MW) with helium as working gas. Gamma-ray spectra in an energy range of 1 to 20 MeV were measured by 5" x 5" NaI(Tl) scintillator and photomultiplier combination surrounded by 50 cm polyethylene and 30 cm lead shield. Schematic view of the measurement system is shown in fig. 1, which shows collimated viewing area in the center of the plasma. The detected signal is processed by CAMAC and pulse height analyzed into 256 channels every 50 ms.

3. Line γ-rays and neutron emission

Typical measured γ-ray spectra are shown in fig. 2 for various values of the line-average electron density. The energies of observed γ-ray lines were 2.1, and 4.4 MeV, which corresponded to the energy level of first excited state of impurity nuclei, respectively. The intensities of the lines are strongly depend on the electron density. Those γ-rays were emitted from inelastic collisions of high energy protons with impurity nuclei of ^{11}B and ^{12}C with threshold proton energy, E_{th}, of 2.5, and 5.0 MeV, respectively.

$^{11}B + p \rightarrow {}^{11}B + p' + \gamma$ (2.1 MeV) (E_{th}>2.5 MeV)

$^{12}C + p \rightarrow {}^{12}C + p' + \gamma$ (4.4 MeV). (E_{th}>5 MeV)

Consequently, it is obvious that the protons were accelerated to the energy more than 5 MeV.

To identify the origin of the γ-ray lines (from the first wall or from impurities in the plasma), neon gas was injected as impurity during 2nd harmonic ICRF experiments. Since line spectrum of the neon (1.7 MeV) which corresponds to the first excited energy of ^{20}Ne was observed as shown in fig. 3, γ-ray lines were originated from impurity ions in the plasma.

In these experiments, neutron signal which originated from reaction $^{11}B+p \rightarrow {}^{11}C+n$ that has threshold energy of 3 MeV was also detected. Some fraction of neutron signals in the ICRF heated plasmas are originated from interaction between lost fast protons and boron at

the first wall. Using this reaction, we have examined the interaction between first wall and MeV-ions (E > 3 MeV) as well as by γ-ray measurements.

4. Behavior of neutron and γ-ray signals after sawtooth crash

The two distinct kinds of temporal behavior of neutron and γ-ray signals after sawtooth crash were observed: (i) slow (~100 ms) and (ii) fast increase (~ 5 ms) in the neutron signal. In the giant sawtooth crash case, the slow rise superposing the fast rise was observed as shown in fig. 4, while in the mini sawtooth crash case, only the fast rise was observed as shown in fig. 5. When neutron signal slowly increases, the γ-ray signal also increases; the increase can be explained by an influx of the boron impurity to the plasma, accompanied with the giant sawtooth crash. Fast rise in the neutron signal is originated from the interaction between lost fast protons and boron at the first wall.

5. Confinement of MeV-ions

In order to investigate the confinement characteristic of MeV-energy protons, dependence of the γ-ray intensity as a function of slowing down time is plotted in fig. 6. Observed γ-ray intensity has strong correlation with $T_e^{1.5}/n_e$ (∝ classical slowing down time). This result suggests that orbital loss process of the ICRF-heated fast ions (2- 6 MeV) in the center is small compared with slowing down process.

6. Energy distribution of MeV-ions through γ-ray spectroscopy

Energy distribution of ions in a range of 2-6 MeV was estimated from intensity ratio of the γ-ray lines. The tail temperature was estimated to 0.6 - 2 MeV which strongly depended on electron density. The tail density was evaluated to be about 2×10^{17} m^{-3} from intensity of the γ-rays which was consistent with tail stored energy estimated by a diamagnetic measurement.

7. Conclusions

(1) γ-line of 1.7, 2.1, and 4.4 MeV were detected these were caused by inelastic collision of proton and ^{20}Ne, ^{12}C, and ^{11}B, respectively.

(2) The two distinct kinds of temporal behavior of neutron and γ-ray signals after sawtooth crash were observed: (i) slow (~100 ms) and (ii) fast increase (~ 5 ms) in the neutron signal..

(3) From the rough estimation, the tail temperature was estimated to 0.6 - 2 MeV and the tail density was evaluated to be about 2×10^{17} m^{-3}

References

1) M. Saigusa et al., in Plasma Physics and Controlled Nuclear Fusion Research 1994 (Proc. 15th Int. conf. Seville, 1994), Vol. 1. IAEA, Vienna (1995) 453.

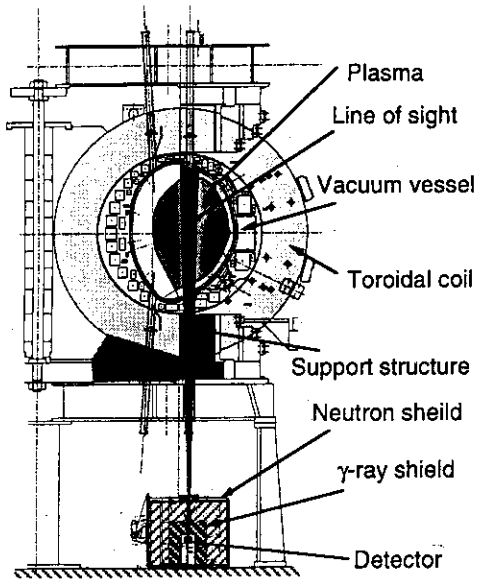

Fig. 1 Schematic of gamma ray measurement system.

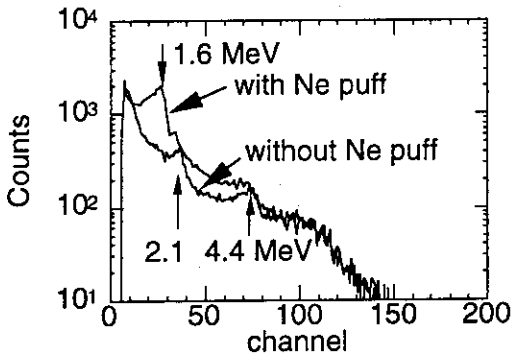

Fig. 3 Gamma-ray spectra with and without neon gas puff.

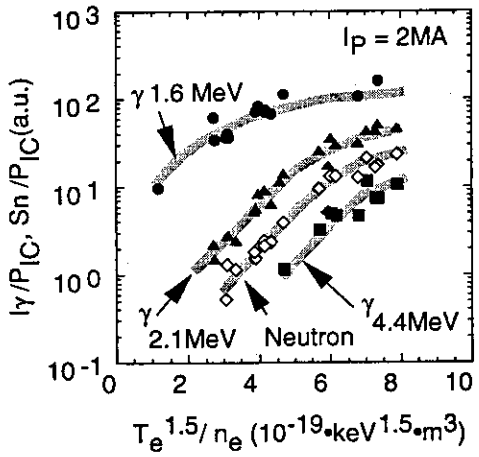

Fig. 6 Gamma-ray and neutron intensity versus $T_e^{1.5}/n_e$.

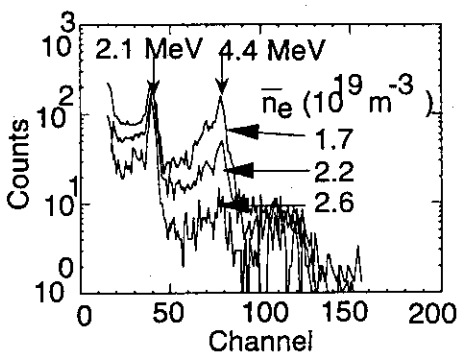

Fig. 2 Gamma-ray spectra in the 2nd harmonic ICRF heating experiment for various values of electron density.

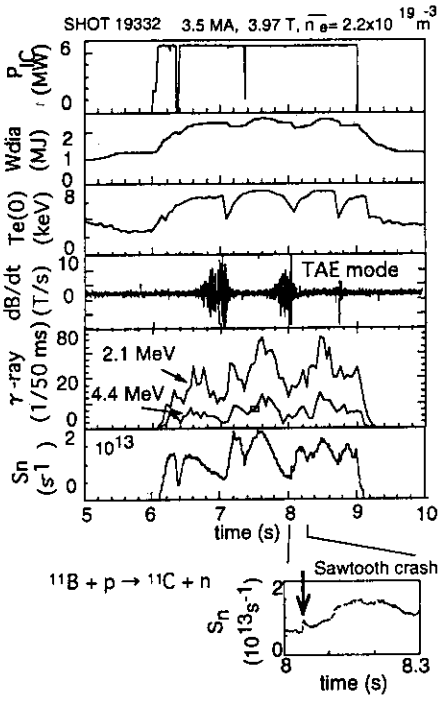

Fig. 4 Typical example of the plasma parameters of 2nd harmonic ICRF experiment. The gamma-ray lines of 2.1 and 4.4 MeV, and neutrons originated from ^{11}B were observed. After sawtooth crash, a slow rise superposing a fast rise in neutron intensity.

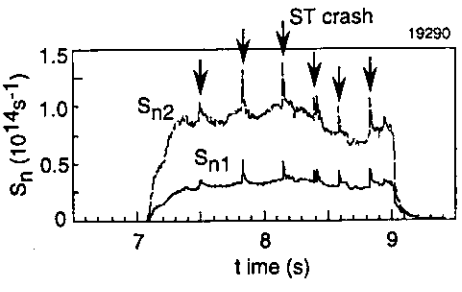

Fig. 5 After sawtooth crash, a fast rise in neutron intensity was observed.

8.4 Proton acceleration in MeV energy range with ICRF and Hydrogen-NB

M. Nemoto, Y. Kusama, V. I. Afanassiev*, K. Hamamatsu, H. Kimura, T. Fujii,
S. Moriyama and M. Saigusa
*) *A. F. Ioffe Physical-Technical Institute, St. Petersburg, 194021, Russia*

1. Introduction

Toroidicity-induced Alfvén eigen (TAE) mode is an intense instability which degrades the confinement of a-particles, and its' investigation has been done with some middle and large tokamaks. Experiments for suppression of TAE mode are carrying out with ICRF and/or NB on DIII-D, TFTR, JET and JT-60U. Since different characteristics are obtained by using of different heating methods, relation between energy distribution of MeV ions and the excitation of TAE mode needs to be investigated, i. e., behavior of passing ions is a key in tangential NB heated plasmas, and one of trapped ions is important in ICRF heated plasmas. In the case of ICRF heating, understanding to characteristics of the ion energy distribution up to MeV energy range is required at first. There is a possibility that higher harmonic ICRF wave heating is available to production of various perpendicular energy distributions, because acceleration by ICRF wave depends on harmonic number[1].

In order to investigate energy distribution in MeV range, we produced simultaneously heating plasmas with NB and ICRF wave of the second harmonic to the fourth harmonic of hydrogen ($2\omega_{CH}$-$4\omega_{CH}$), and measured characteristics of MeV energy ions first and directly with a newly installed neutral particle energy analyzer[2]. Relation between measured energy distributions and improvement of plasma performance is investigated, and the measured characteristics are compared with prediction from the 1-D Fokker-Plank code incorporating the kinetic wave equation[3]. Moreover, characteristics of measured energy distributions to absorbed ICRF power are investigated.

2. Experimental set-up

For characterization of higher harmonic dependence, we scanned toroidal magnetic field on plasma center $B_T(0)$ from 1.59 T to 3.74 T to vary harmonic number n and a location of a resonance layer for hydrogen, shot by shot. Range of the location is shown in Fig. 1. Other resonance layers are out side of the plasma. Both ICRF frequency of 116 MHz and a plasma configuration shown in Fig. 1 are fixed in all of discharges. Other parameters are major radius of plasma R_0~3.54 m, plasma current I_p=1.3-1.5 MA and electron density $\overline{n_e}$=(1.6-2.5)×10^{19} m^{-3}. Here, I_p is regulated to produce stable plasmas in lower B_T condition. Hydrogen neutral beams are injected into plasmas which are helium majority and hydrogen minority. Perpendicular NB units inject NB power P_{NBI}

of 6.4-7.7 MW, and beam lines of them are though plasma core as shown in Fig. 1. ICRF power of 2.7-3.1 MW is injected from launchers installed on ports of low field side. Aiming at efficient plasma heating with ICRF wave, phasing of ICRF wave is set on $(\pi,0)$ mode. Atomic hydrogen flux is measured by the neutral particle energy analyzer (NPA) in a range from 0.25-1.0 MeV. The NPA sights plasma core vertically, as shown in Fig. 1.

For characterization of absorbed ICRF power dependence, we scanned ratio of injected ICRF power to NB power. Plasma configuration and ICRF wave condition are the same as ones in above B_T scan experiment, except for Ip=2 MA. Injected ICRF and NB powers are 2.1-3.0 MW and 1.3-11.7 MW, respectively.

3. Experimental results and discussion

Fig. 2 shows time evolutions of plasma parameters in a typical discharge with $B_T(0)$=3.74 T and Ip=1.5 MA. From the top column, $\bar{n}_e$ is line averaged electron density, W_{dia} is diamagnetic plasma stored energy, P_{IC} is ICRF power, P_{NBI} is injected NB power, and $T_e(0)$ is the central electron temperature measured with electron cyclotron emission measurement system.

Typical energy spectra obtained in those discharges are shown in Fig. 3. For evaluation of T_{tail} in all discharges, it needs setting a constant energy range. Here, we use 0.25-0.8 MeV in where data points in all discharges trend a good linearity. T_{tail} increases according to increase of n, and it is contrary to the previous result obtained in the lower energy range[1]. T_{tail} profile peaks at integer n, as shown in Fig. 4. Dependence of T_{tail} on n is estimated with the 1-D Fokker-Plank code incorporating the kinetic wave equation for discharges of integer n. Calculated T_{tail} is also shown in Fig. 4. Dependence of calculated T_{tail} is similar to experimentally obtained T_{tail}, qualitatively. A reason why calculated T_{tail} and experimental one does not agree quantitatively is not specified yet.

The incremental energy confinement time t_E^{inc} ($\equiv \Delta W_{dia}(IC) / P_{IC}$, where $\Delta W_{dia}(IC)$ is increase in diamagnetic stored energy due to ICRF injection) is available to estimate relation between tail formation and improvement of plasma performance. As shown in Fig. 5, τ_E^{inc} profile peaks at integer n, similar to T_{tail} profile. On the contrary, τ_E^{inc} at peaks decreases according to increase of n. These dependence of t_E^{inc} on n are similar to the previously obtained ones[1]. In order to consider the contribution of the accelerated ions to the stored energy, we evaluate the incremental stored energy of the accelerated ions (W_{tail}(cal)). Dependence of $W_{tail}(IC)$ on n is shown in Fig. 5, and it is consistent with the dependence of τ_E^{inc}.

Characteristics of T_{tail} and t_E^{inc} indicate the following. ICRF power is absorbed mainly by beam-injected ions just after ICRF power injection, and the ions are accelerated well. A diffusion coefficient ($D_\perp$) of low n ICRF wave[3] is less than that of high n ICRF wave, because $D_\perp$ depends strongly on the higher-order Bessel function J_{n-1}. Therefore,

in discharges with high n ICRF wave, a few accelerated ions absorb a large part of ICRF power easily, and the ions are accelerated increasingly due to high $D_{\perp}$, i. e., the tail temperature becomes high. Finally, too fast ions will escape from plasma, and improvement of the plasma performance will be lower than that of low n ICRF wave. From the comparison between characteristics in 0.25-1 MeV and ones in 60-120 keV, it is found that the ICRF power absorption by minority ions around NB injection energy dominated plasma performance improved with beam acceleration in ICRF heated plasmas.

For experiment with respect to absorbed ICRF power dependence, we varied P_{IC}/P_{NB} in order to variation of ICRF power absorbed by beam ions, i. e., P_{IC}/P_{NB} is a measure as ICRF power absorbed by one particle (beam ion). Obtained dependence of T_{tail} on P_{IC}/P_{NB} is shown in Fig. 6. It seems that, in range of $P_{IC}/P_{NB}>0.4$ T_{tail} increases according to increase of P_{IC}/P_{NB} in both B_T conditions. This trend is consistent with theoretical prediction that the quasi-linear diffusion term in the Fokker-Planck equation is proportional to the ICRF power absorbed by ions, and it is similar to characteristics measured in 60-120 keV range[4]. Here, increase of T_{tail} in range of $P_{IC}/P_{NB}<0.4$ on $3\omega_{CH}$ discharges is due to plasma heating as a result of higher NB power injection.

4. Summary

Behavior of protons accelerated by ion cyclotron range of frequency (ICRF) wave of $2\omega_{CH}$ to $4\omega_{CH}$ are investigated with simultaneously heated plasmas with neutral beam (NB) and ICRF wave on JT-60U. Energy distribution from 0.25 MeV to 1 MeV is measured with a charge exchange neutral particle analyzer (NPA), and characteristics of the protons are first and experimentally summarized with previously obtained characteristics in a range of 60 keV to 120 keV. As a result, it is found that the ICRF power absorption by minority ions around NB injection energy dominated plasma performance improved with beam acceleration in ICRF heated plasmas.

References

1) H. Kimura, et al., Plasma Phys. Control. Fusion **35**(1993) 845.
2) Y. Kusama, et al., Rev. of Sci. of Instrum. **66**(1995) 339.
3) K. Hamamatsu, et al., Nucl. Fusion **29**(1989)147.
4) H. Kimura, et al., Nucl. Fusion, **31**(1991) 83.

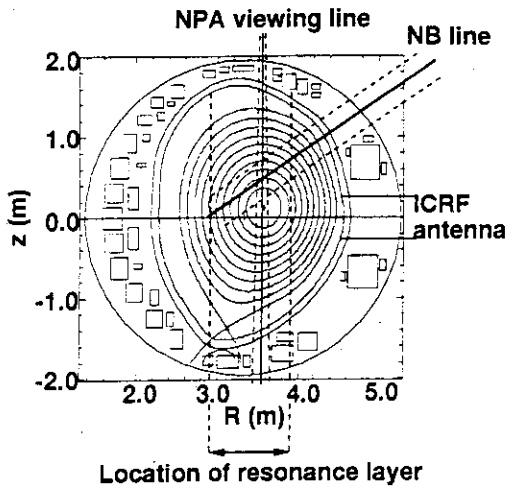

Fig. 1 Arrangement of locating region of resonance layer in 2-4 ω_{CH} discharges.

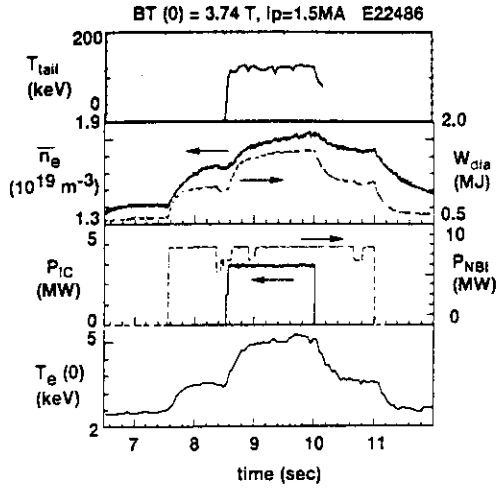

Fig. 2 Time evolutions of typical discharge.

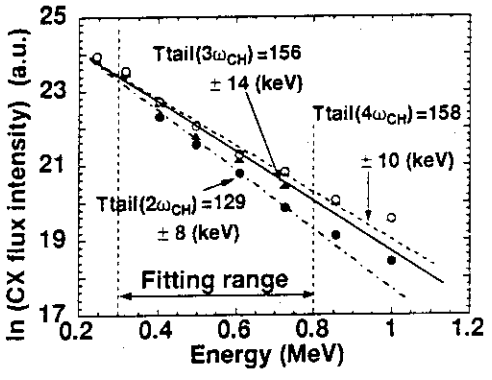

Fig. 3 Measured energy spectra in 2-4 ω_{CH} discharges.

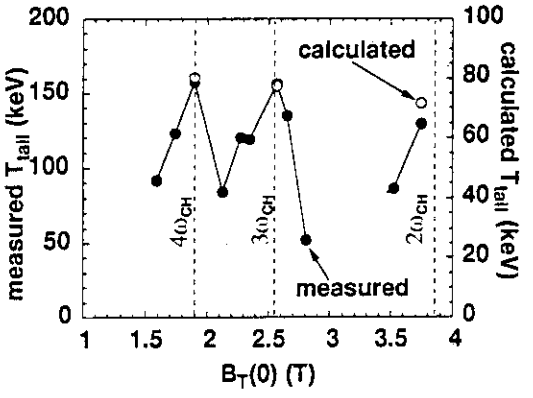

Fig. 4 $B_T(0)$ dependences of measured and calculated T_{tail}.

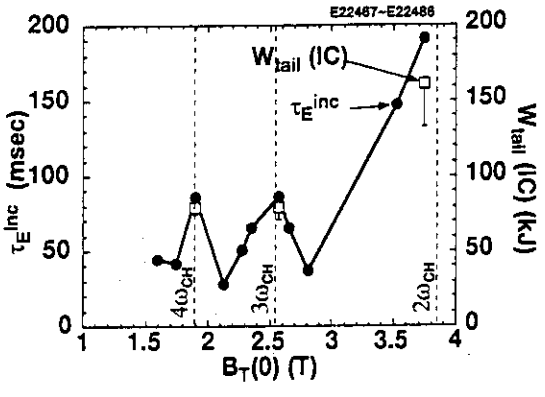

Fig. 5 $B_T(0)$ dependences of measured τ_E^{inc} and and calculated W_{tail} with experimental data.

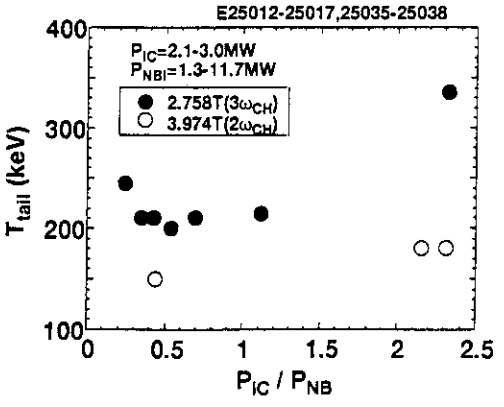

Fig. 6 P_{IC}/P_{NB} dependences of T_{tail}.

8.5 Charge-exchange target effect on measurement of atomic hydrogen energy spectrum in MeV range

V.I. Afanassiev*, Y. Kusama, M. Nemoto, T. Kondoh, A. Morioka,
K. Hamamatsu, S. Moriyama and H. Kimura
*A.F.Ioffe Physical-Technical Institute, Politechnicheskaya 26, St. Petersburg, Russia

1. Introduction

Unexpected large intensity of atomic hydrogen fluxes in a MeV range was measured from neutral particle analysis in ICRF H-minority heating on JET [1] and identified later as related to a strong electron capture reaction between fast tail protons and hydrogen-like impurity ions such as C^{5+} and Be^{3+} [2, 3, 4]. Contribution of direct charge-exchange reaction between beam neutrals and fast protons in 0.3-1.5 MeV range is negligible to be detected[2]. In JT-60U, a role of He^{+} and C^{5+} ions as a charge-exchange target was investigated in He-plasma/H-beam operation, in relation to active charge-exchange effect.

2. Results and discussion

To have a clear experimental evidence of relative role of He^{+} and C^{5+} ions in neutralization process of MeV-energy range protons and to empirically estimate the influence of different target species on charge-exchange measurements in He-plasma/H-beam operation, we carried out the toroidal angle scan experiment. The toroidal angle position of an injected beam was changed shot by shot in ^{4}He-plasma discharges with parameters; B_{to} = 3.8 T, f_{RF} = 116 MHz ($2\omega_{CH}$ resonance), I_p = 2 MA, $n_e = 3\times10^{13}$ cm^{-3}, T_{eo} = 5 keV, T_{io} = 2.5 keV, Z_{eff} = 2.5, P_{IC} =3.2 MW and $P_{NBI}(H_o)$ = 1.3 MW (one perpendicular beam unit injected from the bottom). Energetic atomic hydrogen fluxes were measured with a high energy neutral particle analyzer (NPA) [5]. The dependence of measured hydrogen fluxes with energies of 0.32 MeV and 0.73 MeV on the toroidal angle difference between the NPA location and injected beam location is shown in Fig. 1. The intensity of 0.73 MeV flux is almost constant for positions of beam injection. On the contrary, the low energy flux of 0.32 MeV peaks at the NPA position and decays with the toroidal angle difference. It means that lower energy neutral fluxes are actively enhanced only when neutral beam is injected near the NPA location. Since the charge-exchange fluxes were enhanced in a lower energy rage when a neutral beam in the same toroidal position as the NPA was injected, the tail temperature evaluated over 0.3-0.8 MeV was observed to be decreased about 30%.

Stationary particle balance shows that density of He^{+} and C^{5+} ions in a NBI-heated He-plasma is mainly determined by competition between the charge-exchange reaction with corresponding donor nuclei and the ionization reaction with plasma electrons. For variations of plasma parameters such as $n_e = (1.5\text{-}3)\times10^{13}$ cm^{-3}, T_{eo} = 2-10 keV, T_{io} = 1-5 keV, the electron

ionization rate is not significantly changed and a density ratio $n_{C^{5+}}/n_{He^+}$ depends only on beam density and Z_{eff}. This ratio is evaluated to be 10-15 for plasmas with mentioned parameters and Z_{eff} = 2.5. Figure 2 shows the cross-sections for protons in electron capture reaction with He^+ or C^{5+} ions. The cross-sections are averaged ones over a lot of experimental and theoretical data [6]. In a lower energy range of 0.2-0.5 MeV, electron capture cross-section in reaction with He^+ ions is larger than that with C^{5+} ions. Considering $n_{C^{5+}}/n_{He^+}$ =10-15, their relative neutralization probabilities for $E_p < 0.5$ MeV can be comparable and C^{5+} ion is the dominant for a higher energy range. The mean free path of C^{5+} ion and He^+ ion is mainly determined by electron ionization rate. For plasma parameters of this experiment, we have $\lambda_{He^+} \sim 2.7$ m, $\lambda_{C^{5+}} \sim 33$ m. For particles moving in a toroidal direction along the magnetic field lines, the mean free path is rather different in comparison with one cycle path around the torus ($2\pi R \sim 22$ m, R: major radius of 3.5 m). From these considerations, we can conclude that the contribution of C^{5+} target to active charge-exchange flux is not significantly changed even if neutral beam is injected at different toroidal positions other than the toroidal location of NPA line of sight. On the contrary, we can expect He^+ active target effect only when neutral beam is injected near the NPA location. This active effect is the same order of magnitude as that produced by C^{5+} ion in only a lower energy range of 0.2-0.5 MeV.

Relative portion (p_{rel}) contributing to active charge-exchange flux enhanced with the beam injected at different toroidal position was estimated using next formula:

$$p_{rel} = 0.5 \cdot (e^{-x/\lambda} + e^{-(L-x)/\lambda}) \cdot (1 + e^{-L/\lambda} + e^{-2L/\lambda} + e^{-3L/\lambda} + \ldots) \quad (1)$$

where x is a length of the chord along a torus from the beam to the NPA line of sight, λ is a mean free path of C^{5+} ion or He^+ ion and L is equal to $2\pi R$. This formula is not valid if $L \ll \lambda$ and a poloidal transformation of magnetic field and toroidal and poloidal plasma rotation are not taken into account. In Fig. 1, the dependence of measured hydrogen fluxes on the toroidal angle difference is compared with that expected from Eq. (1) (solid curves). Calculated values are normalized at the NPA location. It should be noted that the measured dependence is in a good agreement with expected one.

In a deuterium plasma operation, the charge-exchange target effect is excluded because carbon impurity only dominates in neutralization process of fast protons. One of examples illustrating this difference between deuterium plasma and helium plasma is presented in Fig. 3. In an "active" phase of discharges, a several units of neutral beams including two (top and bottom) beams at the NPA location were injected simultaneously with ICRF. "Passive" spectra correspond to the ICRF alone phase of discharges. In a case of helium plasma, steeper slope in a lower energy part less than 0.6 MeV is clearly observed in the active phase. On the other hand, no change in spectrum shape is seen for the deuterium plasma case.

Density scan experiment was carried out to check the charge-exchange target effect in helium plasmas when neutral beams are injected. Figure 4 shows the density dependence of effective tail temperature, detected counts of atomic hydrogen fluxes and γ-rays, tail ion stored

energy and H_α emission. The figure compares between ICRF heating alone case [7] and combined ICRF+NBI heating case. For two cases, opposite tendency was observed in effective tail temperature (T_{eff}) and charge-exchange (CX) neutral fluxes. A slight rise tendency of T_{eff} caused by increasing the more energetic atomic flux with plasma density was found for discharges of ICRF heating alone. Meanwhile, significant reduction in 2.1 MeV γ-ray emission reflecting a population of protons greater than 2.5 MeV [8] was observed as well as decrease in the tail ion stored energy (Wtail). It is supposed that the degradation of ion energy spectrum is compensated in atomic fluxes by rather substantial gain of the charge-exchange target density owing to the increase in neutral influx from the wall as seen with H_α emission in the figure. Opposite tendency in T_{eff} and CX fluxes is found in a ICRF+NBI case (closed symbols), where target population is sustained by beam neutrals. These results show that the change in charge-exchange target makes a significant effect on the neutral particle analysis in a MeV range. The validity of the charge-exchange target hypothesis was confirmed.

3 Summary

Relative role of He^+ and C^{5+} ions in fast proton neutralization is comparable in a energy range of 0.2-0.5 MeV for H^0-beam-heated helium plasmas and strongly depends on toroidal position of the injected beam. This makes an active effect in the neutral particle measurement in a MeV range when neutral beam is injected at the same toroidal location as the NPA. In a density scan experiment, the charge-exchange target effect was confirmed to be important in understanding the results of charge-exchange measurement [9].

References

[1] Khudoleev A.V. et al, Tech. Report JET-P(92) 31 (1992).

[2] Petrov M.P. et al, 19th EPS Conference on Controlled Fusion and Plasma Physics 16C(II) (1992) 1031.

[3] Korotkov A.A. et al, 21st EPS Conference on Controlled Fusion and Plasma Physics 18B(I) (1994) 266.

[4] Stuart A. et al., in JET Contributions to 35th Annual Meeting of the APS Division of Plasma Physics (St. Louis) (1993).

[5] Kusama Y. et al, Rev. Sci. Instrum. 66 (1995) 339.

[6] Korotkov A.A. et al, Tech. Report JET (1995), to be published.

[7] Afanassiev V.I. et al, 22nd EPS Conference on Controlled Fusion and Plasma Physics (1995), to be published.

[8] Kondoh T. et al., 21st EPS Conference on Controlled Fusion and Plasma Physics (1994).

[9] Afanassiev V.I. et al, paper in preparation.

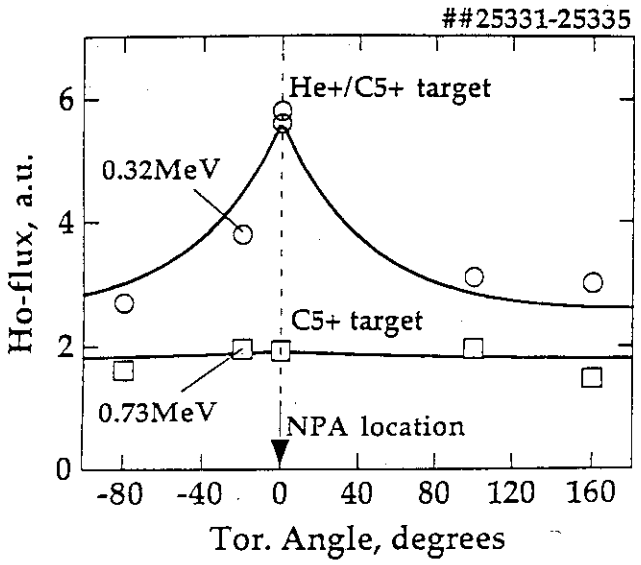

Fig. 1. Dependence of atomic hydrogen flux of 0.32 MeV and 0.73 MeV on toroidal angle difference between the position of injected H^0 beam and the NPA. Solid curves show expected dependence from Eq. (I).

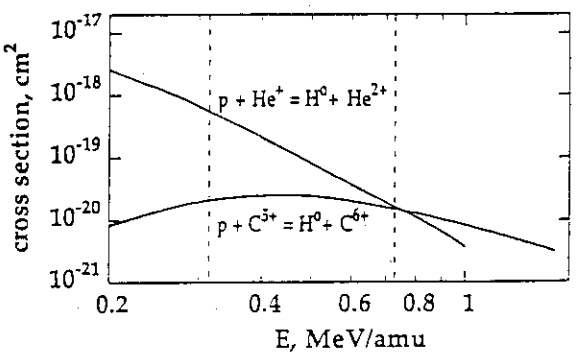

Fig. 2. Electron capture cross-section for fast protons in reactions with He^+ and C^{5+} ions. Energies of 0.32 MeV and 0.73 MeV chosen for analysis of toroidal angle dependence in Fig. 1 are shown with dotted lines.

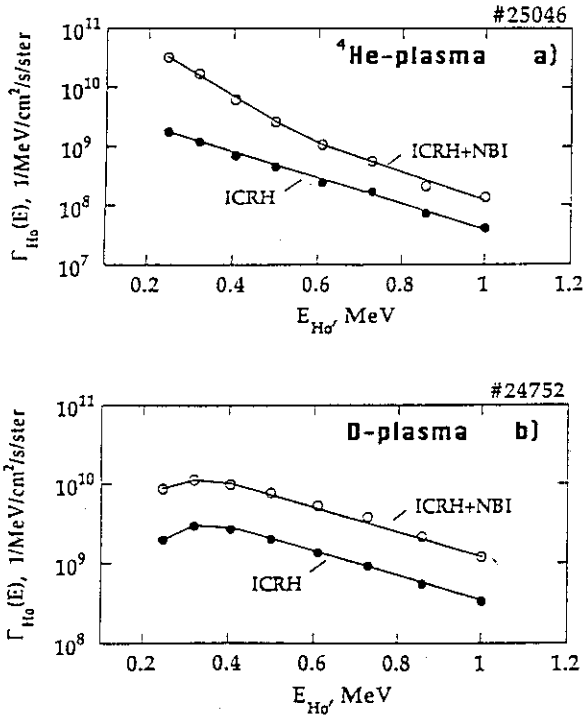

Fig. 3. Comparison between "active" (ICRF+NBI) and "passive" (ICRF alone) energy spectra of hydrogen atoms in a) helium and b) deuterium plasma operation.

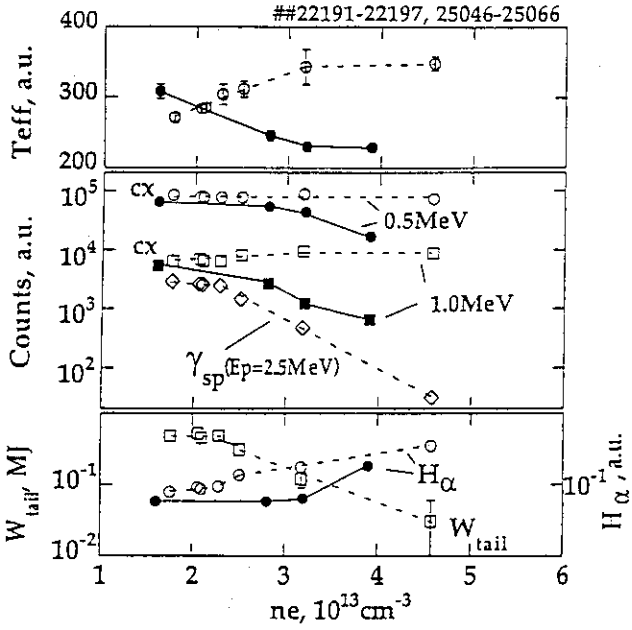

Fig. 4. Dependence of effective tail temperature (T_{eff}), hydrogen fluxes (cx), gamma rays (γ-sp.), tail ion stored energy (W_{tail}) and H_α-emission rate on electron density (n_e). Open symbols are for discharges without NBI and closed ones are for combined ICRF+NBI discharges.

9. TAE Mode

9.1 Effect of the Toroidal Rotation Shear on the Toroidicity-Induced Alfvén Eigen Modes

M. Saigusa, T. Ozeki, H. Kimura, Y. Kusama, T. Fujita, T. Fujii, S. Moriyama, Y. Neyatani

Abstract Toroidicity-induced Alfvén eigen (TAE) modes excited by ICRH was suppressed by the plasma toroidal rotation shear formed by counter-tangential NBI.

Toroidicity-induced Alfvén eigen (TAE) modes [1] are expected to be excited by energetic ions, whose speeds are comparable to the Alfvén speed, in the international thermonuclear experimental reactor (ITER) [2]. The degradation of the energetic particle confinement due to TAE modes was predicted by theoretical calculations [3] and actually observed in experiments [4]. Therefore, the suppression of TAE modes is important for a fusion reactor.

TAE modes have been controlled by changing the current profile [5, 6]. In addition to that, the TAE modes were also suppressed by tangential neutral beam injection (NBI) counter to the direction of the plasma current in JT-60U [7]. The mechanism and the clear experimental evidences for suppressing TAE modes using the counter toroidal rotation were reported in Ref. 8. In this paper, the brief outline of the Ref. 8 are presented.

TAE mode suppression experiments scanning the toroidal rotation have been performed by using ion cyclotron resonance heating (ICRH) and NBI in JT-60U. The time evolution of a typical discharge at a plasma current of 3MA, an effective surface safety factor: q_{eff} of 3.5, and a toroidal magnetic field on axis of 3.8 T are shown in Fig.1. Second harmonic hydrogen ICRH at a frequency of 116 MHz in Deuterium discharges was merely adopted to produce the energetic ions efficiently as a TAE mode driver. The H concentration was estimated to be about 5% with a spectrometer. The counter perpendicular NBI unit (#14) was applied for measuring the profiles of the toroidal rotation velocity with charge exchange recombination spectroscopy (CXRS). Counter tangential NBI (#7b, 1 MW) was applied for measuring the q profile with the motional stark effect (MSE) [9]. Co-tangential NBI (2 MW) was switched to counter-tangential NBI (2 MW) at t = 6.8 s, in order to scan the toroidal rotation, where the accelerated beam voltages were 85 keV. The injection angles of the tangential and perpendicular NB units are ±36° and ±75° with respect to the magnetic axis, respectively. The signals shown in Fig. 1 are the Mirnov coil signal (dB/dt), which corresponds to the TAE mode amplitude at plasma edge, the plasma stored energy evaluated with diamagnetic loop coils (W_{dia}), the line averaged electron density ($\overline{n_e}$), the center cord soft x-ray signal (S_x), the central electron temperature ($T_e(0)$), the toroidal rotation velocities measured with CXRS (V_T) at r=0.31 and 0.43 m, the coupled ICRH power (P_{IC}) of about 4 MW, and the total NBI power (P_{NBI}) of about 5 MW.

The TAE mode appeared about 200 ms after raising the ICRH power over the threshold value (about 3.6 MW) and the amplitude of TAE mode gradually increased during co-tangential NBI. However, the amplitude of the TAE mode decreased gradually after the change of the tangential NBI direction from co to counter streaming at t = 6.8 sec and disappeared abruptly at t=6.98 s. The line averaged electron density was almost constant during the ICRH pulse. The plasma stored energy and the central electron temperature saturated after the appearance of the TAE mode around t=6.7 s and it gradually increased after the suppression of the TAE mode during the ICRH pulse. The soft x-ray signal indicates sawtooth suppression due to the energetic trapped ions produced by ICRH. The direction of the plasma toroidal rotation was always in the counter direction, even if the co-tangential NBI power (2 MW) was two times higher than the counter-tangential NBI power (1 MW) before t=6.8 s.

Figure 2 shows the radial profile of the toroidal rotation velocity of the plasma for the discharge shown in Fig. 1. The closed and open circles show the rotation velocities measured with the CXRS at t=6.7 s and t=7.2 s, respectively. The profile of the toroidal rotation velocity at 6.7 s was almost flat in the radial direction, while a clear shear in counter-toroidal rotation velocity was formed at 7.2 s.

The q profiles measured with the Motional Stark Effect (MSE) at t=6.7 s and 7.2 s for Fig. 1 are shown in Fig. 3. The closed circles and the open squares show the points measured at 6.7 s and 7.2 s, respectively. The solid line shows the fitting q profile which is used for calculating the Alfvén continuum as shown in Fig.4. The MSE data indicate that the q profiles did not change from 6.7 s to 7.2 s within the error bars. Furthermore, the electron density profiles measured with Thomson scattering at t=6.7 s and 7.2 s are almost the same, so that the Alfvén continua did not change from 6.7 s to 7.2 s, except for the effect of the Doppler shift due to the plasma toroidal rotation.

The Alfvén continuum can be controlled not only by the current profile, but also by the toroidal rotation via the Doppler shift. The Doppler shifted shear Alfvén resonance angular frequency at a minor radius of r can be shown as the formula: $\omega_{DAC}(r) \equiv \omega_{AC}(r)+n\bullet V_T(r)/R$, where $\omega_{AC}(r)$ is the shear Alfvén resonance angular frequency in the plasma reference frame, n is a toroidal mode number, and $V_T(r)$ is the local toroidal rotation velocity [8]. The Doppler shifted TAE mode angular frequency can approximately be written as $\omega_{DS} \equiv \omega_{TAE}+n\bullet\tilde{V}_T/R$, where ω_{DS} is the Doppler shifted frequency of the TAE modes in the laboratory frame, ω_{TAE} is the TAE mode angular frequency in the plasma reference frame, and $\tilde{V}_T$ is an effective toroidal rotation velocity which the TAE mode feels.

The toroidal mode number of the observed TAE mode in Fig. 1 is estimated to be 5 or 7. The Doppler shifted Alfvén continua are shown in Fig. 4, where n is assumed to be 7, the effects of Doppler shift are calculated considering the toroidal rotation profiles in Fig. 2. The solid waved lines show the Doppler shifted Alfvén continua at 6.7 s, the dotted waved lines show the Doppler shifted Alfvén continua at 7.2 s. The solid straight line shows the observed

TAE mode frequency at 6.7 s, and the dotted straight line shows the suppressed TAE mode frequency estimated from the Doppler shift due to the toroidal rotation. The abscissa shows the normalized minor radius, while the ordinate shows the angular frequency normalized by ω_0, where $\omega_0 \equiv V_A(0)/(q(a) \cdot R)$, $V_A(0)$ is the Alfvén velocity on magnetic axis, and q(a) is a surface safety factor. The observed TAE mode at 6.7 s intersects the Doppler shifted Alfvén continua at r/a ~0.3 and 1, which is deeper than the suppressed TAE mode at 7.2 s, so that the Doppler shifted Alfvén continuum damping at 6.7 s should be stronger than that at 7.2 s. Therefore, Doppler shifted Alfvén continuum damping of the TAE modes does not seem to be the dominant damping mechanism at t=7.2 s.

TAE modes in a different q profile (q_{eff} ~ 5.2) could be also suppressed by counter-tangential NB injection. Figure 5 shows the time evolution of the two typical discharges at a plasma current of 2 MA, where Fig. 5(a) is for co-tangential NBI and 5(b) for counter-tangential NBI. The behaviors of electron density and the central electron temperature are almost the same in these two discharges. In Fig. 5(a), the amplitude of the TAE modes could have been enhanced by the co-tangential NBI. On the other hand, the amplitude of TAE modes could have been suppressed by the counter-tangential NBI in Fig. 5(b). Figure 6 shows the radial profiles of the plasma toroidal rotation velocity for Figs. 5(a) and 5(b). The closed and open circles show the data for the discharges of E24859 and E24860 at 7.3 s, respectively. The counter-toroidal rotation shear induced by counter-NBI was much stronger than the co-toroidal rotation shear by co-NBI at the same NBI power (~4 MW). Also in this case, the calculated Doppler shifted Alfvén continua could not explain the reason why the TAE mode was suppressed by the increase in the counter toroidal rotation shear.

Phase mixing [10] of TAE mode due to the toroidal rotation shear is thought to be a dominant damping mechanism in these experiments , because the estimated effective rotation shear was consistent with the experimental results [8]. This suppression mechanism is almost independent on n, so that it is also effective for high-n TAE modes.

References

1) C.Z. Cheng et al., Ann. Phys. NY 161, 21(1984).
2) C.Z. Cheng et al., 15 th IAEA Int. Conf., Seville, IAEA-CN-60/D-3-III-2 (1994).
3) D.J. Sigmar et al., Phys. Fluids, **B4**, 1506 (1992).
4) H.H. Duong et al., Nucl. Fusion, **33**, 749 (1993).
5) E.J. Strait et al., Nucl. Fusion **33,** 1849 (1993).
6) H. Kimura et al., Journal of Plasma and Fusion Research, **71**, 1147 (1995).
7) M. Saigusa et al., Plasma Phys. Control. Fusion Res., **37**, 295 (1995).
8) M. Saigusa et al., submitted to Phys. Rev. Lett.
9) T. Fujita et al., submitted to Fusion Eng. Design.
10) H. Grad, Phys. Today **22**, No. 12, 34 (1969).

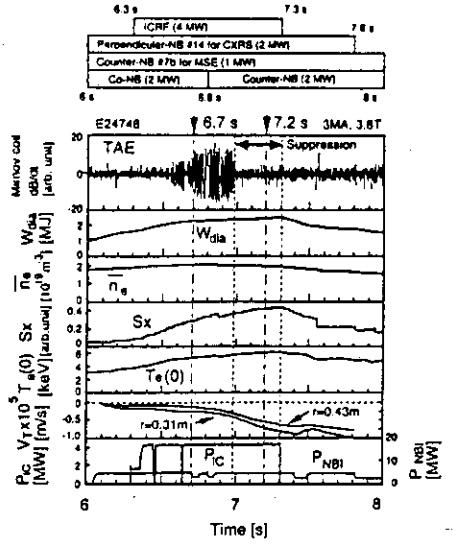

Fig. 1 Time evolution for a typical discharge scanning the toroidal rotation from the co to counter directions using tangential NBI during an ICRH pulse.

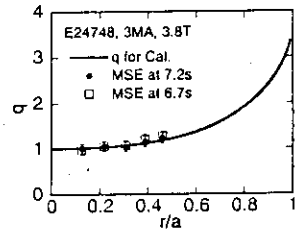

Fig. 3 The q profiles measured with the MSE system for the discharge shown in Fig. 1. The closed circles and the open squares show the points measured at 6.7 s and 7.2 s, respectively.

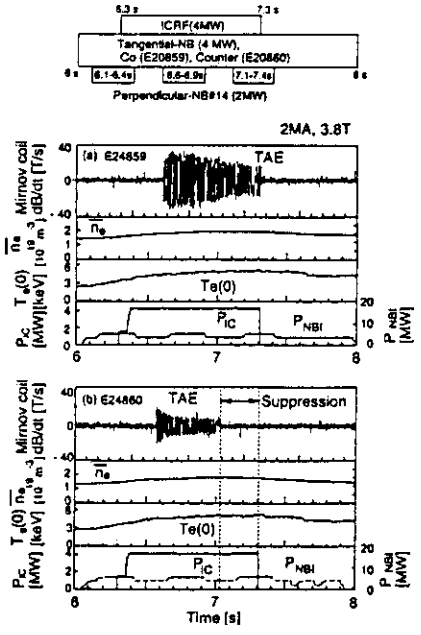

Fig. 5 Time evolution at a plasma current of 2 MA with ICRH and tangential NBI. Fig. 5(a) and 5(b) show the co and counter rotation discharges.

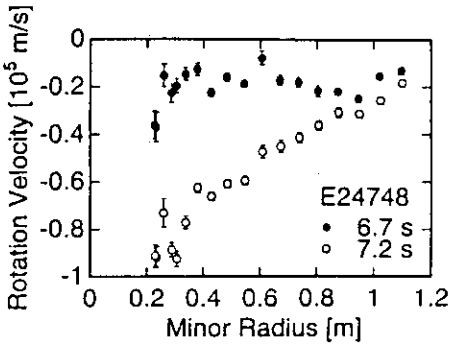

Fig. 2 Radial profile of the toroidal rotation velocity of the plasma for the discharge shown in Fig. 1. The closed and open circles show the data at t=6.7 s and t=7.2 s, respectively.

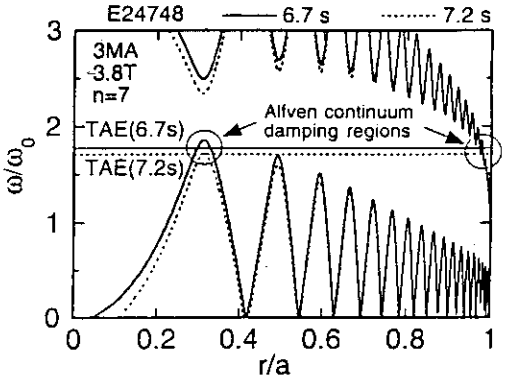

Fig. 4 Doppler shifted Alfvén continua for the discharge shown in Fig. 1. The solid and dotted curved lines show the Doppler shifted Alfvén continua at 6.7 s and 7.2 s, respectively.

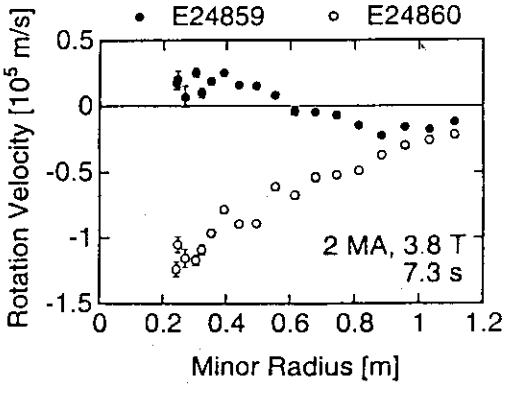

Fig. 6 Radial profiles of the toroidal rotation velocity for the discharges shown in Figs. 5(a) and 5(b). The closed and open circles show the data for the discharges of Fig. 5(a) and Fig. 5(b) at 7.3 s, respectively.

9.2 Initial results of TAE modes excitation with low B_T field

M. Nemoto, Y. Kusama, H. Kimura, M. Saigusa, S. Moriyama, Y. Neyatani
and T. Fujii

1. Introduction

Excitation of TAE modes with ICRF wave has been investigated on JT-60U[1,2,3]. In previous TAE modes experiments on JT-60U, high toroidal field B_T of around 4 T was used because of $2\omega_{CH}$ resonance heating. Since energy of resonating ions is roughly proportional to $(B_T)^2$, the previous investigation focuses on higher energetic ions, such as α-particles.

We need to investigate influence of TAE modes excited by neutral beams produced by negative ion sources (N-NB), because loss of high energetic ions due to TAE modes may lead to difficulty in production of high performance plasmas due to reduction of current drive efficiency. If toroidal mode numbers of excited TAE modes in this low B_T experiment are high, influence on high energy ions around energy range of N-NB (0.5 MeV) will be able to be measured directly by charge exchange neutral particle analyzers (NPA)[4,5]. In addition, behavior of TAE modes in ICRF heating plasmas are based on trapped ions which are accelerated by ICRF perpendicularly ($v_\perp/v \sim 1$). On the other hand, TAE modes may be excited by passing ions ($v_{//}/v \sim 1$) in N-NB experiments. Therefore, as a comparison between different excitation characteristics due to difference in velocity distributions, this experiment is important and valuable.

2. Characteristics of excited TAE modes

The experiment was carried out with following parameters; I_p=2 MA, $B_T(0)$=2.57 T, q_{eff}=3.8, P_{IC}=1.6-5.6 MW, P_{NBI}=8.7 MW and $\overline{n_e}=(1.6\text{-}3.0)\times10^{19}$ m^{-3}. A resonance layer of the third harmonics for hydrogen ($3\omega_{CH}$) was located on plasma center. Hydrogen NB was injected perpendicularly into plasmas which were helium majority and hydrogen minority. Electron density was controlled with helium gas puffing. Figure 1 shows typical time evolutions of plasma parameters. These are, from the top column, fluctuating signal of magnetic field (dB/dt), spectrum of the Doppler-shifted frequency (f_{DS}) which is digitized with fast Fourier transform (FFT) analysis, hydrogen fluxes of 1.0 MeV and 0.5 MeV (N_{proton}) measured by NPA with perpendicular line of sight from top of the torus, toroidal rotation velocity of carbon ion at r/a=0.38 ($v_{toroidal}$) where is around inversion radius on sawtooth crash, diamagnetic plasma stored energy (W_{dia}), line-averaged electron density ($\overline{n_e}$), ICRF power (P_{IC}), NB power (P_{NBI}), neutron yield (S_{neut}) by $^{11}B(p,n)^{11}C$ reaction and the central electron temperature measured by ECE system ($T_e(0)$). TAE modes was excited at 5.3 sec and f_{DS} increased in spite of decrease in $v_{toroidal}$. This behavior was different from the previous experimental results on B_T=3.8 T. Since relation between the

electron density and f_{DS} was similar to that of the previous experiment, the behavior might be caused by variation of q profile, which was not measured by MSE system in this experiment. A sawtooth crash occurred at 5.5 sec, and then *dB/dt* became weak rapidly and S_{neut} decreased. After the crash, W_{dia} and S_{neut} increased in spite of growth of *dB/dt*. NPA was viewing plasma center vertically, and it measured behavior of high energy proton in range of 0.2 MeV to 1.0 MeV. During excitation of TAE modes, NPA did not measure synchronized decrease of the protons. In addition, the tail temperature, which was defined from gradient of energy spectrum in the above energy range, was not changed remarkably. Increase of N_{proton} after the crash suggests that loss of high energetic protons from plasma due to the excitation may be very small and a large amount of the protons was stored in plasmas.

Dependence of amplitude of TAE modes on P_{IC}, in the density range of (1.6-3.0)$\times 10^{19}$ m^{-3}, is shown in Fig. 2. Here, the amplitude is normalized by the square root of the density in order to cancel the dependence of *dB/dt* on the density through the TAE mode frequency f_{TAE} ($dB/dt \propto f_{TAE} \propto (n_i)^{-0.5}$). There is a threshold heating power around 3 MW, and this threshold is the same as the previous result on I_p=3.5 MA and B_T=3.8 T.

The stored energy and the beta thresholds of high energetic ions were roughly estimated. Since we aimed at strong and long excitation of TAE modes first, we injected NB and ICRF powers into OH plasmas simultaneously. As a result of this method, NB heating phase did not exist before simultaneous heating phase and accurate calculation of the incremental stored energy by NB (W_{tail}(NB)) was not possible. Fortunately, we could estimate W_{tail}(NB) from a discharge where ICRF power was not injected unfortunately. At a time when W_{dia} was saturated during NB heating phase, we calculated W_{tail}(NB) with thermal component of stored energy (W_{th}(NB)) as follows; $W_{tail}(NB)=2/3*(W_{dia}-W_{th}(NB))$. Since the discharge was carried out for the excitation in the density range of (1.6-1.8)$\times 10^{19}$ m^{-3}, here, we estimated the fast ion stored energy during ICRF power injection (W_{tail}(IC)) for discharges in that density range only, on the assumption that W_{tail}(NB) was constant in those discharges. Therefore, using thermal component of stored energy (W_{th}(IC)) when ICRF power was injected, equation for the estimation of the fast ion stored energy was given by $W_{tail}(IC)=2/3*(W_{dia}-W_{th}(IC))-W_{tail}(NB)$. The threshold W_{dia}(IC) for the excitation was from 0.1 MJ to 0.2 MJ and the volume-averaged beta threshold ($<\beta_h>$) was from 0.03% to 0.06%. For the stored energy of non-thermal ions which consisted of beam ions and the accelerated ions (W_{tail}(NB+IC)), the threshold was from 0.2 MJ to 0.3 MJ and $<\beta_h>$ was from 0.06% to 0.08%. Here, the stored energy of non-thermal ions was given by $W_{tail}(NB+IC)=2/3*(W_{dia}-W_{th}(IC))$.

Wave frequencies obtained from FFT analysis were in range of 168-196 kHz at (1.7-1.8)$\times 10^{19}$ m^{-3} and 125-135 kHz at (2.8-3.0)$\times 10^{19}$ m^{-3}. These frequency ranges agreed well with wave frequencies measured by RF wave measurement system[6], which

was able to analyze absolutely frequency spectrum of RF wave emitted from plasma. For the discharge shown in Fig. 1, we estimated a radial location of the excited TAE modes and safety factor q at there. Using following parameters; f_{TAE}=175 kHz at t=5.45 sec, A=4, $n_i=8.9\times10^{18}$ m^{-3}, B_T=2.57 T, q became 1.21. Since the inversion radius (q=1) is at R=3.87 m and q at plasma surface R=4.37 m is 4.6, the location became r/a=0.43. They were similar to those of the $2\omega_{CH}$ case with the same q_{eff}.

3. Summary

Using simultaneously NB and ICRF heated plasmas on B_T=2.57 T condition, which corresponds to $3\omega_{CH}$ resonance heating, excitation of TAE modes was made certain and its characteristics were investigated.

Power threshold of ICRF for the excitation was around 3MW, and it was the same as the previous experiment of $2\omega_{CH}$ ICRF heating at B_T=3.8 T. Decrease of high energetic protons was not detected during the TAE modes excitation. Radial locations of the TAE mode gap and q-value were similar to those of the $2\omega_{CH}$ case with the same q_{eff}[3].

References

1) H. Kimura et al., Phys. letter A, 199 (1995) 86-92.
2) M. Saigusa et al., Plasma Phys. Control. Fusion 37 (1995) 295-313.
3) H. Kimura et al., J. Plasma and Fusion Research 71 (1995) 1147-1164.
4) Y. Kusama, et al., Rev. Sci. Instrum. 66 (1995) 339-341.
5) Y. Kusama, et al., see section 12.3 in this report.
6) M. Saigusa, et al., see section 12.7 in this report.

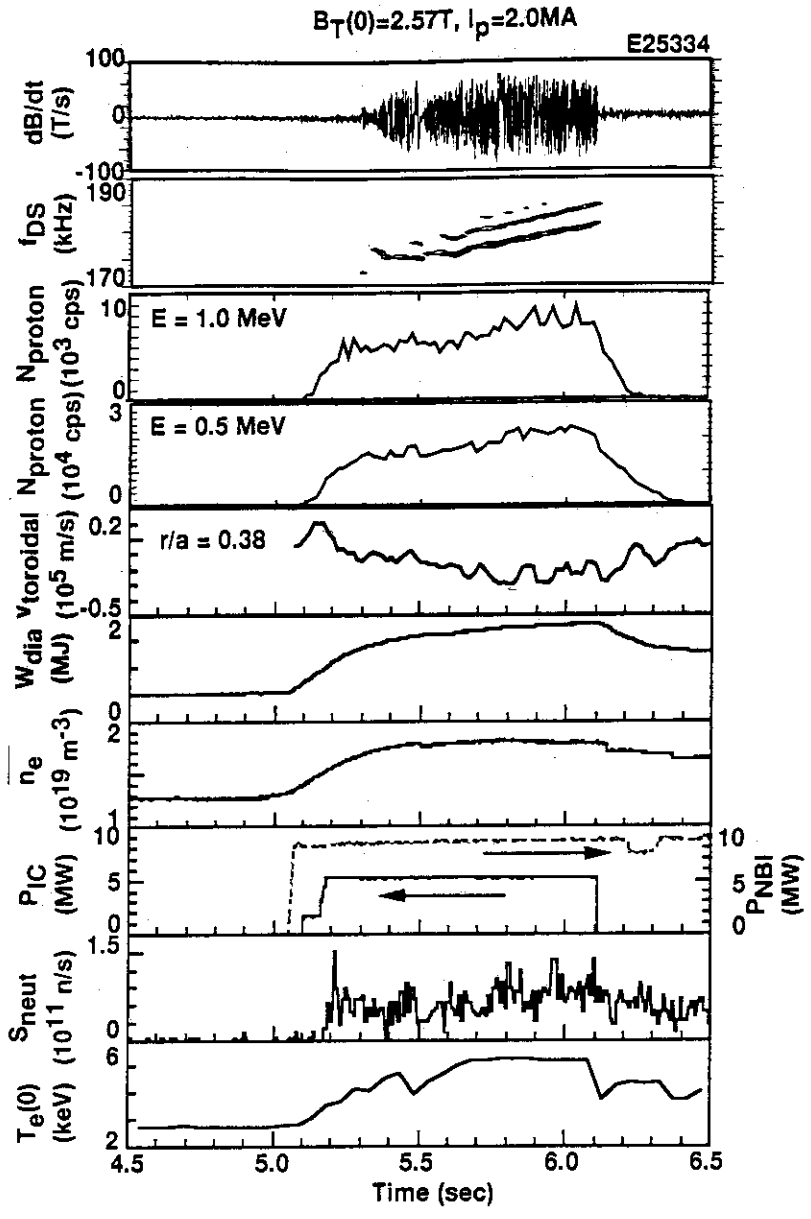

Fig. 1 Typical time evolutions of plasma parameters in simultaneously heated plasma with ICRF and NB.

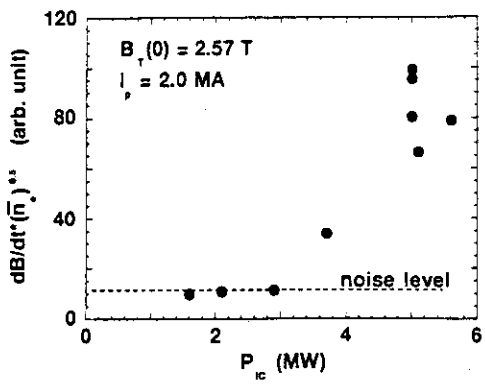

Fig. 2 Normalized amplitude of TAE modes as a function of ICRF heating power.

9.3 Behavior of 14 MeV neutron emission during TAE mode

T. Nishitani, M. Isobe, M. Saigusa, H. Kimura, K. Tobita and Y. Kusama

1. Introduction

The toroidal Alfven eigenmodes (TAE) are of concern for future tokamak devices, since they can induce anomalous alpha losses. In fact, RF induced TAE mode caused loss of fast ions during H-minority ICRF heating experiment in TFTR, which resulted in localized heat load and failure of vacuum vessel welds [1]. The understood mechanism is that the TAE mode induced transition from passing to trapped orbits and radial diffusion produced by stochasticity in fast ion orbits [2].

1 MeV tritons produced in the d(d, p)t reaction have similar kinematics parameters to 3.5 MeV alphas, so that the TAE mode effects on fast tritons behavior is useful to predict that of alphas in the DT plasma. We investigated the fast triton behavior in TAE modes exited by the ICRF minority heating of hydrogen in the deuterium plasma through the triton burnup measurement.

2. Experiment

ICRF of 5 MW was injected for the minority-proton-second-harmonics heating to the plasma with a plasma current (I_p) of 3 MA, toroidal field (B_{T0}) of 3.8 T, and an effective safety factor (q_{eff}) of 3.5, from 6.6 sec to 7.6 sec as shown in Fig. 1. In order to accumulate fast tritons, 25 MW of NB heating was injected before ICRF heating from 5.5 sec to 6.5 sec. The emission of 14 MeV neutrons from the triton burnup is about 100 time less than that of the 2.5 MeV neutrons in the NB heating phase. After NB turn off, the 14 MeV neutron emission has a longer decay time constant han that 2.5 MeV neutron emission.

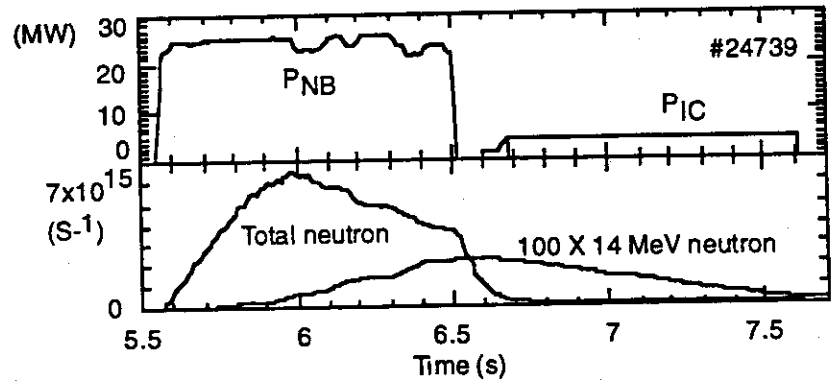

Fig. 1 Experimental waveforms. Here P_{NB} and P_{IC} are neutral beam and ICRF powers, respectively.

Figure 2 shows the plasma configuration with the sightlines of the 14 MeV neutron detector using scintillating fiber (see Sections 10.1 and 12.3 (3)). The plasma have a relatively large volume of 91 m^3 in order to couple to the ICRF antenna, so the maximum toroidal ripple rate is about 2% at outer edge. The 14 MeV neutron emission is measured along center and half radius chords.

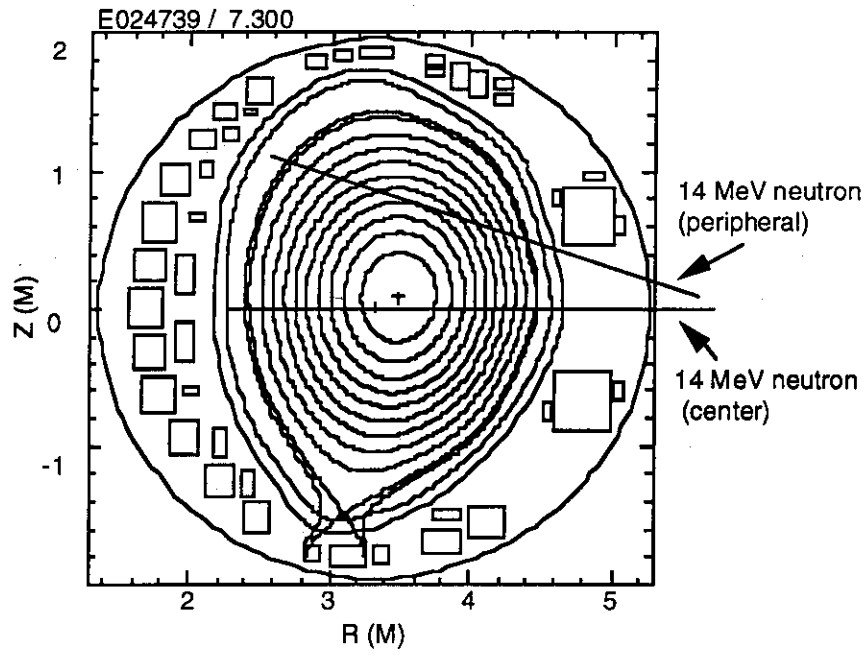

Fig. 2 Plasma configuration and sightlines of the 14 MeV neutron detectors.

3. Results

Diagnostics waveforms in the ICRF heating phase are shown in Fig.3. We identified TAE modes by checking the mode frequencies measured by Mirnov coils installed inside the vacuum vessel. TAE modes were exited from 7.06 sec to the ICRF termination. The frequency was 260 ~285 kHz, and increased with the decrease in the electron density. The measured frequencies were consistent with the theoretical TAE mode frequency represented by,

$$f_{th} = \frac{v_A}{4\pi qR}, \qquad (1)$$

where V_A ($= 2.18 \times 10^{16}$ B/$(An_i)^{0.5}$ m/s) is the Alfvén speed, B the total magnetic field, A the mass number, n_i the ion density, q the local safety factor and R the major radius. From 7.3 sec, the measured frequency kept constant for 100 ms. At the same timing, drops of the intensity were observed in the total and peripheral ($r \approx a/2$) 14 MeV neutron emissions. The soft x-ray wave forms shows that those drops are not due to the sawtooth crash. However,

there was not significant change in the central 14 MeV neutron emission. If the decrease in the peripheral 14 MeV emission is due to TAE modes, the fast triton resonanted to TAE mode in the peripheral region, which is consistent with the results that TAE modes become unstable in the middle part (r ~ a/2) of the plasma cross-section in the JT-60U ICRF experiments [3].

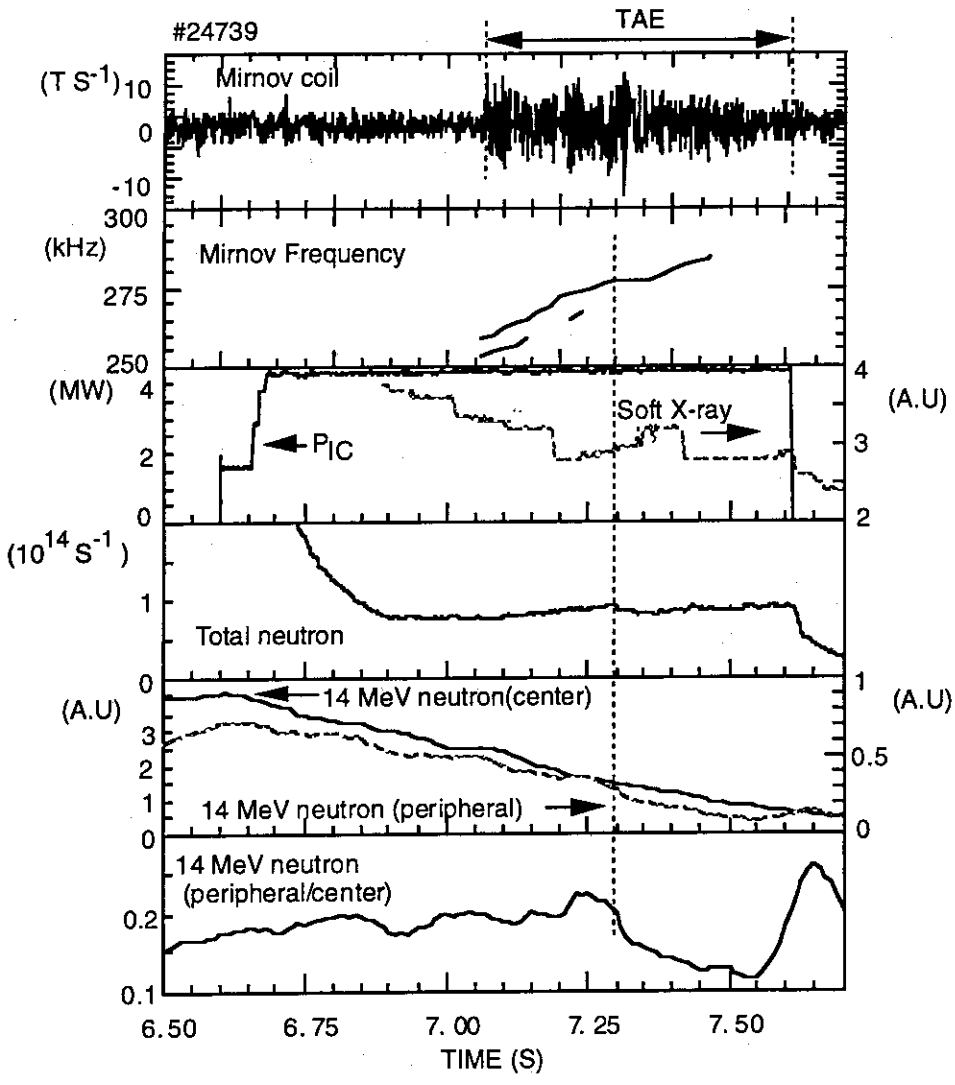

Fig.3. Waveforms of TAE modes exited by the ICRF minority heating of hydrogen in the deuterium plasma. From the top, Mirnov coil signal (dB/dt), Mirnov frequency, ICRF power (P_{IC}), soft X-ray intensity, total neutron emission, 14 MeV neutron emissions from center and peripheral regions, and 14 MeV neutron emission in peripheral over that in center.

Discussion

The 14 MeV neutron emission from the triton burnup is mainly contributed by fast tritons in the energy range of 0.1-1 MeV. Especially, the D-T cross-section become maximum at the triton energy of ~170 keV. Possible explanation of the triton loss 200 ms delayed from

the TAE onset is the precessional drift frequency was resonated with the high *n* TAE modes during the TAE frequency was changing due to decrease in the electron density. The resonant ion energy for the precessional magnetic drift resonance is expressed by

$$E_{res} \approx \frac{Z B r v_A}{2 n q^2} \qquad (eV) \tag{2}$$

where *Z* is the charge number of the resonant ion. In this experiment, Z = 1, B_T = 3.8 T, r = 0.5 m, $v_A = 1.4 \times 10^7$ m/s, q = 1.3, so that we obtained

$$E_{res} \approx 8.3/n \quad (MeV) \tag{3}$$

We did not identify the toroidal mode number *n* in this experiment, but we estimated *n* to be 4-12 from the similar ICRF heating experiments [3]. Fast tritons discussed here has a possibility to resonant to the TAE mode with the toroidal number *n* larger than 10.

Another possibility is that lost fast protons hit the first wall or other in-vessel equipment, which causes the impurity influx resulting in the decrease in the neutron emission. In the fact the increase in the Ni line emission was observed at 7.3 s.

So far we could not identify the reason of the delayed loss in the neutron emission from the available data. We need more precise experiment in future.

References

[1] D.W. Johnson, et al., Plasma Phys. Control. Fusion **37** (1995) A-69.

[2] R.B. White, et al., Phys. Plasma **2** (1995) 2871.

[3] H. Kimura, et al., Phys. Letters A **199** (1995) 86.

9.4 Role of change in local safety factor in TAE mode excitation

Y. Kusama, M. Saigusa, H. Kimura, T. Nishitani, S. Moriyama and Y. Neyatani

1. Introduction

This part describes characteristics of TAE modes excited in discharges for investigation of the TAE mode-triton interaction [1]. Role of change in local safety factor in TAE mode excitation is mainly discussed.

2. TAE mode excitation

The TAE modes were excited with ICRF heating ($2\omega_{CH}$, H-minority) following NB injection or overlapping with NB injection. Plasma current ramp-up was also adopted for decreasing internal inductance (li) because the threshold beta of energetic ions for the TAE mode excitation is low in the discharge of lower li [2]. Plasma parameters were as follows; I_p = 3 MA, B_{t0} = 3.8 T, P_{IC} = 2 - 4 MW. Typical three types of the discharge are (1) ICRF heating after the turn-off of NB, (2) ICRF heating is overlapping with NB in the beginning of the ICRF pulse, (3) type (2) with Ip ramp-up from 2 MA to 3 MA, and are shown in Fig. 1.

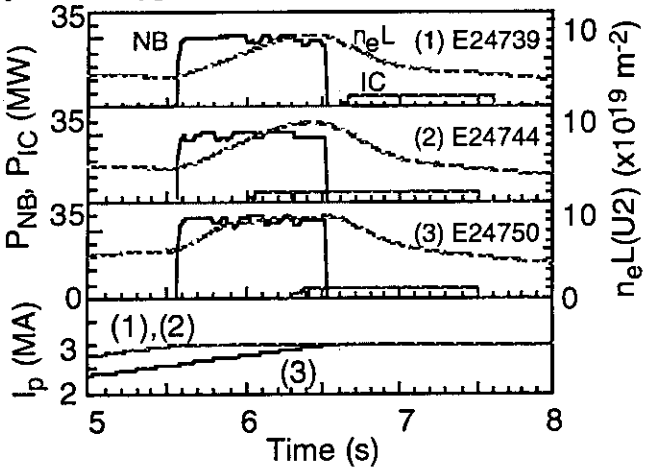

Fig. 1: Typical three types of the discharge. Time traces of P_{NB}, P_{IC}, line-integrated electron density n_eL ($\overline{n_e} = n_eL/2.62$) and I_p are shown.

The TAE modes appear at almost the same time during 6.85-7.08 s even though the injection time of ICRF waves was drastically changed. For three discharges (1), (2) and (3) shown in Fig. 1, temporal behavior of $P_{IC}\langle Te\rangle^{1.5}/n_e$, which is a parameter proportional to the beta value of energetic protons β_h, is shown in Fig. 2. The TAE modes appear on filled symbols connected with a solid line. The beta value of energetic protons increases with the decrease in electron density and with the simultaneous increase in electron temperature. As shown experimentally [2] and as expected theoretically, the TAE modes are shown to be excited when the beta value β_h exceeds the threshold. Figure 2 shows that the time of TAE mode appearance depends on not only β_h. The trajectories of li vs. $P_{IC}\langle Te\rangle^{1.5}/n_e$ for the three discharges are shown in Fig. 3. Kimura et al. reported that the threshold β_h of the TAE mode excitation is higher for higher li [3]. A similar tendency can be seen in Fig. 3. It should be

noted that the TAE mode appears in one discharge, however, does not appear in another discharge on the overlapping region between (1) and (2) and between (2) and (3), where li vs. $P_{IC}<Te>^{1.5}/n_e$ draws a similar trace. In Fig. 3, the safety factor evaluated from $q(r)\sim v_A(r)/4\pi f_{DS}R$ at the onset time of the TAE mode is also shown. One can see that q value takes a similar one when TAE mode appears. This result shows that the TAE mode can be excited for special q values [q=(2m+1)/2n] as expected from the TAE mode theory. Increasing li indicates the peaking of plasma current due to the penetration of the plasma current towards the central region of the plasma and it makes the local safety factor q(r) lower. Figure 3 indicates that gradually decreasing q value satisfies the condition for the q value of the TAE mode excitation.

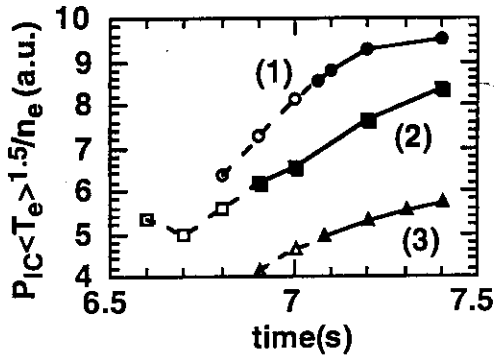

Fig. 2: Temporal behavior of $P_{IC}<T_e>^{1.5}/n_e$ for three discharges.

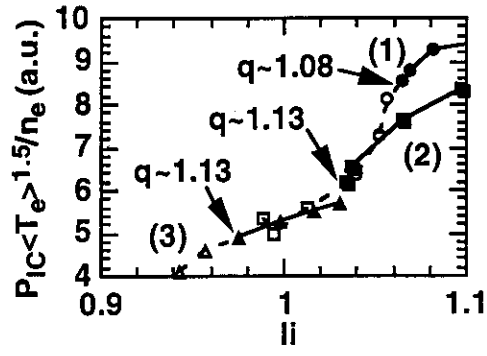

Fig. 3: Trajectries of li vs $P_{IC}<T_e>^{1.5}/n_e$ for three discharges.

3. Effect of giant sawtooth crash on change in toroidal mode number

Figure 4 shows time traces of frequency spectrum, ICRF power, line-integrated electron densities, central electron temperature and intensity of soft X-ray emission of E24739 [same discharge shown as Type (1) in Fig. 1]. In the frequency spectrum, oscillating behavior of TAE modes can be seen for two modes (f1 and f3), which appear and disappear in turn around the mode with a large amplitude (f2). Although giant sawtooth crashes can be seen in electron temperature (plotted every ~50 ms) at 7.12 s and 7.37 s, real crashes considered to occur at 7.19 s and 7.42 s from the soft X-ray emission. The mode f1 is fading out and the mode f3 is growing at around 7.14 s in the sawtooth free period (phase I and II). This sequential appearance of different modes is understood due to the gradual decrease in safety factor q and the toroidal mode number increases in the order of f1, f2 and f3 [3]. Once the giant sawtooth crash occurs, the mode f3 disappears (phase III and V) and lower-n mode f1 appears again (III). When the giant sawtooth crashes, the q-profile suddenly becomes flat and the q value jumps up at $\rho<0.5$ [5]. As the result, the position having the q value for the mode f3 excitation shifts towards the center and goes out of the region where a high pressure gradient is formed by energetic protons. Contrary, and the q-value position for the mode f1 returns into the region. Therefore, the mode f3 disappears and the mode f1 comes back again (III). In a reheat phase after the giant sawtooth crash (IV and VI), the higher-n mode f3 becomes onset because the q

value decreases gradually again. For a lower q value, the q-value condition can not be satisfied in the high pressure gradient region so that the mode f1 dose not appear any more (V). It is considered to be the mechanism of oscillating behavior of the mode f1 and f3.

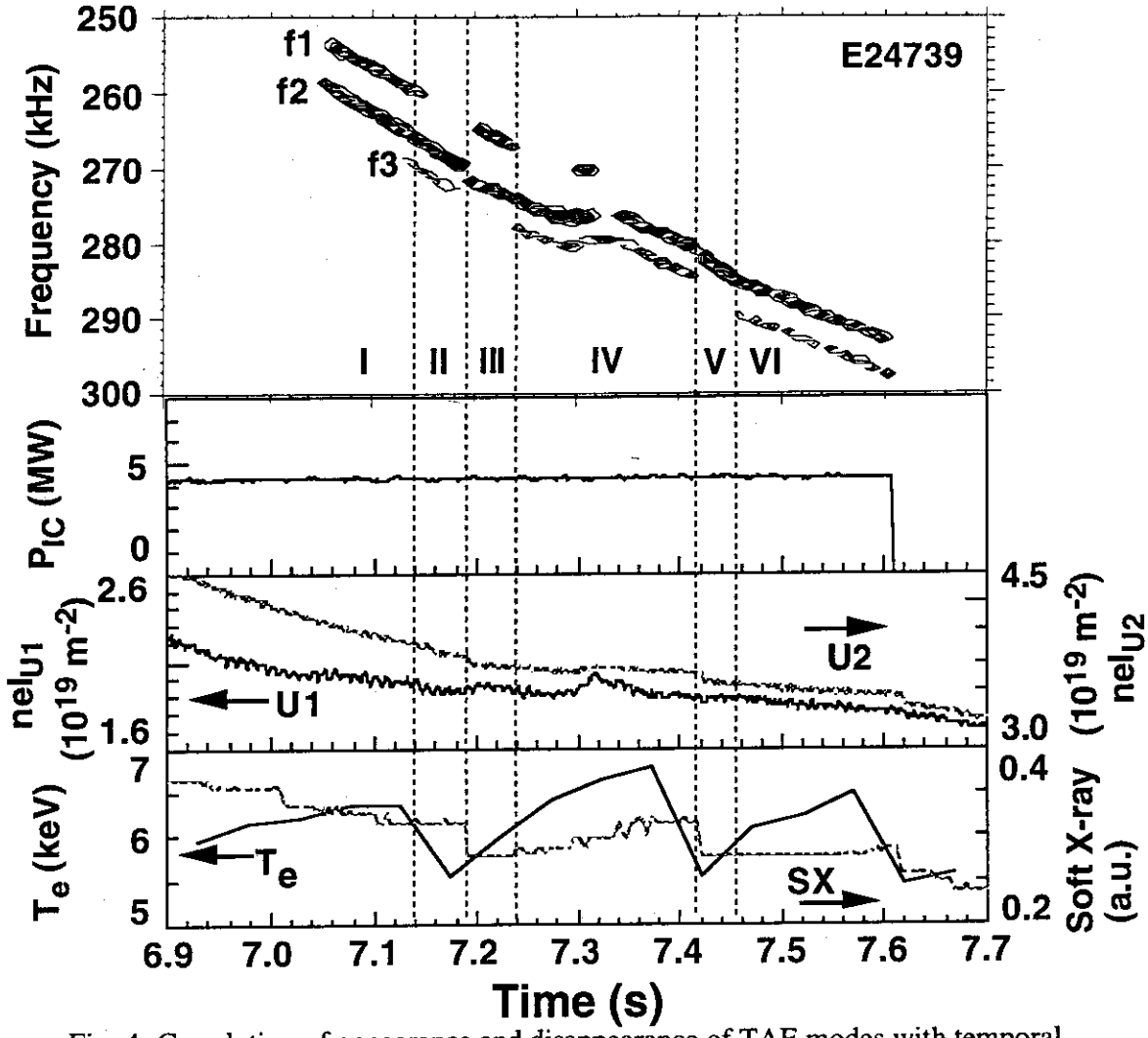

Fig. 4: Correlation of appearance and disappearance of TAE modes with temporal behavior of electron density, central electron temperature and intensity of soft-X ray emission.

4. Number of appeared TAE modes

Figure 4 shows the dependence of number of observed TAE modes (Δn) on the ICRF power. The number increases with the ICRF power with the threshold power of 3.5 MW, which is almost the same as that already reported for 3.5 MA discharges [2]. Maximum number of appeared TAE modes is three and is smaller than that found previously (Δn = 3 -7) for the same plasma current of 3 MA [3]. It is considered to be due to lower ICRF power in this experiment than in previous one (3-6.35 MW). By increasing the ICRF power, the beta value of energetic protons increases and it makes the TAE modes in a wider range of the toroidal mode number excited. Another reason why the Δn is limited to be 3 is that the change in q is as

small as ~0.02 for the mode f2 in Fig. 5 as long as we estimate the q value from $q(r) \sim v_A(r)/4\pi f_{DS}R$.

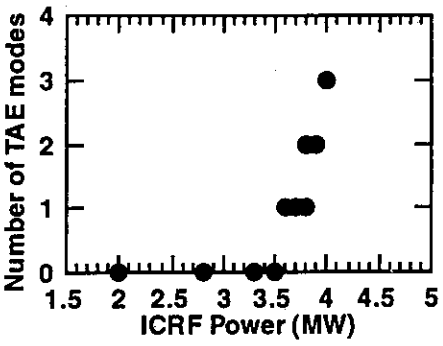

Fig. 5: Dependence of number of appeared TAE modes on the ICRF power.

5. Toroidal mode number

Three TAE modes with different toroidal mode number were observed as shown in Fig. 4. The measured frequencies of the mode f1 and f2 at the onset of the modes are 254 kHz and 259 kHz, respectively. Using the relation (Eq. (5) and (6) in Ref. [2]) between the toroidal mode number (n), mode frequency for q=1 (273 kHz), frequency difference between two modes (~6 kHz) and the toroidal rotation frequency Φ_t (assuming ~1 kHz [2]), the toroidal mode number of the mode f1 is evaluated to be n~3.4 for m=n and n~5.6 for m=n+1. On the other hand, the mode f1 is the odd mode and f2 is the even mode from a toroidal array of Mirnov coils. Therefore, three toroidal mode numbers are considered to be n =3, 4, 5 or 5, 6, 7. The local safety factor $q(r) \sim v_A(r)/4\pi(f_{DS}-\Phi_t)R$ takes $1.08<q<1.13$ for discharges (1), (2) and (3) in Fig. 1. From these evaluation and the Alfvén continuum gap map [3], the toroidal mode numbers are considered to be n =3, 4, 5 for m=n. In planning of this experiment, we expected that TAE modes with the toroidal mode number as high as 10 could be excited in 3 MA plasmas [2] and the high n could reduce the resonant energy less than 1 MeV of triton birth energy. However, the evaluated toroidal mode number is lower than that expected.

6. Summary

The TAE modes were successfully excited for the three types of heating and current ramp scenario. A change in local q value is essential to excite TAE modes in this experiment. Evaluated toroidal mode numbers are thought to be too low to reduce resonant energy less that 1 MeV. It is considered to be the reason why no clear interaction between TAE modes and tritons can be seen.

[1] T. Nishitani, et al., Section 9.3 in this Review.
[2] H. Kimura, et al., Phys. Letters A 199 (1995) 86-92.
[3] M. Saigusa, et al., Plasma Phys. Control. Fusion, 37 (1995) 295-313.
[4] H. Kimura, et al., J. of Plasma and Fusion Research Vol. 71, No. 11, (1995) 1147.
[5] M. Satoh, et al., Jpn. J. Appl. Phys. Vol. 34 (1995) 4200-4206.

10. High Energy Ions

10.1 Evaluation of fast triton diffusivity from triton burnup

T. Nishitani, M. Isobe, H. Harano, G.A. Wurden, R.E. Chrien, K. Tobita and Y. Kusama

1. Introduction

Tritons of 1.0 MeV are produced in the d(d,p)t reaction at approximately the same rate as the 2.5 MeV neutrons from the d(d,n)^{3}He reaction. The behavior of 1 MeV tritons is important to predict the properties of D-T produced 3.5 MeV alphas because 1 MeV tritons and 3.5 MeV alphas have similar kinematics properties, such as Larmor radius and precession frequency. The 1 MeV tritons slow down and may undergo a DT fusion reaction, emitting 14 MeV neutron. The confinement and slowing down of the fast tritons can be investigated by measuring the 14 MeV and the 2.5 MeV neutron production rates.

Loss of alpha particles due to toroidal ripple is one of the most important issues to be solved for a fusion reactor such as ITER. JT-60U has a large toroidal ripple rate up to 2 %, so that it is suitable machine to investigate the toroidal ripple effect on the fast ions. Toroidal ripple loss of beam-injected ions was investigated by the heat load measurements [1, 2] and neutron response after short neutral beam (NB) injections [3, 4], which are consistent with predictions calculated by Orbit-Following Monte Carlo (OFMC) code[5]. The main mechanisms of the ripple induced loss for fast tritons are ripple trapping, stochastic ripple diffusion and ripple banana diffusion. The first is instantaneous convective loss but the others are diffusive processes. The stochastic ripple diffusion is very fast, typically ~ 10 m^2/s or more. This diffusion is important in collisionless regime and localized in the peripheral region of the plasma. The ripple banana diffusion is important in low collisionality regime and has not so fast diffusivity of ~0.1 m^2/s. We expected that the ripple banana diffusion of fast tritons would affect the diminution rate of the 14 MeV neutron emission after NB turn-off, because birth tritons are localized in the core region and tritons are in low collisionality regime near the peak of the DT cross-section. We investigated the fast triton diffusivity by analyzing the time history of the 14 MeV emission after NB turn-off and discuss the toroidal ripple effect on the delayed loss of fast tritons in the range of toroidal ripple rate from 0.4 to 2 % at the edge. Here the time-resolved 14 MeV-neutron measurements have been performed using a new type 14 MeV neutron detector based on scintillating fibers [6] with high time response, as part of a US-Japan fusion collaboration.

2. Diagnostics

The new 14 MeV neutron detector consists of an array of scintillation fibers embedded in an aluminum matrix coupled to a magnetic resistant phototube with a high current-capable base (see Section 12.3 (2)). The detector is mounted in a small collimator box, 40 cm × 61

cm × 61 cm of borated polyethylene. Two sets of detectors have been installed near the midplane of the vessel, just outside the toroidal field coil position. The scintillating fiber detectors have been calibrated by the shot-integrated 14 MeV neutron yield measured with the neutron activation technique using a pneumatic foil transfer system[7]. The total neutron emission is measured with neutron monitors using ^{235}U fission chamber which were calibrated by radioisotope neutron source [8].

3. Time Dependent Analysis

We measured and analyzed the time histories of the 14 MeV emission after turn-off of the 1.5-2 second NB injection in three discharges whose configurations with the toroidal ripple rate contour are shown in figure 6. Plasma parameters for those discharges are listed in Table 1. Shot #21137 has small plasma volume of ~50 m^3 shifted inward. Shots #23664 and #23663 has the plasma volume of ~70 m^3 and almost same plasma parameters except major radius. Shot #23663 is shifted outward. Here r_{eff} is an averaged radius weighted by the triton birth profile as

$$r_{eff} = \frac{\int r \cdot 2\pi r F_{triton}(r) dt}{\int 2\pi r F_{triton}(r) dt} \qquad (1)$$

where F_{triton} is the triton birth profile calculated by the steady state version of the 1.5D tokamak code TOPICS[13]. Shot #23663 has a broad NB deposition profile due to off-center injection resulting in a broad triton birth profile. Wave forms of total and 14 MeV neutron emission in shot #21137 is already shown in figure 4. Those in shots #23664 and #23663 are shown in figure 7, where 14 MeV neutron emission decreased faster after NB turn-off in #23663 than in #23664.

Table 1 Shot list of time dependent analysis

Shot number	#21137	#23664	#23663
Plasma current (MA)	2.2	1.5	1.5
Major radius (m)	3.13	3.19	3.46
Volume (m^3)	49	69	67
q_{eff}	4.5	6.5	5.6
r_{eff}/a	0.36	0.37	0.47
Ripple rate at r_{eff} (%)	0.02	0.06	0.2

The time-dependent 14 MeV neutron emissivity was simulated by a simple classical slowing down model. The plasma was divided into 51 circular shells in the calculation. In each shell, the tritons were divided into 500 groups according to their birth time, with 10 ms time bins. The number of tritons in a group is proportional to the 2.5 MeV neutron emissivity

at the birth time of the tritons. Tritons were allowed to slow down in each shell according to the classical energy loss represented by following formula [9]:

$$\left(\frac{dE}{dt}\right)_{classical} = -\frac{\alpha}{\sqrt{E}} - \beta E \qquad (2)$$

$$\alpha = 1.81 \times 10^{-13} \ln \Lambda_{ii} A^{1/2} Z^2 \sum_j \frac{n_j Z_j}{A_j}$$

$$\beta = 3.18 \times 10^{-15} \ln \Lambda_{ei} \frac{Z^2}{A} \frac{n_e}{(T_e)^{1.5}}$$

where E is the triton energy , T_e is the electron temperature both in eV, n_e is the electron density in m^{-3} and $ln\Lambda$ is the Coulomb logarithm. A and Z are the triton mass and charge number; n_j, A_j, and Z_j are the hydrogen and impurity density in m^{-3}, mass and charge numbers, respectively. First term of R.H.S. of the Eq(1) is the slowing down on electrons and second on is on ions.

The loss of confined tritons was taken into account assuming an exponential decay of the number of tritons of the form $e^{-t/\tau}$ where t and τ are the time since the birth and the confinement time of the tritons, respectively. The diffusivity of fast triton, D_{triton}, was estimated by using the relation for the confinement time $\tau = a_p^2 / 5.8 D_{triton}$, to reproduce the experimental triton burnup ratio. The time history of the 14 MeV neutron emission rate was calculated by using the electron temperature profile from ECE measurement, the ion temperature profile from charge exchange recombination spectroscopy, and the electron density profile from the FIR and CO_2 interferometers as the time dependent plasma parameters. The triton birth profile was calculated using the TOPICS code for a typical time and the shape of the profile was assumed to be constant during the period of the triton burnup. The angular distribution of the

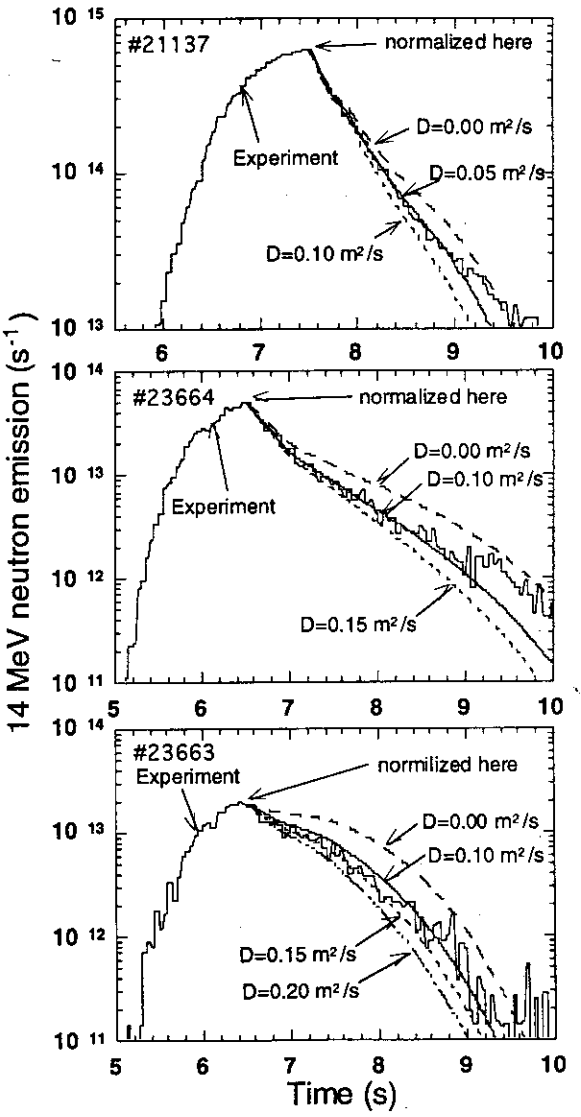

Fig.1 Experimetal and calculated 14 MeV neutron emissions for #21137,#23664 and #23663.

tritons was assumed to be isotropic. First orbit losses were taken into account.

Figure 1 shows the experimental and calculated 14 MeV neutron emissions for three discharges listed in Table 1. Calculated curves are normalized to the experimental data at the time of NB turn-off to reject any systematic error of detection efficiencies for the total and 14 MeV neutron emissions. The fast triton diffusivity, D_{triton}, of 0.05, 0.1 and 0.15 m^2/s give a good agreement with the experimental date in shot #21137, #23664 and #23663, respectively, which indicate that D_{triton} increases with the toroidal ripple rate as shown in Fig.2.

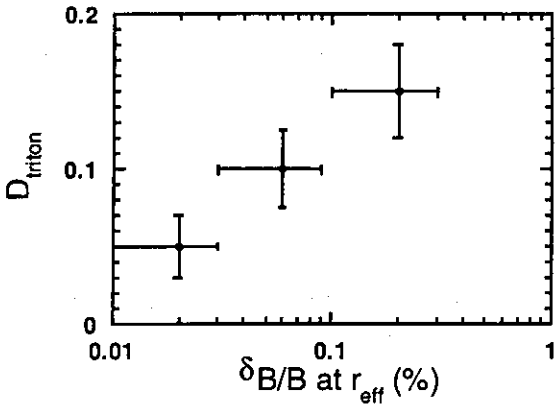

Fig. 2 Fast triton diffusivity plotted against the toroidal ripple rate at the effective minor radius of the triton birth profile.

4. Summary

The time resolved triton burnup measurements have been performed using a new type 14 MeV neutron detector based on scintillating fibers. Time histories of 14 MeV emission after NB turn-off have been analyzed based on the classical slowing down theory. Assuming the loss of fast tritons can be represented as a diffusivity, then values increasing with increasing toroidal ripple were determined between 0.05-0.15 m^2/s, form the modeling of the time histories of the 14 MeV emission after the NB turn-off. We have a plan to evaluate the fast triton diffusivity due the toroidal ripple losses using the OFMC code[5].

References

[1] T. Nishitani, et al., Plasma Phys. and Controlled Nuclear Fusion Research 1992 (Proc. 14th Int. Conf. Wüzburg, 1992) Vol. 1 (Vienna :IAEA, 1993) p 351.

[2] K. Tobita K, et al., Phys. Rev. Lett. **69** (1992) 3060.

[3] K. Tobita K, et al., 1994 Nucl. Fusion **34** (1994) 1097.

[4] Kusama Y et al 1994 Plasma Phys. and Controlled Nuclear Fusion Research 1994 (Proc. 15th Int. Conf. Seville 1994) IAEA-CN-60/A-2-IV-5.

[5] K. Tani, M. Azumi, H. Kishimoto, S. Tamura, . Phys. Soc. Japan **50** (1981) 1726.

[6] G.A. Wurden, et al., Rev. Sci. Instrum. **66** (1995) 901.

[7] M. Hoek, T. Nishitani, Y.Ikeda, A. Morioka, Rev. Sci. Instrum. **66** (1995) 885.

[8] T. Nishitani, et al., Rev. Sci. Instrum. **63** (1992) 5270.

[9] P. Batistoni, Cris W. Barnes, Plasma Phys. Control. Fusion **33** (1991)1735.

10.2 Effect of Ion ∇B Drift Direction on Ripple-Induced Fast Ion Loss in JT-60U

M.Isobe, K.Tobita, T.Nishitani, Y.Kusama, A.Morioka and M.Sasao

1. Introduction

The finite number of toroidal field coils gives rise to perturbation on the toroidal magnetic field(TF ripple), and thus induces TF ripple trapping[1] and the radial drift of banana particles[2]. In a reactor-relevant tokamak having a single null-divertor such as ITER, the ripple amplitude tends to be larger on the upper side than on the lower side because of the requirement of long divertor leg. In single null divertor discharges of several tokamaks, it has been commonly observed that the threshold power for transition from L- to H-mode when the ion ∇B drift is toward the X-point is lower than that when the ion ∇B drift is away from the X-point[3,4]. On the other hand, when the ion ∇B drift is away from the X-point, it seems that the heat load characteristics on the divertor plate is preferable to that for the ion ∇B drift toward the X-point[5]. It is not clear yet which B_t direction is better for the integrated performance as a fusion plasma, therefore, the direction of toroidal magnetic field B_t of ITER should be reversible for unexplored advanced operation scenarios. In a plasma with the ITER-like ripple well, a possible problem concerning B_t reversal operation is that power loss and heat load on the first wall due to the enhanced ripple-trapped loss may increase when the ion ∇B drift is away from the X-point(in the case of JT-60U and ITER, the drift directs upward) because, once trapped in a ripple well, fast ions move toward the deeper side of the ripple well and thus have little chance of detrapping.

The present study on JT-60U was conducted to make sure of the effect of the ion ∇B drift direction on the total loss of ripple induced fast ions, i.e. the summation of ripple-trapped loss and banana drift loss, in plasmas with the up-down asymmetric ripple well, and to verify the possibility for B_t-reversal operation in a fusion reactor tokamak.

2. Experimental Conditions and Method

A ripple trapping region is formed in the region where the effective ripple well parameter $\alpha^*[\equiv(\partial\bar{B}/\partial l)/(\partial\tilde{B}/\partial l)]$ satisfies the condition $|\alpha^*|<1$, where $\partial\bar{B}/\partial l$ and $\partial\tilde{B}/\partial l$ stand for variations of axisymmetric and non-axisymmetric components of B_t along the magnetic field line, respectively. The ripple trapping region of ITER is illustrated in Fig. 1(a) and that of JT-60U with TF ripple contours is illustrated in Fig. 1(b). In the present experiment, the ion collisionality ν_i was ranged around $3s^{-1}$ which was in the intermediate region between ripple plateau diffusion[6] and stochastic diffusion[7]. The plasma parameter were : I_p=1.5MA, B_t=3.5T, V_p=56m^3, q_{eff}=~5.0, n_e=0.3-1.2×10^{19}, $T_e(0)$=3.0-4.8,

Z_{eff}=2.0-6.0. The beam injection energy E_B was typically 90keV throughout this experiments.

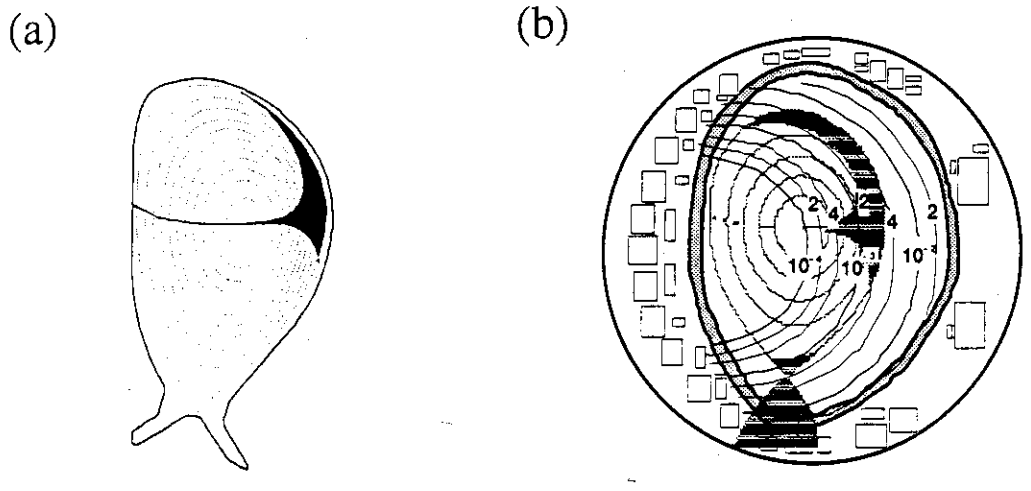

Fig.1 Ripple trapping region(painted area) of ITER(a)[8] and JT-60U(b).

The total ripple-induced loss is deduced from the decay of neutron emission following a short D^0 beam which duration is much shorter than the slowing down time of the injected ions. Such a short pulse of neutral beam allows us to treat the velocity distribution of the fast ions as monoenergetic one. The neutron decay following NB turn-off is approximately exponential. The neutron decay time τ_n is expressed as follows[9],

$$1/\tau_{n\text{-}exp} \approx 1/\tau_c + 2.3/\tau_s$$

where τ_c is the confinement time of fast ions, $\tau_s/2.3$ is the neutron decay time assuming the classical slowing down without loss. Here, τ_s is the slowing down time. The factor '2.3' originates in the D-D fusion reactivity $\sigma_{DD}(E_B)E_B^{1/2}$ for beam-target reaction which is approximately proportional to $E_B/2.3$ in the energy range of 50 to 100 keV.

3. Experimental Result

In order to deduce the ripple-induced loss in the up-down asymmetric ripple well, we injected perpendicular D^0 neutral beam into low density plasmas. Fig. 2 shows the typical neutron decay in a plasma with an ITER-like ripple well region and the calculated neutron decay without loss. After NB turn-off, the neutron emission decays approximately exponentially. It is seen that the measured neutron decay time is faster than the calculated one. The difference between two suggests the loss of fast ions during the deceleration. The ion loss, which is estimated from the difference between the measured and calculated decays, was deduced to be about 13% at 100ms after NB turn-off. Considering the results obtained in Ref. 9, the fast ion loss is attributed to TF ripple loss. By switching the B_t direction, the

effect of the ion ∇B drift direction on the fast ion loss was investigated in plasmas with the up-down asymmetric ripple well. The correlation between τ_n and $\tau_s/2.3$ for the ITER-like configuration is shown in Fig. 3. The closed and open circles indicate data for the upward and downward ion ∇B drift, respectively. The error bars in $\tau_s/2.3$ were determined from the width of τ_s in the area with high neutron yield (normalized minor radius ρ=0.2-0.6). There is no significant difference in the total ion loss between the upward and downward ion ∇B drift, indicating that the fast ion loss does not depend on the ion ∇B drift. The OFMC calculation indicated that the ion ∇B drift direction did not affect the total ion loss but the dominant loss channel was different between the cases of the upward and downward ion drift. In the case of the upward ion ∇B drift, the ripple trapped loss becomes a dominant loss process because the fast ions trapped in the ripple well have little chance to detrap and go out of the plasma.The heat load profile will be locally concentrated on the first wall because of the increased ripple-trapped loss. On the other hand, in the case of the downward ion ∇B drift, the banana drift loss becomes dominant because the trapped fast ions move toward the shallower side of the well and most of them become to follow banana orbit.

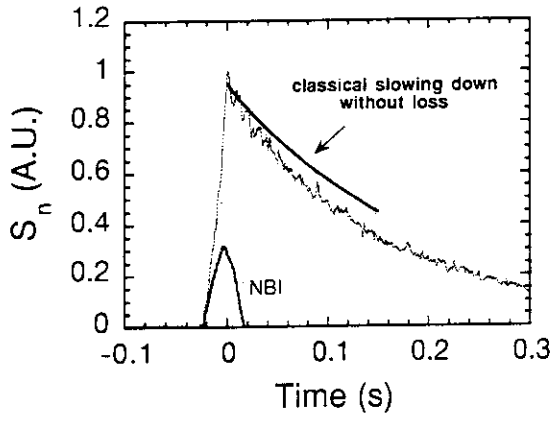

Fig. 2 Measured and calculated neutron decay after NB turn-off in a plasma with ITER-like ripple well.

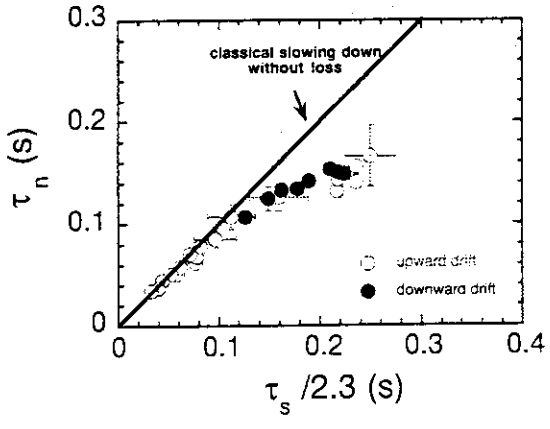

Fig. 3 Neutron decay time τ_n against the slowing down time $\tau_s/2.3$.

4. Summary

In the up-down asymmetric ripple well of JT-60U, the effect of the ion ∇B drift direction on the ripple-induced loss of NB-injected fast ions was experimentally investigated to make sure of the effect of the ion ∇B drift direction on total ripple loss of NB-injected fast ions. Fast ion loss was estimated from the neutron decay following short NB pulse whose duration is shorter than τ_n. No significant difference in the fast ion loss was observed between upward and downward ion ∇B drift. From the viewpoint of the power loss caused by the toroidal filed ripple, the experimental result shows the operation with the upward ion ∇B drift is not limited in a fusion tokamak with the up-down asymmetric ripple like ITER.

References

[1] Anderson, O.A., Furth, H.P., Nucl. Fusion **12**(1972)207.

[2] Davidson, J.N., Nucl. Fusion **16** (1976)731.

[3] Wagner, F., et al., Nucl. Fusion **25**(1985)1490.

[4] Burrell, K.H., et al., Phys. Rev. Lett. **59**(1987)1432.

[5] Reichle, R. et al., in Controlled Fusion and Plasma Physics(Proc. 18th Eur. Conf., Berlin, 1991), Vol.I, EPS(1991)105.

[6] Boozer, A.H., Phys. Fluids **23**(1980)2283.

[7] Goldston, R.J., White, R.B., Boozer, A.H., Phys. Rev. Lett. **47**(1981)647.

[8] Putvinski, S., et al., in Plasma Physics and Controlled Nuclear Fusion Research 1994 (Proc. 15th Int. Conf. Seville, 1994) IAEA-CN-60/E-P 4(1994).

[9] Tobita, K., et al., Nucl. Fusion **34**(1994)1097.

10.3 Measurements and analysis of neutral particle energy spectrum in ripple loss experiments

A.Morioka, K.Tobita, Y.Kusama, M.Isobe, K.Tsuchiya,
M.Nemoto, H.Takenaga and T.Nishitani

10.3.1. Introduction

In JT-60U, the transport of fast ions in ripple loss experiments have been studied by using short neutral beam (NB) pulses[1,2]. If the fast ions are confined well in plasmas, τ_n should be proportional to $\tau_s/2.3$, where τ_n is the decay time of DD neutron emission rate after NB is turned off, and τ_s is the slowing down time of the fast ions[2]. Yet, the experimental τ_n is shorter than the expected in long τ_s regime, as shown in Fig.1. There are two possibility for the unexpected result. One is that fast ions are lost mainly owing to ripple loss, and the other is that the slowing down process of fast ions is not classical . To resolve the cause, the slowing down was studied with a charge exchange neutral particle (CX) analyzer which is viewing the plasma perpendicularly .

10.3.2. Experiments

In the experiment, the plasma current and the toroidal field are 1.5 MA and 3.5 T, respectively. The NB injectors were operated with beam width of 50 msec and supplied 85 keV deutrons into banana orbits. We experimented in the region of $\tau_s \fallingdotseq 0.4$ sec. The experimental slowing down time τ_s (exp.) were estimated from CX energy spectrum.

10.3.3. Experimental results and analysis

Time evolution of energy spectra measured after the termination of NB injection are shown in Fig.2(a). The peak energy of the CX spectrum shifts toward low energy with the time. The peak energy as a function of time after the end of NB injection is shown in Fig.2(b). From this result, τ_s (exp.) is estimated to be 370 ± 80 msec.

To evaluate the birth region of the CX flux with energies of 50～85 keV, we calculated the neutral particle density profile by using a DEGAS code[3]. The neutral particle density(n_0), the fast ion density(n_i), the neutral particle flux($\Gamma_{cx}=n_0 n_i <\sigma v>_{cx}$) and τ_s (cal.) along the line of sight of the CX analyzer are shown in Fig.3. The attenuation of charge-exchanged neutrals in the plasma is neglected since the electron density is low . We found that CX particles from 50 keV to 85 keV were born mainly in the shaded region a vertical in Fig. 3. In the area, the value of τ_s (cal.) are 390 ± 50 msec. This result indicates that the slowing down process of fast ions is classical since τ_s (exp.) agrees with τ_s (cal.) within the error . From the agreement between τ_s (exp.) and τ_s (cal.) , it is found that the discrepancy between the experiment and calculation in τ_n at the long τ_s is caused by the ripple loss effect .

10.3.4. Conclusion

We estimated the slowing down time from decay of the CX spectra and from the simulation code. It was found that the slowing down process was classical.

References

[1] Y.Kusama, et al : Proc.15th Int. Conf. Plasmas Phys. and Contr. Nucl. Fus. Res. , (1994, Seville, Spain) IAEA-CN-60 / A-2-IV-5

[2] K.Tobita, K.Tani, T.Nishitani, K.Nagashima, Y.Kusama : Nuclear Fusion, Vol.34, 1097 (1994)

[3] D.B.Heifetz, et al : J. Compt. Phys. ,46, 309 (1982)

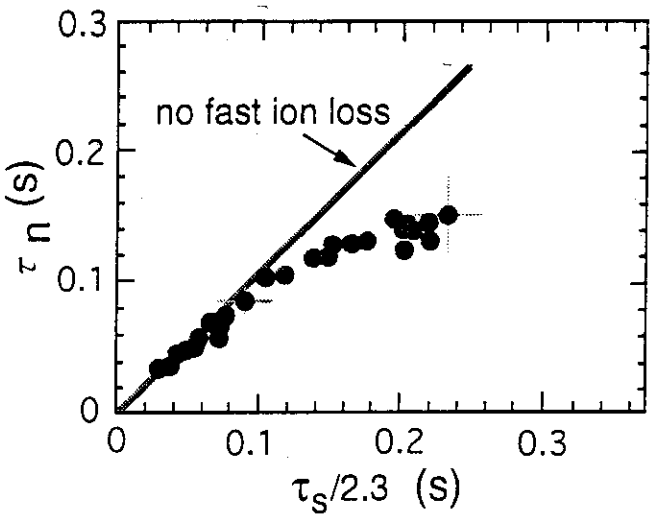

Fig.1 : Correlation between τ_n and $\tau_s/2.3$

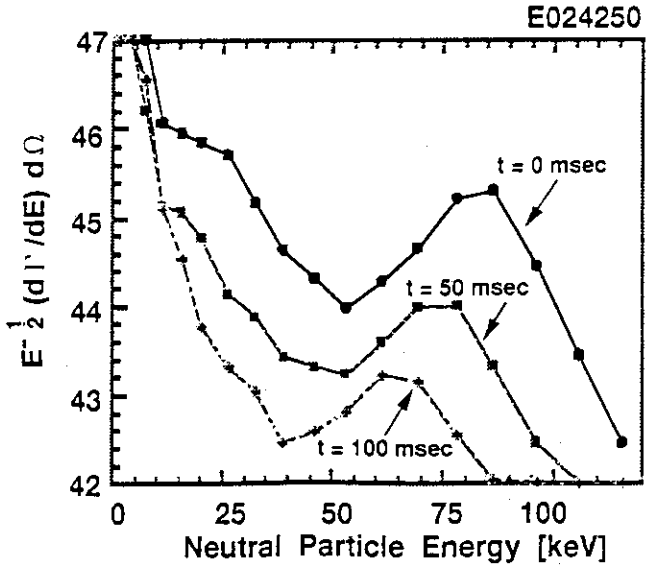

Fig.2(a) : Time evolution of the CX energy spectra measured after NB short pulse injection

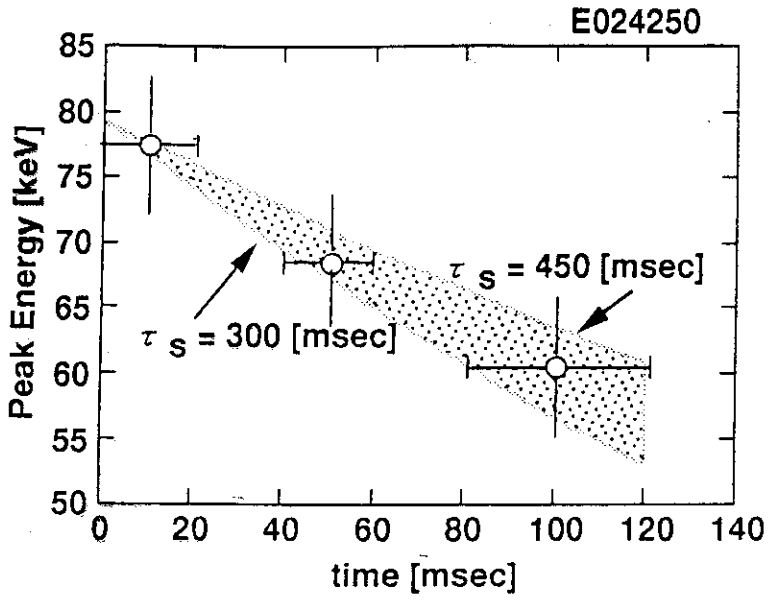

Fig.2(b) : The peak energy of the CX spectra as a function of time

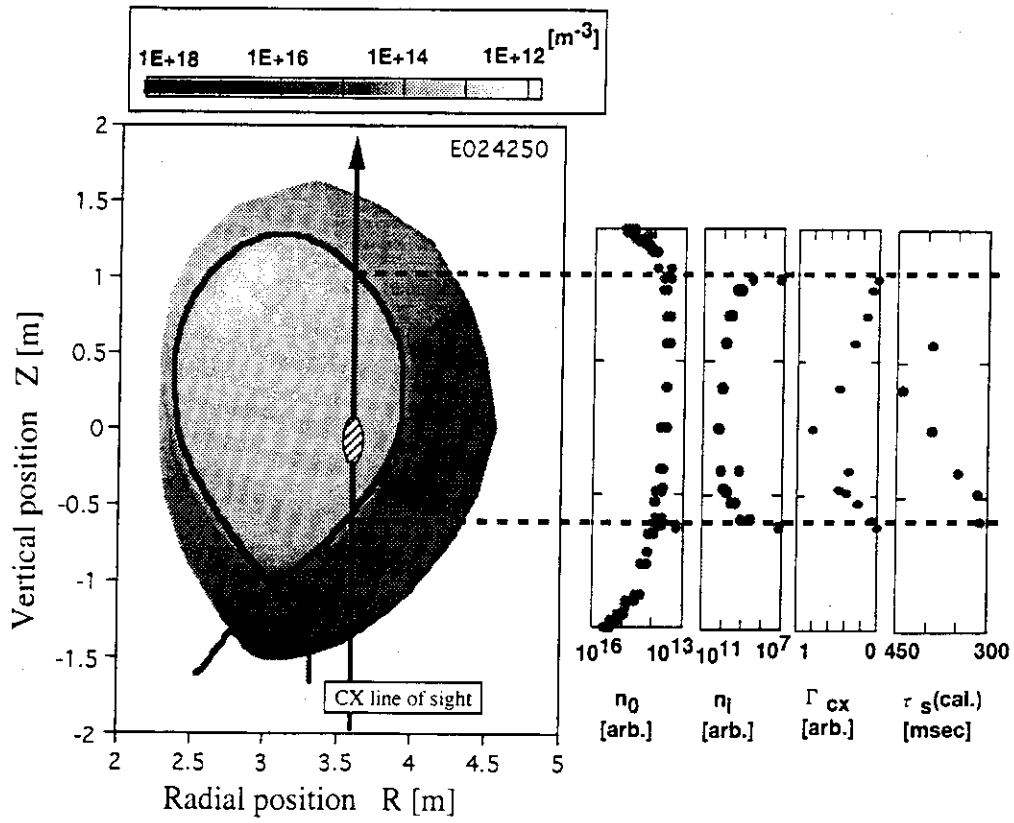

Fig. 3 : The neutral particle density(n_0), the ion density(n_i), the neutral particle flux(Γ_{cx}) and τ_s (cal.) along the line of sight of the CX analyzer

10.4 Analysis of TF ripple up-down asymmetry experiment

K. Tobita, M. Isobe, Y. Kusama, T. Nishitani

For the design of a fusion reactor which will probably have up-down asymmetric toroidal field (TF) ripple because of adoption of a long divertor throat, the question whether or not the asymmetry changes fast ion loss should be answered in advance. Theoretically, Yushmanov et al. found that the up-down asymmetry caused a net radial flux of banana particles but that the asymmetry-induced flux was small compared with the conventional ripple transport [1]. At the same time, however, they also suggested that the asymmetry might induce large particle loss above a critical value of the asymmetry. Calculated with JT-60U low collisionality conditions, fast ion transport can be affected by the asymmetry. In a series of the experiments on the up-down asymmetric ripple below, we aimed to clarify the sensitivity of the asymmetry on fast ion loss. Until now the asymmetry effect has never been observed.

First we preview the asymmetry-induced transport for fast ions expected from intuitive consideration in Section 10.4.1. In Section 10.4.2, the experimental results are summarized concisely and discussion is presented in Section 10.4.3.

10.4.1 Ordering of fast ion flow velocities

As far as ripple transport coefficients are concerned, general theoretical treatments are limited to ordering and we can not deal with any realistic problem precisely at all. But the following rough estimation of fast ion flow velocities will certainly call our attention more to the ripple asymmetry effect, indicating that the asymmetry-induced drift of fast ions is likely to enhance the conventional ripple banana transport.

The up-down asymmetry gives rise to a net radial drift of banana particles. The asymmetry-induced drift velocity $v_d{}^{asym}$ is given by [1]

$$v_d^{asym} \approx \frac{v_d}{\sqrt{\varepsilon}}\left(\sqrt{\delta_+} - \sqrt{\delta_-}\right) \tag{1}$$

$$\approx \frac{v_d}{\sqrt{\varepsilon}}\left(\left\langle\sqrt{\delta_+}\right\rangle_\theta - \left\langle\sqrt{\delta_-}\right\rangle_\theta\right), \tag{1'}$$

where $v_d = v^2/R\Omega$ and ε is the inverse aspect ratio and δ_+ and δ_- denote the ripple amplitudes at the upper and lower banana tips, respectively. And $< >_\theta$ indicates averaging over the flux surface. The direction of $v_d{}^{asym}$ is dependent on the ion ∇B direction.

The net flow velocity of the up-down symmetric TF ripple diffusion is estimated as follows:

$$v^{sym} \sim -D_{rp}\frac{\nabla n}{n} \tag{2}$$

with the fast ion density n and the diffusion coefficient for the fast ions D_{rp}. The diffusion for fast ions with around 90 keV at the dominant neutron-producing area (r/a = 0.2-0.5) is described by ripple banana diffusion at low collisionality and the diffusion coefficient [2] is

$$D_{rp} \sim \frac{N^{9/4} q^{13/4} \nu R \langle \delta^{3/2} \rangle_\theta}{\Omega \varepsilon^{5/2}} \nu_i \quad , \tag{3}$$

with conventional notations.

A comparison between $v_d{}^{asym}$ and v^{sym} for a vertically displaced JT-60U plasma (Fig. 2 (b)) is shown in Fig. 3, indicating that the both speeds are comparable. Since the sign of $v_d{}^{asym}$ changes in accordance with the ion ∇B direction, the calculated result suggests that fast ion transport can be enhanced or reduced by changing the ion ∇B direction. In JT-60U standard operations with the downward ion ∇B, the transport seems to decline because the asymmetry-induced flux and the conventional ripple transport flux try to cancel each other. Note that Fig. 1 indicates only the comparability of $v_d{}^{asym}$ and v^{sym}: D_{rp} has ambiguity of a factor of $O(1)$ and the expression for $v_d{}^{asym}$ by Eq. (1) is rough as well.

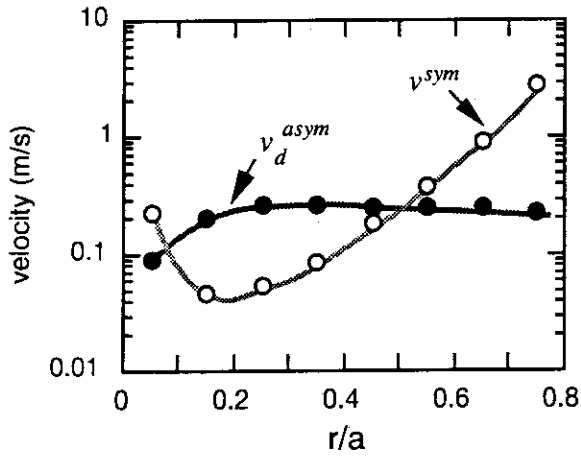

Fig. 1 The estimated velocities for the asymmetry-enhanced drift (Eq. (1')) and the net flow velocity of ripple banana diffusion (Eqs. (2) and (3)) for 90 keV deterium ions.

10.4.2 Experimental results

Opposed to the above intuitive consideration, the following two experiments reveal negative results on the asymmetry effect.

(1) Effect on 90 keV deuterons

First, we estimated the total ripple loss from the DD neutron decay following a neutral beam blip which was injected into banana orbits. The target plasma has very low density of (0.3-1.2)×10^{19} m^{-3}, at which the neutron decay is determined by both beam slowing down and loss. Since the slowing down is well predictable by a classical formulation [3], fast ion loss is derived easily from the experimental neutron decay. By displacing the plasma vertically as shown in Fig. 2 (b), the asymmetry effect on the total ripple loss was estimated. For both plasma configurations, the neutron emission decays faster than the calculation assumed no fast ion loss, as shown in Fig. 2 (a). We expected a

difference in the neutron decays for the asymmetric and symmetric configurations, but the figure (a) shows no difference, leading to the conclusion that the asymmetric effect is too low to be detected.

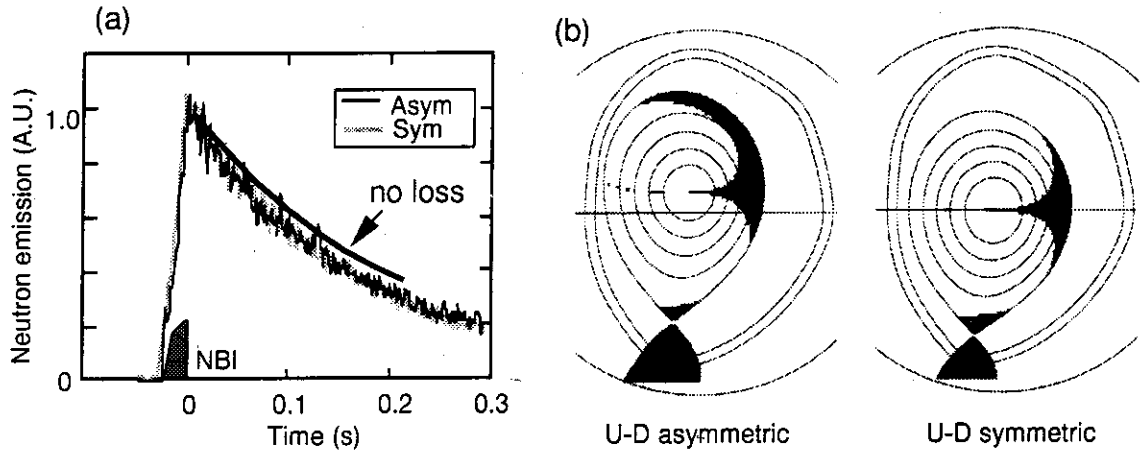

Fig. 2 (a) Neutron emissions for up-down asymmetric and symmetric ripple configurations, and (b) the plasma cross sections and the ripple wells for the configurations. The ion drift directed downwards in the both.

Next, by reversing the sign of the ion ∇B direction, we carried out the same experiment for the up-down asymmetric configuration: here we intended to raise the chance of seeing the asymmetry effect by changing the direction of the asymmetry-induced drift. But no difference was seen again.

(2) Effect on energetic tritons

Triton burnup experiment provides another evidence of little effect due to the asymmetry. Triton burnup ratio is closely related with triton transport, or loss. Here the triton burnup ratio $\Re$ is defined by

$$\Re = \int S_{DT}\, dt / \int S_{DD}\, dt \qquad (4)$$

where S_{DT} and S_{DD} is the fusion reactivities for D-D and D-T reactions, respectively. In Table I, $\Re$ is neither dependent on the ion drift direction nor the ripple asymmetry.

Table I Experimental triton burnup ration

Configuration Ion ∇B Drift	**Triton Burnup Ratio, $\Re$**
Asymmetry ion ∇B, $\Downarrow$	$(5.9 \pm 0.6) \times 10^{-3}$
Asymmetry ion ∇B, $\Uparrow$	$(5.5 \pm 0.5) \times 10^{-3}$
Symmetry ion ∇B, $\Downarrow$	$(6.4 \pm 0.3) \times 10^{-3}$

This implies that the asymmetry does not affect the ripple transport on a detectable scale and that the triton loss is less sensitive to the ripple asymmetry.

10.4.3 Analysis and discussion

Ripple loss of beam ions was calculated with an orbit following Monte Carlo (OFMC) code [4], with the aim of explaining the experimental result. The calculation was done for the ion ∇B reversal experiment. The total orbit loss is almost same for the both ion drift directions and no observation of the asymmetry effect is reasonable, as seen in Table I.. Note that reversing the ion ∇B direction leads to the interchange of the dominant ripple loss channel. But the loss channel does not matter in the above result, in that the loss channels (banana drift and ripple-trapped losses) are *branches* of a single stem, which separate each other at the ripple well boundary very near the edge from the ripple-transported banana particles.

Table I OFMC result for the JT-60U experiment

	Downward drift	Upward drift
banana drift loss	7.7 ± 0.6 %	0.6 ± 0.2 %
ripple-trapped loss	1.8 ± 0.2 %	9.7 ± 0.6 %
total orbit loss	9.5 ± 0.6 %	10.3 ± 0.6 %

As seen in Fig. 1, the asymmetry effect can be important around $r/a = 0.3$ compared with the conventional ripple transport. Also suggested from the figure is that we should perform a *local* measurement of some proper quantity such as charge exchange efflux to observe the effect, rather than the volume-integrated measurements. Assessment of the precise local transport coefficients of the asymmetry-induced diffusion is progressing using the OFMC code. With the result, we will be able to envision what diagnostic is promising and what accuracy we need in the measurement for the purpose.

References

[1] YUSHMANOV, P.N., CARY, J.R., SHASHARINA, S.G., Nucl. Fusion **33** (1993) 1293.

[2] GOLOBOROD'KO, V. Ya. et al., Physica Scripta **T16** (1987) 46.

[3] SIVKIN, D.V., Reviews of Plasma Physics, Vol. 4, Consultants Bureau, New York (1966) 93.

[4] TANI, K., et al., J. Phys. Soc. Jpn. **50** (1981) 1726.

10.5 Interpretation of experimental triton burnup on basis of ripple transport theory

K. Tobita, T. Nishitani

Experimentally, triton burnup — the *T(D,n)* reactivity as a secondary reaction of deuterium-deutrerium plasma — after neutral beam (NB) turn off typically shows the decay time of ~1 s, a time scale comparable with the slowing down time of MeV ions. Seen more carefully, however, the decay indicates that energetic tritons diffuse faster than the axisymmetric neo-classical diffusion and that the seeming diffusion seems to be enhanced by toroidal field ripple [1]. This note is aimed to look at how well *ripple banana diffusion in the low collisionality regime* describes the observed transport of tritons.

10.5.1 Ripple banana diffusion in low collisionality regime

The low collisionality ripple diffusion prevails inside the ripple stochastic boundary [2] given by

$$\delta_c \approx \left(\frac{\varepsilon}{N\pi q}\right)^{3/2} \frac{1}{2\rho_L q'} \quad , \tag{1}$$

where N is the number of toroidal field coils, ρ_L is the fast ion gyro-radius and q' is the radial derivative of q. The others are conventional notations used in ripple transport theory. For the low collisionality diffusion, ν_i should be

$$\nu_i < \sim \frac{\nu_i^*}{(Nq)^2} \quad . \tag{2}$$

For energetic tritons, the low collisionality condition becomes ν_i < ~(10-100) s^{-1}. Under the conditions of the triton burnup experiment, ν_i is in the range of 0.1-1 s^{-1}, and hence the above condition is satisfied and the low collisional ripple diffusion can operate. In the diffusion, both TF ripple and pitch angle scattering are essential to make fast ion orbits chaotic. The diffusion coefficient derived by Goloborod'ko et al [3] is given as follows:

$$D_{rp} \sim \frac{N^{9/4} q^{13/4} \nu R <\delta^{3/2}>_\theta}{\Omega_i \varepsilon^{5/2}} \nu_i \quad , \tag{3}$$

where Ω_i is the ion cyclotron frequency and $< >_\theta$ indicates averaging over the flux surface. As often done in the analytic approach of ripple transport in Eq. (3), a factor of

the order of $O(1)$ for D_{rp} is ignored. Schematic picture of the ripple diffusion domains and rough estimations of the diffusion coefficients are illustrated in Fig. 1. Although the low collisionality diffusion has diffusion coefficients of a few orders smaller than stochastic diffusion, it is still faster than axisymmetric neo-classical diffusion in a large portion of the plasma and the neo-classical diffusion holds only in the core. Note that the transport boundaries where the dominant diffusive processes alter is dependent on fast ion energy.

Importance of the low-collisional diffusion is a connecting role between the MeV-ion-producing *core* and the *edge* region where different transport processes (stochastic diffusion and ripple trapping) dominate. Since the MeV ion source rate is highly peaked at the center, roughly speaking, ripple loss of the fast ions has an aspect of a cascade reaction; *slow* low-collisional diffusion, rather than *quick* edge ripple transport processes, tends to determine the quantity of fast ion loss.

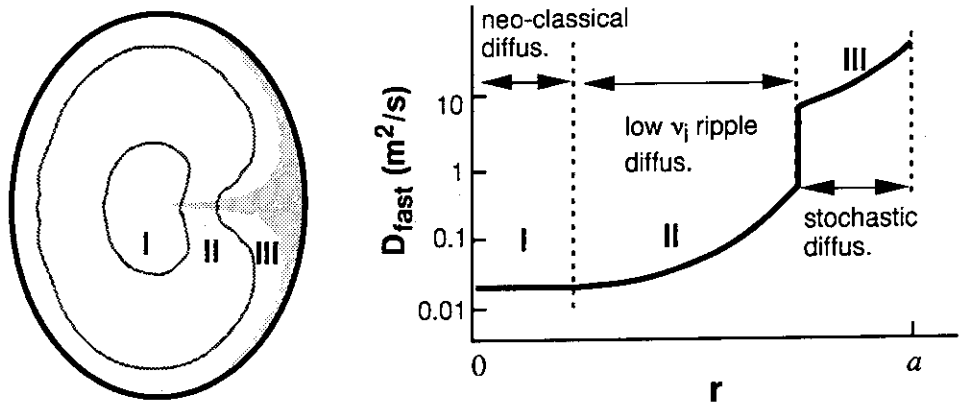

Fig. 1 Poloidal domains where different transport processes prevail: axisymmetric neo-classical transport (I), low collisionality ripple banana diffusion (II), stochastic diffusion (III), and ripple trapping (shaded area). Also shown are rough estimations of the diffusion coefficients as a function of r.

Previous ripple experiments have not been focused on the low collisionality diffusion due to small D_{rp}. Yet, for the low collisionality ripple diffusion, the confinement time of fast ions produced in the core is of the order of 1-10 s ($\approx a^2/4D_{rp}$), which is never negligible in respect of slowing down time (typically ~1 s), most likely resulting in delayed loss. For that reason, more attention should be paid to the diffusion.

10.5.2 Analysis of experimental data

The low collisionality diffusion is studied from triton burnup following neutral beam (NB) heating turn off. A neutron detector views the core region of $r/a \leq 0.6$, mostly affected by the $T(D,n)$ reactivity at r/a = 0.36-0.47, where triton transport is anticipated to

obey the low collisionality ripple diffusion. Thus, the triton burnup is dependent on the local transport process in the core and independent of edge transport processes such as stochastic diffusion and ripple trapping.

A comparison between the experimental and theoretical diffusion coefficients is shown in Fig. 2. The main parameters of the discharges are I_p = 1.5-2.2 MA, B_T = 4.0 T and $\bar{n}_e$ = (0.7-1.3)×10^{19} m^{-3}. The theoretical D_{fast} is calculated using Eq. (3): here, it should be reminded again that the theoretical coefficients have ambiguity of *O(1)*. Considering the cross section for *T(D,n)* reaction — peaks at 0.17 MeV — and the slowing-down distribution of tritons, tritons with energies of around 0.17 MeV contribute much to the experimental triton burnup. In fact, the experiment shown in the figure is comparable with the calculation for 0.17 MeV.

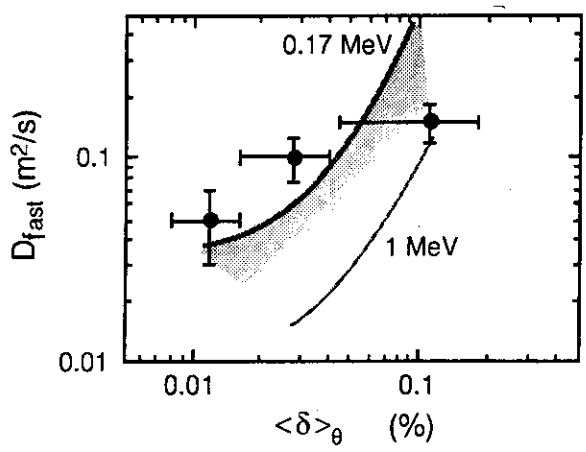

Fig.2
Experimental (●) and theoretical diffusion coefficients for tritons as a function of ripple amplitude.

10.5.3 Discussion

The above comparison does not become a clear evidence of the low collisionality ripple diffusion. Because $D_{rp} \propto 1/E$ theoretically, it is not acceptable to treat the diffusion coefficient of tritons as constant over the considered triton energy range: if theory is correct, in the core region MeV-tritons are almost at rest, and then the diffusion becomes active gradually as they undergo slowing down. Thus estimating the energy-independent D_{fast} from triton burnup is not a proper way. Another key issue in the data analysis is a finite banana width effect. Under the experimental conditions, the full banana widths Δ_B/a are about 0.45 for 1 MeV and 0.2 for 0.17 MeV, respectively. This may make invalid to define a local (flux-surface-averaged) D_{rp} in virtue of dramatic radial change in ripple amplitude.

In order to overcome those difficulties, we should proceed the following experiments and analysis:

(1) To reconstruct the time evolution of the measured burnup using energy-dependent D_{rp} (Eq. (3)), rather than assuming energy-independent diffusion. Moreover, in order to include the finite banana width effect, prudent analysis using an orbit-following Monte Carlo code [4] is required.

(2) To carry out the similar experiment at smaller Δ_B/a, preferably at $I_p \geq 2.5$ MA.

(3) To verify ν_i dependence in an experiment changing plasma density; it will give a straight-forward evidence of the low collisionality ripple diffusion because ν_i simply contributes to D_{rp} as seen in Eq. (3).

References

[1] NISHITANI, T. et al., this report, Section 10.1 :NISHITANI, T., et al, *Triton Burnup Study in JT-60U*, Plasma Phys. Contr. Fusion (in press).

[2] GOLDSTON, R.J., et al., Phys. Rev. Lett. **47** (1981) 647.

[3] GOLOBOROD'KO, V. Ya. et al., Physica Scripta **T16** (1987) 46.

[4] TANI, K., et al., J. Phys. Soc. Jpn. **50** (1981) 1726.

11. Disruption and Plasma Control

11.1 The Killer-Pellet-Injection in JT-60U

R Yoshino, K Itami, N Isei, Y. Kawano, Y Neyatani

1. Introduction

The disruptive termination consists of energy-quench and the following plasma-current-quench (I_p-quench). Thus there are two strategies to ameliorate the disruptive termination; one is softening of energy-quench, and the other one is that of I_p-quench. The former one is aiming intensive reduction of the heat flux onto the first wall, and the killer-pellet injection is one method. In JT-60U, 100% neon-ice-pellets (or killer-pellets) were firstly injected into plasmas in order to generate fast I_p-quench[1], which perfectly conflicts with the softening of I_p-quench. However fast I_p-quench within a time constant of the passive structure (vacuum vessel, in-vessel components) has a merit to suppressing VDE and the halo current owing to small plasma movement.

Demerits of the killer-pellet-injection is the generation of high toroidal eddy current in the passive structure and of runaway electrons. However machine-design against the toroidally uniform eddy current is much easier than that against the halo current with large toroidal asymmetries[2], and the runaway electron generation has been delayed by intense impurity pellet injection as presented in this paper.

2. Comparison of Intense Gas Puffing and Killer-Pellet-Injection

Typical time evolutions of plasma termination caused by the killer pellet injection (KPI) and intense helium gas puffing (IHGP) are presented in Fig.1 and 2. Large differences can be observed between them as the following.

1) Fast drop of the central electron temperature $T_e(0)$ and an increase in heat flux onto the divertor plate can be observed for both cases. A pulsive increase in the line integrated electron density n_el is observed after $T_e(0)$-drop for IHGP, but a simultaneous n_el-rise and $T_e(0)$-drop can be observed for KPI.
2) For IHGP heat flux on to the divertor plate is a intense pulse with short time duration of ~2 ms and without time delay from the $T_e(0)$-drop. On the other hand, heat flux for KPI is a small pulse with a clear time delay of ~600 μs from $T_e(0)$-drop, and its time duration is long of ~10 ms.
3) A negative loop voltage spike and a positive plasma current spike are not clearly observed for KPI, which suggests that the modification of the plasma current profile is much smaller than that for IHGP.

4) Pulsive rise of the particle recycling can be simultaneously observed at the energy quench in both of the main plasma and the divertor regions for IHGP. However a sudden rise of particle recycling in the divertor region delays by ~3 ms from that in a main plasma for KPI, and continuous increase in divertor plate temperature and fast decrease in n_el are observed at the early phase of I_p-quench .

These differences clearly show that the energy quench is not observed for KPI.

3. Delayed Runway Electron Generation

Generation of runaway electrons during I_p-quench is one of serious problems of the disruptive termination, which intensively enhances the plasma-wall interaction. Thus the mitigation of its generation has been studied. The former study for the runaway electron generation suggests that it can be observed for low plasma density just before the energy quench and for low central electron temperature with fast plasma-current-quench[3].

In JT-60U, generation of runaway electrons is frequently observed for KPI, because n_el largely decreases during I_p-quench as shown in Fig.1. Thus three neon ice pellets (3 mmϕx1, 4 mmϕx2) were simultaneously injected to raise the density as shown in Fig.3. The n_el is raised to ~$2.5x10^{20}m^{-2}$, and then very fast decay of n_el is observed at t = 8.12~8.13 sec. At n_el of ~$1.5x10^{20}m^{-2}$ (t ~ 8.13 s), an increase in the hard X-ray emission is observed. However the plasma current has already dropped to 400 kA, which is only ~20% of the flattop plasma current. Thus hard X-ray emission is successfully delayed until low plasma current due to high electron density. Here the electron temperature at t = 8.12~8.13 sec is much lower than 100 eV, and is hard to be measured by ECE heterodyne radiometer.

For simultaneous three neon-ice-pellet injection with high n_el of > ~$2.5x10^{20}m^{-2}$ at the start of I_p-quench, hard X-ray emission could not be observed at the early phase of I_p-quench. On the other hand for one neon-ice-pellet injection with lower n_el of < $2.0x10^{20}m^{-2}$ at the start of I_p-quench, hard X-ray emission was frequently observed at the early phase of I_p-quench. This results suggest that high density is necessary to delay the rise of hard X-ray emission and continuous killer-pellet-injection is required even during I_p-quench.

3. Plasma-Displacements during Plasma-Current-Quench

Killer pellet injection is one method to mitigate the plasma surface interaction and the halo current during the I_p-quench[4].

1) Inward Displacement

The divertor configuration is kept during the disruptive termination caused by KPI with avoiding large vertical displacement. Here fast rise of $\beta_p+l_i/2$ (e.g. see Fig.3, t = 8.124 sec), which is mainly caused by the increase in l_i with the shrinkage of the plasma minor radius, has relaxed the decrease in R_J. An attachment of a plasma to the inboard first wall is avoided due to

this l_i ramp-up until 65% drop of the plasma current. However an inward attachment of a plasma is suspected for the later phase of I_p-quench. In ITER-like fusion reactors, long time constant of the passive components (e.g. 1 sec) is expected to largely reduce this horizontal shift.

2) Vertical Displacement

A fast inward R_J-shift causes a degradation of the field decay index and raises the possibility of vertical positional instability for highly elongated plasmas. However in JT-60U such positional instability has not been observed for KPI as shown in Fig.1 and 3. When the initial vertical plasma position is selected to be near the neutral point, the vertical displacement in the early phase can be largely suppressed due to a balance of up/down toroidally flowing eddy currents in the vacuum vessel [4][5]. In Fig.1 and 3 the initial plasma vertical position is selected to be 10 cm, that is close to the neutral point (15 cm). Thus the vertical plasma displacement is smaller than ~5 cm during a half plasma-current-drop from its flattop value.

6. Conclusions

The killer-pellet is the impurity-pellet, that is injected into a plasma with aiming to terminate a tokamak discharge without causing serious damages onto the machine, and has been investigated in JT-60U using neon-ice-pellets. The disruption caused by the killer pellet injection is much different from the normal density limit disruption and has many advantages.

References

[1] R. Yoshino et al., Proc . of 15th Int. Conf. on Plasma Physics and Controlled Nucl. Fusion Research, Seville, Vol.**1** (1995) 685.

[2] R.S. Granetz et al, in press Nucl. Fusion (1996).

[3] R. Yoshino J. of Nucl. Materials, **220-222** (1995) 132.

[4] R. Yoshino et al., Nucl. Fusion in press (1996)

[5] Y. Nakamura et al., Nucl. Fusion in press (1996)

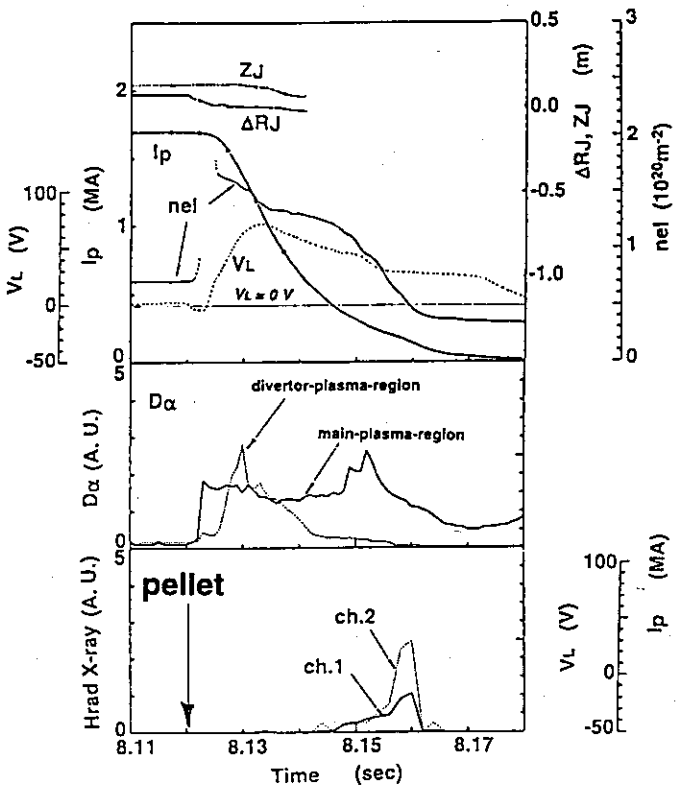

Fig.1 Discharge termination obtained by one neon-ice-pellet injection (3 mmϕ).

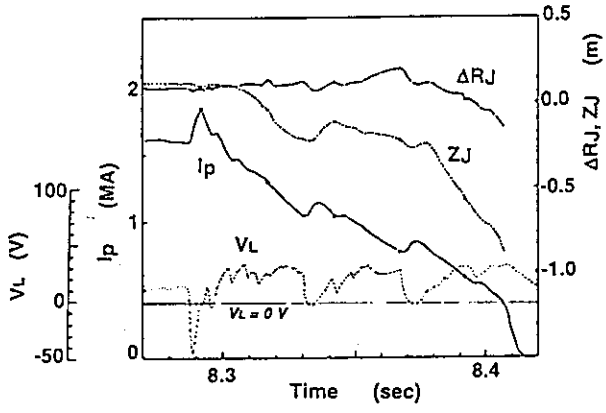

Fig.2 Density limit disruption caused by intense helium puffing.

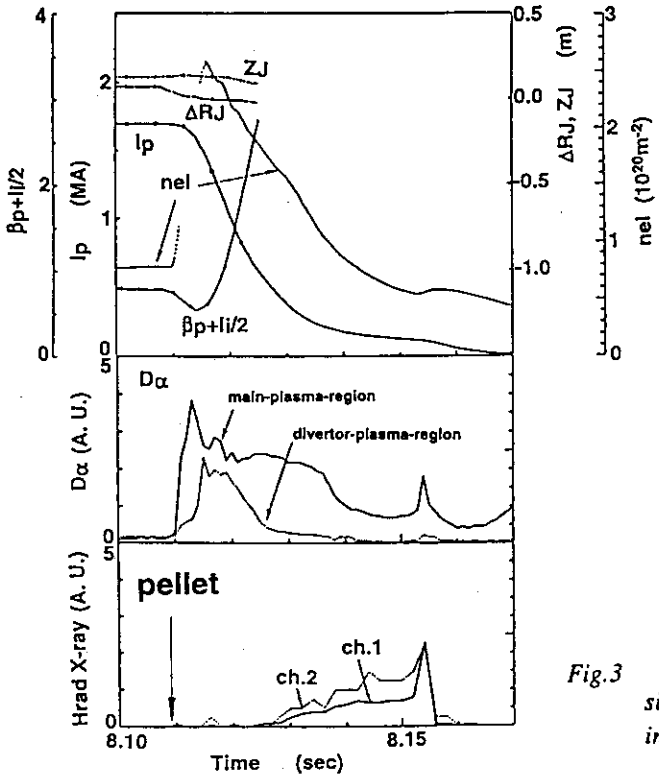

Fig.3 Discharge termination obtained by simultaneous three neon-ice-pellets injection (3 mmϕx1, 4 mmϕx2).

11.2 Regime of generation of runaway electrons during major disruption

Y. Kawano, R. Yoshino, Y. Neyatani, T. Hatae

The fast major disruption which terminates a plasma discharge is a serious issue in a tokamak fusion reactor [1]. A release of plasma kinetic energy (thermal quench) causes severe damage of first wall materials. Subsequent fast release of plasma magnetic energy (current quench) induces large eddy currents which generate large forces on vacuum vessel and in-vessel components. Additionally, first wall materials can be irradiated by energetic runaway electrons generated and accelerated by the large one turn voltage spike during current quench phase.

In ITER, runaway electrons with up to several tens MeV and several tens MJ is expected to be produced [2]. They are considered to cause the very serious damage of plasma facing components. Since it is urgent to resolve these problems for ITER, the comprehensive knowledge of the generation mechanism of runaway electrons is needed. However, it is not clear yet due to lack of reliable plasma diagnostics during the current quench phase especially for electron density and temperature. In JT-60U, a newly developed CO_2 laser interferometer can survive during the fast current quench [3]. More accurate discussion can be possible for runaway electrons by this measurement.

Since runaway electrons were observed in the case of that a plasma current decay time, τ_{decay} defined by Ip/(dIp/dt), was less than 20ms in JT-60U [4], a sequence of tokamak discharges were devoted to produce the fast current quench. Figure 1 shows a diagram of line electron density measured by the CO_2 laser interferometer (n_eL_p) versus one turn voltage (V_{loop}) during current quench phase to understand the generation condition of runaway electrons. Data from discharges with accidentally happened disruption so far were also analyzed. Because energetic runaway electrons can produce photo-neutrons on the target materials through (γ - n) reaction [5], the neutron yield is a good indicator of the presence of runaway electrons. By this reason, all data points in the figure are also classified according to their total neutron yield per each disruption (Y_n).

In Fig. 1, clear presence of runaway electrons are observed in the regime of V_{loop} > 80V and $n_eL_p < 6\times10^{20}m^{-2}$. It is seen that the neutron yield is decreased with the increase in density. Though the photo-neutron process is complicated, including the energy dependence and the threshold, a reduction of the energetic runaway electrons might be possible by increase in density.

In order to understand the generation of runaway electrons, effectiveness of a runaway generation process should be evaluated, e. g. the Dreicer evaporation process [6]. The Dreicer field is written as [7];

$$E_D = n_e e^3 \ln\Lambda / 4\pi\varepsilon_0^2 kT_e \quad (1).$$

For example, at the particular time that the V_{loop} reached its maximum during the current quench, the Dreicer field can be estimated as follows. Considering the CO_2 laser path length of about 6m in the plasma and assuming the uniform profile, the n_e is relatively high of ~$7x10^{19}$ m^{-2} for the case of V_{loop} ~100V in Fig. 1. The electron temperature could not be measured directly for fast disruptions but assuming that kT_e is 4 eV from one of the fast disruption model [7]. The $\ln\Lambda$ is assumed of 15. Substituting these parameters into eq. (1), the Dreicer field is calculated to be E_D ~ 7000V/m. On the other hand, the actual applied field (E_{appl}) to the plasma provided by one turn voltage spike; E_{appl} is estimated to be order of 5V/m (= ~100V / $2\pi R_{VV}$, where is R_{VV} the major radius of vacuum vessel center; 3.32m). Thus the normalized electric field ($\varepsilon = E_{appl} / E_D$) is evaluated as ε = ~ $7x10^{-4}$. It is noted that this value is much smaller than the critical limit of ε_c ~ $3x10^{-2}$ which is the Dreicer process can directly contribute to a significant part of runaway electrons [8]. The Dreicer process becomes effective if T_e is more than 200 eV, which is hardly accepted in the picture of fast current quench. This result itself seems to indicate that the Dreicer process is less effective to generate runaway electrons during current quench phase. So, it is expected that the runaway electrons are generated at earlier phase of disruption, e. g. the thermal quench phase and/or the post thermal quench phase, or more later of current quench phase where the density decreased. Consequently, the process should be analyzed from the beginning to the end of the disruption. Discussions for other processes including the effect of trapped high energy electrons and the avalanche effect should be performed using measured plasma parameters in this study .

References

1) Yoshino R., et al. : J. of Plasma and Fusion Res., 70, 1081 (1994).
2) Zolti E. : Fusion Eng. and Des., 18, 163 (1991).
3) Kawano Y., et al. : Submitted to Rev. Sci. Instrum.
4) Yoshino R. : J. Nucl. Mat. , 220-222, 132 (1995).
5) Jarvis O. N. : Nucl. Fusion, 28, 1981 (1988).
6) Dreicer H. : Phys. Rev. , 117, 329 (1960).
7) Knoepfel H. and Spong D. A. : Nucl. Fusion, 19, 785 (1979).
8) Ward D. J. and Wesson J. A. : Nucl. Fusion, 32, 1117 (1992).
9) Fleischmann H. H. and Zweben S. J. : PPPL report 2914 (1993).

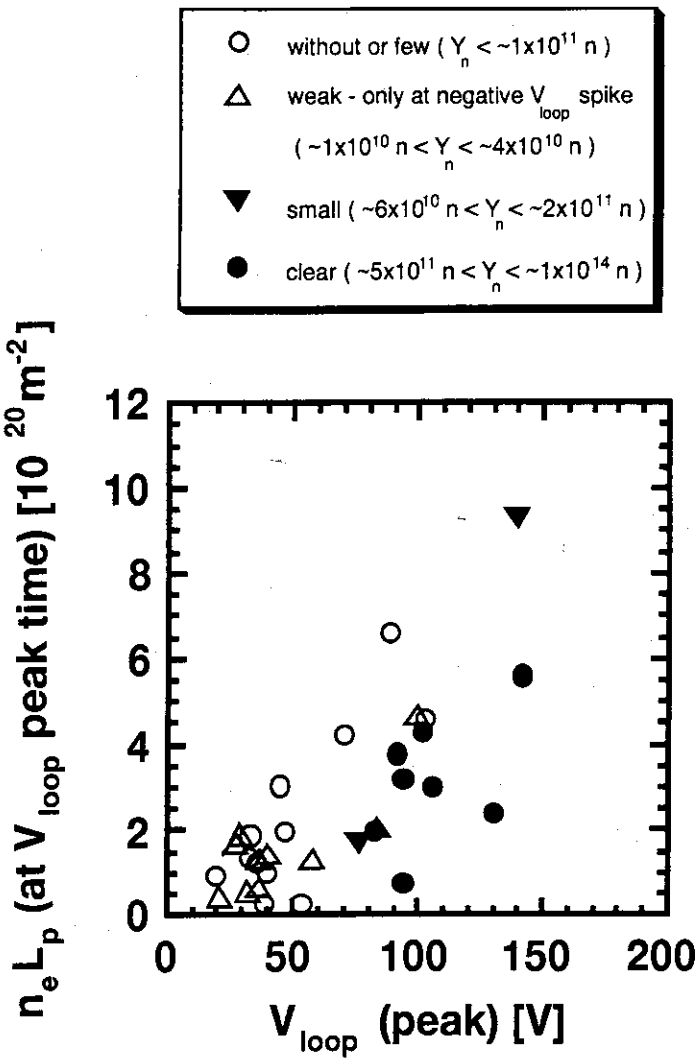

Fig. 1 Map of electron line density ($n_e L_p$) measured by CO_2 laser interferometer versus one turn voltage ; (V_{loop}) for disruptions of plasma current: 0.7 ~ 2.5MA and toroidal field: 1 ~4T discharges. Data were taken at the peak timing of V_{loop} during current quench phase. Path length of CO_2 laser beam in the plasma is about 6m. Closed symbols show the regime where clear (●) and small (▼) runaway electrons were observed. Each data are classified according to total photo-neutron yield per event (Y_n).

11.3 Boronization

S. Higashijima, M. Shimada, S. Tsuji-Iio*, H. Kubo, T. Sugie, A. Sakasai, Y. Neyatani, J. Yagyu, H. Hiratsuka, T. Arai, N. Ogiwara and M. Saidoh.

1. Introduction

Impurity reduction is an important issue for fusion devices because of the radiation power loss and the fuel dilution. To decrease impurity concentrations, in JT-60U all of the plasma facing surfaces were covered with carbon tiles and the various wall conditioning methods have been carried out. One of the wall conditionings is boronization using decaborane ($B_{10}H_{14}$) [1] and boronization has been carried out six times since July 1992. Boronization is effective on oxygen impurity reduction just after the vacuum vessel vented and dramatic reduction of the particle recycling [2]. As a result, in JT-60U the good confinement plasmas in high β_p mode and H-mode could be obtained [3].

As decaborane contains hydrogen atoms, hydrogen concentration in deuterium plasma was increased after boronization and hydrogen degassing was necessary. In the latest 6th boronization the mixture gas of helium and deuterium was used as the supporting gas of the glow discharge and hydrogen contamination in the deuterium plasmas was decreased without increasing particle recycling.

In this part, in JT-60U the effects of boronization are summarized.

2. Set up

In JT-60U boronization using decaborane ($B_{10}H_{14}$) is executed because decaborane is solid in room temperature and can be handled more safety than diborane (B_2H_6). In boronization decaborane is heated, sublimated and guided into the vacuum vessel and boron film is formed in the glow discharge. In order to optimize boronization the various improvements were carried out each time. Table 1 is a summary of each boronization.

Impurity behavior is analyzed by spectroscopic measurements, especially the total of impurity concentrations is decided from both the line intensities analyzed by VUV spectrometer

	1st	2nd	3rd	4th	5th	6th
Date	1992/7/30	1992/9/1	1993/2/17	1993/7/2	1994/2/1	1995/2/28
Shot number just before boronization	15895	16048	16951	18363	19757	22964
Shot number just after boronization	15896	16049	16976	18427	19770	22989
Amount of decaborane	10	15	50	100	99	99.899
Supporting gas	He	He	He	He	He	He(62%)+D2(38%)
Deposition time [h]	10	10	36	57	43	55.5
Wall temp. [℃]	300	300	250	250	250	250
Number of gas inlets	1	1	12	12	12	12
Estimated boron layer thickness [nm]	30	45	150	300	300	300
Measured thickness	−	2 ~ 80	100 ~ 400	210 ~ 1500	−	
Row-f B4C tile	−	−	○	←	←	←
Row-e B4C tile	−	−	−	−	○	←
NB port baking	−	−	○(Tangential 2 ports)	←	○(all ports)	←

Table 1. Summary of boronization in JT-60U.

and Zeff value derived from visible bremsstrahlung lights.

3. Impurity and Particle Recycling

Introducing boronization, oxygen concentration is reduced just after the vent of the vacuum vessel in both OH and NB discharges. Figure 1(a) shows the change of oxygen impurity in OH discharges just before and just after the 4th boronization. After boronization oxygen concentration is decreased specially at low electron density. In OH plasmas carbon concentration does not change so much with boronization and boron impurity is increased as a result of boronization. Because the increment of boron impurity cancels out the decrement of oxygen impurity, Zeff value and radiation power loss from the main plasma do not change. In NB

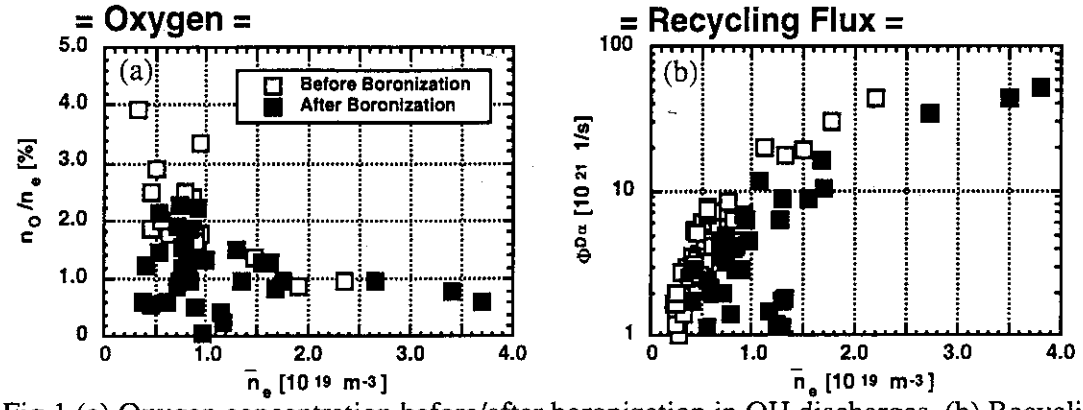

Fig.1 (a) Oxygen concentration before/after boronization in OH discharges. (b) Recycling flux before/after boronization.

heated plasmas, carbon concentration has a tendency to increase and boron concentration certainly increases. Zeff value and radiation power loss from the main plasma are increased. There are two reasons that boronization can not decrease carbon impurity in both OH and NB plasmas. The first reason is that boron film in itself involves carbon since boron film is made in the glow discharge and the second is that boron film at the separatrix legs is immediately lost by repeating high power NB discharges and carbon is just generated from there. Although the concentration of boron impurity decays to several percentages in ~50 shots after boronization and boron concentration becomes low, oxygen impurity concentrations are kept low without the other wall conditioning methods. This means boron film is produced on all of the first wall and the quantity of decaborane is sufficient. But oxygen concentration is a level comparable to the final level achieved by the other conditionings.

The recycling particle flux ($\Phi^{D\alpha}$) is also shown in Fig.1(b) and is defined as the sum of the deuterium (and hydrogen) particle flux derived from Dα (and Hα) intensity in each poloidal cord multiplied by the area of wall corresponding to each cord. The recycling flux after boronization is low in both OH and NB heated plasmas compared to the non-boronized surface. The reduction of the recycling flux shows that the boron layer absorbs not only oxygen but also deuterium and hydrogen particles, and the boronized surface might keep the

particles longer than a carbon surface. Boronization enables us to operate with the vacuum vessel at 300℃ without the helium TDC between tokamak discharges. After boronization high βp plasmas are obtained at low electron densities and then the high βp mode evolves into a combined state with the H-mode [3].

4. Boronization using the Mixture Gas of Helium and Deuterium

As decaborane consists of boron and hydrogen, the generated boron film involves many hydrogen atoms. In the 1st-5th boronizations which the pure helium gas was used as the supporting gas, H/D ratio increased up to ~10 just after boronization and therefore ~200 shots were necessary for decreasing H/D ratio less than ~0.1. In the latest 6th boronization the mixture gas of helium (~62%) and deuterium (~38%) is used as the supporting gas of the glow discharge. Although the pure hydrogen gas was used as the supporting gas at first, a

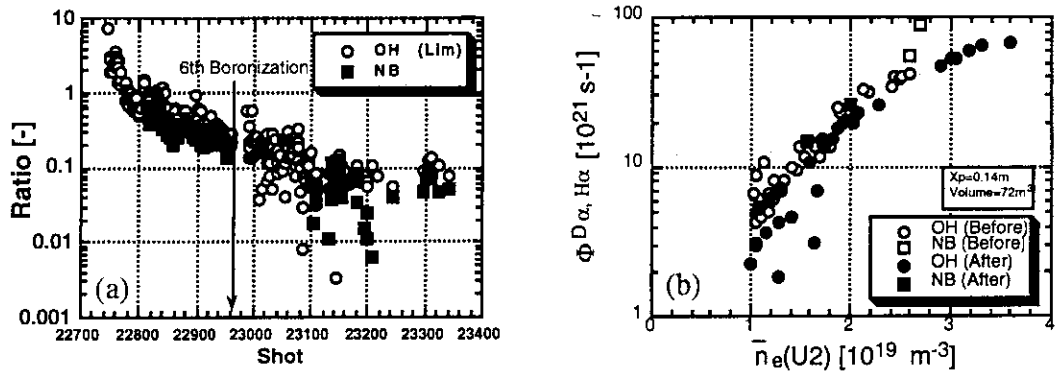

Fig.2(a) the shot history of H/D ratio before/after the 6th boronization. (b) Recycling flux before/after the 6th boronization. Recycling flux is the same level as the case of helium supporting gas.

stable glow discharge could not be obtained and helium gas was finally mixed with hydrogen gas. Figure 2(a) shows the shot history of hydrogen(H)/deuterium(D) ratio. The H/D ratio is ~1 just after boronization and a prominent increase of H/D ratio is not seen after boronization. By the way, to use deuterium gas for the supporting gas may be a defect because it is possible that particle recycling becomes large. Hydrogen and deuterium concentration in the boron film are measured by high energy ERD method. In the case of pure helium supporting gas H/boron(B) ratio in the film is ~10% and in the mixture gas case H/B ratio is ~2% and D/B ratio is ~26%. Hydrogen atom in the film certainly decreases, but in the contrary the sum of hydrogen and deuterium in the film increases from ~10% to ~28%. Figure 2(b) shows the recycling flux before/after the 6th boronization. Recycling flux in the case of mixture gas is the same level of the case of helium gas. As a result, we can decrease the hydrogen contamination in the deuterium plasmas without increasing deuterium recycling. Now, it is not clear why the sum of hydrogen and deuterium in the film increases and recycling flux does not change.

5. Summary

In JT-60U, boronization using decaborane was carried out and the effects of boronization were investigated. It is summarized as follows:

(1) Boronization gets down oxygen impurity in the same extent as achieving by the other wall conditioning just after the vacuum vessel vent and does not affect on carbon impurity.

(2) Particle recycling was dramatically decreased. The main reason for particle recycling reduction is that boron film absorbed hydrogen/deuterium.

(3) Boronization using the mixture gas of helium and deuterium as the supporting gas of glow discharge is executed. Hydrogen concentration in the boron film is decreased and hydrogen/deuterium ratio in the plasma is decreased without increasing recycling flux. But the sum of hydrogen and deuterium in the film is increased.

Acknowledegments

The authors are grateful to Prof. T. Sugai and Dr. M. Yamage of Nagoya university for the cooperation.

References

[1] Saidoh M. et al., Fusion Engineering and Design, 22, 271 (1993).

[2] S. Higashijima et al., J. Nucl. Mater., 220-222, 375 (1995).

[3] Mori M. et al., Nucl. Fusion, 34, 1045 (1994).

11.4 Feedback Control of Neutron Emission Rate in JT-60U

Y. Neyatani, T. Fukuda, T. Nishitani and R. Yoshino

1. Introduction

In order to operate steady state fusion reactor, advanced real-time control system should be established in addition to the present feedback control, such as plasma current, plasma position and shape, electron density. Expected control parameters will be current profile, pressure profile, divertor heat load, fusion power control etc. Especially, fusion power control is the most essential issue for a reactor. Plasma beta has been controlled using diamagnetic signals to control plasma energy [1]. It is one of the power control methods. However, in a long pulse operation, signal with integration circuit such as magnetic measurement is difficult to use FB signals because of accumulation of integration error. In this paper, we tried direct control of fusion power using D-D neutron emission rate in the JT-60U deuterium plasmas.

2. Feedback Control System

In JT-60U, two kinds of real-time control systems are operated for plasma control. One is the Equilibrium Control System which control the plasma current, positions and plasma shapes. The other is the Particle Supply and Heating Control System. This system includes the gas feed, the pellet injection, the neutral beam (NB) and the RF heating systems. The later system was utilized for this study. The D-D neutrons were used as a feedback signal of fusion reaction rate control measured by the ^{235}U fission chamber. The NB was used as a driver of feedback (FB) control as D-D fusion reaction rate depends on ion temperature. We have fourteen NB lines, and a number of unit has been controlled for heating power control followed by the formula (1).

$$N_u = \mathrm{Int}\left[G\left(S_n^{meas.} - S_n^{Ref.}\right)\right] \qquad (1)$$

Nu : Number of NB injection unit
G : Feedback Gain
$S_n^{meas.}$: Measured D-D neutron emission rate
$S_n^{Ref.}$: Preprogrammed D-D neutron emission rate

The waveform of neutron emission rate was preprogrammed as a discharge conditions before operations. The neutron feedback loop is illustrated in Figure 1. Delay of control is depend on the time response of NB injection system and the data sampling period. This delay is 60 ms in case of turning NB on and is 20 ms for off.

3. Demonstration of Feedback Control of Neutron Emission Rate

The FB control of neutron emission rate was demonstrated using FB system described previous section. The S_n was kept constant at $3x10^{15}$ n/s for 5 seconds until NB was turned off (Fig.2). The first column in Figure 2 is the waveform of NB injection power. The last column is the neutron emission rate (S_n). The input power was successfully controlled increase and decrease of S_n. The controllable minimum neutron emission rate is $8x10^{14}$ n/s which comes from the NB power per unit and the time delay of FB system. During the FB control periods, the stored energy was also kept constant at 2.5 MJ as shown in the second column. It is because that the S_n was proportional to the squared stored energy with fixed confinement mode (high β_p H mode) when the plasma position and the density profile do not changed [2]. This relation suggests that the neutron FB can also used for the FB control of the stored energy.

However, the S_n seems to decrease slightly with time. During NB heating period, line averaged electron density gradually increased by the beam fueling. This may be caused by the change of beam deposition profile with changing density profile. The beam deposition in the plasma peripheral region will increase with density because ionization rate increases with density. Then, the central heating power reduced relatively and central ion temperature, which is the most active region, reduced with same injection power. Figure 3 shows the beam deposition power profile at t=5 and 10 seconds calculated by TOPICS code. Peak position of absorption power shifted to outward with time.

4. Summary and Discussions

New real-time control function of neutron emission rate has been developed as a first step of fusion power control. By the control of the number of NB injection units, we successfully controlled neutron emission rate to keep constant during the FB control was turned on (~5 s). The plasma stored energy was also kept constant during the same period. This demonstrated results is expected to be effective for extending the steady state performance.

The technique of FB control by NB is not obtained steady state perfectly. Because, at present, density profile is not controlled, then beam deposition changed gradually. This suggests that density profile control should be combined to the heating control and optimized to more long pulse control.

When the plasma performance reduced largely, for example caused by MHD instabilities, it will not be possible to input enough NB power and the FB function will not operate.

Fusion power in the steady state phase with Q>1 will not be determined by injected heating power directly. The control method using NB controlling the NB power itself may not be feasible to control the fusion power because the major heating power is the fusion reaction power in this phase. However, combination of this function and the fueling control will help the ignition control of plasma near Q~1. It will enable the optimization to control before the ignition starts. It will also be useful for the improved heating plasma performance without catastrophic instabilities such as beta collapse.

References

1) J. E. Lawson, et al. ; Proceedings of 18th Symposium on Fusion Technology, 1994 p.739.
2) T. Nishitani, et al.; Nucl. Fusion 34 (1994) 1069.

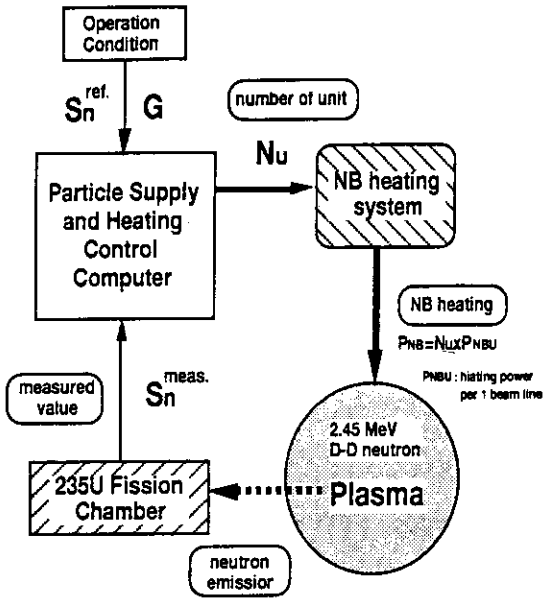

Fig. 1 Illustration of feedback loop for neutron emission rate. NB power is determined by number of unit control.

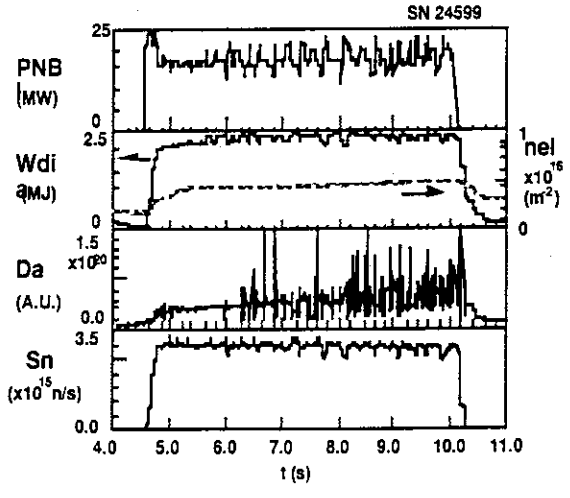

Fig. 2 Feedback control of neutron emission rate by NBI. Figure indicates the waveforms of NB input power (P_{NBI}), the stored energy (W_{dia}) and line averaged electron density (nel), intensity of Dα emission rate (Da) and the neutron emission rate (Sn). The dotted line in the last column is preprogrammed the neutron emission rate.

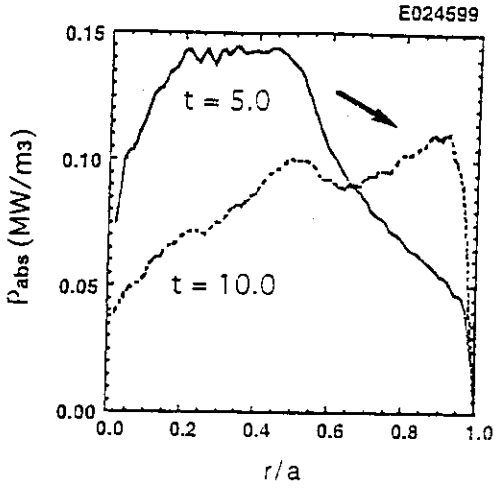

Fig. 3 Deposition profile of NB input power at t=5 and 10 s by TOPICS code.

11.5 Divertor Radiation Feedback Control

S. Konoshima, N. Hosogane, S. Sakata, K. Akiba, H. Akasaka,
Y. Kawamata, Y. Neyatani, R. Yoshino, N. Saito and T. Kimura

A simple feedback control model, in which the divertor radiation power measured by bolometer is used as a control parameter with hydrogen gas puffing as an actuator, has been developed and tested in the JT-60U tokamak. Test results indicate that the total radiation power is able to maintain almost as pre-determined level, if required radiation is modest or less than one third to a half of the total heating power. Stable sustainment of a 6 MW divertor radiation, i.e., 40 % of 15 MW heating power, for about 3 seconds has been achieved successfully.

1. Set up

Six central channels of the top bolometer array covers almost the whole divertor zone from inside strike point to outside strike point of the separatrix field line including x-point. Raw signals of the bolometer are sent directly to the high speed digital computer(Real Time Processor) via isolation amplifiers. Time derivative of the bridge amplifier output voltage, V(t), which is proportional to the temperature rise of a bolometer with cooling time, Tc, gives incident radiation power as:

$$P = a\,(d\Delta V/dt + \Delta V/Tc) \text{ with } \Delta V = V(t) - V(0)$$

Summation of each detector power with a geometrical coefficient gives an approximate number of the total divertor radiation power. The results have been confirmed to agree within 20 percent with the one using whole bolometer array. R.T.P. calculate the radiation power with no time delay (less than 1 milisecond) and transfer the data to JT-60 plasma control computer, ZENKEI. Hydrogen gas throughput rate, Q_{com} is determined such that the measured radiation power, $P_{rad}(obs)$, is equal to that requested value, $P_{rad}(ref)$, in every 0.01 seconds with a following equation:

$$Q_{com} = Q_{pre} + G_1(P_{rad}(ref) - P_{rad}(obs)) + G_2 T_D (dP_{rad}(obs)/dt)$$

Where the coefficients G_1, G_2 and T_D represent proportional gain, differential gain and the response time, respectively.

Prior to the test, previous experiments have been revisited to find JT-60U radiative divertor characteristics. Heavy gas puffing of several tenth Pam^3/s during high power

heating increases divertor radiation linearly with time for about 1 second until abrupt jump happens. This nonlinear rise is often called MARFE onset, formation of large local radiating zone at some particular poloidal location such as x-point. Linear increase of the divertor radiation is plotted in Fig. 1 as a single function of gas puff rate for several discharges with 8 to 14 MW of neutral beam heating power. Normally the MARFE appears at around 50 % of the heating power. The figure suggests that the gain G_1 or equivalently a slope, $\sim\Delta Q/\Delta P$, would be in the range from 10 to 25 [$Pam^3/s/MW$]. Time delay of the radiation increase from a gas pulse, T_D, is typically 0.1 sec.

2. Test results and discussions

Experiment was performed during hydrogen discharge run period for 2 days in Sep. 1995. Operational conditions were as follows ; plasma current, 1.2 (1.8) MA, toroidal field, 2 (3.5) tesla, height of x-point from divertor tiles, 13-15 cm and 6 to 15 MW of 80 kV hydrogen beams for heating. A few sets of gain and the reference power have been tested.

One of the test results is shown in Fig. 2. Feedback control is enabled at 5.5 sec, 1 second after the neutral beam start. Top traces show how the actual radiation (Pr-controlled) followed the requested wave form (Pr-reference) aided with gas pulses. 'Pr-reference' is 6 MW, 40 % of the heating power with a flat top duration of 3 seconds. A large burst of gas pulse is injected so as to compensate the difference between the command in the beginning at around 6 seconds. Gas pulses become small and less frequent as the radiation grows as programmed. Some of the gas pulses appear to respond to noise since differential gain G_2 was slightly larger relative to G_1 in this case.Divertor heat load measured directly with infra-red camera indicated that 12 MW of heat load in the beginning went down to 6 MW as a result of increased divertor radiation. On the other hand, although the reason is yet to be specified, main plasma radiation is kept significantly small relative to the previous experiment referred in Fig.1 and less than 1 MW. In addition, energy confinement until about 6.3 sec observed to improve apparently associate with the reduction of main plasma radiation.

Even though the radiation power is maintained constant, there is slowly evolving profile rearrangement. Radiation near the inner strike point often increase more rapidly than other part and appears to saturate first at around 1.2 MW/m^2. At this time the enhanced radiation zone shift to the outer strike point and to the x-point and again saturate there at similar level with 0.8 to 1 MW/m^2. After the saturation, main plasma radiation starts to increase or the MARFE appears. The situation is shown in Fig. 3 as an another example. Divertor radiation is programmed as to increase slowly in step wise, beginning from 3 MW

at 5.5 sec, to 5 MW at 8 sec and to 7 MW at 9.5 sec for fixed NB heating power of 12 MW. Total power follows almost as programmed until 9 second while again main radiation is kept to be low, less than 0.5 MW. Divertor radiation start loosing control at around 9 sec in Fig.3 because of irrational logic. Regardless of the heating power decrease at this time, the computer keeps requesting additional gas to increase radiation. Gas puff leads to develop further large radiating mantle around the main plasma and plasma start shrinking until ended with thermal collapse at 9.5 sec.

Top three boxes show time evolution of the divertor radiation profiles. Local radiation power near the inside hit point starts to increase more and saturate at about 1 MW/m^2 and after the saturation of outer strike point at 8 sec a large radiation peak appears near the x-point. This change is usually referred to the movement of peak radiation zone moving from divertor plate to the x-point and the fromation of MARFE there. Line integrated power of 1 MW/m^2 could correspond to the local emissivity of MW/m^3 range. The saturation power may depend on the length of field line, since about 40 % higher saturation level has been observed under slightly different condition (Bt increased from 2 to 3.5 Tesla and Ip from 1.2 to 1.8 MA for the same heating power). In addition to the analysis of local power balance in cooperate with more detailed information such as neutral particle source including impurities, further sophistication of the control logic, involvement of heating power for example, would be important.

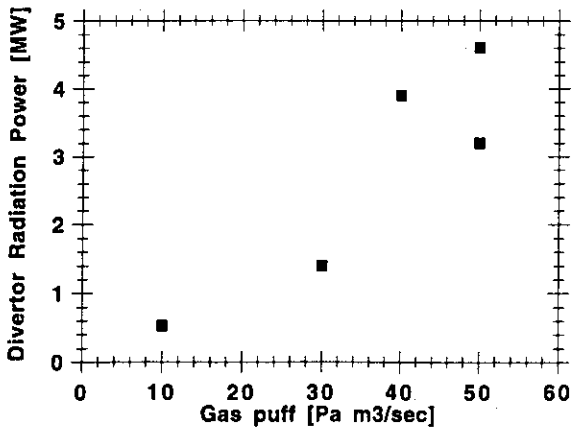

Fig. 1: Divertor radiation power vs. gas throughput rate. (Data taken from 1994 radiative divertor experiment.:#20029-20034. Pnb=8-14 MW, X point height=19-25 cm from divertor tile for upper two points and 9 cm for lower three data)

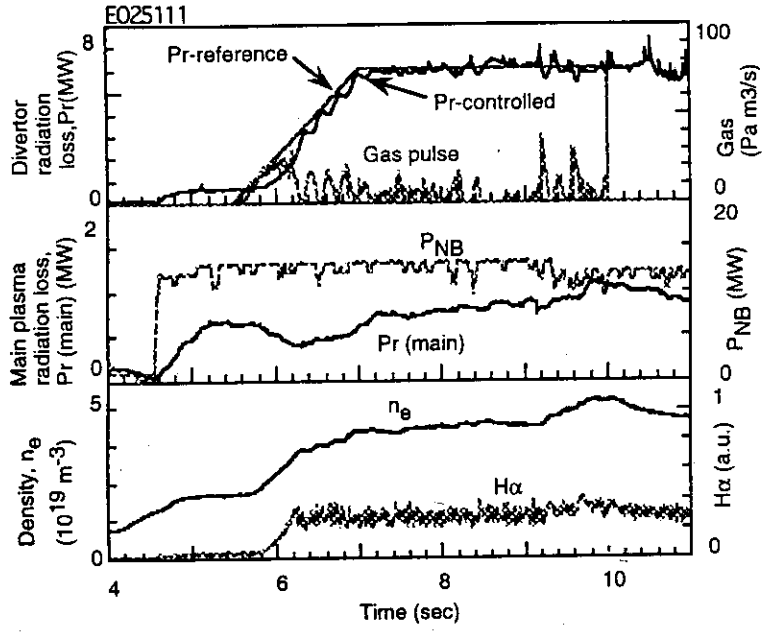

Fig. 2: Real time divertor radiation control with hydrrogen gas puffing. Feedback gains (G_1, G_2) and reference value are (20, 10) and 6 MW respectively. Ip = 1.2 MA, Bt = 2 T and15 MW of hydrogen beams are injected into hydrogen plasma. Transition to the MARFE occurs at 9.2 sec due to a slight beam power drop.

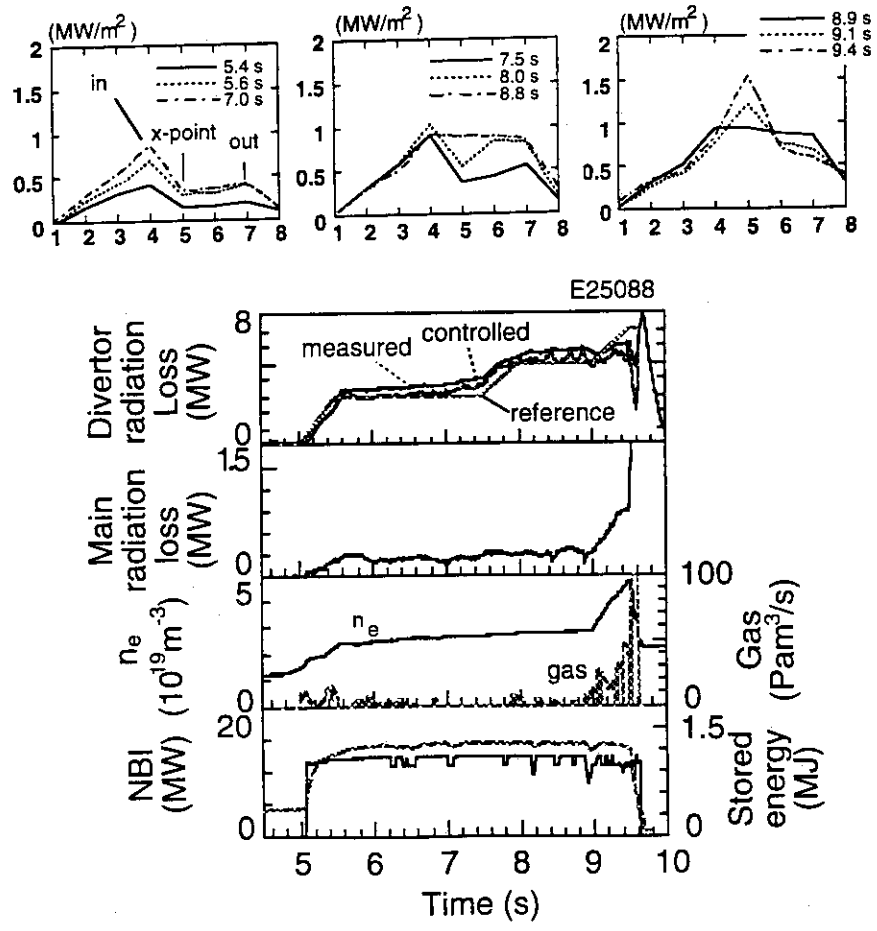

Fig. 3: Gain (G_1, G_2) = (20, 1) were tested for Ip = 1.2 MA, Bt = 3.5 T, hydrogen plasma. Top three boxes shows time evolution of the divertor radiation profiles.Channel 4,5 and 7 correspond to inside hit point, x-point and outside hit point, respectively.

11.6 0.1V/m Plasma Breakdown in JT-60U

R. Yoshino, M. Seki

1. Introduction

Power supply voltages of poloidal magnetic field coils are determined from requirements for plasma current generation (plasma breakdown), plasma equilibrium control, and abnormal events. At abnormal events of minor and major disruptions, the maximum available voltages of power supplies are normally applied to maintain the programmed plasma equilibrium. The control speed of each plasma equilibrium parameter (e.g. plasma current, plasma positions, elongation, triangularity, gaps between the outermost flux surface and the first wall) determines voltages of power supplies[1]. However, in the present tokamak machines and tokamak fusion reactors like ITER, the maximum voltages of power supplies is required during a discharge for realizing the plasma breakdown. Thus the reduction of breakdown loop voltage has a large impact to reduce a size of poloidal field coil power supply system.

The reduction of the breakdown voltage has been investigated in many machines. Electric field of 0.15 V/m obtained in DIII-D with ECH assistance is the lowest documented record[2]. Essential parameters of the breakdown are electric field at the plasma initiation position, pre-filling gas pressure, error or stray magnetic field. Here a stable buildup of plasma current must follow the plasma breakdown, where power balance must be maintained and the control of plasma current and positions should be established.

2. Plasma Breakdown Optimization

For a standard plasma discharge in JT-60U, one-turn voltage (V_L) of 20~30 V is applied from ohmic heating coil and vertical magnetic field coil power-supplies only for 100 ms at the plasma breakdown. Then low V_L of -2 ~ +2 V is applied in the following discharge to control the plasma current for 15 sec. The breakdown condition followed by stable plasma current buildup has been investigated from the start of JT-60U operation, and the loop voltage has been reduced step by step. In the recent experiment ~0.1 V/m has been recorded with a loop voltage of 1.8 V as shown in Fig.1. The electric field is calculated from loop voltage V_L divided by $2\pi R$ with R of 2.4 m. Position of R = 2.4 m is very closed to the inside first wall. Plasma equilibrium analyses using a fast boundary fitting code[3] and fast visible TV with time resolution of 1 ms show that a plasma grows from R ~ 2.4 m for high loop voltage breakdown. For low voltage breakdown a plasma seems to be generated from the central region of a vacuum vessel. Thus E_L of 0.1 V/m at R = 2.4 m can be reduced to E_L of 0.07 V/m at R = 3.3 m. This low voltage breakdown has been realized by the following optimizations.

1) Helium gas pre-filling

Hydrogenic gas is normally used as a pre-filling gas. However pre-filling with helium gas has been firstly achieved in this experiment series. A relation between the pre-filling gas pressure and the electric field (E_L) just before the breakdown is shown in Fig.2. Open points are the successful breakdown followed by stable plasma current ramp-up, and closed points are failed ones. A solid line in Fig.2 is the minimum electric field for the breakdown required for connection length (L) of 1000m as a reference, which is derived from Townsend avalanche theory.

Stable plasma breakdown at $E_L < 0.2$ V/m could not be achieved for deuterium gas, but was obtained for helium prefilling. The same experience was observed in JET[4]. Possible causes of this stabilization effect of helium prefilling gas are the following. 1) Wall absorption of helium gas is much smaller than that of hydrogenic gas. Thus the control of prefilling gas pressure is much easier for helium gas. 2) Re-capture of electron by helium ion is considered to be smaller than that by hydrogen. 3) Charge exchange loss of helium ion is lower than that of hydrogenic ion, which relax the power balance just after the plasma breakdown. Here the helium prefilling has little effect on the following plasma performance due to its small puffing of ~ 0.3Pam^3/s x 0.2 s.

2) LHRF heating to support the power balance

LHRF heating was performed using a launcer closer to the plasma initiation point. LHRF was injected 100 ms before the plasma breakdown as shown in Fig.1, but the breakdown condition was not relaxed. However RF coupling is largely improved at the plasma breakdown as shown in Fig.1, and LHRF of ~1 MW has a large effect to sustain a plasma just after the plasma breakdown. When a modulated LHRF power of ~50 Hz is injected, the plasma current is sustained around 100 kA and plasma horizontal position largely fluctuates with switching on and off of LHRF power.

3) Reduction of stray and error fields

Toroidal eddy current in the vacuum vessel, which is generated by applied loop voltage, produces error fields. Investigation of the breakdown with loop voltage of ~30 V shows that a null point exists close to the inside first wall, which is supported by the equilibrium fitting of a plasma configuration from magnetic probe signals[3]. However for the plasma breakdown with ~0.1 V/m, the same equilibrium fitting analyses suggest that a plasma initiates from the central region of a vacuum vessel.

4) Optimization of the position control after the breakdown

Figure 1 shows that LHRF coupling is improved with the plasma breakdown (see t = 0.35 sec in Fig.1). During low plasma current, plasma position is controlled to keep good coupling with LHRF.

References

[1] R. Yoshino, Fusion Engineering and Design **24** (1994) 375.

[2] B. Lloyd, et al., Nucl. Fusion **31** (1991) 2031.

[3] M. Matsukawa, et al., Fusion Engineering and Design 23 (1993) 341.
[4] P.J. Lomas, et al., ITER Technical Meeting, Naka, April 26-29 (1993).

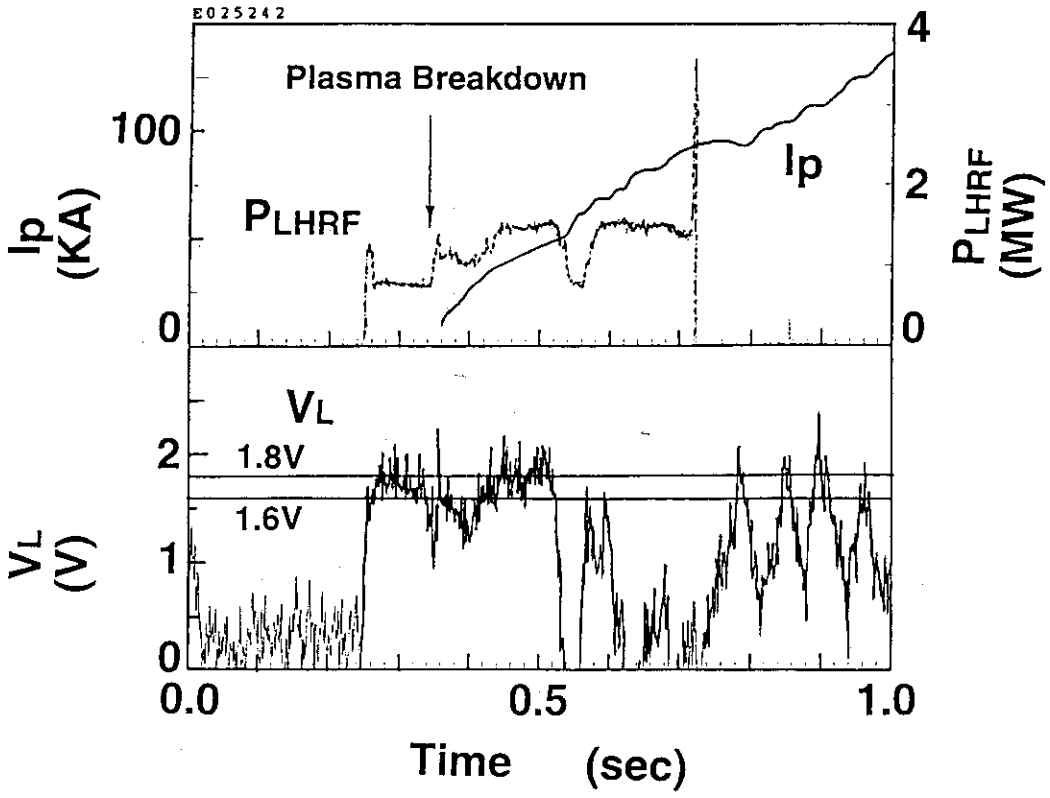

Fig.1 *Time evolution of plasma current (I_p), injected LHRF power into a vacuum vessel (P_{LHRF}), and loop voltage (V_L).*

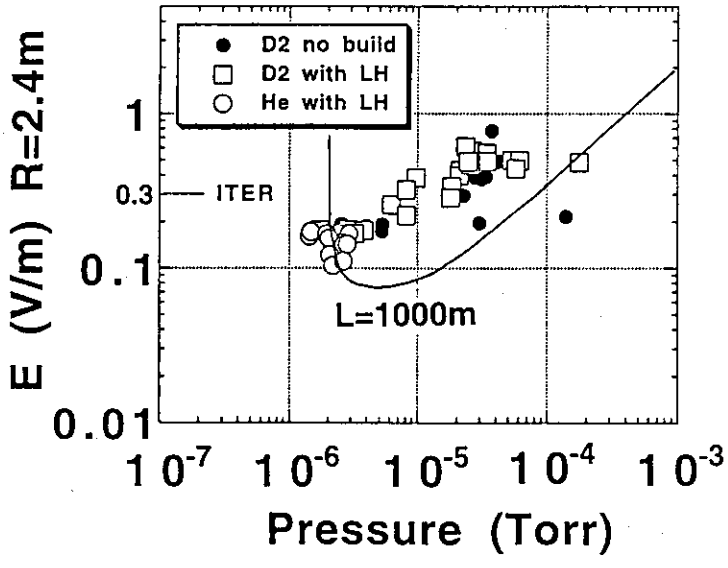

Fig.2 *Electric field and pressure at the plasma breakdown.*
Solid line is the minimum electric field required for the breakdown for connection length (L) of 1000m.

12. Diagnostics
12.1 Removal of CXRS Optic for Background Spectrum

Y. Koide

1. Introduction

One of the optics of charge exchange recombination spectroscopy (CXRS), which was for background spectrum, was removed from P3 section to P14 section in Dec. 1995 due to the installation of N-NBI in P3 section (Fig. 1). In this paper, some restrictions due to this removal are presented.

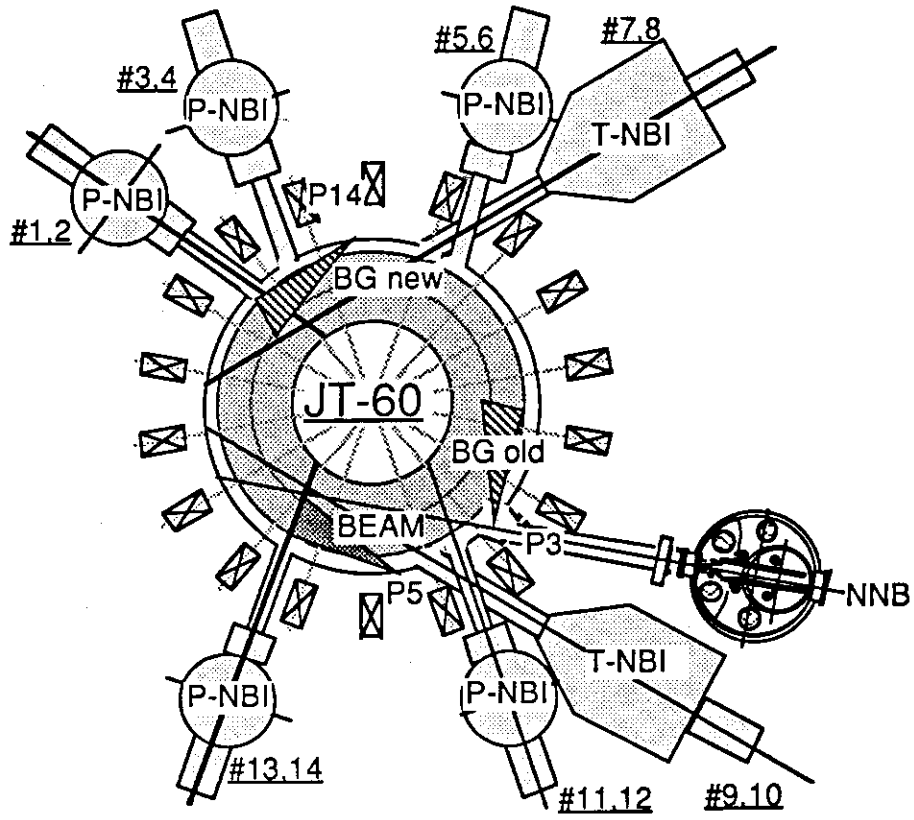

FIG. 1. Top view of JT-60U with the field of view of CXRS and beam lines.

CXRS diagnostic in JT-60U is usually based on the next reaction between neutral beam for heating and carbon impurity,

$$D^0(NB) + C^{6+} \rightarrow D^+ + C^{5+}(n=8)^*$$

$$\rightarrow D^+ + C^{5+}(n=7) + h\nu.$$

Profiles of ion temperature and rotation velocity are deduced from the Doppler broadening and shift of the emitted spectrum, respectively. The measurement is restricted within the intersection region of the neutral beam and the line of sight. A spectral line with the same transition, however, is also produced by electron excitation in relatively peripheral region.

This background spectrum is not negligible compared with that by the above charge-exchange reaction and is not spatially uniform. Therefore it must be evaluated in order to estimate the charge-exchange spectrum.

2. Problems and countermeasure

It is required that background optic doesn't look at any beams. P3 section was the best position from this viewpoint because the region of P3→ 2→ 1→ 18→ 17 is free from beams (Fig. 1). On the contrary, P14 section, i.e. new address, is not adequate basically for the background measurement because many beams are passing through the region. At a glance, #2 and #4 beams (upper perpendicular beams) are visible from the background optic in P14 section. Beams of #1, 3, 7 and 8 might contaminate background spectrum and their effects must be checked in the experiments.

There may be some countermeasures for this problem: 1) no injection of #2 and #4 beams when CXRS measurement is necessary (Fig. 2), 2) modulation of diagnostic beam (#14) (Fig. 3), 3) multi-Gaussian fitting of the detected spectrum, 4) switch over of diagnostic beam from #14 to #2 or #4.

The second idea is not recommended because the effective time resolution will be deteriorated down to ≥0.4 s (each pulse width of ≥ 0.2 s is required) and discussions of physics involved will be limited; it is not guaranteed that the background spectrum at different time is valid. The third one is not recommended because the separation of CX-spectrum and background-spectrum is not always reliable. The fourth one is not acceptable because poloidal array and optic for He transport study look at #14 beam. I would think, after all, that the first one is the easiest and the most reliable way to cope with this problem although it will lead to the reduction of total injection power; calculation of ion temperature, plasma rotation and carbon density will be skipped during the injection period of #2 and #4 beams (Fig. 2).

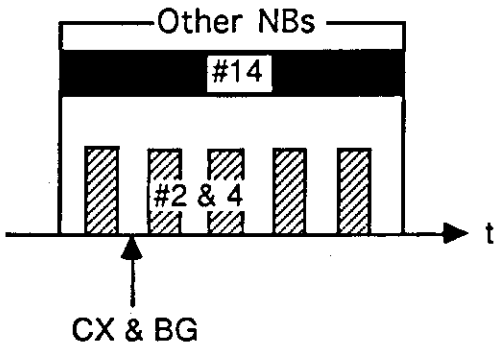

FIG. 2. Beam injection scenario with modulation of #2 and 4.

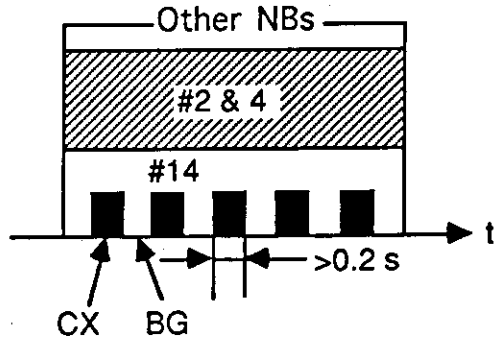

FIG. 3 Beam injection scenario with modulation of #14.

12.2 Recent Activities of Multi-ruby-laser and High-spatially-resolved Multipoint Thomson Scattering System

H. Yoshida and O. Naito

1. System layout

The system layout for the present ruby Thomson as of 1995 is shown in Fig. 1, which is characterized by the high-spatially-resolved multipoint measurement of 60 channels with the flexibility for multi-ruby-laser operation. Using a beam combiner composed of a polarizer plate and a Faraday rotator, two ruby lasers with 10 J, 30 ns of pulse width and a single beam path line have provided either of the transient phenomena measurement such as L/H transition and pellet injection with the minimum time difference of 2ms in the burst mode operation, and of the multi-time-slice measurement with the repetition rate of ~0.5 Hz in the normal mode operation.[1] For the reliable electron density measurement with the multilaser Thomson scattering, the relative beam energy of the two ruby lasers is stably and precisely monitored by a PIN diode in the laser room through a communication optical fiber ~300 m long which guides the laser light uniformly averaged by an integrating sphere located at the beam dump.

Two kinds of collection optics have been working: Cassegrain type mirrors viewing the core plasma with the spatial resolution of 22 mm and double Gaussian lens seeing the edge plasma with 8 mm and 16 mm resolutions. The collected lights are led into three sets of Littrow type grating spectrometer by quartz fiber bundles ~100 m long with about 50% transmission at 632.8 nm. The spectral range of Littrow type grating spectrometer is about 400 nm to 700 nm for the high T_e core plasma measurement, and 550 nm to 700 nm for the edge plasma measurement. The spatially and spectrally resolved output images of the three spectrometers are severally converted to electrical signals by a newly developed high repetition (1 ms) photodiode array (PDA) with spatial and spectral division of 20x12 pixels and also 10x6 PMTs for the core plasma measurement (core PMT), and 30x(4~5) PMTs for the edge plasma measurement (edge PMT). The spectral division of PDA was designed to show a full performance in higher electron temperature regime of T_e ~10 keV with 12 spectral pixels for each spatial point, and that of the core PMT to ensure T_e measurement with good precision even in lower electron density regime of less than 1×10^{19} m^{-3}. The spectral division of the edge PMTs can give a good estimation for the extremely low n_e (~1×10^{18} m^{-3}) and low T_e (~10 eV) condition. Since 1991 the edge PMT has been operational, PDA since 1992 and the core PMT since 1993. Especially for the edge PMT signal flow in the subtraction procedure of the edge plasma background (BG) light from Thomson scattering signal (SG), two corresponding groups of ADC and memory are independently used for the purpose of suppressing the difference in the ELM activity level at SG timing and BG timing. The precise edge plasma profiles can be measured even with giant ELM activity, when the time delay of both the timings is shortened to less than 200 ns.

Each Thomson scattering spectrum is reconstructed with the acquired data from the corresponding CAMAC memories and also with the corresponding calibration data of relative sensitivity of spectral channels, spectral slit functions, relative detector and/or amplifier gains, Rayleigh scattered light intensities, laser energy and so on. The estimation of T_e and n_e together with their error bars is made through a non-linear least squares fit of fully relativistic Thomson scattering spectrum to measured one. In this procedure a detector shot noise, a plasma background light level and a circuit noise are taken into consideration. As the fully relativistic Thomson scattering spectrum, an analytic formula is used which is applicable to a wide range of plasmas with extremely high accuracy of less than 0.1% at 100 keV.[2]

2. Remote adjusting and monitoring of fiber optic field position to beam width

In order to measure n_e profile precisely, a holder stage of fiber bundles is designed to

move slightly in the parallel and rotational direction of the single beam line in each collection optic. The necessity comes from possession of multi-collection-optic itself and also a lack of sufficient allowance of fiber bundle width against beam diameter.

Main components of this remote alignment system for fiber optic field are two special fiber plugs composed of a pair of horizontally separated fiber bundles with the same dimension, four PMTs with a band-pass interference filter for the respective bundles, and two adjustment stages for parallel and rotational directions with precise driving mechanics and electronics for each collection optic. The above two fiber plugs for alignment are mounted at *upper* and *lower* positions against the optical axis of each collection optic. Using the calibrated ratio of scattering signals through a pair of fiber bundles horizontally divided into two in one alignment plug, the relative location of the beam width on the horizontal fiber optic field in the vacuum vessel is easily calculated. Moreover the parallel and rotational quantities of the respective two stages, which are necessary to align the two fiber optic fields with the single beam path line at once, can be estimated by using the two ratios obtained separately through the upper and lower positioned plugs.

This alignment procedure is operational with using not only Rayleigh scattering light but also Thomson scattering light. Namely during plasma discharges it can be monitored what location each fiber optic field is positioned against the whole width of each beam pulse in the vacuum vessel. So even though drifts of the beam line and also displacements of the collection optic box occurs, which are mainly caused by laser troubles and/or repairs and high speed disruptions, respectively, the fiber optic fields can be remotely and immediately just aligned to the single beam line at least in the next plasma discharge. As another basic use of this remote adjustment system, the local beam diameter can be estimated through the intensity variation of strong and monochromatic Rayleigh scattering light with parallel scanning of all the measurement fiber bundles in one holder stage. Figure 2 shows the scanned result for the two lasers at the upper spatial point viewed by the Cassegrain type mirrors, indicating that both the beam diameters are about 5.5 mm which is within the fiber optic field width (~8 mm) of the corresponding bundle. It is also found that the collection optic with the aligned stage position views the whole of the beam width properly. At the center of flat top in Fig. 2 the ratio of the scattering signals through a pair of fiber bundles is unity in both the upper and lower alignment plugs. The most benefit of introducing the remote alignment system of fiber optic field is a major reduction of the quartz fiber cost with keeping the reliable n_e profile measurement.

3. Solutions to coating problem of viewing window

The degradation of a viewing window transmission is still one of practical problems to be solved on visible plasma diagnostics. Through many plasma discharges a dark-brown-colored thin films are gradually coated on the inner surface of the viewing window, which attenuates the light from plasmas to be measured and also gives rise to the spectrum distortion due to the chromatic dependence of its transmission property. Especially in Thomson scattering system, therefore, the coated window may cause a systematic error of an underestimation both for electron density n_e and for electron temperature T_e. This problem is enhanced more severely in higher T_e measurement with wider spectral range. Considering these backgrounds, recently we have developed two approaches to solve this problem. One is a method by which wavelength-dependent transmission of Thomson viewing window can be predicted using a known attenuation of coated film and also a Rayleigh scattering data The other is a laser-blow-off based *in situ* cleaning method. The former is applicable to a window which suffer a slight coating through normal plasma discharges, the latter a more severe one with

almost complete recovery of window transmission.

Generally a transmission of a coated window varies chromatically as

$$T(\lambda) = T_0 \exp[\,-\alpha(\lambda)t\,], \quad (1)$$

where T_0 is the original window transmission of quartz glass (~0.94), $\alpha(\lambda)$ the wavelength-dependent attenuation of the coated film, and t the film thickness considered to be independent of wavelength. $T(\lambda)$ is measured by a spectrophotometer, and t by an ellipsometer. $\alpha(\lambda)$ can be obtained through a polynomial regression for the JT-60U coated window database on film thickness and transmission with an accuracy of less than 7% and an applicable wavelength range of 300 nm to 800 nm. The wide applicability of the obtained expression for the film attenuation to slightly coated windows would be based on the unchagebleness of the film composition. The film composition itself seems to depend on the first wall materials and be irrelevant to the window location on the vacuum vessel. So the chromatic window transmission can be predicted with the window mounted to the vessel, if only the film thickness is found out. The following way is one of possible methods to know it, and can be easily applicable to all the Thomson scattering diagnostics. A Rayleigh scattering light intensity N_0 is obtained through the uncoated window at the first stage just after the window replacement, while N_R through the coated one. If all components of the system are kept in the same condition as at the first stage, the ratio N_0/N_R gives the information on the coated film thickness t_R as follows:

$$t_R = (1/\alpha_R)\, ln(T_0/T_R) = (1/\alpha_R)\, ln(N_0/N_R), \quad (2)$$

where $T_R=T(\lambda_R)$, $\alpha_R=\alpha(\lambda_R)$ and λ_R=694.3 nm for a ruby laser. Inserting t_R in Eq. (1), we can obtain the expression for the chromatic window transmission with practical precision.

The second method is a more direct way of cleaning the coated window. By the blow-off method using a Nd:YAG laser, the deteriorated transmission is regained with a transmission recovery rate of 98~100% at wavelength of over 700 nm and of 92~94% at 400 nm This regained transmission would give systematic errors only of less than 3.0% and 2.5% to the estimation for electron density and electron temperatures of less than and 10 keV, respectively. Up to now the effective blow-off of the coated film is achieved in the beam-hit area of less than about 30 mm diameter (~0.3 J/cm^2), depending on the number of laser pulses and the energy profile of the beam.

4. Recent measurements

The edge PMT system has provided the precise data especially for researching the local transport of the edge region in H-mode plasmas. The profile data from the core PMT system together with the edge PMT one has been of use to investigating the global confinement of OH, NB heating and NBCD experiments and also the heating and current driving characteristics of ICRF and LHRF experiments. In the negative shear experiments, started from 1995, PDA system has shown a good performance for high T_e plasmas. Figure 3 is a typical profile shape of T_e and n_e in NB and ICRF heated negative shear plasma, indicating that the formation of an internal transport barrier for electrons is recognized from the existence of a steep gradient in both T_e and n_e measurement. The curve of T_e in Fig. 3 is drawn on the basis of PDA data. The clear and steep gradient in both T_e and n_e profiles is a distinctive feature of the JT-60U negative shear experiment.

References

[1] H. Yoshida, O. Naito, O. Yamashita, S. Kitamura, A. Nagashima and T. Matoba, Rev. Sci. Instru. **66** (1995) 143.

[2] O. Naito, H. Yoshida and T. Matoba, Phys. Fluids B **5** (1993) 4256.

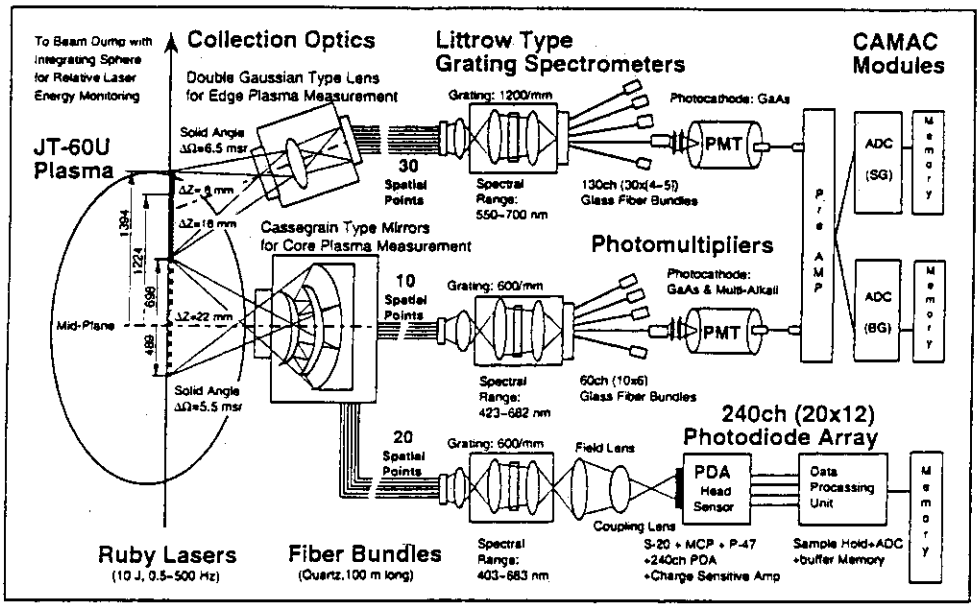

Fig. 1 Primary system layout of collection optics, fiber optics, spectrometers and detectors

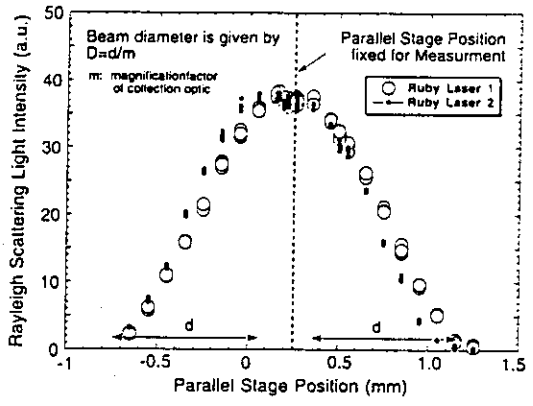

Fig. 2 Variation of Rayleigh scattering light intensity with the parallel scanning of bundle holder stage in Cassegrain type mirrors

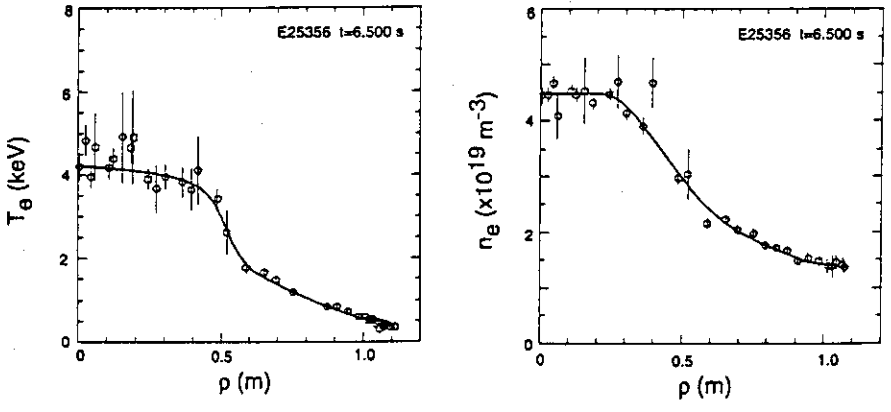

Fig. 3 Profile shape of T_e and n_e in NB and ICRF heated negative shear plasma

12.3 Contribution of Toki Conference

A. Sakasai

Eight papers presented from JT-60U diagnostics group at the 7th International Toki Conference on Plasma Physics and Controlled Nuclear Fusion, "Fusion Plasma Diagnostics" in Japan during the week of 28 November - 1 December in 1995.

The paper "**Divertor Diagnostics and Physics in JT-60U**" is a invited talk presented by A. Sakasai. The following is abstract of the paper.

Three bolometer arrays, IRTV, photodiode array, spectrometers, Langmuir probe array, Penning gauges and quadrupole mass analyzers were installed for divertor diagnostics to study the divertor physics in JT-60U. Radiative cooling divertor is investigated to reduce the heat load on the divertor plates using these diagnostics. The mechanism of radiation losses is spectroscopically studied with visible spectroscopy. The peak heat flux density reaches 300-400 MW/m^2 most of the power is deposited within a few milliseconds due to ELMs. Carbon generation can be modelled very well by physical sputtering from D^+ and Oxygen impurities plus C self sputtering and chemical sputtering from Oxygen in low density discharges or L-mode discharge with high power NB (25 MW) heating. In high density plasmas, the physically sputtered impurities from target plates are reduced, chemical sputtering by neutral particles which strike the divertor plates in the private region becomes dominant in high density plasmas. Helium exhaust from the core plasma is observed due to wall pumping caused by Solid Target Boronization. The He neutral pressure in the divertor and He content in the main plasma were reduced by the He exhaust to 1/3 of those without STB.

12.3 (1) Improvement of dual CO_2 laser interferometer

Yasunori Kawano, Akira Nagashima,
Katsuhiko Tsuchiya, Takaki Hatae and Soichi Gunji

A new phase comparator named VRPC (Very high Resolution Phase Comparator) has been developed to improve phase and density resolutions of a dual CO_2 laser interferometer in JT-60U tokamak. Time discrimination of 39.0625 ps of the VRPC can provide a phase resolution of 1/12800 of a fringe for a 2 MHz interference beat signal, which corresponds to an expected effective density resolution of 1.32×10^{17} m^{-2}. The first operation of the VRPC for actual plasma discharges has been executed. A phase resolution is improved significantly in comparison with that of a previous comparator which has a resolution of 1/100 of a fringe. A density resolution is also well improved to extract noise components which were comparable to a bit noise of the previous comparator. The VRPC has a capability to enable the dual CO_2 interferometer to measure precise and fast density changes in tokamak fusion plasmas.

A comparison of phase resolutions between the VRPC and the previous comparator is shown in Fig. 1. It is noted that very small changes of the phase signal are well detected in the case of the VRPC (Fig. 1(a)) compared with the case of the previous comparator (Fig. 1 (b)). Thus, it is concluded that the phase resolution of the interferometer is significantly improved by the VRPC.

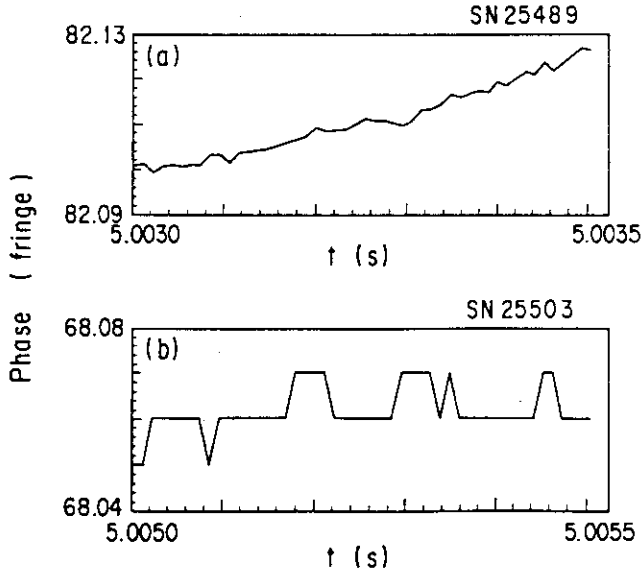

Fig. 1 Phase resolutions measured by (a) VRPC and (b) previous comparator, respectively. Both sampling rates are 10 μs.

12.3 (2) Triton Burnup Measurements using Scintillating Fiber Detector on JT-60U

T. Nishitani, M. Isobe, G.A. Wurden, R.E. Chrien, K. Tobita and Y. Kusama

The new type type directional detector of 14 MeV neutron was developed[1] based on scintillating fibers for the triton burnup measurement in JT-60U deuterium discharges, as part of a US-Japan fusion collaboration. The detector consists of an array of scintillation fibers embedded in an aluminum matrix coupled to a magnetic resistant photo tube with a high current-capable base. Because the maximum recoil-proton range for a 14 MeV neutron is 2.2 mm in plastic scintillator, we chose to use either 1 mm or 0.5 mm diameter scintillation fiber optics. Only the neutron coming on the axis of the fiber gives the highest energy deposition in the fiber, so that this detector has an intrinsic directionality, which was evaluated to be ±30° using the DT neutron generator FNS. The detector is mounted in a small collimator box, 40 cm × 61 cm × 61 cm of borated polyethylene, in order to improve the directionality. Two sets of detectors have been installed near the midplane of the vessel, just outside the toroidal field coil position on JT-60U. Other two sets of detectors are under installing, which will allow us to measure the 2.5 and 14 MeV neutron emission profiles simultaneously. The scintillating fiber detectors have been calibrated by the shot-integrated 14 MeV neutron yield measured with the neutron activation technique using a pneumatic foil transfer system.

The time resolved measurements of 14 MeV neutron emission from the triton burnup have been performed using scintillating fiber detectors with a temporal resolution of 10 ms. The scintillating fiber detector system operates in a background of 2.5 MeV neutrons which are ~100 times brighter than the 14 MeV neutron signal, at the counting rate up to 100 MHz. The peak 14 MeV neutron rate at the time of neutral beam(NB) turn-off is as high as 2% of the total neutron rate. Time histories of 14 MeV emission after NB turn-off have been analyzed based on the classical slowing down theory. Assuming the loss of fast tritons can be represented as a diffusivity, then values increasing with increasing toroidal ripple were determined between 0.05-0.15 m^2/s, from the modeling of the time histories of the 14 MeV emission after the NB turn-off (see Section 10.3). Also MHD effects on the triton burnup have been investigated. The sawtooth effect is not clear in both 2.5 MeV and 14 MeV neutron emissions on high power neutral beam injections. In the quasi-stationary-mode (QSM), both the DD and DT neutron rate decrease drastically. The effects of the TAE modes is discussed in Section 9.3.

References

[1] G.A. Wurden, et al., Rev. Sci. Instrum. **66** (1995) 901.

12.3 (3) High-resolution visible spectrometer for divertor study in JT-60U

H. Kubo, T. Sugie, H. Takenaga, S. Higashijima, and A. Sakasai

Knowledge of the velocity distributions of neutral deuterium and impurity and ion temperature is important for study of deuterium recycling, impurity behavior and plasma transport in divertor plasmas. The velocity distributions and the ion temperature can be estimated from Doppler-broadening of spectral lines from neutral deuterium atoms and impurity ions. In JT-60U, a visible spectroscopic system with high wavelength resolution has been developed to observe the Doppler broadening of the spectral lines emitted from the divertor plasma.

Figure 1 shows a schematic drawing of the cross section of JT-60U and the spectroscopic system. An object optics with a 60-ch optical fiber array observes the divertor region with a spatial resolution of about 1.2 cm. The optical fibers transmit the light from the torus hall to a diagnostics room. At a terminal box 10 fibers are chosen from the 60 fibers, and in a preoptics they are vertically placed in linear configuration along the entrance slit of the spectrometer. An interference filter is used to remove the overlapping orders. The spectrometer is built in the Littrow mounting, because the image should be little astigmatic to obtain the spatially resolved signal with an CCD camera. The focal length of the Littrow lens is 1.2 m and the diameter is 100 mm. The high resolution is obtained by using an echelle-grating (79 grooves / mm) in high spectral order (35 - 61 for the wavelength range of 400 - 700 nm) and the nominal wavelength resolution is 5.3 pm. The image-intensified CCD camera covers a wavelength band of around 1.1 nm.

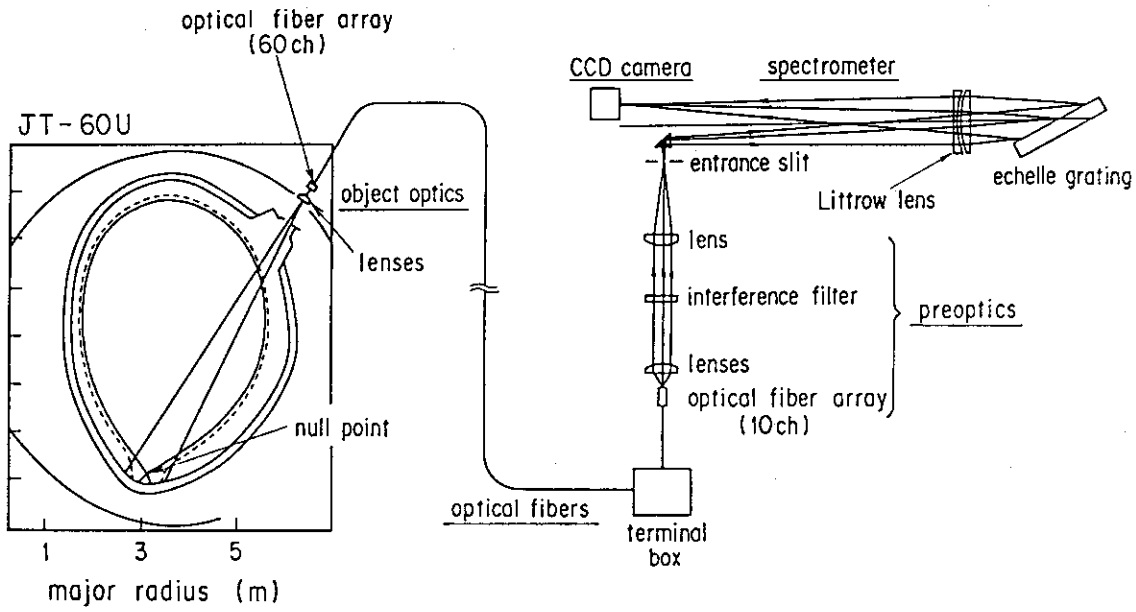

Fig.1 Schematic drawing of the cross section of JT-60U and the spectroscopic system.

12.3 (4) Current Profile Measurement with MSE Polarimeter in JT-60U

T. Fujita, H. Kubo, T. Sugie, N. Isei and K. Ushigusa

A motional Stark effect (MSE) polarimeter has been installed to obtain the current profiles in JT-60U. The collection optics and the polarimeter observe the Dα line from a counter-tangential heating neutral beam (#7) through fused-silica windows via front surfaces of reflecting aluminum mirrors. The polarimeter has 5 viewing points which cover R=3.04-3.42m. The polarization angle of the σ component of the Dα line is measured using a combination of two photoelastic modulators and a linear polarizer.

The change of polarization angle with the reflection at the aluminum-coating mirrors, which was induced by the difference of reflectivity for s and p polarizations and the difference of phase for s and p, was corrected using the results of the calibration with a light source and a linear polarizer before the installation of the polarimeter. The calibration of offset angles, which was induced by the Faraday rotation in the windows in the strong magentic field, was done by flux-conserving rapid motion of plasma during the neutral beam injection. The error in obtained offset angles is estimated to be about 0.2 degrees.As the scope of MSE is small compared to the plasma minor radius (0.7-1.0m), the value of internal inductance measured by magnetics was utilized to obtain the q-profiles in addition to the MSE data. Polarized background light was oberved with intense (typically >15MW) neutral beam heating. The time evolution of this light differs from that of bremsstrahlung. The origin of this polarization is not known. To correct the change of polarization angle by this polarized background light, the polarization of background light was monitored by observing light near the beam emission of one of the 5 channels (CH3). In Fig. 1, polarized components of background light, raw signal and corrected signal are shown. We find the corrected signal almost vanishes without #7 injection, which means that the correction works very well. By this technique, we have become able to obtain q profiles even with high power beam heating.

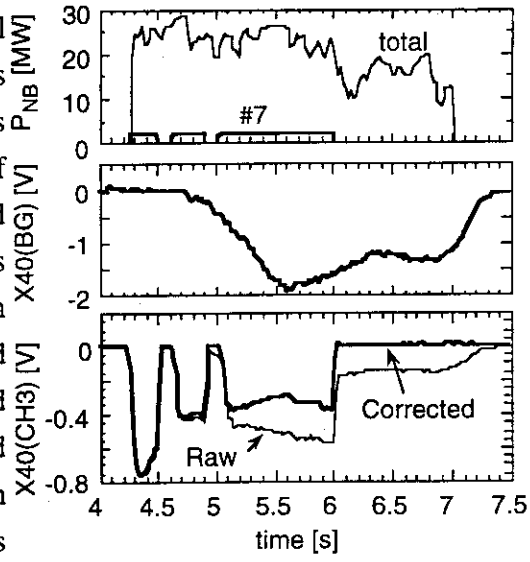

Fig. 1

The change of current profile was studied on the I_p rampdown/rampup, LHCD and so on. In the reverse shear experiments where neutral beams were injected during the initial current ramp, q-profiles with negative shear were observed.

12.3 (5) Measurements and Analysis of ECE in JT-60U

M. Sato, S. Ishida, N. Isei, A. Isayama, H. Shirai, T. Oyevaar, M. Teranishi[1], N. Iwama[1] and K. Uchino[2]

1)Toyama Prefectual University, 2)Kyushu University

1. ECE measurements

In order to obtain the time evolution of the electron temperature in JT-60U plasmas, an ECE measurement system with fast time and high spatial resolutions has been developed. The system in JT-60U device consists of three different instruments: a Fourier transform spectrometer system (FTS) [1], a 20-channel grating polychromator system (GPS) [2], and a 12-channel heterodyne radiometer system (HRS) [3]. The frequency of measured second harmonic ECE is from 100 GHz to 300 GHz. It is main purpose for FTS to determine whether ECE is emitted from the thermal electrons and to obtain absolutely calibrated electron temperature profiles. The GPS and HRS are relatively calibrated to measure electron temperature profiles with fast time (~ 2 μs) and high spatial (~ 1 cm) resolution. The HRS has a better SN ratio than the GPS for an electron temperature below 1 keV and *vice versa*.

2. ECE Analysis

The importance of relativistic down-shift frequency effect on the determination of the electron temperature profile in a reactor-grade tokamak has been recognized. [4] Recently it was pointed out that the radial shift of the electron temperature profile obtained using the radial dependence of the non-relativistic electron cyclotron frequency due to the relativistic effect is not negligible in a medium temperature plasma. [5] When the toroidal magnetic field is higher, electron density is lower for a fixed electron temperature, the shift is bigger. When the electron temperature is higher for a fixed optical depth, the shift is bigger. For precise measurement of the electron temperature profile it is important to correct the shift due to relativistic down-shift frequency.

3. Summary

An ECE measurement system with fast time (~ μs) and high spatial (~ cm) resolution has been developed in order to obtain the time evolution of the electron temperature in JT-60U plasmas. The ECE system consists of three different instruments: A FTS, a 20-channel GPS, and a 12-channel HRS. For precise measurement of the electron temperature profile it is important to correct the shift due to relativistic down-shift frequency in present day tokamak.

Reference

[1] M.Sato, H. Yokomizo *et al.*, Kakuyugo Kenkyu Supplement **59** (1988) 47

[2] S. Ishida, A. Nagashima, M. Sato, N. Isei *et al.*, Rev. Sci. Instrum. **61** (1990) 2834.

[3] N. Isei, M. Sato, S. Ishida, K. Uchino *et al.*, Rev. Sci. Instrum. **66** (1995) 413.

[4] M.Sato, S.Ishida and N.Isei, J. Phys. Soc Jpn. **62** (1993) 3106.

[5] M.Sato, N.Isei and S.Ishida, Jpn. J. Appl. Phys. **34** (1995) L708.

12.3 (6) Neutral Particle Analyzer with Energy Range up to 4 MeV for both Alpha Particle and Protons

Y. Kusama, M. Nemoto, V.I. Afanassiev*, S.S. Kozlovskij**, S.Ya. Petrov*,
M. Satoh, A. Morioka, Y. Tsukahara, A.I. Kislyakov*, M.P. Petrov*, H. Takeuchi

Neutral particle analyzer with an energy range up to 4 MeV for both protons and alpha particles was developed under the collaboration between the JAERI and the Ioffe Institute. A second detector array was installed on the opposite side of the middle plane of analyzer. Electric field in the electrostatic deflector is directed oppositely to the magnetic field when we measure protons over ~2 MeV using the detector array. With these improvements, the maximum energy for protons was increased twice in comparison with a previous analyzer [1, 2]. Use of the thinnest possible scintillator produced a remarkable decrease in neutron and g-ray sensitivity for the measurement of 0.1-0.5 MeV beam ions. The energy spectrum of atomic hydrogen fluxes was successfully measured with this analyzer in ICRF-heated plasmas as shown in Fig. 1.

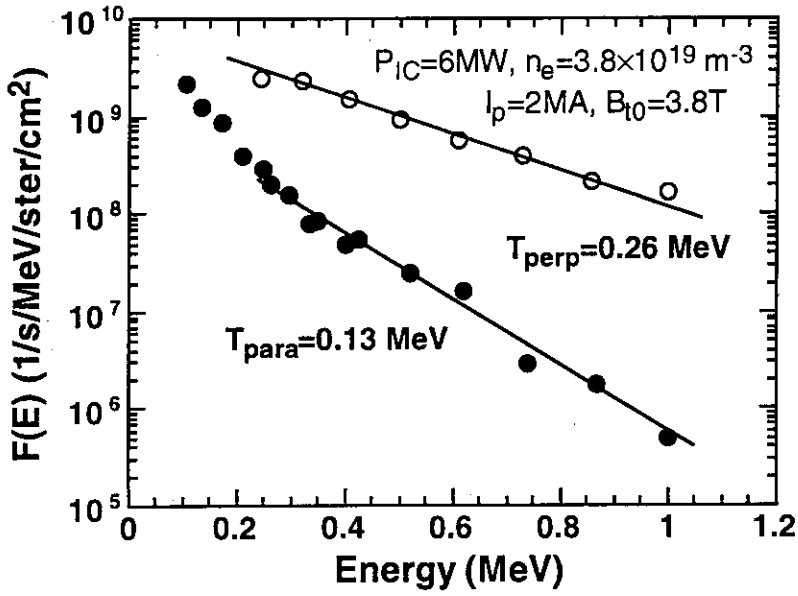

Fig. 1: Energy spectra of atomic hydrogen fluxes measured with this analyzer (full circles) and with the previous one (open circles) in a ICRF-heated plasma.

References

[1] Y. Kusama et al., Rev. Sci. Instrum. 66(1) (1995) 339-341.
[2] V.I. Afanassiev et. al., 22nd EPS Conference, Bournemouth, UK, 1995.

---

*A. F. Ioffe Physical-Technical Institute, St. Petersburg 194021, Russia
**State Technical University, St. Petersburg 195251, Russia

12.3 (7) YAG Laser Thomson Scattering System

Takaki HATAE, Akira NAGASHIMA, Hidetoshi YOSHIDA, Osamu NAITO, Osamu YAMASHITA, Sigeru KITAMURA, Daisuke KAZAMA, Yoshiaki ONOSE and Tohru MATOBA

12.3.7.1 Introduction

The YAG laser Thomson scattering system is being developed for the purpose of measuring the time evolution of electron temperature (T_e) and density (n_e) profiles with pseudo-continuity of time in addition to Ruby Thomson system in JT-60U. The polychromator and avalanche photodiode (APD) detector are newly developed to cover the various plasma operations in JT-60U, and are able to measure the range of $20eV \leq T_e \leq 20keV$ and $5\times10^{18}m^{-3} \leq n_e \leq 2\times10^{20}m^{-3}$. Presently this system provides T_e and n_e periodically every 100ms at five spatial points.

12.3.7.2 Apparatus

The 10Hz multipulse Nd-YAG laser (wavelength 1064nm) produce a Gaussian like beam of 2J. The polychromator is a successive interference filter type, which comprises six wavelength channels, suitably designed for the wide temperature range. The scattered spectrum is measured by Si-APD detectors, of which the sensitivities are more than 20A/W at 1064nm and internal gains are 100. In order to prevent the temperature effect on gain change of APD, each APD element is mounted on Peltier thermo-stabilizing element, the temperature is stabilized to 25±0.1°C.

12.3.7.3 First operation results and Future plan

This system was examined to be able to measure the time evolutions of T_e and n_e profile for NBI heating plasma, as shown in Fig.1. Obtained data were comparable to the ECE diagnostic and Ruby Thomson scattering.

Additional four spatial channels will be installed for the central measurement. A new collection optics is under construction in order to measure the peripheral plasma, and will have three spatial channels initially. To obtain higher time resolution, the YAG laser repetition rate will be increased from 10Hz to 50Hz. These installation will be carried out in 1996.

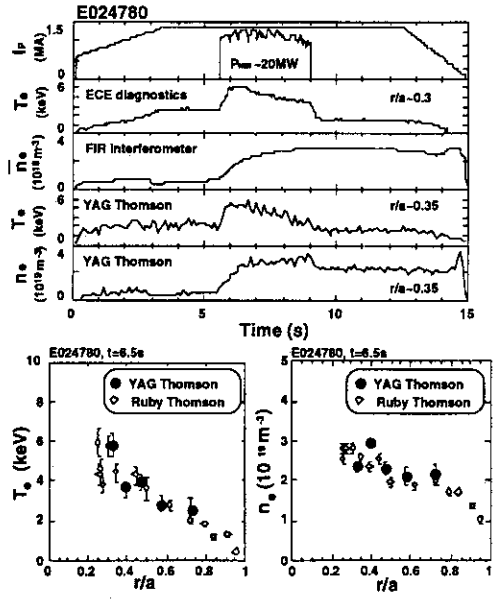

Fig.1 First operation results of YAG laser Thomson scattering system
Upper:Time evolution of Te and ne
Lower:Spatial profile of Te and ne

12.4 Estimate of Local Turbulence Diffusivity via Correlation Reflectometry

T. Fukuda, M. Mori, K. Nagashima, H. Shirai and K. Mima*

1. Introduction

Recent transport analysis shows that the ion diffusivity χ_i either in high β_p or Hot-ion H-mode is close to the values of neoclassical estimate, while electron transport is still in the anomalous regime [1]. Bearing in mind that the alpha heating power is dominantly transferred to electrons in a fusion reactor, detailed investigation of electron transport has been highlighted in the recent tokamak confinement research. In order to examine the result of analytical estimate, a fair amount of work has been done in the experimental documentation of the local diffusivity and definition of its limitations.

One of the most popular technique of detecting the local diffusivity is the perturbation method, of which descriptions are found elsewhere [2]. Several experiments were carried out in the past, where was estimated either at the sawtooth crash or at the pulsed ECH [3,4]. Gas puff modulation technique was also applied on various tokamaks [5]. Consistency with the power balance analysis was also analytically investigated [6].

In this work, exploratory approach of evaluating the diffusivity of turbulent fluctuations has been undertaken to demonstrate its feasibility. The favorable spatial resolution of less than a centimeter for the reflectometric measurement has been confirmed in the laboratory experiment with a plasma produced by microwave. Its result was first believed to violate the geometrical constraints [7]. However, as the actual correlation measurement in fusion devices reports the similar scale of resolution, further theoretical work was carried out. It has been shown recently that the experimentally documented resolution is consistent with the 2-D full-wave equation analysis [8].

2. Evaluation Method

Assuming turbulent fluctuation is included in the advective non-linearity term of the fluid equation below, and $\tilde{S}$, $\mathcal{L}_d$ representing the free energy source, an operator responsible for that energy,

$$\left(\frac{\partial}{\partial t} + (v + \tilde{v})\cdot\nabla + \mathcal{L}_d\right)\tilde{\xi} = \tilde{S}. \qquad (1)$$

The two point evolution equation of correlation obtained hereby is, after standard diffusive normalization,

$$[\partial t + (v_\theta' - \frac{v_\theta}{r_+})\, r_-\partial y_- - \partial r_-\mathcal{D}_-(r_-,y_-)\partial r_- + \mathcal{L}_d]\, \langle\tilde{\xi}_1\,\tilde{\xi}_2\rangle = \mathcal{J}. \qquad (2)$$

* Institute of Laser Engineering, Osaka University
Yamada-oka, Suita-shi, Osaka-fu 565, Japan

Here, $(r_{\pm}, v_{\pm}) = (r_1 \pm r_2, v_1 \pm v_2)$, $(y_- = r_+\theta_-)$ and $\mathcal{J}(r_-, y_-)$ characterizes the predominantly radial turbulent diffusion of fluctuation [9]. After re-formulation, (2) is reduced to

$$(\partial_t + \tau_f^{-1}) < | \tilde{\xi} / \xi_o |^2 > \equiv D / L_\xi^2 . \tag{3}$$

τ_f^{-1} : fissuring rate

Substituting the standard result of mixing length estimate $< | \tilde{\xi} / \xi_o |^2 > = (\Delta r_t / L_\xi)^2$, equation (3) is re-written as

$$\tau_f^{-1} \approx \frac{D}{\Delta r_t^2} , \tag{4}$$

where Δr_t is the scale length of turbulence. With the assumption that autocorrelation time τ_c is alternatively used for the fissuring rate and Δr_t is substituted with γ_L, we obtain $D \approx \gamma_L^2 / \tau_c$. This assumption is not valid in the case of high shear flow, where radial scattering and poloidal shearing can couple. Actually, the decorrelation frequency $\Delta\omega_k$, which is inverse of the fissuring rate is expressed as $\Delta\omega_k = (\omega_s^2 \Delta\omega_t)^{1/3}$, includes the shear frequency term ω_s. Therefore, the absolute value of diffusivity calls for detailed considerations regarding precise knowledge of the flow velocity shear profile. However, we will show in the later subsections that the relative changes of diffusivity is well described with the equation (4). The physical meaning of equation (4) is that it takes the time defined by the autocorrelation time for a turbulent fluid element to diffuse the distance of one radial correlation length.

It is noteworthy that equation (4) is similar in form to the standard definition of particle diffusivity in a Lorentz gas. Defining the particle flux which goes through the unit surface S after the collision in the scattering volumes as $d\Gamma_x$, and density, collision frequency and mean free path respectively as $n(x)$, ν and ℓ,

$$d\Gamma_x = -\frac{\nu}{6} n(x) e^{-\frac{x}{\ell}} dx + \frac{\nu}{6} n(x) e^{-\frac{|x|}{\ell}} dx . \tag{5}$$

By Taylor expanding $n(x)$, and applying the 2nd kind Euler integral, we obtain

$$\Gamma_x = -\frac{\ell^2 \nu}{3} \left(\frac{dn}{dx}\right)_{x=0} = -D \left(\frac{dn}{dx}\right)_{x=0} . \tag{6}$$

Hence, diffusion coefficient $D = \ell^2 \nu$, which is the square of scale length divided by characteristic time, as in the expression (4).

3. Test of the Evaluation Method

This technique was applied to a discharge, which experiences several L to H and H to L transitions, due to the insufficient heating power for the given condition. The description of the JT-60U reflectometer is found in Ref. 10. One of the most favorable features of this method introduced in this work is that the evaluation of the turbulent diffusivity, which is intimately related to the anamalous transport, can be carried out at any time without perturbing the plasma.

Figures in the upper row of Fig. 1 show the squared coherence well in the L-mode (let column) and at right before the H-mode transition. Time separation of the data acquisition was 140 ms, however, the changes of the spatial position of reflection layers (at ρ = 0.86 and 0.95) were not obvious in the density profile evolution data. Here, standard correlation analysis method was used, and preparation for the bispectral analysis is in progress. It can be clearly in the upper figures that the reduction of coherence down to nearly the noise level of the analysis of ≈ 0.2 is documented at the transition. This is relevant to the decrease of the radial correlation length. Here, the interlayer distance was around 7 times the poloidal ion Larmor radius. Therefore, the speculation is that long wavelength mode of turbulence is manifesting the L-mode confinement (Bohm like features), but at the H-transition the correlation length becomes less than 7 ρ_{pi} ≈ 70 mm to result in the suppression of the radial transport (Gyro Bohm characteristics).

Lower figures show the increase of time lag i.e., the enhancement of the correlation time τ_c from 10 μs to 100 μs at the transition, from which it can be deduced that the reduction of the degree of turbulence was realized at the transition. From the equation (4), it can be concluded that the reduction of the coherence length and the decrease of correlation time is directly relevant to the reduction of the turbulence diffusivity.

In order to evaluate the coherence length, the value of squared coherence was linear fitted. Fig. 2 shows the divertor D_α intensity (upper) as well as the density fluctuation intensity (middle) and the turbulence diffusivity, together with the diamagnetic stored energy. The I_p and B_T are 1.5 MA and 2.5 T, respectively. Although the NB heating power of nearly 24 MW was injected, plasma stays in the marginal state to attain the H-mode, seemingly since this discharge was produced right after the vessel maintenance. It is clearly shown that density fluctuation intensity responds to the transitions, and the reduction of turbulent diffusivity sharply drops at the H-mode transition. Behaviour of D also at the back transition is remarkable. In addition, it is also noteworthy that the edge local diffusivity responds in much faster time scale than the diamagnetic stored energy.

References

[1] M. Mori and the JT-60 Team: Plasma Phys. Controlled Fusion, 36, 181 (1994).
[2] K. Gentle: Plasma Phys. Controlled Fusion, 29, 1072 (1987).
[3] S. K. Kim et al.: Phys. Rev. Lett., 60, 577 (1988).
[4] N. J. Lopes Cardozo and J. C. M. De Haas: Nucl. Fusion, 30, 521 (1990).
[5] K. Nagashima, A. Sakasai and T. Fukuda: Nucl. Fusion, 33, 1677 (1993).
[6] A. C. C. Sips et al.: JET-P(89)80, 123 (1989).
[7] I. H. Hutchinson: Plasma Phys. Control. Fusion, 34, 1225 (1992).
[8] L. G. Bruskin et al.: submitted to J. Japan Soc. Plasma Sci. and Nucl. Fusion Res.
[9] H. Biglari, P. H. Diamond and P. W. Terry: Phys. Fluids, B2, 1942 (1990).
[10] T. Fukuda et al.: Rev. Sci. Instrum., 61, 3524 (1990).

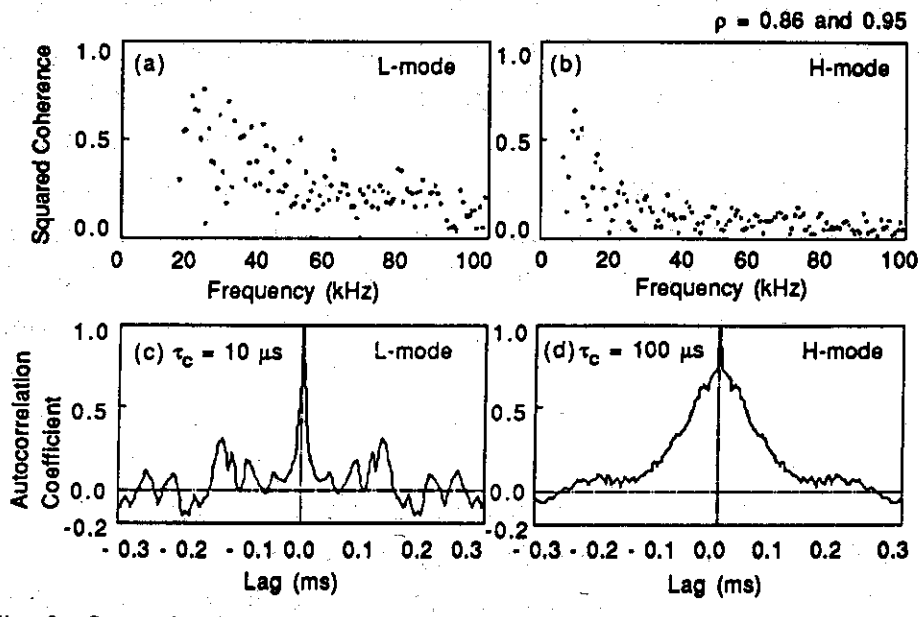

Fig. 1 Squared coherence (upper row) and autocorrelation coefficients (lower row) respectively well in the L-mode (right column) and at right before the H-mode transition (left column). The spatial location of the measurement is ρ = 0.86 and 0.95.

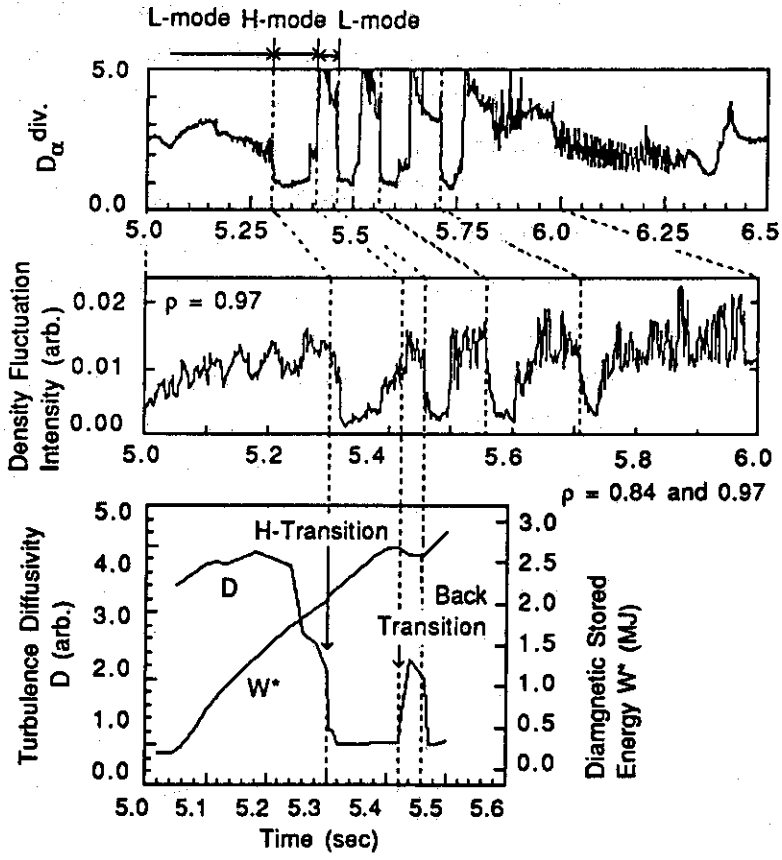

Fig. 2 The waveforms of the divertor D_α (upper), density fluctuation intensity (middle) and the turbulence diffusivity (bottom) evaluated at the repetitive H-mode transitions, together with the diamagnetic stored energy.

12.5 Development of Scanning Collective Scattering Diagnostic at JT-60U

T. Fukuda, G. J. Kramer, M. Mori, K. Nagashima and K. Mima*

1. Introduction

Although having found that ion transport can be near neoclassical level in hot-ion and high β_p H-mode discharges, electron anomaly was still persisting. It has invoked numerous experimental works in search for the consistency with theoretical predictions [1]. However, generic definition of the mode of turbulence in L-mode plasmas was not straightforward. However, reduction of the local electron thermal diffusivity at the edge region of H-mode plasmas and near the null shear region of a heuristic reversed shear discharges provided us a clue as well as an incentive of untangling the physics of electron anomalous transport, which can contribute to the remarkable enhancement of fusion performances of large tokamaks.

Conventional Bragg scattering [2], Fraunhofer forward scattering [3] and beam emission spectroscopy BES [4] were the major schemes employed to resolve the issue hereupon mentioned in the recent tokamak experiment. In this work, descriptions of the collective scattering diagnostic developed for JT-60U are given, which is in general not suitable to resolve the low k_θ components with adequate spatial resolution [5]. However, it is superior (1) to the beam emission method for the high density plasma diagnostic with much higher time resolution without the common mode noise, and (2) to the forward scattering which does not provide the spatial resolution.

2. Description of the Collective Scattering Diagnostic at JT-60U

2.1 Scattering geometry

Scattering geometry was chosen in a way inevitably similar to that of ASDEX [6] and DIII-D [7] as shown in Fig. 1, due to the accessibility limitations, and it has a capability of adjusting the scattering plane orthogonal to the pitch angle of the local magnetic field line, which contributes to the improvement of the spatial resolution [8]. For this function, W-band flexible waveguides are installed to connect to the rigid X-band oversized transmission line. The scene beam is reflected by a graphite made reflector which has a multiple corner cube structure on the surface. The actual reflectivity of the graphite tile was ≥ 80% at 137 GHz and ≥ 98% at 212 GHz. Due to the engineering constraint found in the previous JT-60 divertor interferometer [9], which manifested that

* Institute of Laser Engineering, Osaka University
Yamada-oka, Suita-shi, Osaka-fu 565, Japan

a reflector for the laser wavelength was not feasible on the inbound wall of the tokamak vessel because of the impurity influx generation and degradation of optical flatness, millimeter range wavelength was chosen. The receiving antenna sees the forward scattered radiation from the reflected beam intensity. Here, back scattering component with larger k_θ is assumed to make negligible contributions to the scattered signal. The antenna gain is calculated to be 47.6 dBm.

2.2 Source frequency

The scene frequency was selected at 211.5 GHz in O-mode. An EIO transmitter (Varian Canada Model VKY 2441L1) is used as a source, which provides approximately two watts of power. The actual injection power is approximately 0 dBm, seemingly due to the long transmission line, although the oversized X-band waveguide is mainly used. All the tuning capabilities of the transmitter power supply is remotely controllable with CAMAC interface. Ranges of toroidal magnetic field and density on JT-60U vigorously restrict the practically available frequency. 60 GHz region with X-mode propagation, is limited in terms of the narrow window for the probing wave to pass through right between the lower cutoff and upper hybrid resonance frequencies [10]. In addition, the availability of high power watt level sources as well as the waveguide components are limited to the frequency range up to 220 GHz. Since X-mode is either significantly absorbed by the 2nd ECE harmonic layer, or reflected below 190 GHz, 212 GHz O-mode wave was chosen. The ray refraction is much less stringent than 60 GHz X-mode; i.e., deflection angle is 0.65° when the beam axis misses the plasma center by 100 mm, and absorption of 212 GHz is typically two to three percent.

2.3 Receiver capabilities

The detection range of the normalized wavenumber $k_\theta \rho_i$ varies from 37 to 499 at B_{To} = 3.5 T and T_{io} = 5.0 keV with a parabolic distribution, as evaluated at half the minor radius. However, lowest observable k_θ is reduced down to 18 for the lime integral measurement. The scene microwave beam emitted from an horn antenna with a Fresnel lens propagates without significant divergence at 120 mmϕ.

The detection circuitry employs the forward tracking technique [11] with the adjustment of RF delay line. Therefore, the jitters of the source frequency is in principle negligible. Dynamic range of the RF input is from -30 to -85 dBm, and the analog bandwidth is the IF unit is 4 MHz, which produces the last IF stage frequency of 2 MHz.

2.4 Scanning unit

Unique feature of the developed scattering diagnostic is that k_θ and the scattering position can be swept during the discharge, remotely by a UNIX work station (HP Model 747i). For this purposed the receiving horn antenna has a reflector close to the 0.27 m x 0.61 m racetrack shaped vacuum window. It takes one second to scan reflector for the full k_θ range of 91 to 48.8 m^{-1} at half the minor radius and whole plasma diameter. Multiple scans of up to four in a single discharge is also possible with the time lag of

around 1.5 second. The driving unit is comprised of two precision stepping motors, each for the linear and rotating motion, and they are located out side of the toroidal coils in order to suppress the malfunctions by the magnetic field. The mechanical drive shaft power transmission system with universal joints is utilized to make connection between the driving unit and the mirror stage. As to the controller, Micro control Model TVC98 is used, and it communicates with the workstation via GPIB interface. The time lag is determined by the transfer speed of the scanning position data sent from the scanning controlled to the workstation. The resolutions of the linear and rotation motion are respectively 0.1 mm and 0.01°.

2.5 Data acquisition and control system

The scattering signal is fed to a VXI standard 20 MHz digitize (HP1429B) with 12 bit resolution, and its total memory size is extended to 4 MB. The data transfer speed is literally limited to 750 kB by the GPIB interface between the VXI controller and the workstation. This restriction will be reduced in 1996 with the use of the MXI interface, which provides the data transfer speed of a few MB. The reflected wave intensity is also monitored to examine the possibility of severe ray refraction. The UNIX workstation automatically arms and starts digitizing the input data, making internet communications with the JT-60 main frame. The bursting timing signal is produced by CAMAC modules, which is also controlled by the workstation. It also works as an front end processor; it FFT transform and compress the data and transfers the condensed data set to the main frame. Data acquisition timing can be set by another UNIX work station used to program the tokamak operating conditions.

3. Commissioning test results

The RF power to the receiver excluding the free space transmission in side the vessel was - 30 dBm. Since the free space transmission loss is presumably around 15 dB, there still remains the dynamic range of 40 dB. Actually, even with 30 dB attenuator in the transmission line, well resolvable IF signal was observed. The scanning unit was tested during the tokamak discharge, and it showed no malfunctioning due to the magnetic field. The tranmitter power supply suffer from the noise, which is seemingly induced at the NNBI breakdown. Hoever, it has been overcome by changing the grounding circuitry.

The expected dispersion has been calculated based on the JT-60 L-mode parameters at half the minor radius, in order to examine first the existence of η_i-mode. Hamaguchi-Horton model was used for the simulation [12]. The detection range of wavenumber described above is favorable to examine the elimination of toroidal η_i-mode spectra at 440 m^{-1} and $\omega / 2\pi \leq 133$ kHz. As mentioned earlier, core fluctuation characteristic of reversed shear plasmas would also be a point of interest, in order to examine which mode of turbulence is actually suppressed.

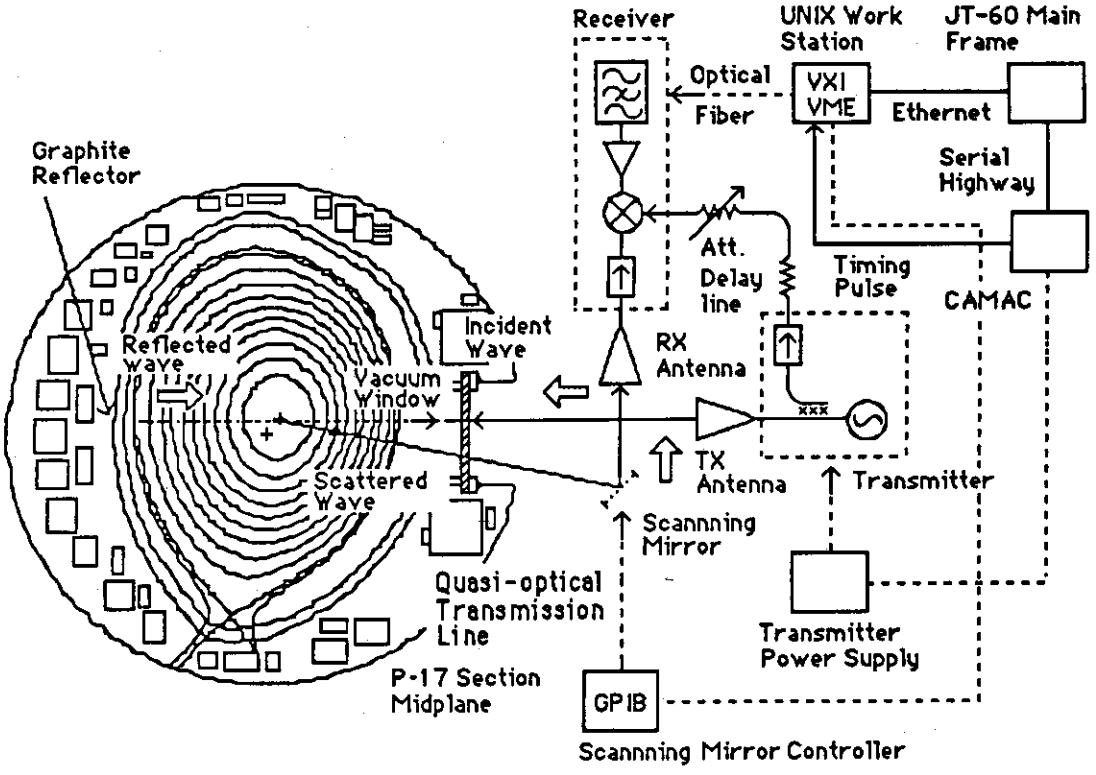

Fig. 1 Diagnostic scheme of the collective Scattering at JT-60U.

References

[1] P. C. Liewer: Nucl. Fusion, 25, 543 (1985); R. R. Domingues and R. E. Walz: Nucl. Fusion, 27, 65 (1987).

[2] R. E. Slusher and C. M. Surko: Phys. Fluids, 23, 472 (1980).

[3] D. E. Evans et al.: Plasma Phys., 24, 819 (1982).

[4] R. J. Fonck et al.: Plasma Phys. Contr. Fusion, 34, 13 (1993).

[5] E. Holzhauer and J. H. Massig: Plasma Phys., 20, 867 (1978).

[6] E. Holzhauer, D. Dodel and ASDEX Team: Rev. Sci. Instrum., 61, 2117 (1990).

[7] R. Philipona et al.: Proc. 17th EPS Conf., 14b Part IV, 1604 (1990).

[8] P. Devynck, X. Garbet, C. Laviron et al.: EUR-CEA-FC-1453 (1992).

[9] T. Fukuda et al.: J. Nucl. Mater., 162, 258 (1989).

[10] N. Brez et al.: Rev. Sci. Instrum., 59, 1538 (1988).

[11] J. L. Doane: Rev. Sci. Instrum., 60, 1080 (1989).

[12] B. -G. Hong and Horton: Phys. Fluids, B2, 978 (1990).

12.6 Installation of New Power Divider in ECE Transmission Line

A. Isayama, N. Isei, S. Ishida, M. Sato, C. Hwang[1)]
1) Korea Atomic Energy Research Institute

1. Introduction

The relocation of diagnostic systems followed the installation of NNB(negative neutral beam) system. The diagnostic port for grating polychromator system became unavailable because the diagnostic port for charge exchange recombination scattering was installed instead of it. In order to operate all of the present ECE systems ---Fourier transform spectrometer system(FTS)[1], grating polychromator system(GPS)[2] and heterodyne radiometer system(HRS)[3]--- with only one diagnostic port which had been used for FTS and HRS until October 1995, a new power divider is installed in FTS-HRS transmission line to lead ECE to GPS. The power divider is located in the diagnostic room I after 40m transmission line from the ECE diagnostic port in the torus hall. Schematic views of waveguide configuration in the diagnostic room I before and after the installation are shown in Fig.1.

2. Specification of power divider

The power divider is made in St. Andrews university in U.K. The design of it is shown in Fig.2. The waveguide is WRJ-3 and the flange is BRJ-3. There are wire grids in the power divider and they are arranged with a checked pattern to output non-polarizing wave. Part of input power is reflected on the wire grids and rest of them is transmitted. The ratio of reflection power to transmission power is designed to be 4:1 at 300GHz since GPS needs stronger radiation power to measure ECE. The transmission characteristic calculated by St. Andrews University is shown in Fig.3. The fraction of reflectance becomes large as frequency increases since the ratio of wavelength to the wire grids becomes small.

3. Measurement and the results

First, we set the power divider in front of the Fourier transform spectrometer in order to measure the reflection and transmission characteristics of the power divider. The input terminal of the power divider was oriented to the blackbody radiation source with liquid nitrogen temperature or room temperature using Eccosorb. One of the output terminals of the power divider was connected to the Fourier transform spectrometer and the other was closed by Eccosorb to prevent unnecessary radiation. The frequency spectrum were obtained by Fourier-transforming the interferogram.

Transmittance and reflectance are defined as the ratio of reflection power and transmission power to that for replacing straight waveguide for the power divider. The transmittance is straightly increases as frequency increases, and the reverse is the case for the reflectance as shown Fig.4. The measured transmittance agrees well with the calculated one. In the frequency region of 100-250GHz, where we use for electron temperature measurement, 85-90% of input power is led to GPS. The sum of transmittance and reflectance is almost unity in a whole range. Thus the loss in the power divider is as small as that in the straight waveguide.

Secondly, we set the power divider in the transmission line where it is normally set in ECE measurement in order to determine the calibration factor for ECE measurement. The blackbody source was set at the position 'X' in Fig.1(b). Since radiation from the source takes about 5m longer transmission line and there are 2 bends and another power divider(type A) in the transmission line, the intensity becomes much weaker than that in the former measurement. Roughly speaking, the intensity is 10 times weaker. In order to retain equivalent S/N ratio, the number of data must be increased by 100 times. About 600,000 data were taken and averaged to determine the calibration factor.

Thirdly, we closed the output terminal to GPS with Eccosorb in order to prevent unnecessary wave from GPS transmission line. Comparing the spectrum for the second experiment and that for the third experiment, the reflectance in the former experiment is larger than that in the latter one over about 280GHz as shown in Fig.5. The reason is explained as follows. That is, in the GPS transmission line, four grating bends are used as low-pass filter to cut unnecessary harmonic wave[4]. The transmittance of grating bends is shown in Fig.6. Radiation over about 280GHz is reflected on them and cannot reach GPS detector. The reflected wave goes back and can enter the FTS-HRS transmission line.

The ratio of power to each diagnostics(FTS, GPS, HRS) is shown in Fig.7. The ratio of the power led to FTS to total input power does not show significant change in wide frequency range. The radiation which will be led to FTS transmits the wire grids in the first power divider(type B) whose transmittance increases with frequency as mentioned above and reflects on the wire grids in the second power divider(type A) whose reflectance decreases with frequency as shown in Fig.8. Thus the frequency dependence becomes small after the two power dividers. On the other hand, the power to HRS become nearly zero at 130GHz. Since observation frequency range of HRS is 176-188GHz, several percent of total input power is led to HRS.

4. Summary

A power divider is installed in FTS-HRS transmission line to operate all of the present ECE measurement systems. The ratio of reflection power to transmission power is designed to be 4:1 at 300GHz. At 200GHz, the percentage of power led to GPS, FTS and HRS is 86%, 8% and 6% of input power, respectively. By introducing the power divider, we can get an outlook for full operation of present ECE measurement systems.

References

[1] SATO M., ISEI N. and ISHIDA S. : JAERI-M 93-057, "Development of Fourier Transform Spectrometer System", 359 (1993).

[2] ISHIDA S., NAGASHIMA A., SATO M., ISEI N. and MATOBA T. : Rev. Sci. Instrum., 61, 2834 (1990).

[3] ISEI N., SATO M., ISHIDA S., UCHINO K., NAGASHIMA A., MATOBA T. and OYEVAAR T. : Rev. Sci. Instrum. 66, 413 (1995).

[4] SATO M., ISEI N. and ISHIDA S. : J. Plasma and Fusion Research 71, 748 (1995) [in Japanese].

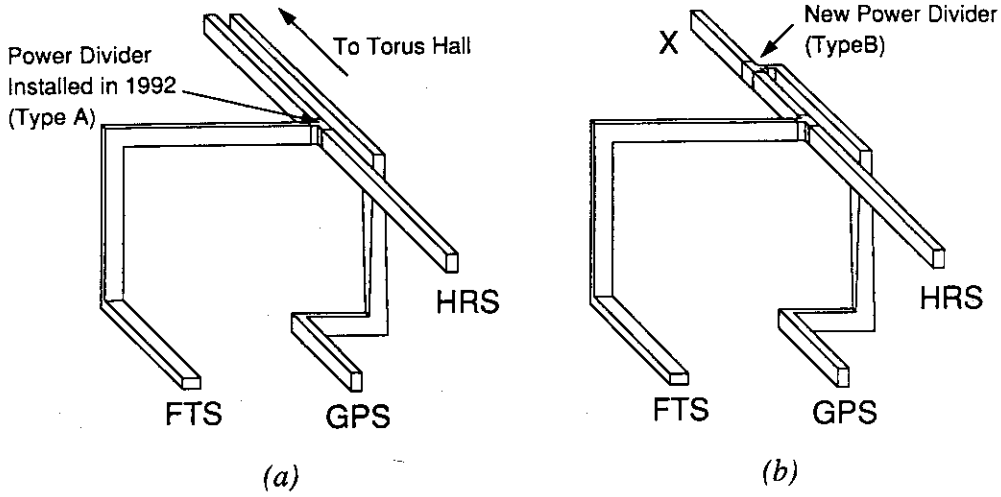

Fig.1: Schematic views of ECE transmisson line in diagnostic room I (a)before modification and (b)after modification.

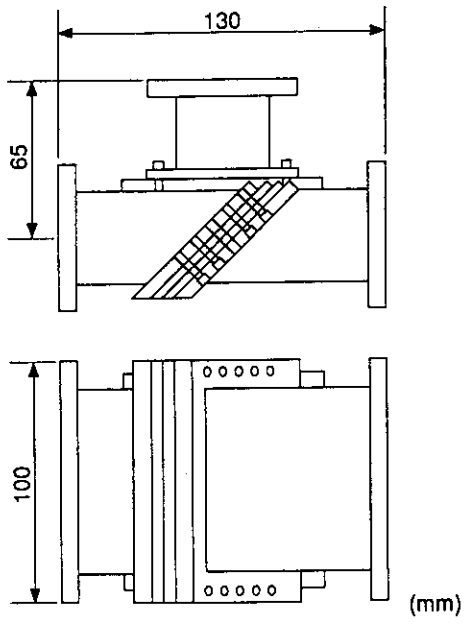

Fig.2: Design of power divider

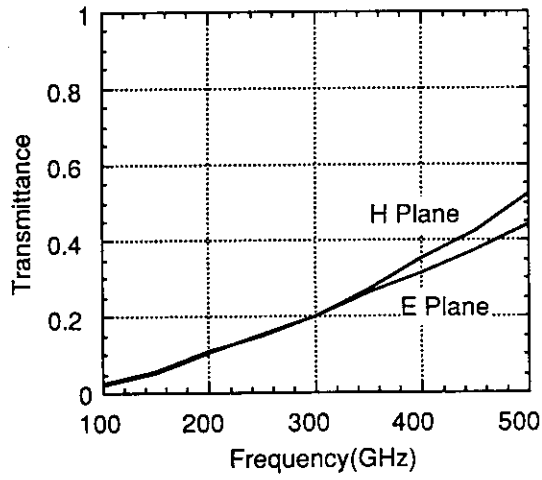

Fig.3: Transmission characteristic of power divider obtained by calculation. The ratio of transmisson power to reflection power is dedigned to be 1:4 at 300GHz.

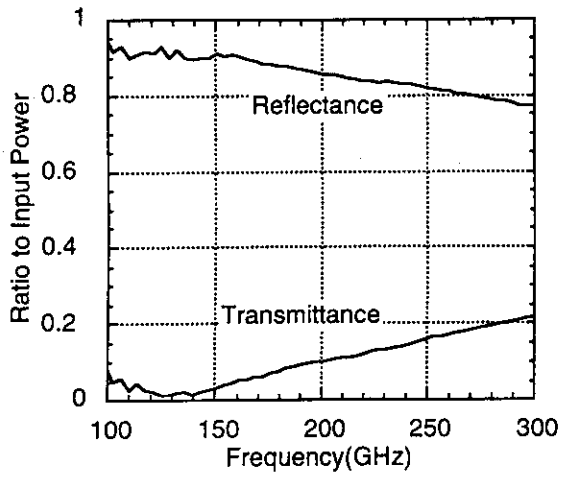

Fig.4: Transmittance and reflectance of power divider.

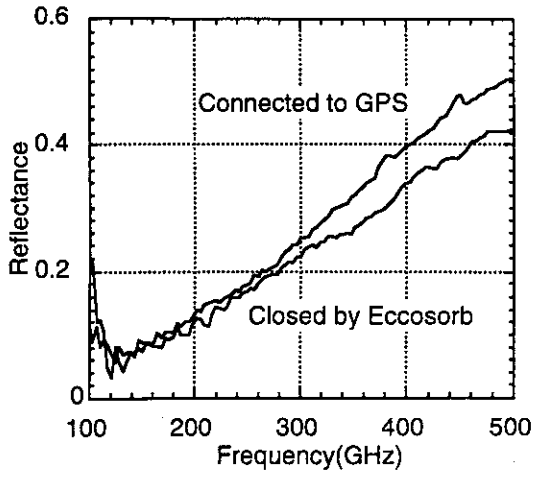

Fig.5: Reflectance for the case of connencting the output terminal to GPS and the case of closing it with eccosorb.

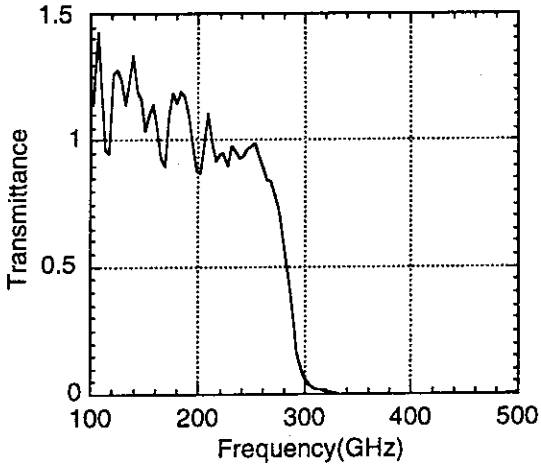

Fig.6: Transmission characteristic of grating bends.

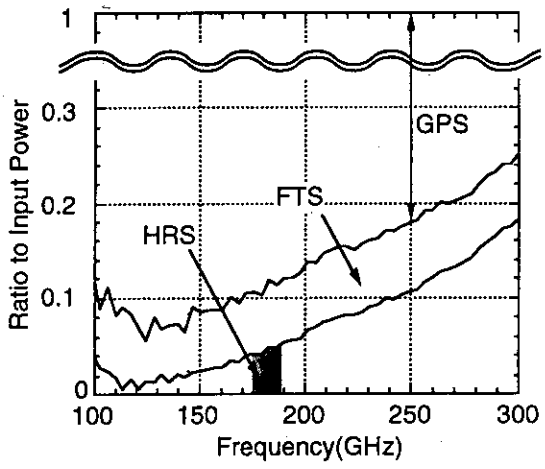

Fig.7: The ratio of power led to each diagnostics(FTS, GPS, HRS).

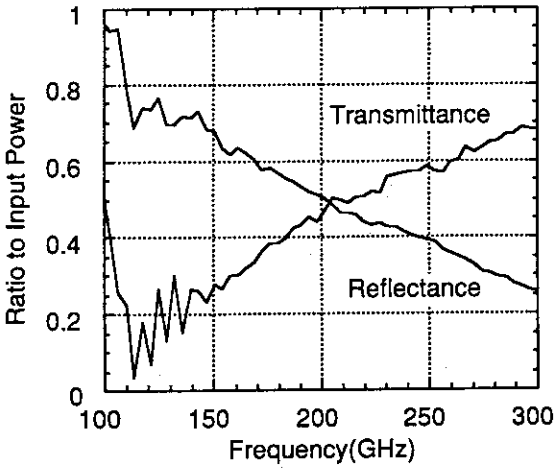

Fig.8: Transmittance and reflectance of power divider installed in 1992(type A). The ratio of reflection power to transmission power is designed to be 1:1 at 200GHz.

12.7 Fast sampling system and spectrum analyzing system for magnetic fluctuation

M. Saigusa, S. Moriyama, H. Kimura, Y. Neyatani, T. Fukuda, K. Tobita

Abstract A fast sampling system connected to present Mirnov coils was prepared for measuring toroidicity-induced Alfvén eigen (TAE) modes. On the other hand, the spectrum analyzing system, which consists of two spectrum analyzers connected to the present Mirnov coils and the RF probes, was prepared for the TAE modes and ion cyclotron emission.

1. Fast sampling system

Mirnov coil array is effective for investigating Toroidicity-induced Alfvén eigen (TAE) modes[1] in many tokamaks. However, the present sample rate (200 kHz) of the Mirnov coil system in JT-60U was prepared for the low frequency fluctuation whose frequency is less than 100 kHz[2]. Therefore, the fast sampling system connected to the Mirnov coil array was prepared for measuring toroidal mode number and fast behavior of the TAE mode. The fast sampling system consists of four digitizers (HP E1429B, 2 ch/module), a 2 GBytes hard disk and a control program installed in the workstation prepared for mm-wave scattering system constructed by T. Fukuda[3]. The four digitizer modules were also installed in the VXI main frame of mm-wave scattering system.

The basic specifications are shown in Table 1. The connected Mirnov coils are arrayed in a toroidal direction as shown in Fig.1. The signal flow diagram is shown in Fig.2. There are two measured modes which are the continuous mode and the burst mode similar with the mm-wave scattering system. The time sequences of two modes are shown in Fig.3.

Table. 1 Present basic specification

Sampling Rate	0.1-20 MHz (1, 2, 5 Step)
Number of channels	8 ch (only 1 ch data is sent to ISP)
Number of samples /ch	512 kSa/ch (HP E1429B, 2 ch/module) (1,536 kSa/ch using HP E1488A)
Upper Frequency limit	about 300 kHz
Sample points/a burst	2048 x n points (n=1, 2, 4)
Frequency resolutions	Sample rate/(2 × sample points) 244 Hz at 1 MHz sampling rate with 2048 samples

References

1) C. Z. Cheng et al., Ann. Phys. NY 161, 21 (1984).
2) Y. Neyatani, et al., 14th Symp. of Fusion Engineering, San Diego (1991).
3) T. Fukuda, et al., Sec. 12.5 of this report.

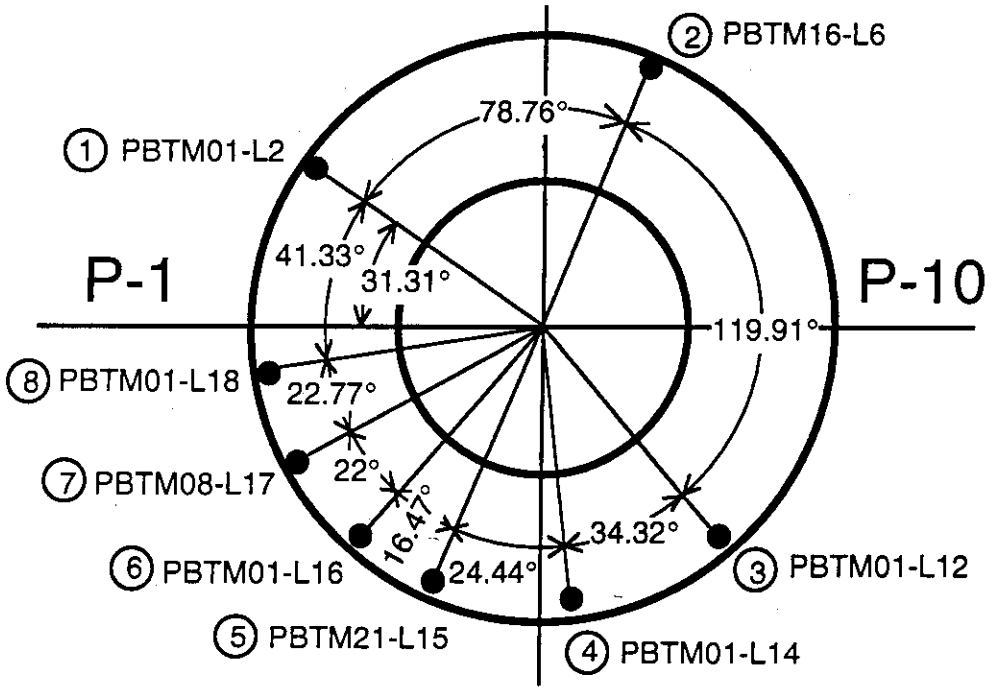

Fig. 1 Positions of Mirnov coils connected with a fast sampling system

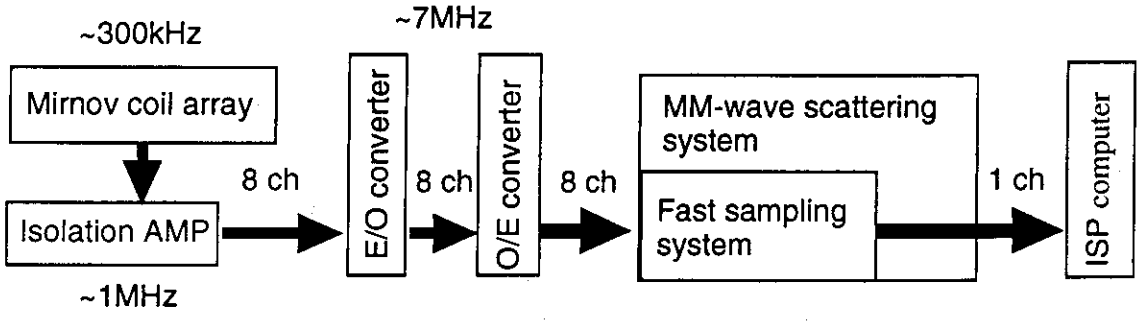

Fig. 2 Signal flow diagram for fast sampling system

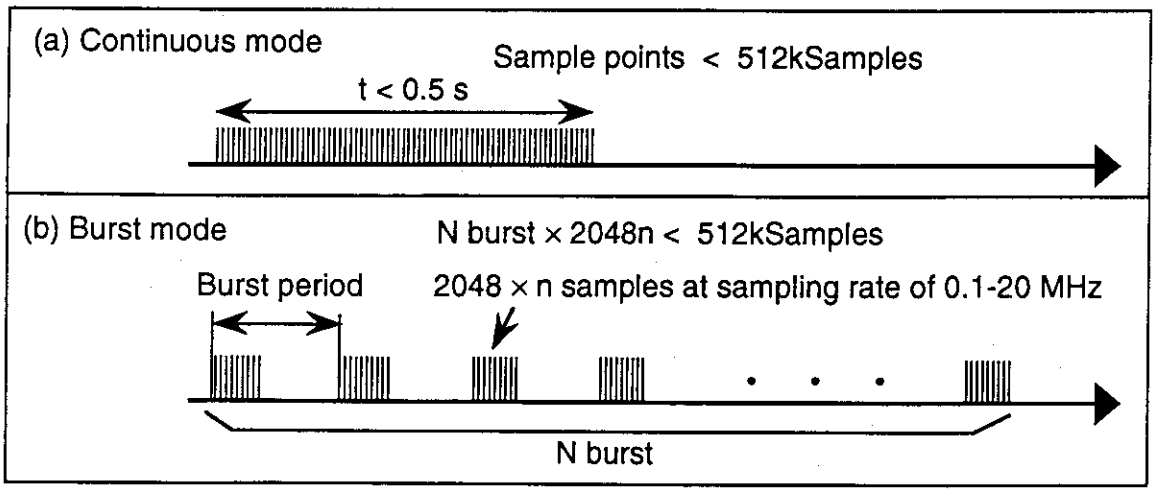

Fig.3 Time sequence of the two sampling modes

2. Spectrum analyzing system

Two spectrum analyzers are used for absolute frequency measurement of the Milnov coil signal and the RF probe signal. The Milnov coil signal is usually used to investigate TAE mode as shown in the previous section, and the RF probe signal is usually used to investigate ion cyclotron emission from the high energy particles. Schematic diagram of the system is shown in Fig. 4.

The spectrum analyzer scan the frequency in a period of T_{scan} and repeat such scan every T_{repeat} with some interval time. T_{scan} and T_{repeat} vary with the required frequency span and the resolution bandwidth. Typical values of setting and T_{scan} and T_{repeat} are shown in Table 2. The signal intensity in such frequency scan is converted to the voltage signal output which is called "video-out" signal as well as spectrum graphic on the display of the analyzer. Another signal out put called "high-sweep" signal which is high during the frequency scan (for T_{scan}) and is low during the interval time. The "high-sweep" signal is used in the graphic display program on the ISP computer to make relation between the signal amplitude and the frequency. An example of the signal output is shown in Fig. 5. These signals are digitized by the multiplex analog-digital converter, and are converted to optical signal by the EOH module, and are sent to the ISP computer through TMDS (Track #17).

Table. 2 Typical settings of the spectrum analyzers

Main Purpose	TAE-mode	Ion Cyclotron Emission
Spectrum Analyzer	HP-8591E	HP-8594E
Frequency Range	100 kHz - 300 kHz	~0 MHz - 200 MHz
Resolution Band Width	3.0 KHz	1.0 MHz
Dynamic Range	80 dB	80 dB
Sweep Time : Tsweep	100 msec	20 msec
Repeat Time : Trepeat	~150 msec	~ 70 msec
Sampling Time	20 μsec	20 μsec
Period of Data Acquisition	15 sec	15 sec

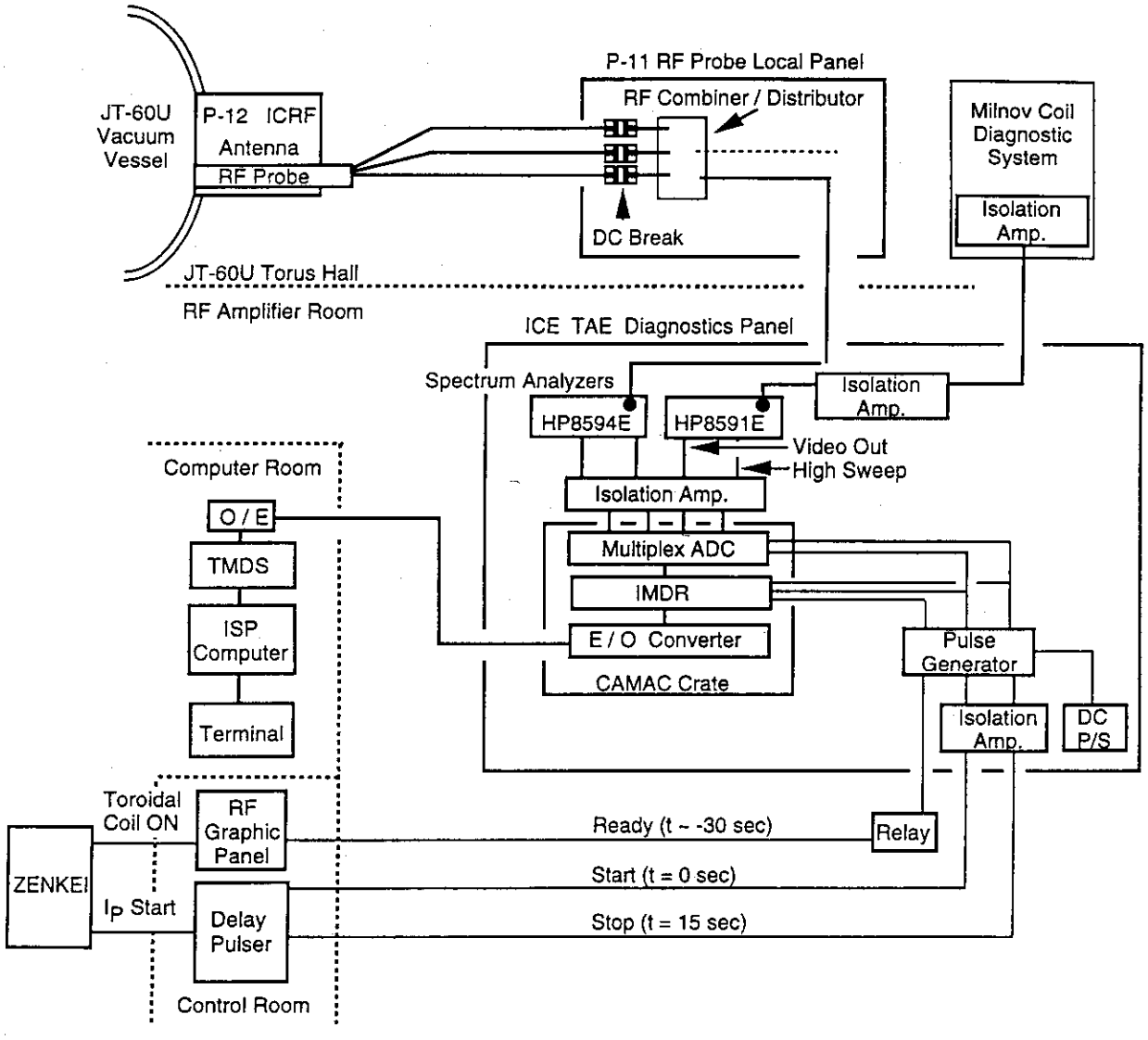

Fig. 4 Schematic diagram of the system

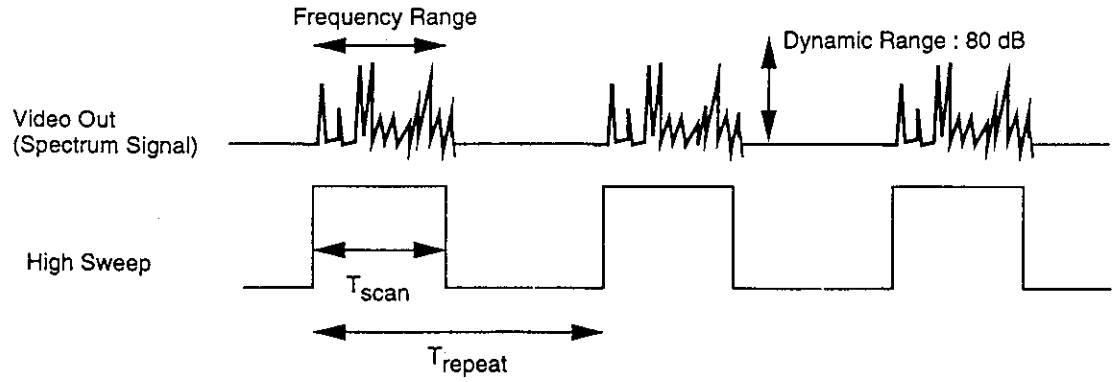

Fig.5 An example of the signal output

12.8 Fast Reciprocating Probe System for Local Scrape-off Layer Measurements in front of The Lower Hybrid Launcher

N. Asakura, S. Tsuji-Iio[1], Y. Ikeda, Y. Neyatani, M. Seki

1. Introduction

A fast reciprocating probe system (RPS) has been incorporated into a multi-junction launcher system for Lower Hybrid (LH) wave injection. It has provided high spatially-resolved profiles of the local electron temperature T_e and density n_e in the scrape-off layer (SOL). Measurement of the local plasma parameters in front of the LH launcher is crucial to study the improved coupling mechanism of the radio frequency wave to the core plasma [1]. At the same time, SOL plasma data such as characteristic length and fluctuations between the last closed magnetic flux surface (LCFS) and the vacuum vessel wall are required to investigate the plasma transport mechanism in the plasma boundary region. Details are described in Rev. Sci. Instrum., Vol.66, No.12, p.5428 (1995).

2. System Description

2.1 Location and drive components: Fig. 1 illustrates the location of the RPS and the LH launcher which has 16 oversized waveguides. The axis of the probe head is located 36 cm below the equatorial plane. The starting location of the probe head reciprocation can be changed from 2.7 to 17.7 cm horizontally behind the front edge of the launcher face, using a stepping motor drive unit mounted on the launcher support. During a fast scanning operation, the probe head is reciprocated over the stroke of 25 cm with the pneumatic cylinder drive and springs which are fixed on the probe system support.

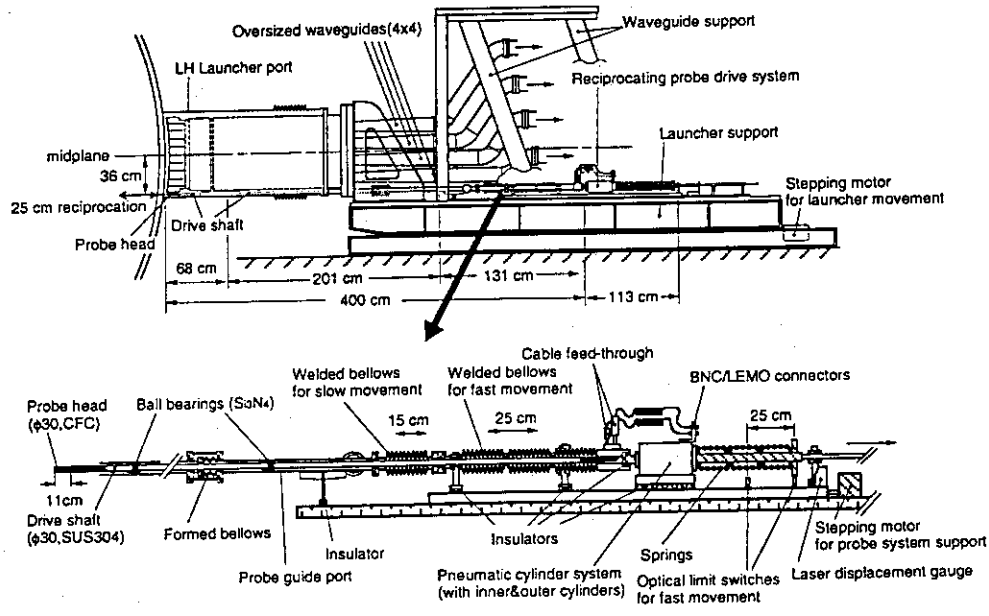

Fig. 1: *Fast reciprocating probe system (RPS) is incorporated into LH launcher.*

A 4-m long stainless steel drive shaft (SUS304) connects the piston of the pneumatic cylinder to the probe head. The long shaft consists of three circular pipes. Stainless steel joints are used, and the shaft is electrically connected to the probe head. Two sets of 8 silicon-nitride (Si_3N_4) ball bearings are built in the joints reducing the drag force during

[1]Present address: Research Laboratory for Nuclear Reactors, Tokyo Institute of Technology.

the movement. These provide electrical insulation of the drive shaft from the shaft guide and the probe guide port. The shaft bends a maximum of 1.2 mm at the middle of the joints when stationary, which increases to 1.7 mm during operation. However, this is smaller than the clearance of 3–4 mm from the inner surface of the port. The total mass of the moving components is about 20 kg.

The drive components of the RPS consist of a compact pneumatic cylinder and steel springs (SUP10). The inside of the pneumatic cylinder is divided into two layers; inner cylinder (piston room) and outer cylinder (air reservoir). A solenoid valve is mounted on the pneumatic cylinder and separates the two layers. Opening the solenoid valve, the compressed air with a pressure of 4 atm is released into the inner cylinder, and this produces the forward thrust. When the probe reaches an optical forward-limit switch, the valve switches the direction of the compressed air to the left side of the piston room, starting the backward movement. In the event of a power or valve failure, the backward-thrust of springs brings the probe to the starting position; i.e behind the first wall.

Two sets of Si_3N_4 ball bearings, alumina cylinders and poly-ether-ether-ketone (PEEK) plastic insulators electrically isolate the moving components (the probe head, drive shaft, edge-welded vacuum bellows and cable feedthrough) from the probe system support and the launcher support (grounded to the vacuum vessel potential). This isolation prevents any bending force to the drive shaft, which would be caused by an axial current interacting with the magnetic field during the probe insertion.

2.2 Probe head assembly: Fig. 2 shows the probe head assembly. Carbon fiber composite (CC312) is used for the probe body and electrodes. This provides maximum bending and compressive strengths and high resistance to the thermal shock experienced during immersion in the boundary plasma.

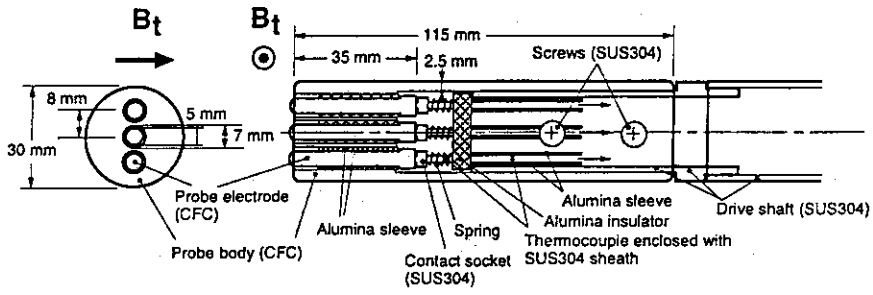

Fig. 2: *Probe head assembly viewed from the front (left), and cross-sectional view (right).*

Three dome-type Langmuir probe electrodes are supported in alumina sleeves, and are electrically insulated from the probe body. Each probe electrode is 5 mm in diameter with its spherical apex protruding 1 mm into the plasma. A separation between the adjacent electrode axes is 8 mm, and the three electrodes are arranged in the poloidal direction to prevent shadowing of the SOL plasma flow along the local field line. The electrical signal from the electrode is transmitted to a stainless steel sheath of a chromel-alumel thermocouple, through a stainless steel contact socket. The thermocouple measures the local temperature at the contact socket and monitors the heat flux to the probe electrode.

2.3 Operation and data aquisition: Operation and data aquisition of the RPS are preprogrammed by a CAMAC system and a microcomputer (Apple, Macintosh Quadra 840AV). The probe reciprocation is initiated by a trigger signal from the CAMAC timing module, which opens the solenoid valve for the pneumatic cylinder, triggers a function generator and starts to sample data.

Movement of the probe head during a reciprocation for the SOL plasma profile measurement is shown in Fig. 3. The fast displacement is measured with a laser displacement

gauge (KEYENCE, LB-300) using an infrared (780 nm wavelength) semiconductor laser, which provides high spatial resolution of less than 1 mm and fast time response of 1 ms. These values are several times better than the standard linear potentiometer, and therefore is mainly used to monitor the displacement of the probe system support relative to the LH launcher support.

The voltage waveform for the Langmuir probe measurement is preprogrammed into the function generator, and amplified by two series-connected power amplifier. The maximum voltage is ±400 V and current is 2 A. For the double probe method, a triangle-waveform voltage with the peak voltage of ±300 V and the period of 4 ms is typically applied between the two probe electrodes. The third probe electrode is used to measure the floating potential relative to the potential of the probe body. The potential of the probe body referenced to the vacuum vessel potential is also measured.

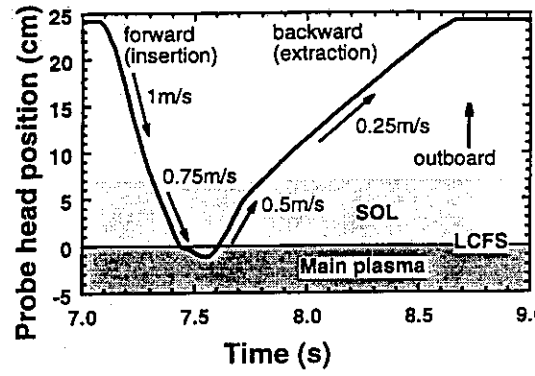

Fig. 3: *Movement of the probe head in the plasma boundary. The starting location is changed by a stepping motor drive system.*

3. Measurement

3.1 Fitting: Since the probes are inserted horizontally at 36 cm below the equatorial plane, the probe tips are located on different magnetic surfaces. The displacement between the probe tips corresponds to 2−3 mm in the plasma minor radial direction, depending on a local curvature of the magnetic surface. Fig. 4 shows the floating potential profiles measured by two floating probes during a probe insertion. The LCFS location is determined by the equilibrium code FBI/SELENE. The accuracy of the LCFS is about ±5 mm, and this uncertainty is indicated by the shaded area. In the vicinity of the LCFS (in particular inside the LCFS), the large gradient of the floating potential profile, 15−20 V/mm is observed. Whereas there is significant correlation of the fluctuations in the two signals, the difference of the floating potential between the two probes is increased up to 20−25 V inside the LCFS. A new probe head, which is designed to fit the curvature of the local field line (poloidally tilting angle of 15°), will be installed in 1996.

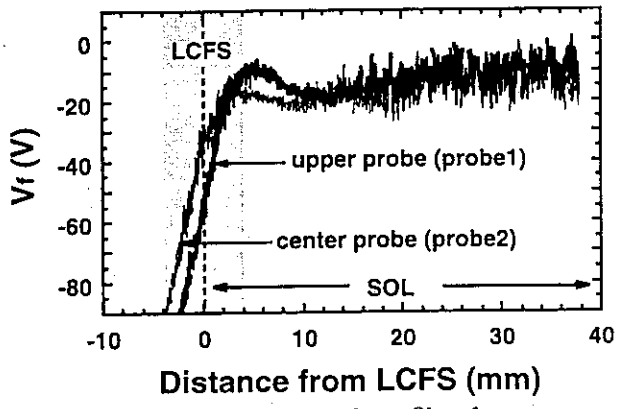

Fig. 4: *Floating potential profiles for upper and center probes during a probe insertion as a function of the probe head distance from the LCFS.*

As a result, the double probe method is mostly used to deduce local I_s^+ and T_e with fitting the following function to current-voltage, $I-V$, characteristics;

$$I = I_{s,2}^{+} \frac{-1 + \exp\left[(V-\Delta V_f)/T_e\right]}{1 + (I_{s,2}^{+}/I_{s,1}^{+})\exp\left[(V-\Delta V_f)/T_e\right]}, \qquad (1)$$

where $I_{s,1}^+$ and $I_{s,2}^+$ are I_s^+ for the probe channels 1 and 2, and ΔV_f is the potential difference between the probes. n_e is given by $2I_s^+/(eA_\perp c_s)$, where $A_\perp$ is the effective

collection area of the probe (assuming the area projected to the local field line for the ion and electron sides; 8 to 9 mm^2 depending on the pitch angle of the magnetic field) and $c_s = [k(T_i + T_e)/m_i]^{1/2}$ is the ion acoustic speed (assuming that $T_i = T_e$).

3.2 Results during LH wave injection: During an extraction (backward movement) of the probe, 1 MW at the LH frequency of 2 GHz is injected into the deuterium discharge with $I_p = 1.5$ MA, $B_t = 4$ T and $\bar{n}_e = 0.8\times10^{19}$ m^{-3}. Good coupling of the wave to the plasma, where the fraction of the reflected power is less than 10%, is obtained when the distance between the LCFS and the launcher face, δ, is 11 cm at the equatorial plane. This distance is a few cm smaller than the critical distance to obtain good coupling [1]. Local n_e and T_e profiles between the LCFS and the launcher front are compared in Fig. 5(a) and (b), respectively. Since a local curvature of the magnetic flux surface in the outer SOL region is larger than that of the first wall (Fig. 5(c)), Ψ_{wall} represents the inner flux surface touching the first wall. The location of the LH launcher front is 5 mm outside the first wall.

Two SOL regions with different characteristic lengths are observed in the T_e and n_e profiles. The inner SOL extends up to 4 cm outside the LCFS, and the n_e and T_e profiles have small e-folding lengths, λ_{n_e} and λ_{T_e}, of 2.0 cm and 2.9 cm, respectively. During the LH wave injection (i.e. probe extraction), the profiles in the inner SOL are similar to those during OH (i.e. probe insertion). The n_e rises inside the LCFS during the LH injection, whereas T_e remaines at 120 eV. In contrast, a significant local heating is observed in the outer SOL region (i.e. in front of the LH launcher mouth). The T_e profile with λ_{T_e} of 6.2 cm in OH changes to a nearly flat profile since the heating power is supplied from the LH wave rather than cross-field diffusion. While, λ_{n_e} stays at 4.5−5.5 cm, thus the cross field diffusion of the particles is not enhanced in the SOL region. Local n_e in front of the LH launcher mouth is $(7-10)\times10^{16}$ m^{-3}. Measured n_e profiles at different values of δ are applied to calculate the reflection coefficient using the multi-junction Launcher analysis code [2], and are able to quantitatively explain the large reduction of the reflection coefficient when the local n_e is higher than the cut-off density of $\sim 5\times10^{16}$ m^{-3}.

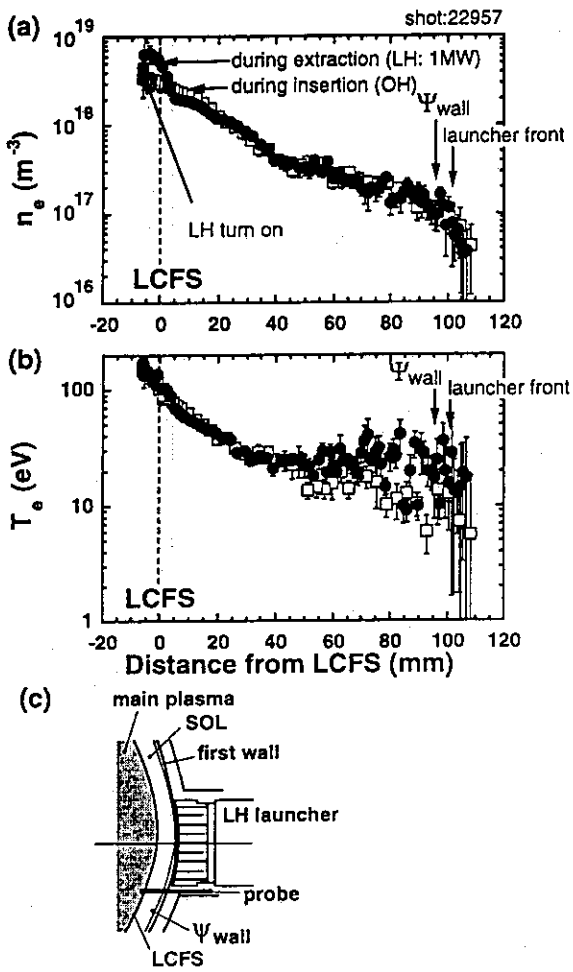

Fig. 5: *(a) n_e and (b) T_e profiles for the good coupling case. (c) locations of LCFS, probe head and the launcher front are illustrated.*

References:

1) Ikeda Y., *et al.*: J. Vac. Sci. Technol. A 8, 534 (1990).
2) Tuccillo A.A., *et al.*: Proceedings of 11th Topical Conference on Radio Frequency in Plasmas, Palm Spring, CA, 1995 (American Institute of Science, New York, in Press).

Acknowledgments

The authors wish to acknowledge the dedicated efforts of the members of Japan Atomic Energy Research Institute in the support of the JT-60U experiments reported here. They also wish to express their gratitude for domestic and international collaborations for the JT-60U program. The contributions of collaborators from many institution and universities have been critical to the success of these experiments.